

## **Characterization of the cell-substrate interface using surface plasmon resonance microscopy**

Eva Maria Kreysing

Schlüsseltechnologien / Key Technologies

Band / Volume 189

ISBN 978-3-95806-369-3





Forschungszentrum Jülich GmbH  
Institute of Complex Systems  
Bioelectronics (ICS-8)

# **Characterization of the cell-substrate interface using surface plasmon resonance microscopy**

Eva Maria Kreysing

Schriften des Forschungszentrums Jülich  
Reihe Schlüsseltechnologien / Key Technologies

Band / Volume 189

---

ISSN 1866-1807

ISBN 978-3-95806-369-3

Bibliografische Information der Deutschen Nationalbibliothek.  
Die Deutsche Nationalbibliothek verzeichnet diese Publikation in der  
Deutschen Nationalbibliografie; detaillierte Bibliografische Daten  
sind im Internet über <http://dnb.d-nb.de> abrufbar.

Herausgeber  
und Vertrieb:           Forschungszentrum Jülich GmbH  
                                  Zentralbibliothek, Verlag  
                                  52425 Jülich  
                                  Tel.: +49 2461 61-5368  
                                  Fax: +49 2461 61-6103  
                                  zb-publikation@fz-juelich.de  
                                  www.fz-juelich.de/zb

Umschlaggestaltung:   Grafische Medien, Forschungszentrum Jülich GmbH

Druck:                    Grafische Medien, Forschungszentrum Jülich GmbH

Copyright:              Forschungszentrum Jülich 2018

Schriften des Forschungszentrums Jülich  
Reihe Schlüsseltechnologien / Key Technologies, Band / Volume 189

D 82 (Diss., RWTH Aachen University, 2018)

ISSN 1866-1807  
ISBN 978-3-95806-369-3

Vollständig frei verfügbar über das Publikationsportal des Forschungszentrums Jülich (JuSER)  
unter [www.fz-juelich.de/zb/openaccess](http://www.fz-juelich.de/zb/openaccess).



This is an Open Access publication distributed under the terms of the [Creative Commons Attribution License 4.0](https://creativecommons.org/licenses/by/4.0/),  
which permits unrestricted use, distribution, and reproduction in any medium, provided the original work is properly cited.

It's still magic even if you know how it's done.

Terry Pratchett – A hat full of sky



# Acknowledgments

This work would not have been possible without the support and help of many great people. I would therefore like to thank:

- Prof. Dr. Andreas Offenhäusser for entrusting me with this project, for supporting my quest for accuracy and for sharing my enthusiasm for science, for being a supervisor I could always rely on.
- Hossein (Erfan) Hassani, for working with me in this project during the last years. For writing the analysis software for the SPRM, for taking crazy ideas seriously and for so much fun in this project.
- My brother Dr. Moritz Kreysing for supporting my work with scientific input and for the critical questions nobody else dared to ask. These questions made this work what it is.
- Prof. Dr. Timo Betz for inspiring discussions regarding the measurement of action potentials.
- Dr. Silke Seyock for her interest in my work, her support regarding the correlation of SPRM and FIB and for returning to the institute to finish our collaboration successfully.
- My father Klaus Kreysing for working with me on the chemical background of this work, for supporting my interest in neurobiology since school times and for proofreading.
- Daniel Haarhoff for his constant and absolute support. For discussing my work every single day during the last three years, for scientific and technical discussions, proofreading and introducing me to Terry Pratchett.

- Michael Prömpers for producing homogeneous gold layers and photoresist markers on the most fragile substrates imaginable.
- Dr. Sabrina Weidlich for her support of the lab work and manuscript writing.
- Tina Breuer, Timm Hondrich and Dr. Vanessa Maybeck for the neuron-isolation, support in the lab and Dr. Vanessa Mayback for proofreading.
- Elke Brauweiler and Dr. Elmar Neumann for the FIB cuts and the S(T)EM images.
- Nico Hampe for his help in establishing a protocol for cardiomyocyte culture on gold, for confocal microscopy images and for the help with the installation of an additional microscope on my setup.
- Prof. Dr. Hiroshi Kano for teaching me accuracy in SPRM alignment in his lab.
- Prof. Dr. Koji Toma for building the first prototype of the SPRM and for the discussions about possible changes.
- Dr. Mana Toma for introducing me to the institute and explaining the prototype setup.
- Fabian Brings, Dr. Tamar Ziehm, Mathis Ernst, Prof. Dr. Bernhard Wolfrum, Prof. Dr. Rudolf Merkel, Prof. Dr. Jochen Guck, Dr. Alexey Chizhik, Prof. Dr. Jörg Enderlein for scientific discussions.
- Dr. Thorsten Auth and the fellows of the my graduate school "IHRB BioSoft" for many interesting discussions.
- The mechanical workshop of the ICS-8 for building many different parts for the setup.

- The IT team for finding solutions to store giant volumes of data.
- My mother Mariele Kreysing and my half-twin sister Dr. Anna Kreysing for their constant and absolute personal support.



# Zusammenfassung

Im Rahmen dieser Arbeit wurde ein verbesserter Oberflächen-plasmonen-resonanz-mikroskopie- (SPRM) Aufbau entwickelt, der einen Projektor-basierten SPRM-Weitfeld-modus mit mehreren SPRM-Scanningmodi zur Untersuchung der Zell-Substrat-Schnittstelle kombiniert.

Weitfeld SPRM kann zur qualitativen Abbildung der Zell-Substrat-Adhäsionsflächen verwendet werden. Hier ist die Auflösung stark von der Lichtquelle abhängig. Während kohärentes Laserlicht zu Speckle-Rauschen führt, welches die Auflösung kleiner zellulärer Strukturen wie neuronaler Dendriten behindert, ermöglicht die Verwendung eines Projektors als inkohärente Lichtquelle eine hochauflösende Bildgebung.

Mit dem Scanning SPRM kann der Zell-Substrat-Abstand quantitativ bestimmt werden. Bisher wurde die Genauigkeit dieser Messungen durch die Annahme eines homogenen Brechungsindex (RI) beeinträchtigt. In dieser Arbeit wird gezeigt, dass der RI aus dem SPRM-Signal an jedem Scanningpunkt an der Zell-Substrat-Grenzfläche extrahiert werden kann, was eine Verbesserung der Genauigkeit um den Faktor 25 gegenüber der Standardanalysetechnik mit einer Abstandsgenauigkeit von bis zu  $1.5\text{ nm}$  ermöglicht. Die RI- und die Abstandsmessungen konnten über verschiedene Referenzmessungen validiert werden.

Der RI der Zelle gibt interessante Einblicke in die Zellstruktur und zelluläre Prozesse. Beim Scannen der Zell-Substrat-Grenzfläche konnte gezeigt werden, dass das RI-Profil einer Zelle die Position von Zellorganellen detektieren und quantitative Werte für deren Brechungsindizes

angeben kann. Außerdem ermöglicht der Scanningmodus auch die Rekonstruktion der 3D-Struktur der adherenten Membran.

Neue Aufnahme- und Analysetechniken ermöglichen die Auflösung dynamischer Prozesse an der Grenzfläche zwischen Zelle und Substrat. Das Scannen eines Punktes an der Grenzfläche eines periodisch kontrahierenden Kardiomyozyten mit gleichzeitigem Calcium-Imaging konnte die durch das Aktionspotenzial ausgelöste Dynamik der Zellmembran und des RI auflösen. Die Kombination großer Mengen dieser zeitabhängigen Messungen entlang der Grenzfläche ermöglichte die Rekonstruktion der Bewegung der gesamten adherenten Zellmembran.

Zusätzlich wurde mit SPRM die Wirkung der chemischen Fixierung auf den Zell-Substrat-Abstand an der neuronalen Membran bestimmt. Diese Messungen wurden mit dem etablierten Ansatz des fokussierten Ionenstrahl Schneidens (FIB) in Verbindung mit Elektronenmikroskopie der Zell-Substrat-Grenzfläche korreliert, so dass erstmals Artefakte, die durch die Zellpräparation eingebracht wurden, identifiziert werden konnten.

# Abstract

In this thesis an improved surface plasmon resonance microscopy (SPRM) setup has been developed which combines a projector based SPRM widefield mode with several SPRM scanning modes for the investigation of the cell-substrate interface.

Widefield SPRM can be used to image the cell-substrate adhesion areas qualitatively. Here, the resolution is strongly dependent on the light source. While coherent laser light gives rise to speckle noise, which frustrates the resolution of small cellular structures such as neuronal dendrites, using a projector as an incoherent light source allows for a high resolution imaging.

Scanning SPRM can be used to determine the cell-substrate distance quantitatively. So far, the accuracy of these measurements was compromised by the assumption of a homogeneous refractive index (RI). In this thesis, it is shown that the RI can be extracted from the SPRM signal at each scanning point at the cell-substrate interface which allowed for an improvement of the distance accuracy by a factor of 25 compared to the standard analysis technique realizing a distance accuracy of up to  $1.5\text{ nm}$ . The measurements of RI and distance were validated by several reference measurements.

The RI of the cell gives interesting insights into the cellular structure and cellular processes. Scanning the cell-substrate interface, it could be shown that the RI profile of a cell can reveal the position of cell organelles and give quantitative values for their refractive indices while the scanning SPRM also allows for the reconstruction of the 3D structure of the basal cell membrane.

New acquisition and analysis techniques facilitate the resolution of dynamic processes at the cell-substrate interface. Scanning one point at

the interface of a periodically contracting cardiomyocyte over time with a simultaneous calcium imaging could resolve RI variations caused by the action potential as well as the dynamics of the cell membrane. Combining large numbers of these time-dependent measurements along the interface allowed for the reconstruction of the movement of the entire basal cell membrane.

Additionally, SPRM was used to determine the effect of chemical fixation on the cell-substrate distance at the neuronal membrane. These measurements were correlated with focused ion beam sectioning (FIB) combined with electron microscopy of the cell-substrate interface allowing artefacts introduced by the cell preparation to be identified for the first time.

# Table of Contents

<b>Acknowledgment</b>	<b>i</b>
<b>Zusammenfassung</b>	<b>iv</b>
<b>Abstract</b>	<b>vii</b>
<b>Table of Contents</b>	<b>ix</b>
<b>1 Introduction</b>	<b>1</b>
<b>2 Biological background</b>	<b>7</b>
2.1 Cell types . . . . .	8
2.1.1 Cellular structure of neurons . . . . .	8
2.1.2 Cardiomyocytes . . . . .	10
2.2 Cell membrane . . . . .	12
2.2.1 Membrane structure . . . . .	12
2.2.2 Membrane potential . . . . .	14
2.3 Cell adhesion . . . . .	22
2.4 Cell dynamics at the interface . . . . .	26
2.4.1 Cell migration . . . . .	27
2.4.2 Excitation-contraction coupling in cardiomyocytes	29
<b>3 Imaging techniques for the cell-substrate interface</b>	<b>33</b>
3.1 Fluorescence . . . . .	34
3.1.1 Super-resolution microscopy . . . . .	36
3.2 RICM . . . . .	37
3.3 FLIC . . . . .	40
3.4 MIET . . . . .	43
3.5 FIB . . . . .	46
3.6 Surface plasmon resonance imaging . . . . .	48

<b>4</b>	<b>Surface plasmon resonance theory</b>	<b>51</b>
4.1	Surface plasmon excitation . . . . .	51
4.2	Transfer matrix method . . . . .	53
4.3	SPRM types . . . . .	55
4.3.1	Prism based SPRM . . . . .	56
4.3.2	Objective-based SPRM . . . . .	56
<b>5</b>	<b>SPRM Setup</b>	<b>63</b>
5.1	Introduction of the SPRM at the ICS-8 . . . . .	64
5.1.1	Prior work on the SPRM at the ICS-8 . . . . .	64
5.1.2	Overview on the modifications of the setup . . .	67
5.2	General description . . . . .	68
5.3	Live imaging . . . . .	70
5.3.1	Laser live-imaging . . . . .	70
5.3.2	Projector live-imaging . . . . .	74
5.3.3	Comparison of laser live-imaging and projector live-imaging SPRM . . . . .	77
5.4	Scanning . . . . .	82
5.4.1	Physical realization of the scanning modes . . .	82
5.4.2	Scanning acquisition modes . . . . .	84
5.4.3	Processing of the scanning data . . . . .	85
5.5	Further setup elements . . . . .	96
<b>6</b>	<b>Validation</b>	<b>99</b>
6.1	Angle validation . . . . .	100
6.2	Refractive index validation . . . . .	107
6.2.1	Critical angle dependence on last layer . . . . .	107
6.2.2	Refractive index validation measurements . . .	109
6.3	Distance validation . . . . .	112
6.3.1	Measurement of microlenses . . . . .	113
6.4	Discussion . . . . .	120

<b>7</b>	<b>Cardiomyocyte experiments</b>	<b>123</b>
7.1	Experimental . . . . .	124
7.2	Live-imaging of cardiomyocytes . . . . .	127
7.2.1	Correlation of live- and confocal imaging after labeling . . . . .	129
7.3	Single-spot measurements . . . . .	131
7.4	Time dependent area scan . . . . .	135
7.4.1	Discussion . . . . .	140
7.4.2	Calculations of changes in the RI . . . . .	145
<b>8</b>	<b>Neuron experiments</b>	<b>147</b>
8.1	Correlation of SPRM with FIB-SEM . . . . .	147
8.1.1	Experimental . . . . .	148
8.1.2	Analysis . . . . .	150
8.1.3	SPRM measurements . . . . .	153
8.1.4	Discussion . . . . .	162
8.2	Other experiments with neurons . . . . .	167
8.2.1	Measurement of cell organelles . . . . .	167
8.2.2	Measurement of growth cones . . . . .	171
8.2.3	Failed measurement series . . . . .	177
8.2.4	Time series of neurons . . . . .	178
<b>9</b>	<b>Discussion</b>	<b>181</b>
9.1	Development of the technique . . . . .	181
9.1.1	What has been done? . . . . .	181
9.1.2	What remains to be done? . . . . .	183
9.1.3	Problems and issues . . . . .	184
9.1.4	Comparison with other techniques . . . . .	187
9.2	Biological measurements . . . . .	190
9.2.1	What has been measured? . . . . .	190
9.2.2	What could be measured in the future? . . . . .	191
<b>10</b>	<b>Abbreviations</b>	<b>193</b>

<b>11 Protocols</b>	<b>195</b>
11.1 Sample production . . . . .	195
11.1.1 Chip design . . . . .	195
11.1.2 Layer deposition . . . . .	196
11.1.3 Sample assembly . . . . .	197
11.2 Coatings . . . . .	198
11.2.1 Fibronectin coating . . . . .	198
11.2.2 PLL coating . . . . .	198
11.3 Cell culture of cardiomyocytes . . . . .	199
11.3.1 Thawing, plating, maintenance . . . . .	199
11.3.2 Calcium imaging of cardiomyocytes . . . . .	200
11.4 Cell culture of neurons . . . . .	200
11.5 Preparation of samples for FIB . . . . .	202
11.5.1 Fixation with glutaraldehyde . . . . .	202
11.5.2 Heavy metal staining and resin embedding . . . . .	202
11.6 Fixation and staining for immunofluorescence . . . . .	204
11.6.1 Fixation and staining . . . . .	204
11.6.2 Antibodies and additional stainings . . . . .	205
11.6.3 CB Buffer . . . . .	205
11.7 Scripts . . . . .	206
11.7.1 Grid markers on chips . . . . .	206
11.7.2 Background correction . . . . .	207
11.7.3 Animation of contracting cardiomyocyte . . . . .	208
11.7.4 SPRM profile cuts along the entire interface . . . . .	215
11.7.5 Align and compare distance profiles . . . . .	218
<b>12 Appendix</b>	<b>237</b>
12.1 Angle validation . . . . .	237
12.2 Additional measurements and specifications . . . . .	238
12.2.1 Scanning parameters . . . . .	238
12.2.2 Detached lamella . . . . .	238
12.2.3 Surface defects . . . . .	238

12.3 Analysis software optimization . . . . .	240
<b>Bibliography</b>	<b>249</b>



# Introduction

In the field of bioelectronics, interfaces between biologic and electronic systems are used for the recording and stimulation of neuronal activity. The predominant forms of these interfaces are multielectrode arrays (MEAs) [1, 2, 3, 4] and field-effect transistors (FETs) [5, 6, 7]. These can be used as a substrate for primary neuron cultures, thereby providing a non-invasive technique for the study of neuronal communication and the development of neuronal networks under diverse circumstances. Going beyond fundamental research, insights gained during the development and use of these interfaces build the basis for developments in implant and prosthesis technologies.

One of the most important parameters in order to transmit the low electric signal from the cell to the electrode is the seal resistance  $R_{seal}$  [8]. As described in [9, ch. 2], the seal resistance is proportional to the ratio of membrane area that is adhering to the electrode  $A_{cell-electrode}$  and the area of the entire electrode  $A_{electrode}$  while it is inversely proportional to the cell-electrode distance  $d_{cell-electrode}$ , with  $\rho_{electrolyte}$  being the resistance of the electrolyte.

$$R_{seal} \sim \rho_{electrolyte} \cdot \frac{1}{d_{cell-electrode}} \cdot \frac{A_{cell-electrode}}{A_{electrode}} \quad (1.1)$$

Ergo, the cell-substrate adhesion plays a key role for extracellular recordings with a high signal-to-noise ratio. As the cell-electrode adhesion represents one of the bottlenecks towards good cell recordings, a good understanding of the cell-substrate adhesion mechanisms is crucial in order to develop new approaches to reduce the cell-electrode distance. The corresponding biological background is explained in chapter 2.

## 1 Introduction

The central role of the cell-substrate distance also explains the urgent need for characterization methods of the cell-substrate interface. Only if characterization methods are sophisticated enough to resolve distances in the nanometer range, it can be studied whether certain approaches are effective at reducing the cell-electrode distance.

Therefore, many attempts have been made to characterize the cell-substrate adhesion [10, 11, 12, 13] (see chapter 3). As these techniques all involve either labeling or even fixation of the cells, it is likely that this interference with the living system introduces artefacts. Therefore, a new technique was created that allowed for the investigation of the cell-substrate distance *in vitro* and without labeling. The first study of cell-substrate adhesion with surface plasmon resonance microscopy (SPRM) was carried out in 1999 [14]. This method is based on the excitation of surface plasmons (collective oscillations of electrons) in a thin gold layer, which is used as a substrate for cell culture. As the plasmon resonance frequency depends strongly upon the environment of said gold layer, the presence of a cell in the vicinity of the gold layer can influence said resonance frequency. It was shown, that plasmons are even sensitive enough to respond to changes in the nanometer range regarding the cell-gold distance [15]. The fundamental theory on surface plasmon resonance is introduced in chapter 4.

In these first experiments [14], the resolution in the lateral as well as in axial direction was still compromised. However, it could be shown to be a promising tool for the characterization of the cell-substrate interface. In 2014, Dr. Koji Toma (currently professor at the Tokyo Medical and Dental University in Japan) built the first SPRM capable of measuring the cell-substrate distance with a high lateral and axial resolution [15] in collaboration with Prof. Dr. Hiroshi Kano (currently professor at the Muroran Institute of Technology in Japan). This setup will be introduced in chapter 5. It was estimated to have a lateral resolution at the diffraction limit, while the sensitivity in z-direction

was assumed in the nanometer range. The accuracy of this setup was unknown though.

This setup built the basis for the research which was carried within the framework of this thesis. As the previous work on the prototype left several open questions and offered room for improvement regarding the optical system as well as the data acquisition and analysis, it was decided to start the project from scratch while profiting from the knowledge which was accumulated by Dr. Toma and Prof. Dr. Kano. In contrast to the prototype, the new setup is not only able to study the cell-substrate distance of static cells but also the dynamics at the cell-substrate interface.

It could be shown that the recorded SPRM signals can also give insights into the refractive index of the cytosol. An analysis algorithm could be developed that extracts this variable from the data. This procedure has two important advantages compared to the analysis used in the prototype. On the one hand, the refractive index of the cytosol is of interest as it can provide insights into positions of cell organelles. On the other hand, it allows for a strong improvement of the accuracy of SPRM distance measurements. This is caused by the nature of the data analysis: In order to analyze the cell-substrate distance, the optical properties of the entire sample consisting of a glass coverslip, a chromium adhesion layer, a gold layer, the culture media, the cell membrane and the cytosol need to be taken into account. Usually, in SPRM, researchers assumed an average refractive index value for the cytosol while in reality, the refractive index in a cell can vary strongly.

In this work, it could be shown, that this assumption strongly compromised the accuracy of the distance analysis. Due to the decoupling of the refractive index and distance, the accuracy of the analysis algorithm could be improved by a factor of 25 from  $\sim 40 \text{ nm}$  to  $\sim 1.5 \text{ nm}$ .

## 1 Introduction

In order to validate the SPRM measurements, many different experiments have been designed and carried out which confirm that the measured values are in the expected range. These validation experiments are presented in chapter 6.

In chapter 7, experiments with cardiomyocytes are shown. These cells periodically produce an action potential followed by a contraction of the cell which induces changes in the cytosolic refractive index as well as in the cell substrate distance. It could be shown that the new technique makes it possible to study the dynamics in both variables and reconstruct the 3D profile of the basal cell membrane in an animated manner representing the changes at the cell-substrate interface over the cycle of a cell contraction. Thus, the dynamics at the cell-substrate interface could be studied for the first time. The study of the dynamics of both variables promises great potential for the study of many other biological questions such as the label-free, non-invasive study of neuronal action potential in long-term experiments.

In chapter 8, correlative measurements of neuronal cells with SPRM and electron microscopy are shown. In these experiments, neuronal cells have been measured *in vitro* and after chemical fixation. Afterwards, the samples were stained with heavy metals which give rise to a good contrast between certain intracellular structures as well as cell membranes and the extracellular space in the electron microscopy images.

The investigation with an electron microscope also requires the dehydration of the samples as the microscope works in a vacuum. Therefore, a resin embedding protocol was executed that allowed for the replacement of the intracellular water against a specific resist. The cells are cut with a focused ion beam (FIB) before the thusly generated cross section was imaged with a scanning (transmission) electron microscope (S(T)EM). This way, it could be demonstrated which artefacts regarding the cell-substrate distance are introduced by the chemical fixation and

which artefacts are probably introduced by the embedding process. As FIB-S(T)EM has been used frequently for the characterization of the cell-substrate interface in the last decade, this correlation gives important insights into potential artefacts and therefore the combination of the two complementary methods allows for the improvement of the preparation protocols in the long run.

In the last section of chapter 8, it is shown that SPRM can also be used in order to measure the position of cell organelles under specific circumstances as well as the dynamics of neuronal growth cones. However, the low thickness of the growth cone does not agree with the cellular structure assumed in the analysis. Therefore, it is not surprising that the analyzed refractive indices and cell-substrate distances show values which appear unrealistic. These experiments show the limits of the technique.

In chapter 9, the results of this thesis as well as problems and limitations of the technique are summarized. In the end, ideas for future applications are provided.

## **Additional information**

Shortly after my start of this PhD project, Hossein Hassani joined this project as a master student. During his master's project, he developed a new acquisition and analysis software *SPRing* and supported the work on the optical setup. He then started his work as a PhD student. During the first year, we continuously developed and improved the analysis software *SPRing* in cooperation in order to obtain optimal accuracy.

The additional software developed in this project was written by myself using MATLAB, Python, FFmpeg and ImageMagick.

## 1 Introduction

This thesis contains parts of the publication by E. Kreysing *et al.* "Nanometer-resolved mapping of cell-substrate distances of contracting cardiomyocytes using Surface Plasmon Resonance Microscopy" [16].

# Biological background

The work described in this thesis involves several studies of the cell-substrate interface using different cell types. In order to interpret the results of the cell measurements correctly, the biological background specific to the experiments is introduced in this chapter.

First, the two cell types that were used in the experiments are introduced: neurons and cardiomyocytes (see section 2.1). Their structure as well as some functionalities which have been studied in the experiments, will be explained.

In section 2.2, structures and processes at the cell-substrate interface of these cell types will be illustrated. As the cell membrane is of central importance for most of the processes, its structure will be introduced in a separate section. This will be followed by the description of the creation of the resting membrane potential and the action potential for both cell types.

In section 2.3, cell adhesion will be introduced. This involves cell-cell adhesion and cell-matrix adhesion. Cell-cell junctions play an important role regarding the electric communication between cardiomyocytes while cell-matrix adhesion is crucial for cell migration and the contraction of adhering cardiomyocytes.

In section 2.4, cell dynamics such as cell migration as well as excitation-contraction coupling in cardiomyocytes will be discussed.

Unless cited otherwise, the information specific for cardiomyocytes is based on the textbook “Cardiovascular Physiology Concepts” by R. Klabunde [17], while the remaining biological background is based on the textbook “Molecular Biology of the Cell” by B. Alberts *et al.* [18].

## 2.1 Cell types

The experiments described in this thesis have been carried out with cortical neurons and cardiomyocytes. The neurons have been isolated from Wistar rat embryos on day 18 at the ICS-8 (approved by Landesumweltamt für Natur, Umwelt und Verbraucherschutz Nordrhein-Westfalen, Recklinghausen, Germany, number 84-02.04.2015.A173).

The cardiomyocytes were purchased from a company which derived the cells from human induced pluripotent stem cells (iPSC). Details regarding the cell culture can be found in section 11.3 and section 11.4.

### 2.1.1 Cellular structure of neurons

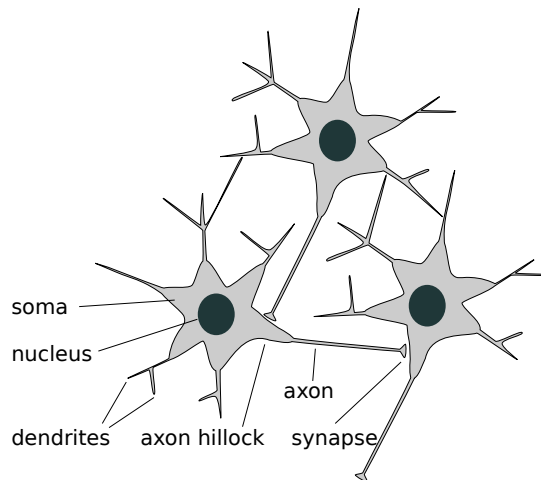


**Figure 2.1:** Neurons form networks that permit the cells to communicate with one another. An electric signal (the action potential) can be produced by the cell and travel along the axon towards the synapse where the membrane potential of the postsynaptic cell can be influenced.

The brain consists mainly of two cell types: Glial cells and neurons. Glial cells are responsible for maintaining the structure of the brain,

supplying neurons with nutrients and oxygen, insulating the neurons from one another and for destroying and removing dead cells. Neurons in contrast are responsible for the electric communication within the brain as well as for the regulation of muscles and organs in the rest of the body. Inside the brain, they form a dense network and communicate with one another via small contact areas, the synapses.

In order to investigate the electrical communication between neurons *in vitro* using FETs or MEAs, the neurons should be ideally separated from the glial cells, since the glial cells tend to build an insulating layer between the electrodes and the neurons. Therefore, the culture media is specifically adapted to the needs of the neuron population while it suppresses the growth of glial cells (see section 11.4). As one aspect of this thesis is to characterize the interaction of neurons with gold layers (which are also used as electrode materials), the same approach was chosen here.

Mature neurons are polar. This means, spatial inhomogeneity induces a certain directionality e.g. for electrical conductivity. A mature cortical neuron consists of a cell body (the soma) that contains the nucleus, the dendrites which are fine, branched extensions at the edge of the soma and the axon. The axon represents a special extension which is connected to the soma by the axon hillock and ends in the synapse. As cortical neurons tend to develop networks under ideal conditions (see Figure 2.1), electrical activity can be passed from one cell to one or multiple others.

Regarding the transfer of electrical information, there are four different tasks which can be assigned to the different cellular structures: the dendrites and the soma collect information (1) that is encoded in transmembrane voltage. The changes in the membrane potential are integrated over at the axon hillock (2). If the membrane voltage is elevated above a certain threshold at this position, the cell starts an

## *2 Biological background*

active transmission of the electric signal (3) along the axon towards the synapse. This active transmission of the electrical signal is called an action potential. At the synapse, the action potential induces a depolarization of the membrane that results in a release of neurotransmitters into the synaptic cleft. The transmitter diffuses through the cleft (4) and induces a change in the membrane potential of the postsynaptic cell.

The membrane potential is caused by a difference in ion concentrations between the extracellular and the intracellular space. For an unexcited cell, this potential is called the resting membrane potential which will be introduced in section 2.2.2. This membrane potential allows neurons to transmit electric signals. Changes in the membrane potential can be induced e.g. by other neurons or external factors.

### **2.1.2 Cardiomyocytes**

The heart is composed of cardiac fibroblasts, endothelial cells, vascular smooth muscle cells and cardiomyocytes.

The iPSC derived cultured cells, which were used in this thesis did not consist solely of cardiomyocytes but also contained fibroblasts. In contrast to fibroblasts, cardiomyocytes have the ability to contract spontaneously. As only contracting cells have been studied in the experiments shown in chapter 7, this paragraph only introduces the different kinds of cardiomyocytes which might be found in this culture.

Cardiomyocytes are the electrogenic cells that conduct the electrical signals through the heart tissue. They can vary regarding their cellular structure, their size and their membrane potential (see section 2.2.2). These cells are responsible for guiding electric signals along a well defined path through the heart and induce the contraction of the organ. Figure 2.2 shows the structure of the heart. The easiest way to

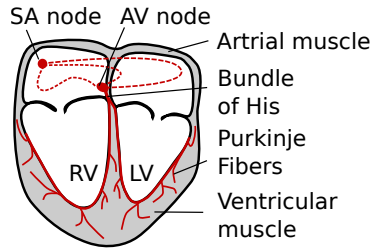


**Figure 2.2:** Structure of the human heart. Figure adapted from [17].

understand the different functionalities of the different cell types is by retracing the conduction path. The sinoatrial (SA) node is the first pacemaker node which generates action potentials that initiate the electric activity. As discussed later, these pacemaker cells are able to generate action potentials autonomously.

The SA node is innervated by the parasympathetic and the sympathetic nerves, which can slow down or speed up the action potential production, respectively. The parasympathetic nerves release the transmitter acetylcholine, which slows down the spontaneous activity while the sympathetic nerves release noradrenaline, which speeds up the pacemaker potential. If the SA node cells were isolated from the nerves, they would depolarize at a rate of 100 to 110 beats per minute. The influence of the innervation reduces this rate to around 60 to 100 at rest while rates of over 200 beats per minute can be reached under stress.

The action potential is conducted by the non-pacemaker cells through the right and left atrium. Non-pacemaker cells do not produce action potentials spontaneously but they can establish a conducting connection by producing action potentials as a response to membrane depolarization (see section 2.2.2). Next, the signal reaches the atrioventricular (AV) node which consists of pacemaker cells with a low spontaneous depolarization rate of around 40 beats per minute. Usually, the action potentials arrive at the AV node with the frequency given by the SA

## *2 Biological background*

node, forcing the AV node to depolarize and generate action potentials at the higher rate. However, if the connection between the SA node and the AV node fails, the AV node would act autonomously. The AV node is in direct contact with the Bundle of His (pacemaker cells with a frequency of 20 - 30 beats per minute) which conduct the action potential to the left and the right ventricle where they branch into the Purkinje Fibers.

The electric conduction through the cells of the entire heart is essential to initiate a common heart beat. This is facilitated by a contraction mechanism that follows the action potential (see section 2.4.2).

As the used cardiomyocytes culture can potentially contain each of the cell types which have been introduced in this section, it is to be expected to find differences between the individual cells regarding their action potentials, their contraction frequency as well as their shape.

## **2.2 Cell membrane**

### **2.2.1 Membrane structure**

The cell membrane represents the border between the cell and its environment and thereby defines the intracellular and extracellular space. It is a selectively permeable layer, which consists of lipids, proteins and carbohydrates [18, ch. 10]. A phospholipid bilayer builds the basis of the membrane. The molecules arrange in such a way that the hydrophobic fatty acids, called the “tails” are facing each other while the hydrophilic phosphate groups, called “heads” are exposed to the aqueous environment. The pure lipid bilayer has a thickness of around

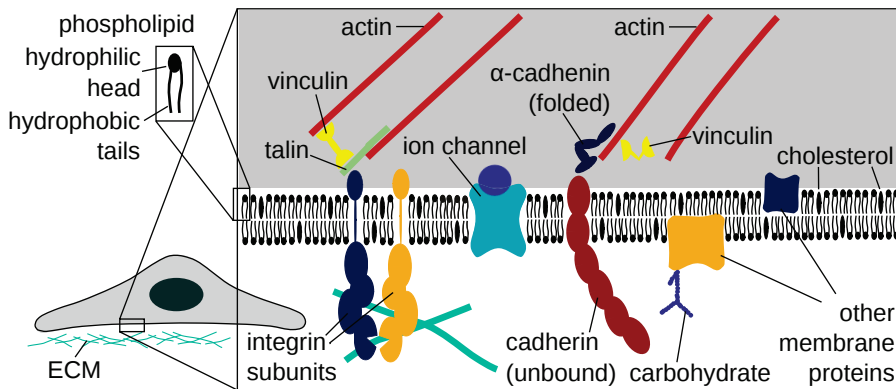


**Figure 2.3:** The cell membrane consists of a phospholipid bilayer which incorporates cholesterol and a huge variety of proteins while attached carbohydrates form the glycocalyx. Some of the transmembrane proteins function as ion channels or pumps, others mediate cell adhesion by connecting the cytoskeleton to the extracellular matrix (ECM) e.g. integrins or to membrane proteins of other cells e.g. cadherins (shown here in an unbound state).

5 nm and is permeable for water and other small molecules while ions cannot pass the membrane.

In an animal cell membrane, the lipid bilayer incorporates a large variety of proteins that constitute around 50% of the membrane's mass [18, ch. 10]. As the membrane is highly dynamic, the proteins can laterally diffuse within the bilayer. The proteins differ in their composition, size, the way they are anchored in the membrane and their functionality. Some proteins are attached to the inner or the outer leaflet of the membrane while other proteins span through it. Some transmembrane proteins form pores or pumps which allow for passive or active transport of certain substances through the membrane, respectively. This allows for the generation of concentration gradients across the membrane which is essential for the generation of electrical and chemical potentials representing the basis for electrical cell signaling.

Other transmembrane proteins like integrins or cadherins mediate cell

## 2 *Biological background*

adhesion by binding to the extracellular matrix (ECM) or cadherins in neighboring cell membranes, respectively (see section 2.3, [18, ch. 19]). Connecting the cytoskeleton to the extracellular space, integrins can also facilitate cell migration (see section 2.4.1). As proteins are large in comparison to phospholipids, they can stick out of the lipid bilayer and increase the average membrane thickness. For example, integrins which are transmembrane proteins, have been shown to expand around 20 *nm* into the extra cellular space [19]. As cell-substrate adhesion is mediated by transmembrane proteins, even the membrane areas that adhere well to the substrate in cell culture are expected to have a non-zero cell-substrate distance. To mediate a better cell-substrate adhesion in cell culture, the substrates are usually coated with certain polypeptides or proteins which facilitate the binding of the transmembrane proteins to the substrate. Additionally, cell are known to secrete their own ECM [18, ch. 19]. These factors might influence the cell-substrate interaction and therefore the cell-substrate distance.

There are countless other proteins which are indispensable for proper functioning of the cell. As this work is mainly focused on cell adhesion and dynamics at the cell-substrate interface, addressing these is beyond the scope of this work.

### **2.2.2 Membrane potential**

As the cell membrane is impermeable to ions, it sustains an ion gradient between the intracellular and extracellular space. The resulting voltage that is created across the membrane at rest is called the resting potential. Ion pumps and voltage gated ion channels allow for changes of the membrane potential. A fast depolarization followed by a repolarisation of the membrane that restores the resting potential is referred to as action potential.

The neuron represents probably the most famous cell type that communicates via electric signals but there are more cell types to which electric signaling is crucial. As discussed earlier, the heart is driven by spontaneous electrical activity of cells in certain areas that cause large quantities of heart muscle cells to contract and our heart to beat. As both neurons and cardiomyocytes have been used in the experiments described in this thesis, the resting potential as well as the action potential will be introduced for both cell types one after another.

## Resting potential at the neuronal membrane

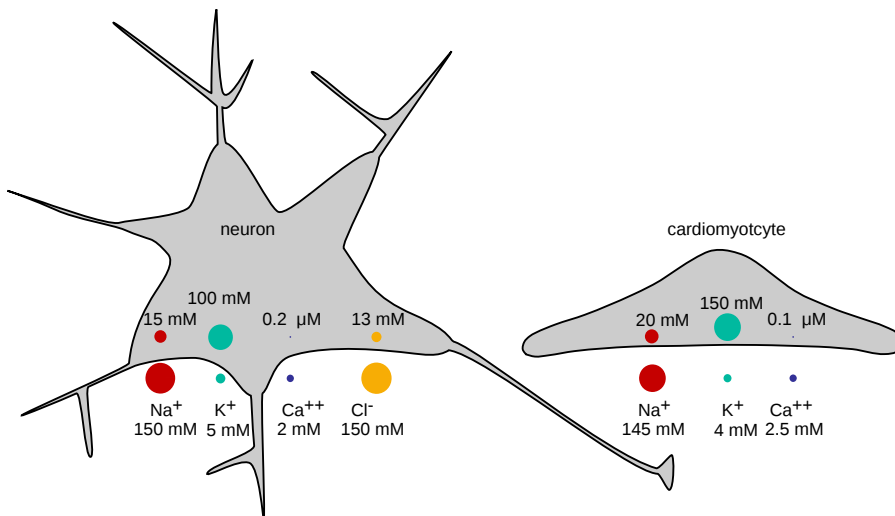


**Figure 2.4:** Ion distribution across a neuronal membrane and a ventricular cardiomyocyte membrane at rest (values taken from [20, 17], respectively)

As described before, the cell membrane separates the intracellular space from the extracellular space. It allows for the creation of concentration gradients of certain ion types across the membrane resulting in an electrical voltage across the membrane. Due to ion specific membrane channels, certain ion types can pass the membrane. Open channels

## 2 *Biological background*

allow for an ion diffusion through the membrane along a concentration gradient of the respective ion type. In contrast to this passive ion transport, there are ion pumps, which transport ions against their concentration gradient consuming energy provided by adenosine triphosphate (ATP).

Figure 2.4 shows the ion distribution across a neuronal and a cardiac membrane at rest. As the movement of sodium and potassium ions are the most important processes for the maintenance of the resting potential, this paragraph focuses mainly on these two ion types. The concentration of potassium ions in the cytosol is much higher than at the extracellular space. For sodium ions, the intracellular concentration is lower than the extracellular concentration. The permeability of the membrane at rest is higher for potassium ions than for sodium ions. As a result, the number of potassium ions moving along their concentration gradient (out of the cell) is higher than the number of sodium ions moving into the cell. This corresponds to a flux of positive charges out of the cell. Consequently, the intracellular space, which is already negatively charged would become more negatively charged. But at the same time, a sodium-potassium pump exchanges 3 sodium ions (out) for 2 potassium ions (in). This contributes to maintaining the resting concentration gradient.

There are several different approaches for estimating the resting potential. The first approach considers the influence of the concentration gradient of only one ion type which generates a voltage across the membrane. The flow of ions through a membrane is driven by the electrochemical gradient. This is a combination of the voltage gradient and the concentration gradient. When the forces generated by the two gradients are in equilibrium, there is no net flux of this ion type across the membrane. The voltage gradient that is measured in equilibrium is called the equilibrium potential for the ion, which can be calculated by

the Nernst equation:

$$V = \frac{RT}{zF} \ln \frac{C_o}{C_i} \quad (2.1)$$

with  $R$  being the gas constant,  $z$  the charge of the ion,  $T$  the absolute temperature,  $F$  Faraday's constant,  $C_{o,i}$  the extracellular and the intracellular concentration, respectively. Calculating the equilibrium potential for potassium using  $C_i = 100 \text{ mM}$  and  $C_o = 5 \text{ mM}$  gives an equilibrium potential of  $V = -80 \text{ mV}$ . Even though this value is only based on the concentration gradient of potassium and neglects the influence of the other ions, the resulting voltage is relatively close to the physiological values measured across the membrane,  $V = -65 \text{ mV}$ .

The Goldman equation represents a second approach to calculate the membrane potential. It takes several ion types into account when calculating the membrane potential. This models the membrane potential more realistically and gives a better estimate for the voltage. But it requires a more detailed knowledge regarding the membrane properties, such as the relative permeability  $P_j$  and the concentration  $C_j$  for the specific ion types:

$$V = \frac{RT}{F} \ln \frac{\sum_{j=\text{ion types}} P_j \cdot C_{j_o}}{\sum_{j=\text{ion types}} P_j \cdot C_{j_i}} \quad (2.2)$$

## Resting potential at the cardiac membrane

Figure 2.4 shows that the ion distribution between the intracellular and the extracellular space differs between the neuronal and a ventricular cardiac cells at rest. The intracellular concentration of sodium and potassium are higher in cardiomyocytes while the influence of chloride ions on the resting potential can be neglected. The resting potential at a ventricular cardiomyocyte is around  $-90 \text{ mV}$ . As described for the

## 2 *Biological background*

neuronal resting potential, the sodium and potassium ions follow their concentration gradient and leak into and out of the cell, respectively. A sodium-potassium pump exchanges the ions as described for neurons. At the same time calcium leaks into the cell, which is then removed an ATP-dependent calcium pump and a sodium-calcium exchanger which removes one calcium ion from the cytosol in exchange for 3 sodium ions entering the cell. The activity of the latter depends strongly upon the intracellular sodium concentration. Therefore a change in the sodium-potassium pump activity can lead to less calcium efflux. This in turn can increase the myocyte contraction which is strongly calcium dependent, as discussed in section 2.4.2.

### **Neuronal action potential**

Initially, the neuron is at rest (see Figure 2.4), corresponding to a membrane potential of around  $-65\text{ mV}$ . If a stimulus depolarizes the membrane above the threshold, voltage gated sodium channels open and the sodium ions move into the cell, depolarizing the membrane further. Thus the intracellular space gets positively charged. The sodium ion channels close after  $1-2\text{ ms}$  and cannot be reopened immediately (refractory time). Voltage gated potassium channels react slower than the potassium channels. They open, when most of the sodium channels are already closed. Potassium diffuses out of the cell leading to a fast repolarization followed by a slight hyperpolarization of the membrane. The potassium channels close and the sodium-potassium pump restores the resting potential by pumping sodium out of the cell and potassium in.

As the voltage gated ion channels are represented by individual transmembrane proteins, which change their conformation depending on the local transmembrane voltage, it is obvious that the axonal mem-

brane cannot be depolarized at once but the depolarization “travels” along the membrane. As soon as the threshold is reached at the axon hillock, the neighboring channels open, which leads to a depolarization in their vicinity and so on. Due to the summation of the voltage at the axon hillock the electrical activity follows the all-or-none law: if the threshold is reached, the action potential travels towards the synapse. Therefore, the neuron works digitally i.e. it does not give stronger or weaker action potentials. Thus, the strength of a stimulus can only be coded into the frequency of action potentials. Within a network, neurons show a polar behavior regarding the transmission of information. Once the decision to generate an action potential is made at the axon hillock, the action potential travels from the hillock to the synapse. When the action potential arrives at the synapse, the synaptic membrane is depolarized and voltage gated calcium channels open. Calcium flows into the neuron terminal where it triggers the release of neurotransmitter into the synaptic cleft. The neurotransmitter diffuses through the cleft and eventually binds to specific receptors at the postsynaptic membrane. Here, this can trigger ion channels to open, which can result in a depolarization or a hyperpolarization of the postsynaptic membrane depending on the receptor.

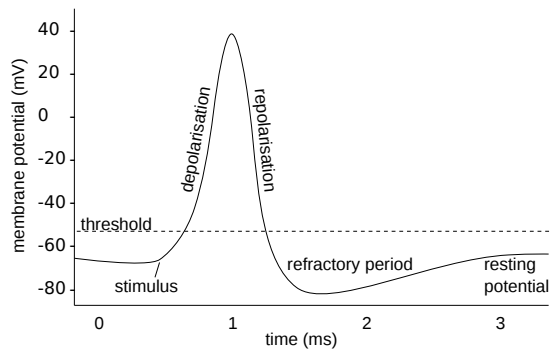


**Figure 2.5:** Neuronal action potential (Figure adapted from [20])

## **Cardiac action potential**

Cardiac action potentials are relatively slow compared to neuronal action potentials. They last between  $200\text{ ms}$  and  $400\text{ ms}$  while neuronal action potentials last around  $2\text{ ms}$ . Depending on the origin of the cardiomyocyte, the involved ion types and the shape of the action potential vary.

One can distinguish between non-pacemaker (ventricular, atrial and Purkinje fiber cells) and pacemaker cells (cells from the SA node, the AV node and the His bundle). Their action potentials will be introduced at the example of ventricular cells (non-pacemaker) and cells from the sinoatrial node (pacemaker).

Ventricular cardiomyocytes have a resting potential of around  $-90\text{ mV}$  as described above. Voltage gated sodium channels open when the cell membrane is depolarized. This results in a sodium influx and a membrane depolarization. At the same time, the conductance for potassium is reduced. Interestingly, each sodium channel has a slightly different activation threshold and opening time [17]. As the resulting depolarization of the membrane is fast compared to pacemaker cells, the action potential is called the “fast response” action potential. Voltage gated calcium channels open which induces a slow increase of the intracellular calcium concentration (this triggers an additional intracellular signaling cascade which will be explained in section 2.4.2). Afterwards, a specific kind of potassium channel opens and causes an initial repolarisation. Finally, delayed rectifier potassium channels open and repolarize the cell to the resting potential.

In contrast to ventricular cardiomyocytes, pacemaker cells do not have a steady resting potential but the cells slowly depolarize spontaneously. The responsible mechanisms are not entirely clear. Small amounts of sodium and calcium appear to be leaking into the cell slightly depolarizing the membrane. When a potential of around  $-40\text{ mV}$  is reached,

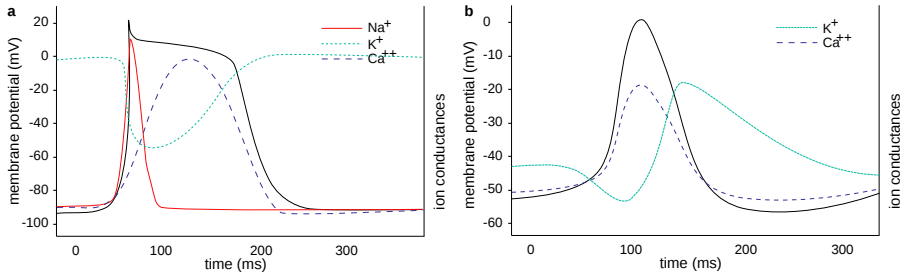


**Figure 2.6:** The ventricular cardiac action potential (a) and sinoatrial (SA) action potential (b) differ regarding the involved ion types, the shape and the amplitude of the action potential. In contrast to SA cells, ventricular cells have a resting potential. Voltage-gated sodium channels open at individual thresholds and initiate the action potential by opening when the membrane is depolarized. In SA cells, the action potential is initiated due to a depolarization caused by inward leaking calcium. (Figures adapted from [17])

L-type calcium channels open while the conductance for potassium is decreased which contributes to the depolarization. The depolarization causes voltage gated delayed rectifier potassium channels to open and repolarize the membrane while the calcium channels close [17, ch. 2].

Cardiomyocytes communicate via gap junctions. These junctions represent electrical synapses that are formed by directly connected ion channels called connexons (see section 2.3). These electrical synapses allow for direct transmission of ions between neighboring cells. This way, a change in the ion concentration in one cell can cause a depolarization at the membrane of its neighbor and initiate an action potential. This way of communication is faster than the transmission of excitation via chemical synapses and allows for a quick propagation of the excitation through the heart tissue.

## 2 Biological background

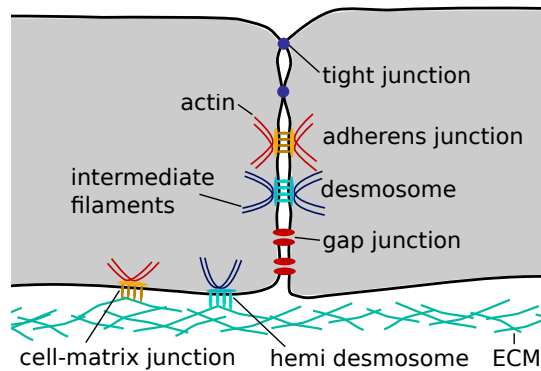


**Figure 2.7:** Cells form different types of adhesion junctions. Tight junctions connect the membranes of neighboring cells directly. So do gap junctions which also allow for ion exchange between the cells. Adherens junctions and desmosomes connect the cytoskeleton of neighboring cells via the relatively long cadherins. Actin linked cell-matrix junctions and hemidesmosomes link the cytoskeleton to the ECM via integrins. Figure adapted from [18, ch. 19]

## 2.3 Cell adhesion

There are many different types of cell adhesion that are fundamental to holding cells together and building a functioning body. They are crucial to forming tissue and organs that are resistant to external influences like mechanical stress but they can also transmit forces generated by the cells themselves e.g. during muscle contraction. They are essential for cell migration and even for the exchange of ions between neighboring cells. Figure 2.7 shows the most relevant cell junctions at the example of two neighboring epithelial cells.

Tight junctions represent the cell-cell adhesion complexes resulting in the closest cell contacts. They are mediated by the transmembrane proteins claudin and occludin. These junctions have been found in epithelial cells where they guarantee a sealing of the extracellular space. This inhibits molecules from diffusing from the basal side to the apical side through the cleft between the cells. This prevents the body from losing water through the skin.

Adherens junctions and desmosomes represent another form of cell-cell junctions that connect the cytoskeleton of neighboring cells. Adapter proteins (for a list of adapter proteins see [18], p. 1037) connect the filaments of the cytoskeleton to transmembrane proteins that belong to the superfamily of cadherins. In the presence of calcium, the opposing cadherins can bind and said junctions can be formed. Adherens junctions connect bundles of actin filaments of adjacent cells while desmosomes connect bundles of intermediate filaments. In a similar way, the cytoskeleton can be anchored to the ECM.

Actin-linked cell-matrix junctions and hemidesmosomes anchor actin filaments and intermediate filaments to the ECM, respectively. In contrast to the cell-cell junctions discussed earlier, these junctions are mediated by integrins instead of cadherins. These junctions also differ regarding the adapter proteins that connect the cytoskeleton to the transmembrane proteins. Integrins can exist either in an active or inactive state (see Figure 2.8). In their inactive state, the extracellular part of the subunits are folded and show a low binding affinity, while the intracellular parts are coiled in such a way that an interaction with the cytoskeleton is inhibited. In their active state, the extracellular parts are unfolded and show a strong ligand binding affinity while the conformational change of the intracellular part shows a strong adapter-protein binding affinity.

However, the protein structure sticks out of the lipid bilayer in both states. The size of the transmembrane proteins suggests, that even in areas with integrin mediated cell-substrate adhesion, distances around  $20\text{ nm}$  are to be expected. Even though integrins do not mediate the cell-substrate adhesion in their inactive state, the size of these protein complexes might influence the cell substrate distance locally as the lipid bilayer can not approach the substrate closer as the size of the protein complex allows.

## 2 *Biological background*

Most of these cell-matrix junctions but also the adherens junctions, involve connections between actin filaments and non-muscle myosin. Myosin is a motor protein which allows for contraction of parts of the cell by binding to actin and bending small head-like structures. When no forces are applied, the adapter proteins can remain in an inactive state (similar to adapter proteins associated with the unbound cadherin in Figure 2.3).

If myosin initiates a contraction, the actin and myosin filaments move past each other, changing the state of the adapter proteins and create a link between the cytoskeleton and the transmembrane proteins. The interaction of the integrins with the ECM facilitates cell migration by creating focal adhesions at the edge of the cell and pulling on them. This way, the cell moves towards the focal adhesion point. Focal adhesion points tend to form dense plaques at the end of actin filament bundles.

Costameres represent special kind off cell-matrix adhesion and are specific for muscle cells and cardiomyocytes [21]. Similar to focal adhesion complexes, costameres connect the cytoskeleton via mediating proteins to the ECM. On the cytoplasmic side, Z-discs, which limit the contractile sarcomeres, are connected to a combination of two transmembrane proteins via a large number of adapter proteins. The transmembrane proteins, integrin and dystrophin [22], both connect to the ECM. Costameres are very stable and withstand the stress arising during the contraction of the cell.

The last junctions which shall be discussed here are gap junctions. As they are essential for the electrical activity in cardiomyocytes, they have been introduced briefly when discussing action potentials. These junctions are formed by opposing connexons which represent hemichannels that can form a transmembrane channel connecting the cytosol of two adjacent cells. This represents the basis for electrical synapses which

have been found between adjacent heart muscle cells, as well as between certain motoneurons and the corresponding muscle cells [23, p. 575].

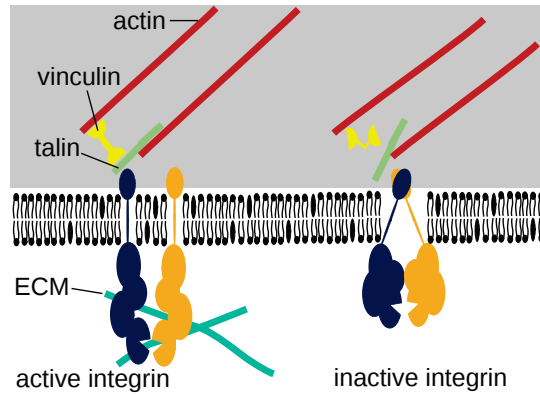


**Figure 2.8:** Integrins can exist in an active or an inactive state. In their active state, the subunits are unfolded and the adapter proteins connect them to the actin filaments. In their inactive state, the extracellular part is folded and has a low binding affinity. The intracellular part is coiled and does not bind to the adapter proteins

In this section, several different concepts of cell-adhesion have been introduced. These concepts explain how cells adhere one to another or to the ECM. Under culture conditions, the cell-substrate adhesion might differ from these adhesion concepts.

However, it is important to keep some of the facts which were introduced in this section in mind in order to judge experimental observations. The size of integrins suggests that cell-substrate distances in the order of  $20\text{ nm}$  can be expected in areas, where cultured cells adhere via integrins or costameres.

As neurons and cardiomyocytes do not build tight junctions, distances in the order of a few nanometers are not expected in these cultures.

## *2 Biological background*

Some of the transmembrane proteins might not contribute to the cell-substrate adhesion directly for example when they are in an inactive state. However, it might be possible that these proteins might be crosslinked to the coating of a substrate, when cells are fixated. As the influence of chemical fixation is studied in chapter 8, this idea will be referred to later.

In the study of the dynamics of cardiomyocytes, singular cells as well as cell-clusters are investigated (see chapter 7). It will be shown, that structures which resemble costameric adhesions establish a tight cell-substrate contact while cell-cell junctions such as adherens junctions can have a strong influence on the cell-substrate interface.

Additionally, it will be shown in the next section that cell adhesion is fundamental in order to introduce cell dynamics.

## **2.4 Cell dynamics at the interface**

In this section, two different concepts of cell dynamics will be introduced: cell migration and cell contraction.

As cell migration is observed in many cell types, the concept will be first introduced in a general manner before the concept is specified to the dynamics at neuronal growth cones. These explanations will refer to some concepts which were introduced in section 2.3.

Afterwards, the periodic contraction of cardiomyocytes will be explained. Therefore, it will be referred to the cardiac action potentials which were introduced in section 2.2.2.

Understanding these fundamentals will help to interpret the results of the experiments shown in chapter 7 and chapter 8.

## 2.4.1 Cell migration

Figure 2.9 illustrates the major processes during cell migration: In order to move, the cells first build a leading edge protrusion. Unpolymerized actin is transported towards this position. Here, the actin polymerizes and elongates the existing actin filaments. Those push the cell membrane forwards. Focal adhesions are formed at the leading edge that connect the cytoskeleton to the substrate. As mentioned earlier, the actin filaments are mostly connected to non-muscle myosin. The contraction of the myosin-heads results in forces applied to the focal adhesions. The rear is pulled towards the center while the front of the cell moves towards the newly formed focal adhesions. The actin at the rear of the cell is depolymerized and transported to the leading edge.

Protruding leading edges that expand mainly in one dimension are called filopodia. They are formed during the migration of growth cones of neurons. Two-dimensional, sheetlike structures, called lamellipodia are formed by epithelial cells, fibroblasts and neurons.

When neurons are seeded on a suitable surface, the soma can adhere to one position while the neurites start growing in several directions. The tip of a growing neurite, called the growth cone, consists of many finger-like structures, the filopodia which are connected by the sheet-like lamellipodium containing a dense actin network. The filopodia explore the environment by extending and retracting.

This process involves actin polymerization and myosin mediated contraction of the cytoskeleton in the lamellipodium. The movement of the leading edge of the growth cone is determined by the difference between outward pushing actin polymerization and a retrograde actin flow. During the migration of the growth cone, the actin network partially transmits the pulling forces to the leading edge where the actin network is coupled to the substrate via adhesion sites while another

## 2 Biological background

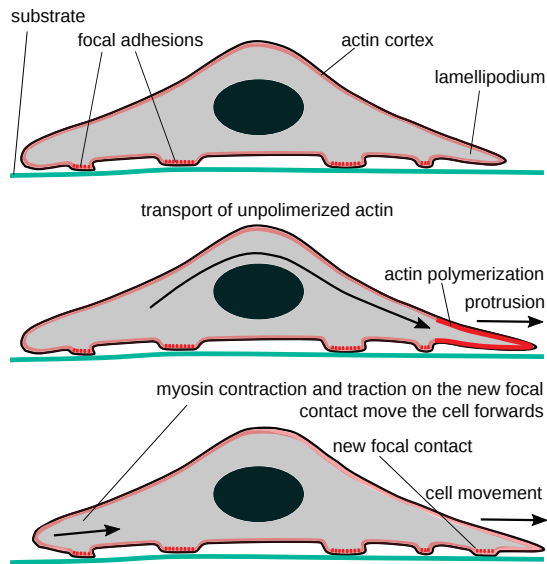


**Figure 2.9:** First, the cell forms a lamellipodium. The cell transports unpolimerized actin towards the leading edge where the actin polymerizes. This pushes the protrusion forwards. A new focal contact is formed which is connected to bundles of actin filaments. By contraction of myosin in the cytoskeleton, the rear is pulled towards the center while the force applied to the new focal contact pulls the cell towards the new focal contact. (Figure adapted from [18, ch. 16])

part of the energy is dissipated via deformation of the actin network [24].

The strong dynamics at the growth cones are likely to influence the cell-substrate distance. Whether or not these dynamics can be determined quantitatively with SPRM, will be studied in section 8.2.2.

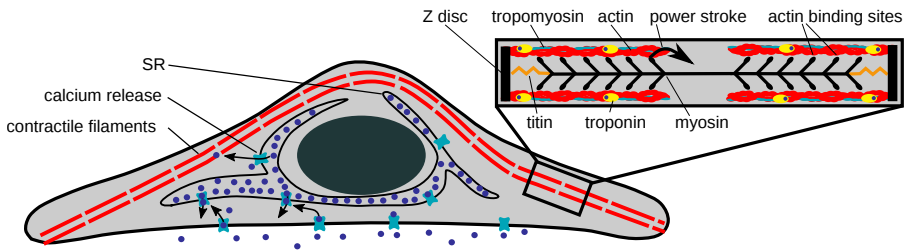


**Figure 2.10:** During the action potential, a calcium influx induces a calcium release from the sarcoplasmic reticulum (SR). The released calcium ions diffuse through the cytosol and bind to troponin. As a consequence, troponin changes its conformation and pulls on tropomyosin which is moved and from the actin binding sites. The myosin heads bind to the actin binding sites. Eventually the myosin heads can exert a power stroke leading to a contraction of the cell.

## 2.4.2 Excitation-contraction coupling in cardiomyocytes

As described in section 2.1.2, the heart contains of many different types of cardiomyocytes. These cells differ regarding their structure, their resting potentials and their action potentials (see section 2.2.2). However, there are structural details the cells have in common. They contain large quantities of sarcomeres, which represent the basic contractile unit in a muscle. The sarcomeres consist of protein filaments like actin and myosin, which are connected to Z-disks (see Figure 2.10). These filaments can move with respect to one another causing the sarcomere to contract. The cells also contain a large organelle called the sarcoplasmic reticulum (SR).

The SR is a tubular network enclosed by a membrane that is responsible for storing calcium and controlling the intracellular calcium concentration. The SR membrane contains calcium sensitive calcium channels, which enable the SR to increase the cytosolic calcium concentration. As discussed earlier, the action potentials of pacemaker as well as non-pacemaker cells include a calcium influx. The resulting increase of the

## 2 *Biological background*

cytosolic calcium concentration is relatively small but it triggers the ryanodine-sensitive calcium release channels in the SR membrane to open. As a result, the intracellular calcium concentration increases by a factor of 100 [17].

This mechanism represents the key to excitation-contraction coupling because calcium is essential to the contraction. Diffusing through the cell, many calcium ions reach the sarcomeres where they bind to troponin. This protein, which is connected to tropomyosin chains, changes its conformation and thereby pulls on tropomyosin. This changes the position of the tropomyosin chains on the actin filaments, exposing the actin binding sites. Actin binding sites are specific areas on the actin filaments that are suited for myosin heads to bind when exposed to tropomyosin removal. The bound myosin heads bend and thereby contract the sarcomere. This bending is known as the “power stroke”. Afterwards, the myosin heads stay in this position until ATP detaches the myosin heads from the actin binding sites and activates the myosin heads for a new power stroke. The power stroke can repeat as long as the actin binding sites are exposed. The forces generated during the contraction are transmitted from the sarcomeres to the extracellular matrix by costameric adhesion sites and focal adhesion sites [25].

When the calcium ions detach from the troponin, the tropomyosin slides back into its initial position and covers the actin binding sites. The calcium ions are transported back into the SR by the SERCA pump.

As cardiomyocytes periodically generate an action potential, they represent an excellent model system in order to test the performance of MEAs or FETs. Here, the cell-substrate distance is one of the crucial parameters towards a good SNR (see chapter 1). As the contraction of cardiomyocytes in culture can be easily observed with a conventional light microscope with a 20x objective, it is plausible, that this

conformational change of the cellular structure might also affect the cell-substrate distance. This question will be studied in chapter 7.



# Imaging techniques for the cell-substrate interface

# 3

In this chapter, some standard techniques suited to image the cell-substrate interface will be introduced. Some of these techniques involve fluorescent labeling. Therefore, the basic principle of fluorescence is explained at first (see section 3.1).

This section also includes the explanation of two specific fluorescence techniques which have been used for correlative measurements in this thesis: Calcium imaging which allows for the detection of action potentials as well as fluorescent immunostaining which has been used in order to analyze the intracellular structure (see chapter 7). As super-resolution microscopy is based on fluorescent imaging, this field will be referred to in section 3.1.1.

Afterwards, the most common optical techniques which can be used to determine the 3D structure of the basal cell membrane in a non-invasive manner will be introduced. These sections are meant to provide enough background knowledge in order to put this work on SPRM into context.

Reflection interference contrast microscopy (RICM) is a label-free method which allows to determine the cell-substrate distance based on the interference of light reflected at the interfaces within the sample (see section 3.2).

Fluorescence interference contrast microscopy (FLIC) only works on specifically designed substrates. Here, the determination of the cell-substrate distance is based on the determination of the fluorescence intensity of the labeled membrane (see section 3.3).

### *3 Imaging techniques for the cell-substrate interface*

Metal induced energy transfer (MIET), also involves specific substrates and fluorescent labeling of the cell membrane while the cell-substrate distance is determined based on the fluorescence lifetime (see section 3.4).

Afterwards, focused ion beam (FIB) sectioning in combination with electron microscopy will be introduced (see section 3.5). In contrast to the other optical methods, it does not work *in vitro* and it represents an invasive method, but due to its high resolution, it has been frequently used in the past decade to visualize the adhering cell membrane. It allows to resolve cell-substrate distances in the nanometer range and additionally provides insights into the intracellular structure.

In the end of this chapter, a short introduction of the working principle of surface plasmon resonance imaging will be given (see section 3.6).

The final comparison of all the techniques (including surface plasmon resonance microscopy) will be given in the end of the thesis section 9.1.4.

## **3.1 Fluorescence**

Fluorescence imaging can be useful to localize specifically stained cell structures such as the membrane, filaments, the nucleus or other cell organelles but it can also be used to observe specific processes such as calcium release during an action potential. Fluorescent molecules can be excited by light within their absorption spectrum. Non-radiant transitions induce a change towards lower energy levels of the molecules. The energy level is decreased further by emitting a photon (see Figure 3.1 marked as fluorescence). The spectrum the fluorescent molecules can emit is referred to as the emission spectrum. The difference between

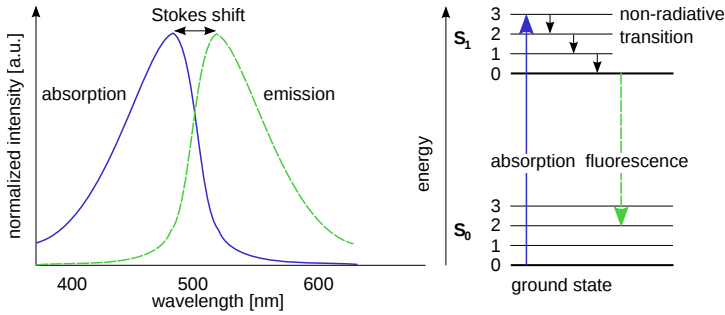


**Figure 3.1:** A fluorescent dye can be excited from the ground state to an excited state by absorbing light within its absorption spectrum. The molecule transfers to slightly lower energy levels through non-radiant transitions. By emission of a photon, the molecule returns to the ground state.

the maxima of the excitation and the emission spectrum is called the Stokes shift.

There are different approaches in order to realize fluorescing of a biological sample. Some dyes can be dissolved in membrane-permeant solvents (such as Dimethyl sulfoxide (DMSO)) which allow the dye to enter the cell *in vitro*. One example for such a dye is Fluo-4. This calcium sensitive dye has a low fluorescence in absence of calcium whereas it fluoresces brilliantly (100x stronger compared to the absence of calcium) in presence of calcium [26]. Therefore, this calcium sensitive dye can be used to detect action potentials in neurons and cardiomyocytes. Its excitation and emission maximum are found around 494 nm and 516 nm, respectively.

Immunofluorescence is based on labeling antigens using specific antibodies. One distinguishes between primary and secondary immunofluorescence. Primary immunofluorescence only uses one antibody (primary antibody) which is chemically linked to a fluorophore while the secondary immunofluorescence uses two antibodies. The primary antibody specifically binds the target molecule. The secondary antibody is fluorescently labeled and binds to the primary antibody. As many sec-

ondary antibodies can bind to the same primary antibody at the same time, the fluorescence intensity is much higher compared to primary immunofluorescence. In order to allow the antibodies to enter into the cytosol, one usually fixates the cell and permeabilizes the membrane using a detergent such as Triton X-100 (see section 11.6). In order to get insights into cell-adhesion, immunostaining can be used for example to stain against specific proteins such as vinculin which mediates the cell-substrate adhesion in focal adhesions (see section 2.3).

As an alternative to the described staining methods, specific viruses can be used which insert genes that encode fluorescent proteins into the cultured cells. In order to use this approach for calcium imaging, the cells can be manipulated to express GCaMP (see section 11.4). This protein is a combination of a green fluorescent protein (GFP), a calcium sensor calmodulin (CaM) and the peptide sequence M13. This combination results in a green fluorescent calcium sensor. An important advantage of this technique is, that the calcium sensor is only present in the cell and not in the surrounding media, which reduces the background fluorescence.

For all of these methods, one needs to make sure that light within the excitation spectrum can excite dye molecules while only light within the emission spectrum gets detected. Therefore, specific wavelength filters are built in the optical path.

#### **3.1.1 Super-resolution microscopy**

Super-resolution microscopy describes the field of light microscopy with a resolution beyond the diffraction limit which is mostly based on fluorescent imaging.

Even though super-resolution techniques such as photoactivated localization microscopy (PALM) and stochastic optical reconstruction microscopy (STORM) can reach a resolution of  $15\text{ nm}$  in all three dimension by imaging with two opposing objectives using interferometric approaches [27], these techniques will not be introduced in detail because of several reasons: The methods mostly require a fixation of the cells and are therefore not suited to image the cell dynamics. The light intensities required by these techniques are very high compared to the conditions during the evolution of life (around a factor of  $10^4$ ). Therefore, it is not surprising that these techniques show very fast bleaching and a strong phototoxicity [28]. Due to said reasons, PALM and STORM cannot be considered non-invasive [28]. Super-resolution techniques are very powerful and can give deep insights into many biological questions but as they are neither a standard technique in the field of cell adhesion nor have they been used in this work, introducing their working principle is beyond the scope of this thesis.

## 3.2 RICM

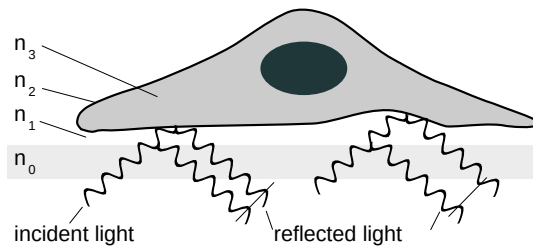


**Figure 3.2:** The substrate is illuminated from the bottom. The light is partially reflected at each interface of the sample. This results in different optical path length of the light. A detector measures the intensity of the interfering light and the cell substrate distance can be calculated based on the local intensity.

Reflection interference contrast microscopy (RICM) has been first used

### 3 Imaging techniques for the cell-substrate interface

by A. Curtis in 1964 [29] in order to study cell-substrate adhesion. It is a label-free technique which is based on the reflectance of monochromatic light at the successive layers at the cell-substrate interface: the coverslip as the substrate, culture media, cell membrane and cytosol with the refractive indices  $n_0, n_1, n_2, n_3$ , respectively. The sample is illuminated through the coverslip with monochromatic light which is partially reflected at each interface. At that time, it was assumed, that the refractive index of the membrane did not differ considerably from the refractive index of the cytosol. Therefore, the influence of the membrane was neglected and the intensity of the reflected light was modeled based on a three-layer system with  $n_2 = n_3 = n$ .

As the optical path length of the reflected light differs depending on the layer the light is reflected at as well as the thickness of the traversed layers, the light acquires different phase shifts which leads to interference effects at the camera revealing the cell-substrate distance. The reflectance intensity was modeled with the following equation:

$$I = \frac{n_1^2 (n - n_0)^2 \cos^2 \left( \frac{\pi}{\lambda} 2n_1 d \cos \theta \right) + (n_1^2 - n_0 n)^2 \sin^2 \left( \frac{\pi}{\lambda} 2n_1 d \cos \theta \right)}{n_1^2 (n + n_0)^2 \cos^2 \left( \frac{\pi}{\lambda} 2n_1 d \cos \theta \right) + (n_1^2 + n_0 n)^2 \sin^2 \left( \frac{\pi}{\lambda} 2n_1 d \cos \theta \right)}$$

With  $\theta$  being the angle of incidence. This equation shall not be discussed in detail, but it is important to notice, that the determination of the distance depends upon the refractive indices of all the layers involved in the system and therefore the assumption of constant refractive indices represents a potential error source for the study of cells.

Using the surrounding of the cell as a reference, Curtis determined the cell-substrate distance of cultured embryonic chick heart fibroblasts to  $d = 10 \text{ nm} - 100 \text{ nm}$  (see Figure 3.3). As the model system was based on strong simplifications, it is difficult to estimate the accuracy of these measurements. Curtis estimated that a deviation in the refractive index of  $\pm 0.001$  of the cytosol would result in an error of  $2 \text{ nm}$  in the

cell-substrate distance.

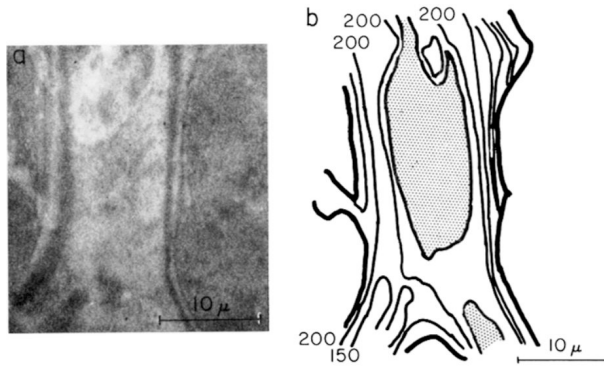


**Figure 3.3:** a) A RICM photograph of a chick heart fibroblast was used to estimate the cell-substrate distance based on the gray values in the picture. b) The estimated cell-substrate distances are given in Å. Figure adapted from [29].

Even though the accuracy of the technique might have been compromised due to simplifications, this publication answered a very important question: The cell-substrate cleft which had been observed before in electron microscopy [30] exists *in vitro* and is not a fixation artifact.

In 2009, the description of the reflected intensity was strongly improved by deriving the theory for a 5 layer system (corresponding to a sample structure consisting of buffer-filled vesicles on a protein-coated glass substrate) based on the Fresnel equations [31]. The resulting equation for the reflection coefficient is rather bulky and shall not be discussed in detail.

However, it should be mentioned that the intensity depends on the distance in an oscillating manner which introduces ambiguity of the signal. As the reflectance is also wavelength dependent, the distance can be determined clearly by measuring with two different wavelengths if the remaining parameters (refractive indices of all layers as well as thickness of the protein layer, and the lipid layer) are known.

It could be shown, that this method is capable of resolving the membrane-substrate distance with an accuracy of  $4\text{ nm}$  and that it can be used to quantitatively measure membrane fluctuations. RICM works without labeling and could therefore be used for long term investigations. A limiting factor of this technique is the shotnoise, which makes it impossible to evaluate the distance in certain areas. Another disadvantage is, that a reliable height determination requires the knowledge of the refractive index of each layer. Therefore, in order to investigate the cell-substrate distance, one would need to determine the intracellular refractive index first.

## 3.3 FLIC

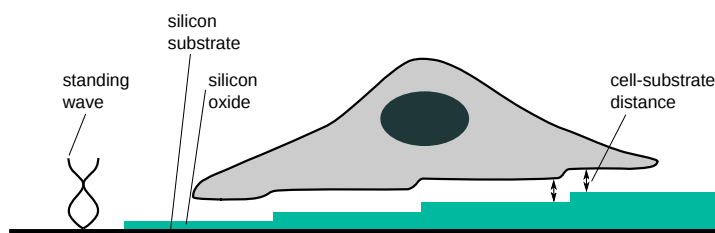


**Figure 3.4:** FLIC requires a specifically designed substrate with variable thickness of silicon oxide on top of a highly reflective layer such as silicon. Standing waves are excited above the silicon layer which interact with the fluorescent dye molecules in the cell membrane.

In 1996, A. Lambacher and P. Fromherz published their experimental work supported with detailed theoretical background on fluorescence interference contrast microscopy (FLIC) [32] as a method to measure the distance between fluorescent dye molecules and a highly reflective surface such as a silicon wafer with sub-nanometer accuracy.

The experimental setup is based on a basic fluorescence upright micro-

scope. If fluorescent dye molecules are illuminated with light within the excitation spectrum, the light can excite the dye molecules with probability  $P_{ex}$ . This probability depends on the orientation of the dye molecules in relation to the plane of incidence, the polarization of the incident light as well as the phase relation between photons that irradiate the dye molecules directly and those which get reflected by the surface before arriving at the molecules. The phase relation is key to the calculation of the cell-substrate distance as shown later, because it depends upon the optical path length difference between the photons and therefore on the distance between the dye molecule and the reflective surface. The excited dye molecules can relax into the ground state by spontaneously emitting a photon with probability  $P_{em}$  which is proportional to  $P_{ex}$ .

A detector is used to capture the fluorescence signal. The emitted photons can reach the detector directly, after a reflection at the surface (similar to the excitation photons) or miss the detector. If the molecules are illuminated stationarily, the detector captures a flow of photons  $J_f$  which is proportional to the product of said probabilities  $J_f \sim P_{ex} \cdot P_{em}$ . The relations that are found between the parameters are proportionalities but not equalities. As a consequence, this method needs a reference in order to determine absolute distances.

For the determination of cell-substrate distances, the authors proposed to stain the cell membrane with a fluorescent dye and use a silicon wafer with an additional silicon oxide layer with variable thickness (see Figure 3.4). The variable thickness of the spacer layer allows them to relate the fluorescent intensities captured from two neighboring steps in the spacer layer. In case of a constant cell-substrate distance  $\Delta$ , the quotient of the theoretical values for the fluorescence intensities  $I_{1,2}$  corresponding to the two adjacent steps with heights  $d_{1,2}$  is equal to

### 3 Imaging techniques for the cell-substrate interface

the quotient of the measured signals:

$$\frac{I_1}{I_2} = \frac{J_f (d_1 + \Delta)}{J_f (d_2 + \Delta)} \quad (3.1)$$

In their publication, the authors reported a strong dependence of the axial accuracy upon the lateral resolution due to the noise in the captured signal. Lateral resolutions of  $0.9 \mu\text{m}$ ,  $2.5 \mu\text{m}$ ,  $6 \mu\text{m}$  have been reported to result in accuracies of  $0.61 \text{ nm}$ ,  $0.31 \text{ nm}$ ,  $0.06 \text{ nm}$ , respectively [32]. The accuracy is almost unaffected by variations in the refractive index of the cytosol. The difference in the calculated cell-substrate distance in case of a cytosolic refractive index of  $n = 1.33$  and  $n = 1.40$ , has been determined to be around  $0.5 \text{ nm}$  [11].

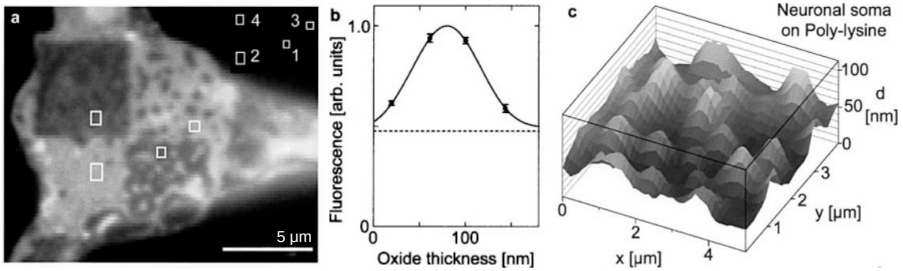


**Figure 3.5:** FLIC image and analysis of a neuron cultured on PLL. a) The FLIC image of the neuron shows different intensities on different oxide thicknesses. Relatively homogeneous areas are chosen within different parts of the structured substrate (marked with white frames). b) The fluorescence intensity is fitted based on the four measurement areas marked in (a). c) The distance profile within one square is determined based on the fit shown in (b) and the intensities shown in (a). Figure adapted from [11].

Afterwards, FLIC has been used to study the cell-substrate interface of neurons (see Figure 3.5) and astrocytes on different coatings [11, 33]. The reported values for the average minimal neuron-substrate distances on day in vitro (DIV) 4 were smallest for Cys-axonin-1 with  $37 \pm 10 \text{ nm}$  (for  $n = 16$  cells), medium for poly-L-lysine  $54 \pm 9 \text{ nm}$  ( $n = 7$ ) and furthest for laminin with  $91.9 \pm 4 \text{ nm}$  ( $n = 7$ ) [33].

FLIC works *in vitro* and can yield sub-nanometer accuracy and gave very important insights into neuronal cell adhesion. Unfortunately, the accuracy decreases if the lateral resolution is increased. Additionally, the technique is based on the assumption that the cell-substrate distance is constant [32]. This might give rise to errors if the 3D structure of the basal cell-membrane is very inhomogeneous.

As fluorescence gives rise to phototoxicity, FLIC is not suited for long term studies. The technique is limited to silicon-silicon oxide substrates which have to be produced with very high accuracy. As cell-substrate adhesion depends on the 3D structure of the substrate, the substrate itself might also influence the behavior of the cell [34, 13, 35, 36].

## 3.4 MIET

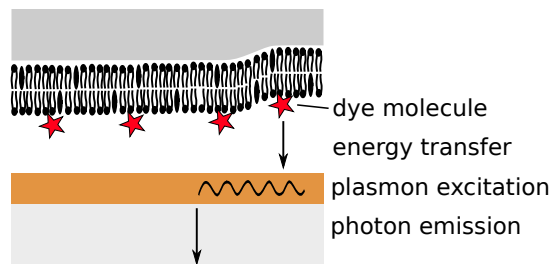


**Figure 3.6:** In MIET, cells are cultured on gold-coated coverslips. The membrane is stained with a fluorescent dye emitting in the red spectrum. The metal layer introduces a non-radiative decay channel and the energy is transferred into plasmons which dissipate into heat or reradiate by photon emission. The lifetime of the fluorophore is distance dependent. Measuring the intensity of the reradiated photons, one can calculate the dye-substrate distance.

Metal induced energy transfer (MIET) is an optical method to determine the distance of a specifically stained membrane to a gold covered glass substrate [37]. It is inspired by Förster resonance energy transfer

### 3 Imaging techniques for the cell-substrate interface

(FRET)[38], which will be introduced very briefly before going into the details of MIET.

FRET is based on the interaction of two different fluorophore molecules, the donor and the acceptor, in close vicinity (the distance between the molecules is typically in the range of 1 – 10 nm). If the donor emission spectrum and the acceptor excitation spectrum overlap, an excited donor molecule can transfer the excitation energy to the acceptor molecule via dipole-dipole interaction. The energy transfer efficiency  $E$  depends on the sixth power of the distance between donor and acceptor molecule:

$$E = \frac{1}{1 + \left(\frac{R}{R_0}\right)^6} \quad (3.2)$$

with  $R$  being the distance between the dye molecules and  $R_0$  being the distance at which  $E (R = R_0) = 0.5$  is fulfilled [39, ch. 45].

The acceptor molecule introduces an additional non-radiative decay channel for the donor molecule [39, ch. 45]. This results in an increase of the total decay rate of the donor molecule. As a consequence the lifetime  $\tau_D$  and the fluorescence intensity  $I_D$  of the donor are decreased.  $E$  can be expressed in terms of the relative donor intensity reduction  $\frac{I_{DA}}{I_D}$  or in terms of the relative lifetime reduction  $\frac{\tau_{DA}}{\tau_D}$  (subscripts  $D$ ,  $DA$  refer to the parameter without and in the presence of the acceptor molecule, respectively):  $E = 1 - \frac{I_{DA}}{I_D}$ ,  $E = 1 - \frac{\tau_{DA}}{\tau_D}$  [39, ch. 27]. Replacing the acceptor molecule with a gold layer, the energy can be transferred into excitation of plasmons in the metal layer. The plasmons either dissipate into heat or reradiate by photon emission.

The description of the lifetime and the intensity of a fluorescent dye molecule in distance  $d$  to a metal layer built the basis for the quantitative analysis used in MIET [40]. Here, the variation of the lifetime of the dye molecules is used to calculate the cell-substrate distance. In contrast to the fluorescent intensity, the lifetime variation is unaffected by

inhomogeneous distribution of dye molecules in the cell membrane.

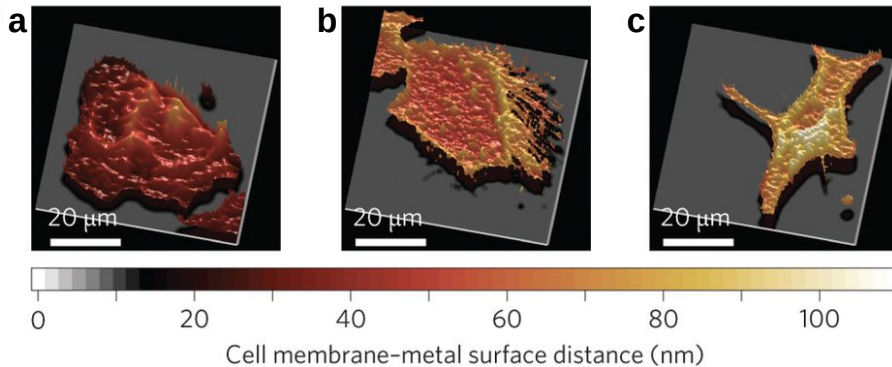


**Figure 3.7:** The cell-substrate distances of three different cell types were determined with MIET. (a), (b), (c) Show the profile of the basal cell membrane of an MDCK-II cell, an MDA-MB-231 cell and an A549 cell, respectively. Figure adapted from [37].

The experimental setup is based on a standard confocal microscope while the substrates used for cell culture consist of coverslips coated with a  $\sim 20$  nm thick, semi-transparent gold layer. MIET has been used to study the 3D structure of the basal cell membrane of several adherent cell lines. The average cell-substrate distances have been determined to  $28 \pm 5$  nm,  $54 \pm 8$  nm and  $67 \pm 7$  nm for MDCK-II, MDA-MB-231 and A549 cells, respectively (see Figure 3.7). Repeated measurements of the same area could be used to study variations in the structure caused by cell migration.

The axial accuracy of MIET has been reported to reach 3-4 nm whereas the lateral resolution corresponds to the resolution of the confocal microscope with  $\sim 200$  nm. The disadvantage of this method is the usage of fluorescence since phototoxicity might affect the cell behavior in long-term experiments.

## 3.5 FIB

Focused ion beam sectioning (FIB) in combination with electron microscopy has been used frequently to characterize the cell-substrate interface within the last decade [13, 35, 41, 36]. Specifically prepared cells are imaged with a scanning electron microscope (SEM) before they are cut using a focused ion beam. Ultrathin sectioning with FIB allows to realize large numbers of cross sections, which can be imaged with SEM and facilitate the reconstruction of the 3D structure of the basal cell membrane (see [36]).

As electron microscopy only works in vacuum, the cells need to be dehydrated before the FIB sectioning. There are two methods which can be used for this purpose: critical point drying and resin embedding. As the cells used in this work were all prepared using resin embedding, this method will be introduced here (protocol described in section 11.5).

First, the cells are fixated with glutaraldehyde. Glutaraldehyde cross-links the proteins in the cell membrane and in the cytosol by covalent binding of the proteins to their neighbors. Afterwards, osmium tetroxide ( $\text{OsO}_4$ ) is used which binds to the fatty acids of the phospholipids inside the membrane [42]. On the one hand this stabilizes the membrane. On the other hand the atomic weight of  $\text{OsO}_4$  is very high and leads to effective scattering of electrons which results in an enhanced contrast of the cell membrane and organelle membranes in electron microscopy. Afterwards, tannic acid is used to improve the fixation of the cell and mediate the binding of Uranyl acetate. Uranyl acetate binds to proteins and lipids enhancing the contrast in a similar manner due to its high atomic weight.

After these fixation assays have been applied, the water molecules in the cytosol can be slowly replaced by ethanol by exposing the sample to a water-ethanol mixture with successively increasing the ethanol

content. Afterwards, the ethanol is replaced by a resin-ethanol mixture. The resin diffuses into the cell while the ethanol content is reduced. The resin content on the sample is slowly increased until the sample is exposed to pure resin. The supernatant is washed with ethanol before the resin is cured by baking.

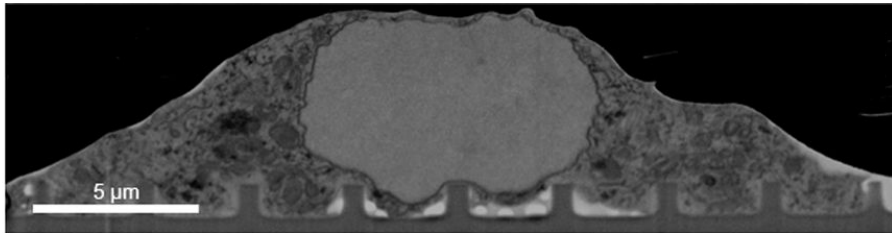


**Figure 3.8:** SEM image after FIB sectioning of an HL-1 cell cultured on a substrate structured with nano pillars. Some small cavities can be observed at the cell-substrate interface. Figure adapted from [36].

The cell-substrate interface can be observed with a scanning electron microscope (SEM) after cutting through the cell using a focused ion beam (see Figure 3.8). FIB can also be used to cut very thin lamellas by cutting the cell of interest from two sides until the thickness of the remaining lamella is in the order of  $100\text{nm}$ . A lamella can then be imaged with a transmission electron microscope (TEM) or a scanning transmission electron microscope (STEM) with higher spatial resolution ( $\sim 2\text{nm}$ ) compared to SEM imaging [12].

FIB is of significant importance to this work as it has been used as an alternative quantitative method for the correlation with the SPRM results chapter 8. It should be kept in mind, that the artifacts which are induced by the extensive fixation, staining and resin embedding procedures are so far unknown. The correlation of SPRM and FIB which will be shown in chapter 8 represents one approach to identify these artifacts.

## 3.6 Surface plasmon resonance imaging

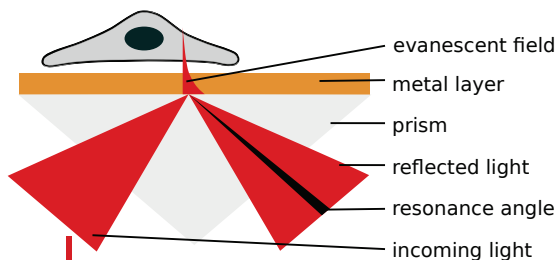


Figure 3.9: Kretschmann configuration

Surface plasmons resonance (SPR) imaging is a very sensitive technique and can be used to visualize cell-substrate contacts qualitatively (widefield imaging/live-imaging) or for the quantitative investigation of the cell-substrate distance (scanning SPR). Both methods require a transparent substrate such as glass which is coated with a thin layer of metal such as gold (Au), silver (Ag), copper (Cu) or aluminum (Al).

Plasmons are collective oscillations of electrons whose resonance frequency depend upon the properties of the material they are excited in as well as upon the environment of the material. Under specific conditions which are going to be discussed in detail in section 4.1, they can be excited by illumination of the substrate with visible light. One of the key points is, that the light cannot directly excite the electron oscillations (due to a momentum mismatch) but only by the creation of an evanescent field which requires incidence angles higher than the angle of total internal reflection (also known as the critical angle).

The Kretschmann configuration is probably the most intuitive way to fulfill these requirements. Such a setup is based on a glass prism coated with a thin metal layer (see Figure 3.9). Incident light can pass through the prism before it is reflected at the metal layer and travels

towards a detector [43, ch. 12]. The angle of incidence is variable. If it is chosen higher than the critical angle, an evanescent field is created. If the incident angle is chosen such that the excitation condition (see Equation 4.4) is satisfied, surface plasmons are excited.

The plasmon resonance angle corresponds to the angle of minimal reflection. Its position is very sensitive to any change in the dielectric constants within the penetration depth of the evanescent field. The dependence of the reflected intensity on the angle can be modeled based on the transfer matrix method (see section 4.2). Under certain conditions, the analysis of the reflectance allows for an accurate calculation of the cell-substrate distance.

In contrast to this quantitative analysis, live-imaging gives qualitative information about the cell-substrate interface. If the interface is illuminated under the resonance angle of the substrate-media interface while the interface is imaged on a sensor, the field of view appears relatively dark in those areas surrounding the cells. In contrast, those areas covered with adhering cells, appear relatively bright as the presence of a cell alters the resonance angle locally and the incident light is mostly reflected.

SPRM imaging of the cell-substrate interface has first been realized based on a Kretschmann configuration by Giebel *et al.* in 1999 [14]. Giebel *et al.* imaged living glial cells on aluminum films. In this analysis, they found cell-substrate distances between 25 *nm* and 160 *nm*. They estimated the accuracy to be around 10 *nm*. The lateral resolution was limited to 1  $\mu\text{m}$  in direction of the plasmon momentum due to the plasmon propagation and by the diffraction limit in perpendicular direction.

Since then, many different attempts have been taken to improve the technique (see section 4.3). The live-imaging has been improved to reach the diffraction limit by exciting localized surface plasmons and

### *3 Imaging techniques for the cell-substrate interface*

used to reveal cell adhesion sites [44] and to measure cell-substrate distances of HEK cells [15]. Intracellular structures have been resolved using a projector-based illumination[45], action potentials of neurons have been observed using a live-imaging setup [46] and time-laps scanning has been used to investigate cell migration over several days based on surface-plasmon-interference microscopy [47].

# Surface plasmon resonance theory

# 4

This chapter shall provide the theoretical background which is necessary to understand under which conditions surface plasmons can be excited by visible light (see section 4.1). Additionally, it will introduce the transfer matrix method as a method to model the interaction of the incident light and the sample (see section 4.2) and introduce several different concepts for the realization of SPRM setups (section 4.3).

## 4.1 Surface plasmon excitation

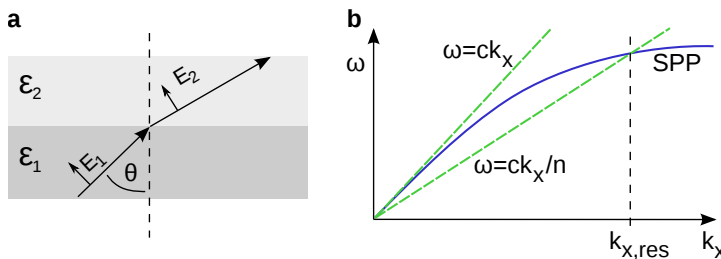


**Figure 4.1:** a) P-polarized light travels through media 1 and is diffracted at the interface b) The dispersion relations of photon propagation through free space and plasmons reveal that free photons cannot excite plasmons as the graphs do not cross. A medium with a refractive index  $n > 1$  can be used to fix this energy mismatch.

Surface plasmons are collective oscillations of electrons which can be formed at an interface between two media such as glass and metal (e.g. gold, silver, aluminum or copper). Taking into account that the oscillating charges generate an electric field, the entire excitation is referred to as “surface plasmon polariton” (SPP).

#### 4 Surface plasmon resonance theory

In order to understand how plasmons can be excited, the behavior of the electric field  $\underline{E}_j$  and the magnetic field  $\underline{H}_j$  ( $j = 1, 2$  numbers the media) of p-polarized light at the interface between two media with the permittivity  $\epsilon_j$  at the plane  $Z = 0$  (see Figure 4.1) is described by:

$$\underline{E}_j = \begin{pmatrix} E_{x_j} \\ 0 \\ E_{z_j} \end{pmatrix} e^{ik_{x_j}x + ik_{z_j}z - i\omega t}, \quad \underline{H}_j = \begin{pmatrix} 0 \\ H_{y_j} \\ 0 \end{pmatrix} e^{ik_{x_j}x + ik_{z_j}z - i\omega t} \quad (4.1)$$

At the interface between the two layers, the boundary conditions need to be satisfied  $E_1^\parallel = E_2^\parallel$ ,  $H_1^\perp = H_2^\perp$ . In combination with Maxwell's equations  $\nabla D = 0$  and  $\nabla \times H = \frac{\delta D}{\delta t}$  (for  $J = 0$ ), the dispersion relation can be deduced. As the derivation is quite tedious, only the final result is given here (for a detailed derivation see [43, ch. 12]):

$$k_x = \frac{\omega}{c} \sqrt{\frac{\epsilon_1 \epsilon_2}{\epsilon_1 + \epsilon_2}} \quad (4.2)$$

In order to excite surface plasmons, energy and momentum have to be conserved:

$$\omega_{photon} = \frac{c}{n} k_x \stackrel{!}{=} \omega_{SPP} = \sqrt{\frac{\epsilon_1 + \epsilon_2}{\epsilon_1 \epsilon_2}} k_x c \quad (4.3)$$

$$k_{x_{photon}} = k_0 \sin \theta \stackrel{!}{=} k_{x_{SPP}} = \frac{\omega}{c} \sqrt{\frac{\epsilon_1 \epsilon_2}{\epsilon_1 + \epsilon_2}} \quad (4.4)$$

As one can see in Figure 4.1b, the energy of a plasmon is always lower than the energy of a photon traveling through vacuum. In order to excite a plasmon, a media with refractive index  $n_1 > 1$  is introduced. This way, the energy conservation is satisfied (one can observe a crossing of the energies in Figure 4.1b).

The wave vector  $k_{SPP}$  of the plasmons is always larger than the wave vector of light in free space  $k_{photon}$  [43, ch. 12]. A typical method to overcome this momentum mismatch, is by creating an evanescent field

at the interface (therefore  $n_1 > n_2$  needs to be satisfied) by irradiating the interface with angles  $\theta$  larger than the critical angle (angle of total internal reflection). This in turn means that  $k_z$  is imaginary. Due to  $|k_0| = \sqrt{k_x^2 + k_z^2}$ , the x-component of the wave vector can be larger than the absolute value of the wave vector  $k_x > |k_0|$ . This is the reason why the SPRM setups which will be discussed later are based on total internal reflection.

The relations that have been shown in this section hold true for a simple interface between two layers only. Considering more layers in the derivation, the system of equations becomes larger and therefore more difficult to solve because the boundary conditions have to be satisfied at each interface. Therefore, the equation systems become more complex with each additional layer (see [48, ch. 1]). For a sample consisting of a substrate with cultured cells, the sample involves 6 layers resulting in a massive equation system. As the dispersion relation is not used for any calculations within this thesis, this will not be discussed in detail.

Instead, the transfer matrix method (see section 4.2), which models the reflection and transmission of the incident light at each interface will be introduced. This method is used in this work in order to analyze the data.

## 4.2 Transfer matrix method

This section contains a revised version of the methods part of the publication by

E. Kreysing *et al.* "Nanometer-resolved mapping of cell-substrate distances of contracting cardiomyocytes using Surface Plasmon Resonance Microscopy" [16].

#### 4 Surface plasmon resonance theory

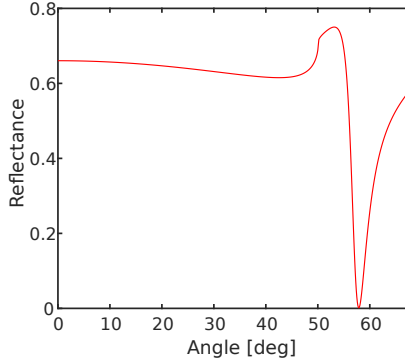


**Figure 4.2:** The reflectance curve gives the intensity of the light reflected at the sample as a function of the angle.

The transfer matrix method (TMM) models the interaction of incident light with a sample consisting of a stack of layers which differ in their refractive indices and thicknesses. It can be used to determine the intensity of the light reflected by the sample as a function of the angle. The resulting curve is known as the reflectance curve (see Figure 4.2).

As it can be shown that plasmons cannot be excited with s-polarized light [43, ch. 12], an illumination with purely p-polarized light is assumed here. The sample is illuminated with a defined range of angles. The reflection and transmission of the incident light at each layer can be modeled by the characteristic matrix  $M_i$  [49]:

$$M_i := \begin{pmatrix} \cos(\beta_i d_i) & -i \frac{\sin(\beta_i d_i)}{q_i} \\ -i \sin(\beta_i d_i) q_i & \cos(\beta_i d_i) \end{pmatrix} \quad (4.5)$$

with  $\beta_i := k_0 n_i \cos(\theta_i)$ ,  $q_i := \cos(\theta_i) \sqrt{\frac{\mu_i}{\epsilon_i}}$ , and  $d_i$ ,  $k_0$ ,  $n_i$ ,  $\theta_i$ ,  $\mu_i$ ,  $\epsilon_i$  representing the layer thickness, wave number in vacuum, refractive index, angle of incidence, magnetic permeability and the permittivity, respectively. The characteristic matrices of all the layers within the sample

are multiplied  $M = \prod_{i=1}^N M_i$ , where  $M$  describes the propagation of light through the sample.

The reflectance  $R = |r|^2$  can then be calculated based on the reflection coefficient:

$$r = \frac{q_1 (M_{11} + q_N M_{12}) - (M_{21} + q_N M_{22})}{q_1 (M_{11} + q_N M_{12}) + (M_{21} + q_N M_{22})} \quad (4.6)$$

This shows that the reflectance depends upon the refractive index of each layer and the thickness of each layer except for the thickness of the two boundary layers as they are assumed to be infinite.

In the case of an SPR sample, the layers usually consist of a glass substrate, an adhesion layer which mediates the adhesion of the adjacent metal layer to the glass, the metal layer the plasmons should be excited in, and one or more additional layers specific to the experiment. SPR is sensitive even to very small changes in the sample composition. Therefore it became an essential method for the detection of molecule-surface binding events (commercialized systems are available from many different companies). But it is also a valuable tool for measuring the thickness of an intermediate layer within the stack in cases where all involved refractive indices are known.

## 4.3 SPRM types

In order to give an overview of the most common SPRM types, several prism based and objective-based SPRMs will be introduced in this section.

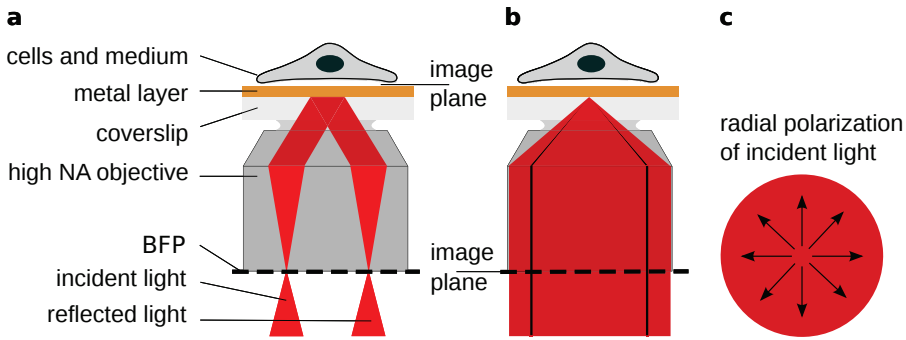
### 4.3.1 Prism based SPRM

Figure 3.9 shows the Kretschmann configuration as one example for a prism-based setup which was first realized in 1971 [50]. A glass prism is coated with a thin metal layer. The illumination arm contains a laser diode and a lens system used for expanding the beam while the recording arm contains an objective, an eyepiece and a camera. The angle of the incident light can be varied while imaging the entire field of view. The cells are cultured directly on the prism. As mentioned before, the lateral resolution is limited by the propagation length of the surface plasmons to around  $1 \mu\text{m}$  in propagation direction and by the diffraction limit in perpendicular direction which strongly limits the investigation of cellular structures.

For the sake of completeness, the Otto configuration shall also be mentioned here. The first realization was reported in 1968 [51]. In contrast to the Kretschmann configuration the glass and metal layer are separated by an air gap. A total internal reflection at the glass-air interface creates an evanescent field which interacts with the lower side of the metal layer and excited plasmons at the air-metal interface. This configuration has been reported to be experimentally inconvenient as the air gap is difficult to control [43, ch. 12] and cannot be used for imaging the cell-substrate interface.

### 4.3.2 Objective-based SPRM

Objective-based SPRM setups have several advantages compared to prism based setups: the cells can be cultured on metal-coated coverslips which can be easily glued to Petri dishes instead of culturing the cells directly on the prisms. This can increase the throughput of the method due to lower sample costs and more convenient handling.



**Figure 4.3:** A live-imaging mode (a) and a scanning mode (b) can be realized in the same objective-based SPRM setup via different illumination concepts. Radially polarized light (c) improves the lateral resolution of the scanning mode.

Objective-based setups are based on TIRF-objectives. These objectives are characterized by their numerical aperture (NA). As the NA characterizes the range of angles  $0^\circ < \theta < \theta_{max}$ , which is captured by the objective ( $NA = n \sin(\theta_{max})$ ), only objectives with a high NA (usually  $NA \geq 1.4$ ) can facilitate an illumination under the plasmon resonance angle ( $\theta_{res} \sim 60^\circ$ ).

Objective-based SPRM setups allow for many different illumination concepts. These can be divided into the two fields of widefield imaging and scanning SPRM.

Widefield imaging can be realized by focusing incident light on the back focal plane (BFP) of the objective, which results in an illumination of the cell-substrate interface with parallel light. By imaging the substrate plane onto the sensor of a camera, the surface can be observed in real time. Therefore, widefield SPRM modes are also known as live-imaging modes.

Scanning SPRM is based on a pointwise illumination of the interface. Therefore, the entire BFP of the objective is illuminated with parallel light. This incident light is focused by the objective at one point at the

surface of the sample resulting in an illumination of this point with a broad angle spectrum. In this scheme, the BFP is imaged onto the camera sensor. From this image, one can extract the reflectance curve, which can give information on the sample structure using an analysis technique based on the TMM. This mode is referred to as the scanning mode.

### **Objective-based live-imaging**

The easiest implementation of an objective-based live-imaging setup is by focusing a linear polarized laser beam onto the BFP (see Figure 4.3a). If the axis of the incident light is parallel to the axis of the objective, this results in an illumination with parallel light of the field of view. The illumination angle at the metal surface depends on the distance of the focus spot at the BFP from the objective axis. The position and the polarization direction are chosen such that the interface is illuminated with p-polarized light under the resonance angle of the metal-media interface.

Imaging the metal-media interface onto the sensor of a camera, objects that differ in the refractive index from the surrounding media can be observed as areas with a relatively high reflectivity. This method has been used for imaging contact areas between the metal surface and a large variety of objects such as PDMS stamps [52], lipid bilayers, polymer microspheres [53] and living cells [15].

Live-imaging SPRM suffers from a low lateral resolution in direction of the plasmon propagation. Additionally, if coherent light is used, speckle noise compromises the resolution of fine structures such as neuronal axons or dendrites.

A. Peterson *et al.* realized a live-imaging setup based on a projector

illumination [45]. They projected a crescent arc pattern onto the BFP of the objective. The position of the arc on the BFP is chosen in the same way as the position of the focus spot in the objective-based laser live-imaging. As the projector provides incoherent illumination, Peterson *et al.* could improve the image quality by avoiding speckle noise. In order to compensate for an inhomogeneous illumination of the field of view, they divided one image taken with p-polarized illumination by one image take with s-polarized illumination. This was realized by using a projector which provides randomly polarized light and a linear polarization filter which can be rotated by 90°. With this setup, they realized a lateral resolution in the sub-micrometer regime: in direction of the plasmon propagation they achieved a resolution of  $\approx 600 \text{ nm}$  while a resolution of  $\approx 300 \text{ nm}$  was realized perpendicular to the propagation direction. This allowed for the first time to resolve intracellular structures such as cell organelles.

A similar illumination concept was used in [54] where a spatial light modulator was used to project an entire ring onto the BFP instead of a crest arc and diffused laser light was used instead of an projector lamp. Unfortunately, this system was still suffering from a relatively low resolution in propagation direction. Quantitative values for the lateral resolution have not been given in this publication.

## **Objective-based scanning**

Scanning SPRM with radial polarized light has been shown to reach a lateral resolution at the diffraction limit [55] by exciting localized surface plasmons. Here, the entire BFP of the objective is illuminated with radial polarized light (see Figure 4.3b, c). By focusing the light onto the cell-substrate interface, the objective generates an illumination with the entire angle spectrum allowed by the NA of the objective. Those

parts of the light which satisfy the excitation condition, excite plasmons whose momenta lie parallel to the surface and are spread inside the metal layer. These parallel momenta are referred to as  $k_{xy}$  as they do not have a preferred direction within this plane. Consequently, the excited plasmons spread in all the directions within the plane. According to [55], the propagating plasmons interfere with one another and localize around the focus spot. Due to the localization of the surface plasmons, the lateral resolution of this illumination scheme is strongly improved compared to the live-imaging mode where the lateral resolution is limited by the propagation length.

The majority of the light is reflected at the metal layer and travels back through the objective. By imaging the BFP on a camera sensor, it is possible to extract the reflectance as a function of the angle (see Figure 4.2). The reflectance curve can be fitted using the TMM (see section 4.2). This way, the cell-substrate distance can be determined [15]. In order to determine the cell-substrate distance at the entire cell-substrate interface, one has to capture the BFP for many scanning points and reconstruct the 3D topology of the basal cell membrane. In theory, the sensitivity allows for measuring distances with nanometer accuracy if the reflection curves can be fitted ideally [15].

For the sake of completeness, fiber-coupled scanning SPRM combined with an interferometric heterodyne detection will be briefly introduced even though the working principle differs significantly from the other methods. First, laser light passes through an electrically controllable polarizer which allows to switch between linear, azimuthal and radial polarization. The light is then divided by a beam splitter into an illumination arm and a reference arm. The light in the illumination arm is focused by a high NA objective at the cell-substrate interface where plasmons can be excited in a gold layer. The fraction of the light which is reflected at the interface exits the objective and is recombined with the reference beam and detected by a photomultiplier.

A Piezo stage is used in order to alter the X-, Y-, and Z-position of the sample. At each scanning point (X-Y- position), the Z-position of the sample is varied automatically while the signal is detected by the photomultiplier. This allows to recombine a Z-stack of SPR images of the scanned object. As a result, intracellular structures such as the nucleus can be imaged [56] and adhesion sites can be visualized[47]. The lateral resolution reaches the diffraction limit.

In contrast to other presented SPRM methods, this method is not used to investigate the cell-substrate distance. As its working principle differs fundamentally from the SPRM techniques discussed before, its significance for this work is minor compared to the other methods.



# SPRM Setup

This chapter describes the SPRM setup at the ICS-8 including the optical setup as well the data analysis and performance of the technique. In section 5.1, the SPRM prototype which was built at the ICS-8 by Dr. Koji Toma will be introduced. This includes the optical setup as well as data processing. Afterwards, a short overview covering the modifications of the setup and the analysis software is given.

In section 5.2, an overview on the current status of the physical setup is given which lists all the different imaging modes combined in the setup. In section 5.3, the laser- and projector-based live-imaging mode are introduced in detail and their resolutions compared. In section 5.4, the physical realization of the setup is explained before the three different scanning data acquisition modes are discussed in detail. Afterwards, the processing of the scanning data as well as the improved accuracy of the distance measurement are explained. Furthermore, the performance of the automated fitting procedure will be compared to a manual fitting process. Finally, the limitations of the setup due to the pixel accuracy are evaluated. In section 5.5, further setup elements and additional imaging modes will be introduced.

## 5.1 Introduction of the SPRM at the ICS-8

### 5.1.1 Prior work on the SPRM at the ICS-8

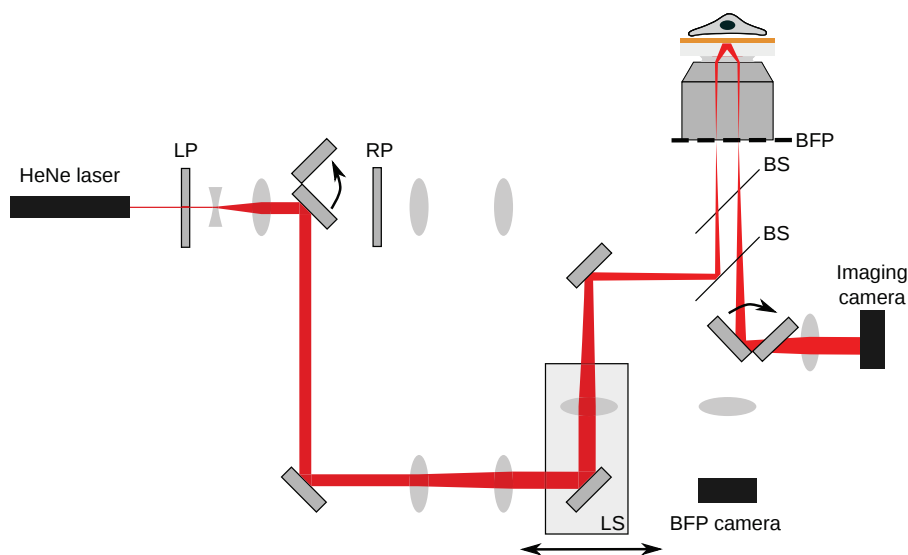


**Figure 5.1:** Laser-based live-imaging mode of the first prototype built by Dr. Koji Toma. Abbreviations: HeNe: helium neon, LP: linear polarizer, RP: radial polarizer, BFP: back focal plane, BS: 50:50 beamsplitter, LS: linear stage.

The setup used in this work is based on a prototype built by Dr. Koji Toma in collaboration with Prof. Dr. Hiroshi Kano. The prototype was created following the design presented in [44]. The objective-based setup combined a laser live-imaging SPRM (see Figure 5.1) and a scanning SPRM using radially polarized light (see Figure 5.2). In order to switch from one mode to the other, the illumination path as well as the recording path had to be changed manually using flipping mirrors.

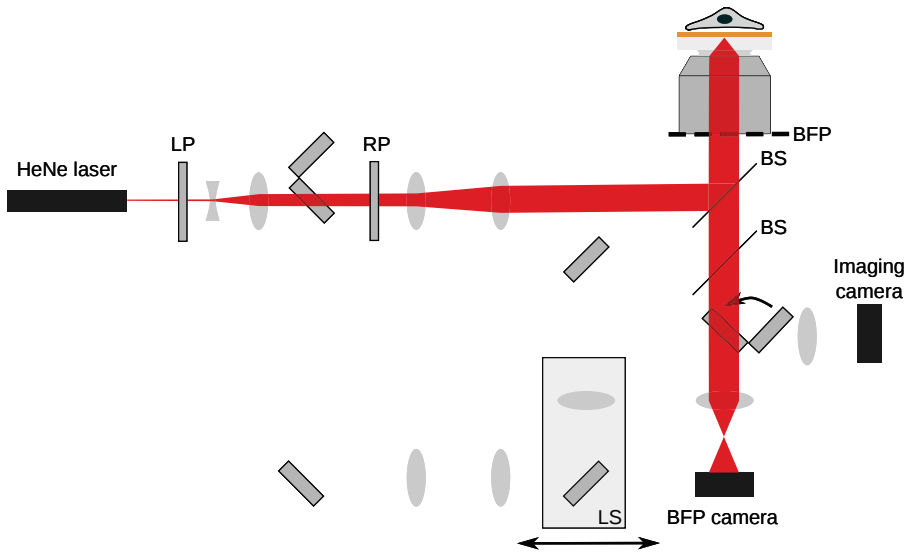


**Figure 5.2:** Laser-based scanning mode of the first prototype built by Dr. Koji Toma. Abbreviations: HeNe: helium neon, LP: linear polarizer, RP: radial polarizer, BFP: back focal plane, BS: 50:50 beamsplitter, LS: linear stage.

It was possible to localize an object in the live-imaging mode, determine the scanning parameters, switch manually to the scanning mode and record BFP images. The data was analyzed using a combination of custom-made scripts and *WINSPALL*, a free software which is popular in the SPR community.

*WINSPALL* allows the manual fit of the reflectance curves based on the TMM. It was used to determine the average sample structure based on the averaged reflectance curve. This curve is obtained by averaging the reflectance profiles from all the scanning points within the scanned area. In the analysis of the sample structure, the refractive indices and the thicknesses of the involved layers were assumed as constant except for the thickness of one layer. In case of a cell measurement, this was the thickness of the culture media layer. As a result, it was possible to generate a 3D profile of the basal cell membrane.

## 5 SPRM Setup

Toma *et al.* showed that the setup could be used to first localize HEK cells in the live-imaging mode and subsequently determine the cell-substrate distance based on the scanning mode with nanometer sensitivity. It will be shown in section 5.4.3, that the accuracy of the scanning data was strongly compromised as the refractive index of the cytosol was assumed to be homogeneous. This led to errors in the order of 100 *nm*.

It had been previously shown that the lateral resolution of the scanning mode in a comparable setup reached the optical diffraction limit [57]. As Dr. Koji Toma built his setup following this specific design, a resolution at the diffraction limit was also assumed for the scanning mode of this setup. However, due to the coherent laser illumination, the strong speckle noise in the live-imaging frustrated the resolution of intracellular structures as well as fine structures such as neuronal dendrites (see Figure 5.8).

As is the case with most prototypes, the setup showed some problems caused by the choice of components or the way of assembly. The prototype setup contained a pellicle beamsplitter, which consists of a membrane with a thickness in the micrometer range. These beamsplitters (BS) avoid the creation of ghost images but are also extremely noise sensitive. This proved to be a problem as sound and vibrations in the building (e.g. closing doors) disturbed the SPRM measurements.

Another inconvenience was caused by the field of view (FOV) in the live-imaging mode. The imaged area was around  $35 \times 35 \mu\text{m}^2$ . This allowed for the localization of HEK cells but it turned out to be too small when studying larger cell types such as cardiomyocytes or neurons, as the cells were usually larger than the FOV. This was caused by the focal length and the position of the lens on the linear stage (LS) (see Figure 5.1) as well as the position of the tube lens in front of the live-imaging camera and the position of the camera itself.

## 5.1.2 Overview on the modifications of the setup

This section gives an overview regarding the changes in the setup as well as the current configuration of the optical setup. As the experimental inconveniences mentioned in section 5.1.1 needed to be solved and new features which allow for better alignment should be introduced, the optical setup had to be strongly modified. Therefore, it seemed to be easiest to rebuild the setup from scratch.

In the new setup, the lens on the LS was exchanged against a lens with shorter focal length while the LS was moved closer to the objective. As a consequence, a larger area at the cell-substrate interface is illuminated. This is one of the two important steps towards an increased FOV. The second step is to “zoom out” by repositioning the tube lens as well as the imaging camera. Thus, the FOV was increased from  $35 \times 35 \mu\text{m}^2$  to  $50 \times 50 \mu\text{m}^2$ .

Exchanging all the used BS for BS cubes reduced the noise sensitivity of the setup while exchanging the position of BS and flipping mirrors made it possible to image the substrate interface and the BFP at the same time (see Figure 5.4). This is very helpful during a several of the alignment procedures as will be shown in section 5.3 and section 5.4.

In order to improve the resolution of the live-imaging mode, an additional illumination path based on an LCD projector was included. It is now possible to chose between the projector light source and the laser light source using an additional flipping mirror (see Figure 5.4, Figure 5.6). The respective optical paths will be discussed in section 5.3.2 and section 5.3.1.

Additionally, it was crucial to install an upright microscope on top of the SPRM setup in order to correlate the SPRM results with DIC or fluorescent images of the cells. The upright microscope has also proven

to represent an excellent light source for an additional bright-field imaging: the objective of the upright microscope acts as a condenser while the TIRF objective of the SPRM setup collects the light passing through the semi-transparent sample (Figure 5.17). This allows the capture of bright-field images with the same ROI as the SPRM live-imaging pictures.

Regarding the LabVIEW acquisition software as well as the analysis routine, fatal problems were faced in the beginning of this work. Therefore, the software used for acquisition and analysis of the BFP images was recoded from scratch. This was realized by Hossein Hassani as his Master's thesis within this project [58].

## 5.2 General description

The SPRM setup was custom made and assembled on a dampened optical table. The prototype setup consisted of a laser live-imaging mode and a scanning mode. During my PhD, the setup has been extended and the up-to date configuration comprises:

- a laser live-imaging mode
- a projector live-imaging mode
- a scanning mode
- an upright fluorescence microscope (commercially available)
- an inverted bright-field microscope mode

Figure 5.3 shows the physical setup of the SPRM. It is not suited for the introduction of the optical paths but it should give an impression of the physical arrangement. The heart of the setup is a TIRF objective

with  $NA = 1.7$ . While almost the entire optical path lies within a plane (P1) parallel to the table, the incident light has to be reflected upwards in order to enter the objective whose axis is perpendicular to the table. Most of the the incident light is reflected at the sample and exits the objective through the BFP before it is reflected back into the plane P1. This configuration allows the study of samples which are placed in parallel to the table plane.

The used SPRM samples consist of special high index coverslips coated with an adhesion-mediating chromium layer and a gold layer (see section 11.1.2). The substrates are glued to polystyrene Petri dishes with a hole in the bottom (coated side facing the interior of the dish, see section 11.1.3). These are used as a basis for cell culture and filled with culture media throughout the entire experiments. In order to image cells on such a sample with the SPRM, the bottom of the sample is brought in contact with the objective's immersion oil. This facilitates an illumination through the TIRF objective. At the same time, an upright light microscope can be used to image the cells from the top.

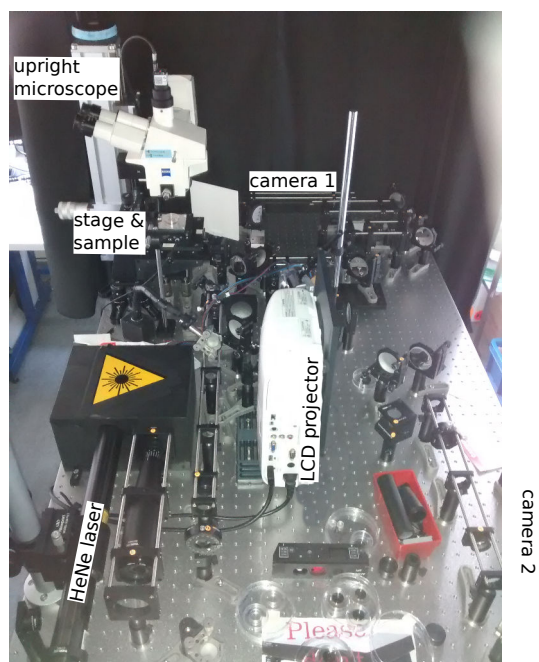


**Figure 5.3:** The optical setup of the SPM at the ICS-8. Camera 2 is cut at the right edge of the picture. Its position is marked by the label.

## 5.3 Live imaging

### 5.3.1 Laser live-imaging

As described before, the FOV was increased by replacing the lens on the linear stage, decreasing the distance between said lens and the objective and repositioning the tube lens and the imaging camera. Figure 5.4 shows the current optical path of the laser live-imaging. A  $10\text{ mW}$  HeNe laser is used as a light source and dampened by a neutral density filter (not shown) to a power of  $\sim 1\text{ mW}$  inside a shielding box before it enters the open setup. The beam is filtered by a linear polarization filter (LP) and expanded using a beam expander (represented by two lenses behind the LP) as well as an additional set of lenses in front of the linear

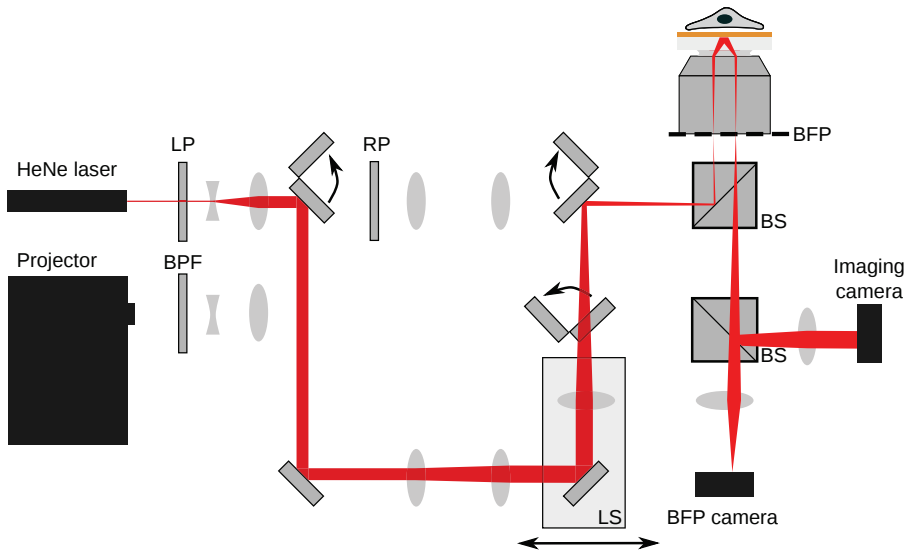


**Figure 5.4:** Optical paths of the live-imaging SPRM

stage (LS). The lens on the linear stage is used to focus the light onto the BFP of the objective passing through a 50:50 beamsplitter cube (BS) in front of the objective. By changing the position of the linear stage, one can change the distance  $r$  between the optical axis of the objective and the focus spot on the BFP. This distance can be directly related to the illumination angle  $\theta$  at the interface using the Abbe sine condition  $\sin(\theta) = \frac{r}{f \cdot RI}$  with  $f$  being the focal length of the objective and  $RI$  the refractive index [59].

The light illuminates the substrate-gold interface where it gets partially reflected and partially absorbed. The reflected light exits the objective through the BFP and passes through the BS again. The fraction of the light which passes straight through this BS travels towards another 50:50 BS which divides the light onto two different recording paths. In the first recording path, the lens images the substrate-gold interface onto the sensor of the imaging camera. In the second recording path, the lens images the BFP of the objective onto the sensor of the BFP

camera.

At first, the widefield live-imaging is introduced, which is based on the first recoding path: Let us imagine an SPRM sample with a liquid medium such as water or culture media on top. If the incidence angle  $\theta$  is chosen such that the excitation condition of the bare gold-media interface is matched, the field of view in the live-imaging mode appears relatively dark as light arriving under the resonance angle excites plasmons inside the gold layer and little light is reflected. If an object with a different refractive index is now inserted into the media within the field of view and within the evanescent field, this will result in a local shift of the resonance angle. As a consequence, the position the object becomes visible in the image since the reflectivity at this position is higher and a relatively bright area will appear in the FOV corresponding to the position of the object. The same principle allows for the imaging of cell-substrate contacts (see Figure 5.8).

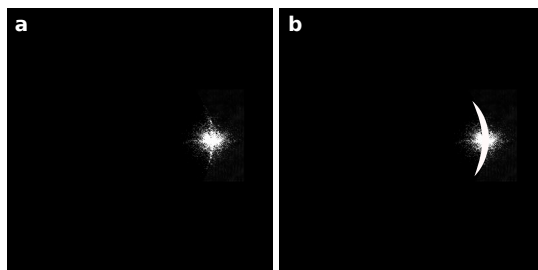


**Figure 5.5:** Image of the BFP during illumination in the live-imaging mode. The laser light is focused on one spot on the BFP resulting in an illumination of the gold surface with parallel light. The illumination angle can be chosen by choosing the position of the focus spot on the BFP. Most of the light is reflected at the interface and appears as a bright spot on the BFP (a). If the resonance angle is matched, a faint arc originating from the center of the spot can be observed. This arc is retraced in (b).

In the laser live-imaging mode, the incident light is focused on one spot at the BFP with the distance  $r$  from the optical axis. Consequently, the cell-substrate interface is illuminated with parallel light under the

angle  $\theta$ . A fraction of the light is absorbed while the rest is reflected under the angle  $\theta$  and focused again at one spot with distance  $r$  to the optical axis.

Using the prototype SPRM, the illumination angle had to be chosen “blindly”. This means, that one was observing the interface using the imaging camera while changing the angle of incidence by moving the LS. This resulted in a changing contrast in the image. In theory, the contrast between the background and the object is optimal, when the illumination angle is chosen such that it matches the resonance angle of the surrounding area. This procedure works nicely for objects with a distinct shape. In the case of diffuse objects it is more difficult, as the observed structures as well as the surrounding area cannot be easily identified. In this case it is advantageous to image both, the interface as well as the BFP at the same time, which is possible with the new setup because the BFP camera allows imaging of the position of the focus spot (the position where the light exits the objective on the BFP).

If the illumination angle of the incident light matches the average resonance angle of the field of view, one can observe a weak arc of light appearing around the focus spot on the BFP (see Figure 5.5). This could be explained by the following mechanism: The incident light excites surface plasmons, which propagate inside the gold layer and either dissipate into heat or scatter at non-uniformities in the layer. The scattering process can cause a reradiating process. The momentum of the scattered plasmon can be transferred to the scattering partner and a photon. This reradiated photon can then exit through the BFP and reach the BFP camera.



inside the enclosure (its size was limited by the size of the enclosure). This allowed for the focusing of the majority of the light which then leaves through the opening in the enclosure. Here, it passes directly through a laser-line band-pass filter (diameter: 1") which is placed as close as possible to the projector. This filter transmits a narrow range of red light (central wavelength  $\lambda_c = 632.8nm \pm 10nm$ ), while the remaining spectrum of the projector lamp is reflected.

Additionally, a lens-system consisting of biconcave and a biconvex lens (diameter: 2") and an additional flipping mirror was placed onto the optical table in front of the projector. This unit facilitates the imaging of the projected pattern onto the BFP. The flipping function of the mirror is important to guarantee a fast switching between the projector live-imaging mode and the laser live-imaging.

The optical paths of the laser and the projector live-imaging follow the same principle: light is focused at a specific position on the BFP in order to realize parallel illumination of the sample under a variable angle of incidence. For this purpose, an arc pattern, consisting of either one arc or two opposing arcs, is projected onto the BFP (see Figure 5.7d, f).

The radius, thickness and opening angle of the arc(s) are variable. The radius determines the average angle of incidence, the thickness of the arc defines the spectrum of angles contributing to the incident light and the opening angle changes the amount of background illumination. Choosing an opening angle of  $180^\circ$ , the photons corresponding to the center of the arc would provide an illumination with p-polarized light and thus be able to excite surface plasmons, whereas photons corresponding to the tips of the arc result in an illumination of the surface with s-polarized light which cannot excite surface plasmons. The parameters used to generate the arc pattern can be chosen in the setup acquisition software.

## 5 SPRM Setup

As the projector itself contains many optical components such as lenses and prisms, it was not possible to generate a Köhler illumination in the live-imaging mode. The strong inhomogeneity of the field of view was also mentioned by Peterson *et al.*. They overcame the problem by recording one image with p-polarized and one image with s-polarized light at each position and dividing the subsequent images. Dividing the intensity of each pixel recorded with p-polarized light by the intensity of each pixel with s-polarized light, high resolution images were obtained.

It was found that the LCD-projector used in this work provides linearly polarized light, which is probably caused by an internal filter or a polarizing prism which could not be localized as most of the parts of the projector were difficult to access. Therefore, the approach by Peterson *et al.* for the background correction could not be applied here.

Thus, different approaches to remove the background were used. One approach is to record a video while moving the stage, calculate the average intensity for each pixel and subtract this average intensity pixelwise. Afterwards the dynamic range is adjusted in order to provide a higher contrast (see section 11.7.2). This method was used in the experiments shown in chapter 7.

A different method uses a contrast mask which can be generated on basis of the recorded picture itself. For this, a Gaussian filter is applied, which blurs the cellular structures. Afterwards, the colors of this layer are inverted. The resulting mask is combined with the original picture by a weighted overlay of the two images. The weighting factor needs to be individually tuned for each original picture. Finally, the dynamic range is optimized in order to enhance the contrast. This method was used in the experiments shown in chapter 8.

In case of very prominent objects with a high contrast in the original live-images, it might be advantageous to generate the contrast mask from another live-image (or an averaged picture generated from a stack) recorded with the same settings.

In a third attempt, a frosted cover glass was placed in front of the projector lamp to act as a diffuser and avoid imaging the filaments of the projector lamp into the light path. This decreases the background pattern in the live-imaging but also decreases the light intensity and therefore increases the necessary exposure time. Unfortunately, these frosted glass slides cannot stand the heat radiating from the projector lamp for a long time and eventually crack. Therefore, they have to be replaced frequently. After the first experiment with cardiomyocytes, the diffuser was removed completely as the frequent changes were very time consuming and the remaining light intensity was so low, that a good contrast in cell live-imaging was only obtained via post-processing.

### **5.3.3 Comparison of laser live-imaging and projector live-imaging SPRM**

In this section, the two live-imaging modes will be compared using two different samples. The first sample was coated with a polystyrene beads of a diameter of  $2\ \mu\text{m}$  while the second sample was a substrate used for culturing cardiomyocytes.

During these experiments, the previously discussed diffuser was used. In the experiments with the first sample, the diffuser cracked leading to a bright line in the center of the live-images. It was replaced before imaging the second sample and therefore does not appear in those images.

## 5 SPRM Setup

In Figure 5.7 a, c, e, live-images of a constant FOV are recorded while the first sample was illuminated with the laser, one projected arc and two projected arcs. The coherent laser illumination leads to speckle noise which compromises the image quality (see Figure 5.7 a). It is therefore difficult to discriminate between surface defects and beads. The images of the beads show a shadow tail on the right hand side which is caused by the interference of the propagating plasmons. The exposure time was set to 10 *ms*.

The incoherent projector illumination prohibits speckle noise. The image is smoother and it is easier to discriminate between the observed beads and surface defects (see Figure 5.7 c). As observed before, a shadow tail can be observed next to the bead. In this case the shadow appears at the left hand side as the illuminating light enters the objective from the opposite side. The exposure time was set to 200 *ms*.

Projecting two arcs on the BFP of the objective, the light intensity in the imaging plane is higher compared to the illumination with one projected arc while the exposure time was kept constant. The arcs on the BFP appear asymmetric. This is caused by a slight tilt of one of the lenses which is placed manually within the housing of the projector. The shadow tails disappear and the illumination is more homogeneous compared to the illumination via one arc, which is also to be expected as the light enters from both sides of the objective at the same time.

These differences between the three illumination schemes can also be seen in the images of the cardiomyocytes. The laser live-imaging (see Figure 5.8 a) shows the adhering area at the cell-substrate interface with a high light intensity and a high contrast at an exposure time of  $\sim 10$  *ms*. The speckle noise and the propagation of the plasmons frustrate the resolution of sub-cellular structures. The projector live-image was recorded with an exposure time of 200 *ms* and post-processed using the mask-approach described in section 5.3.2.

The contrast between the cell and the background is lower compared to the laser live-imaging but the projector live-imaging allows for deeper insights into cellular structures. Therefore, in the following experiments, live-images of cells were recorded using the projector setup, only.

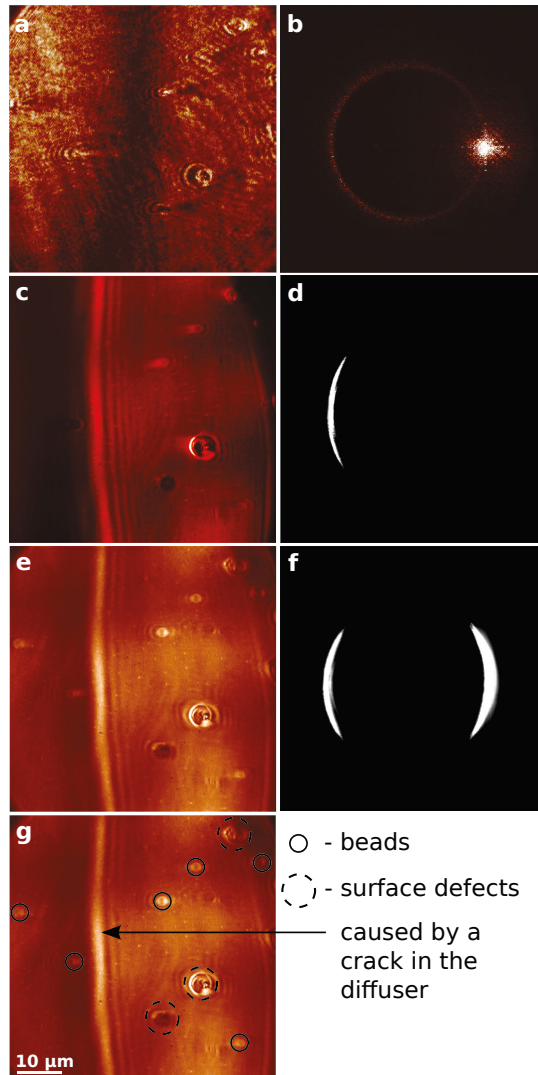


**Figure 5.7:** Live-imaging of polystyrene beads with a diameter of  $2\ \mu\text{m}$  using different light sources. (a), (c), (e) show the same field of view illuminated by the laser, one projected arc, two projected arcs, respectively. (b), (d), (f) show the BFP during the imaging. (g) shows the same image as (e) including markers for the observed structures.

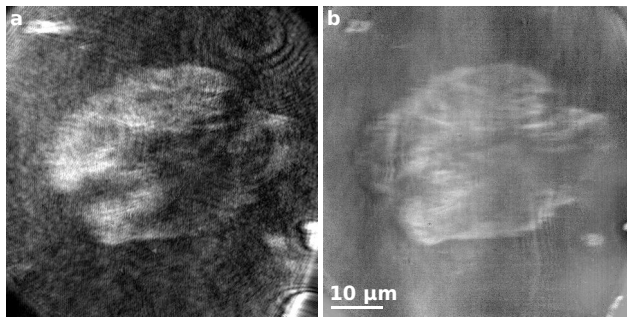


**Figure 5.8:** Live imaging of a cell-substrate interface of a cardiomyocyte. a) Laser live-imaging of the cell suffers from speckle noise and leaks to resolve sub-cellular structures. b) The projector live-imaging is based on an incoherent light source and therefore does not suffer from interference effects. This allows for the resolution of sub-cellular structures.

## 5.4 Scanning

### 5.4.1 Physical realization of the scanning modes

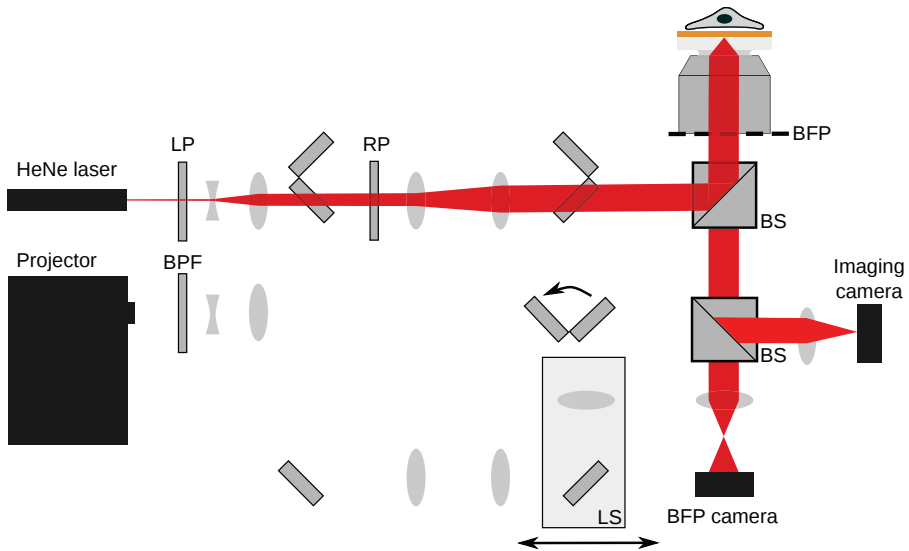


Figure 5.9: Optical path of the scanning mode

The optical path corresponding to the scanning mode is shown in Figure 5.9. As described before, the realization of the recording path has been changed such that the BFP and the interface can be recorded simultaneously. However, the illumination principle of the sample in the scanning mode has not been changed and still follows the same concept as in the SPRM prototype (see Figure 5.2) even though some optical components have been changed.

As in the laser live-imaging mode, the laser beam is expanded by the first set of lenses. Afterwards, the collimated light passes through a radial polarizer (RP). The radially polarized light is expanded again by a second pair of lenses before it is partially reflected by the first BS

and illuminates the entire BFP of the objective. The light is focused onto the substrate resulting in an illumination with the entire angle spectrum permitted by the NA of the objective. While most of the light is reflected, those parts of the light which satisfy the excitation condition are absorbed and lead to the excitation of surface plasmons in the gold layer. The reflected beam exits through the BFP, passes through the first beamsplitter again and gets divided onto the two recording paths by a second BS. The imaging camera shows the illumination spot at the substrate-interface while the BFP camera shows the fully illuminated BFP.

In contrast to the prototype setup, the BFP and the interface can be imaged simultaneously. This is a great advantage in order to guarantee a reasonable alignment of the setup. As the area which will be scanned is chosen in the measurement software by marking the desired area in the live-imaging mode, it is very important that the two cameras are aligned precisely to each another. Otherwise, a shift between the chosen area and the actually scanned area occurs. This is due to the fact that the FOV in the live-imaging is not maximized but the tube lens generates an optical zoom. Consequently, the center of the illuminated interface and the center of the FOV can be slightly shifted while the edges of the FOV would not appear in the image. Thus, the two modes need to be aligned by hand.

To assist with this alignment the *overlay* tool was implemented in the acquisition software. This tool displays an overlay of the images of the two cameras. In the scanning mode, this tool shows the BFP and the position of the illumination spot on the sample (see Figure 5.10). The red disk corresponds to the BFP, while the dark ring on the BFP represents the resonance angle. The blue spot shows the position of area which is illuminated in the scanning mode. If the center of the red disk and the blue spot coincide, the cameras are correctly aligned.

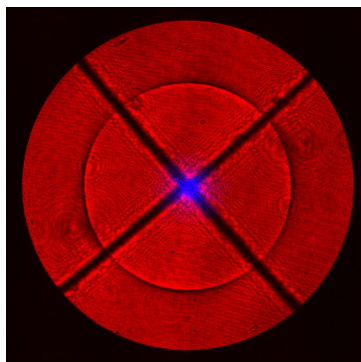


**Figure 5.10:** The BFP is illuminated in the scanning mode and appears as a disk (shown in red) in the BFP camera (the black cross is caused by the radial polarizer and can be neglected). Imaging the sample surface at the same time with the live-imaging camera, the light is focused on a spot which is shown here as a blue spot. As the centers of the two images coincide, the imaging paths are well aligned with respect to one another.

### 5.4.2 Scanning acquisition modes

In the prototype of the setup, there was only one acquisition mode for recording scanning data; the area scan which allows one to record one BFP image per scanning position. Such a measurement allows for the analysis of a three dimensional profile of the basal cell membrane. In the improved setup, two additional scanning acquisition modes were created: the single-spot measurement and the time-dependent area scan. The details regarding the different acquisition modes will be explained in the following paragraphs.

In the area scan, one can choose a scanning area while observing the FOV in the live-imaging mode. Parameters such as the region of interest (ROI), the step widths in X and Y-direction, the exposure time and the time between scanning of two points can be chosen before switching back to the scanning mode using the flipping mirrors. Afterwards, one BFP image is recorded for each scanning point. This type of scan can be used in order to investigate the 3D profile of cells which do not move

significantly over the scan's duration. At highest speed and highest resolution, the scanning of the soma of a cortical neuron usually takes 10 to 20 minutes. It will be shown in the next section, that the improved analysis technique additionally gives information about the cytosolic refractive index. Therefore, scanning data recorded in this mode, can also be used to create a map of the cytosolic refractive index.

The single-spot measurement was introduced in order to record BFP images at one single position over time. Again, the exposure time and the time between scanning of two points can be chosen. This mode is very useful for studying fast cell dynamics such as the membrane fluctuations and dynamics of the cytosolic refractive index induced by the beating of a cardiomyocyte.

In order to generate a 3D profile of a beating cardiomyocyte, the time-dependent area scan was introduced. This recording mode is a combination of the two other modes: The ROI, the step widths, the exposure time, the number of BFP images recorded at each position and the time between the recording of the BFP pictures are defined prior to the measurement. Afterwards, a series of BFP images is recorded at each scanning point. This way, the minimum, average and maximum cell-substrate distance can be determined at each scanning point. At the same time membrane fluctuations can be quantified at each position. Additionally, a refractive index map can be generated and also here the fluctuations can be quantified.

### 5.4.3 Processing of the scanning data

This section contains a revised and significantly extended version of supplementary material part on processing of the scanning data which is part of the publication by E. Kreysing *et al.* "Nanometer-resolved

mapping of cell-substrate distances of contracting cardiomyocytes using Surface Plasmon Resonance Microscopy” [16].

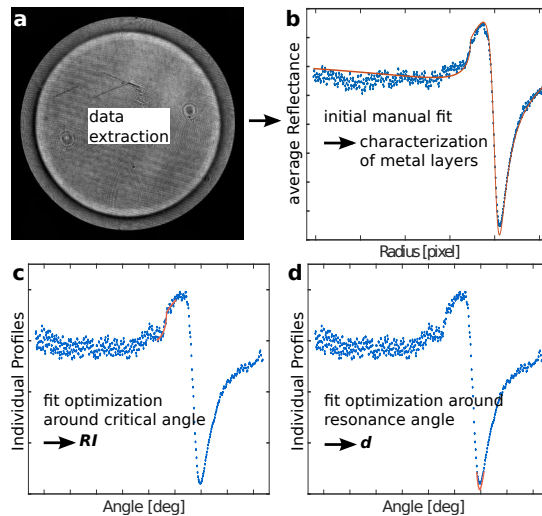


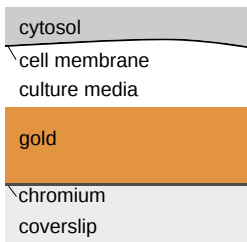
**Figure 5.11:** Analysis process of scanning data. a) The reflectance profiles are extracted from the BFP images by scanning the pixel intensity from the center to the periphery of the BFP. b) The extracted data from all BFP images is averaged and a multilayer system is manually fitted. The thicknesses of the metal layers which are determined this way are kept constant throughout the rest of the analysis process. c) The reflectance profiles corresponding to each individual BFP image are analyzed in two steps. First, a narrow range around  $\theta_c$  is fitted and the refractive index  $RI$  is determined. d) In a second step the area around the resonance angle is fitted and the distance  $d$  is determined.

During the time of the prototype SPRM, the recorded data had to be converted manually into a data type which was supported by *WINSPALL*. This process was very time consuming and required manual generation of an extensive spreadsheet. The most important problem with this analysis procedure was that it could not take into account variations in the cytosolic refractive index which was one of the most important error sources in the distance-analysis of SPRM.

The analysis procedure has been developed in collaboration with Hossein Hassani by generating a test data set which was analyzed using

many different approaches (see Appendix, section 12.3). The analysis routine giving the best results was then chosen as the standard method for data analysis.

At first, the subprogram *SPRing Extract* is used to extract the reflectance profile from each individual BFP image. Afterwards, these profiles are averaged and the subprogram *SPRing Model* is used to manually fit the initial reflectance curve (see Figure 5.11a, b). For this step, the measured data points are shown in the background while a reflectance curve is simulated based on the TMM (see Figure 5.11b and Figure 5.12). The number of layers, their complex RI and their thicknesses can be adjusted manually in the subprogram while the shape of the reflectance curve is updated immediately. This allows for the optimization of the overlay of the simulated curve and the data points. In contrast to a fully automated fit, this procedure allows to prioritize the fit in certain areas of the curve while apparent noise can be neglected (see Figure 5.11b).



layer	refractive index	thickness	source
coverslip	1.7880	$\infty$	Olympus
chromium	$3.3000 + i 4.2731$	2 - 5 nm	[60]
gold	$0.1943 + i 3.5921$	38 - 55 nm	[61]
media	1.3350	0 - 150 nm	measured
membrane	1.5000	8 nm	[62]
cytosol	1.3400 - 1.4000	$\infty$	[63]

**Figure 5.12:** A sample used in cell culture is represented as a multilayer system. The values which are used for the simulation and analysis of the multilayer system throughout the entire thesis are given in the table.

While adjusting the thicknesses of the metal layers, typical features of the reflectance curves such as the height and the shape of the maximum as well as the depth and width of the minimum help in finding the optimal parameters. Fortunately, variations in the thicknesses of the two metal layers influence the shape of the curve in different ways.

## 5 SPRM Setup

These changes in the shape are difficult to describe, but can be learned with practice.

Variations in the RI of the cytosol shift the position of the critical angle  $\theta_c$ , which is represented by a prominent edge in the curve (see Figure 5.13). But these variations also shift the resonance angle. Therefore, neglecting local and temporal variations in the cytosolic RI can lead to errors in the analyzed cell-substrate distance in the order of 100 nm (see section 5.4.3).

Once the thicknesses of all the layers and the cytosolic RI have been adjusted (the membrane is assumed to be constant in thickness and RI throughout the entire analysis, see Figure 5.12), the thicknesses of the metal layers are kept constant throughout the rest of the analysis process.

The sub-program *SPRing Apply* loads the parameters that have been previously determined in the manual fitting. It simulates and fits the reflectance profile for each individual BFP image separately around the critical angle and the resonance angle. The fitting procedures which are used here are realized either based on a least-squares or a least-residuals optimization, which needs to be decided by the user when starting the analysis.

At first, the reflectance curve is fitted in a narrow region of  $\theta_c \pm 2^\circ$  by variation of  $\theta_c$  (see Figure 5.11c).

In order to restrict the fitting algorithm to a physically reasonable range in  $\theta_c$ , the data is multiplied with a specifically designed weighing function. This weighing function is similar to a symmetrically designed step function, which is 1 for a defined interval and 0 otherwise. It was found empirically, that the performance of the optimization increases if the shoulders of the step are not chosen as an infinite slope. The mathematical formulation of the final weighing function is based on the

Fermi-Dirac distribution. By multiplying a function of the same structure as the Fermi-Dirac distribution with a function whose structure is inverted compared to the other, a pulse-like function with adjustable slope is created:

$$F = \frac{1}{1 + e^{(RI - RI_{max})/T}} \cdot \left( 1 - \frac{1}{1 + e^{(RI - RI_{min})/T}} \right) \quad (5.1)$$

The values  $RI_{min}$  and  $RI_{max}$  determine the boundaries of the refractive index range for the cytosol and are usually set to  $RI_{min} = 1.34$  and  $RI_{max} = 1.40$ . The slope can be modified by adjusting the parameter  $T$ . The advantage of using the pulse function is that noise appearing in the reflectance curve close to the critical angle but outside of the pulse-window does not lead to false positives, which was a major problem before the weighing function was introduced.

After  $RI$  has been determined by the optimal fit, all the parameters of the multilayer system are known except for  $d$ . Therefore, in a last step the curve is fitted around the minimum and  $d$  is determined (see Figure 5.11 d).

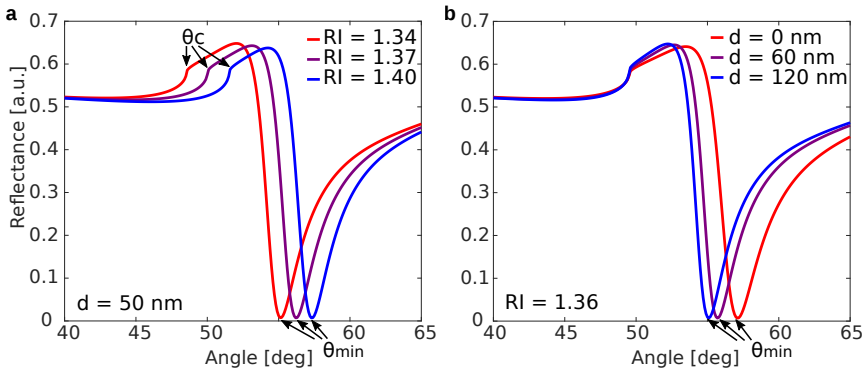


**Figure 5.13:** Typical reflection curves for adhering cells on SPRM samples. Thicknesses of the metal layers have been chosen as 3 nm Cr and 47 nm Au. Figure adapted from [16].

## Improvement of the accuracy by decoupling of observables

As mentioned earlier, during the time of the prototype SPRM, the data was analyzed using *WINSPALL*. This limited the accuracy of the cell-substrate distance ( $d$ ) as the refractive index of the cytosol ( $RI$ ) was taken to be constant. In order to quantify the improvement of the distance accuracy, a test data set was created consisting of artificially generated BFP images, which were analyzed with two different versions of *SPRing*. The first version is based on the same working principle as *WINSPALL* and assumes a constant  $RI$ . The second version of *SPRing* was coded in such a way that  $RI$  was analyzed separately for each individual BFP image (see section 5.4.3).

The test data set was generated using a multilayer system with parameters corresponding to the setup of a sample used in cell culture. The metal layers are chosen as  $d_{Cr} = 2 \text{ nm}$  and  $d_{Au} = 45 \text{ nm}$ , while  $d$  and  $RI$  vary between  $d = 0 - 150 \text{ nm}$  and  $RI = 1.34 - 1.40$ . Based on these parameters, an artificial area scan of  $10 \times 10 \mu\text{m}$  was generated. Within this scanning area,  $RI$  and  $d$  increase linearly in direction of the X- and Y-axis, respectively (see Figure 5.14a, b).

Afterwards, reflectance curves are simulated based on the described layer properties for each of the  $11 \times 11$  generated scanning points in this area. From these reflectance curves, artificial BFP images are created by generating a grey disk on a black background. The radial intensity profile of the disk corresponds to the reflectance curve (see Figure 5.14c, d). Thus, a set of 121 BFP images was generated and analyzed with the two different versions of the analysis software. The results of the two analysis processes were compared to the simulated distance values.

Figure 5.14e shows the analyzed distances using the first analysis approach. The software determined an average RI of  $RI = 1.3529$  and

used this value for the calculation of  $d$  in the further analysis. Comparing these results to the initial values shown in subfigure (a), differences between initial values and the analyzed distance

$\Delta d = d_{generated} - d_{analysis}$  of up to  $95 \text{ nm}$  (see Figure 5.14f) were found while the average accuracy was determined to  $37 \text{ nm}$ .

The same procedure was repeated for the analysis software, which determines the values for  $RI$  and  $d$  separately as described in section 5.4.3. The resulting distance is plotted in Figure 5.14g. A maximum deviation of  $4.5 \text{ nm}$  between the initial and the measured values is found (see Figure 5.14 h) while the average accuracy was determined to  $1.5 \text{ nm}$ .

Comparing the average accuracies of the two different analysis schemes, an improvement by a factor of 25 could be determined. Locally, the improvement in the distance analysis can be even higher. This shows that the separation of the two variables solved one of the major problems in the cell-substrate distance calculation in SPRM.

This approach has been evaluated in collaboration with Hossein Hasani who carried out the simulation.

## 5 SPRM Setup

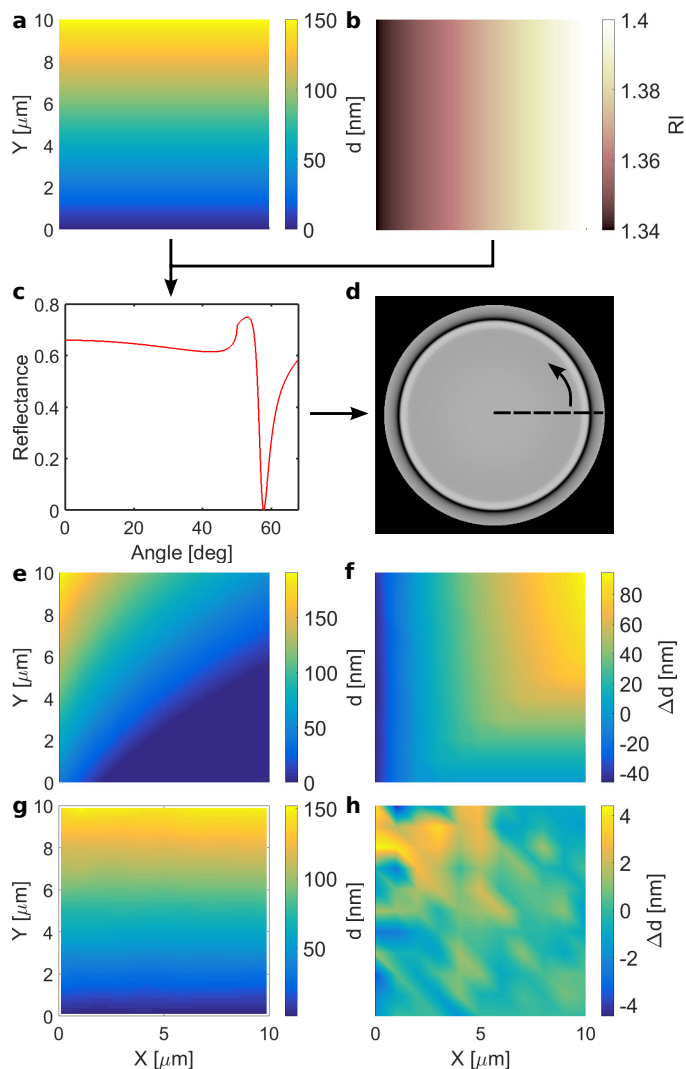


**Figure 5.14:** The test data set has been generated in such a way that it corresponds to the measurement of a sample used in cell culture. a) Modeled distance at the cell-substrate interface. b) Modeled cytosolic RI. c) The reflectance profiles have been simulated for each artificial scanning point and BFP images have been generated from the corresponding reflectance profiles (d) which represents the test data set. The test data set has been analyzed with the analysis software which assumes a fixed RI (e). f) The analyzed distance shows large variations  $\Delta d$  from the modeled distance. g) The distance has been analyzed with a variable RI scheme. h) The difference between the modeled and the analyzed distance is in the order of  $1 \text{ nm}$ . This figure is part of the publication by E. Kreysing *et al.* "Nanometer-resolved mapping of cell-substrate distances of contracting cardiomyocytes using Surface Plasmon Resonance Microscopy" [16].

## Comparison of manual and automated fitting

This section contains a revised version of the supplementary material part on the performance of the automated fitting algorithm which is part of the publication by E. Kreysing *et al.* “Nanometer-resolved mapping of cell-substrate distances of contracting cardiomyocytes using Surface Plasmon Resonance Microscopy” [16]. The comparison of the signals was executed by Hossein Hassani.

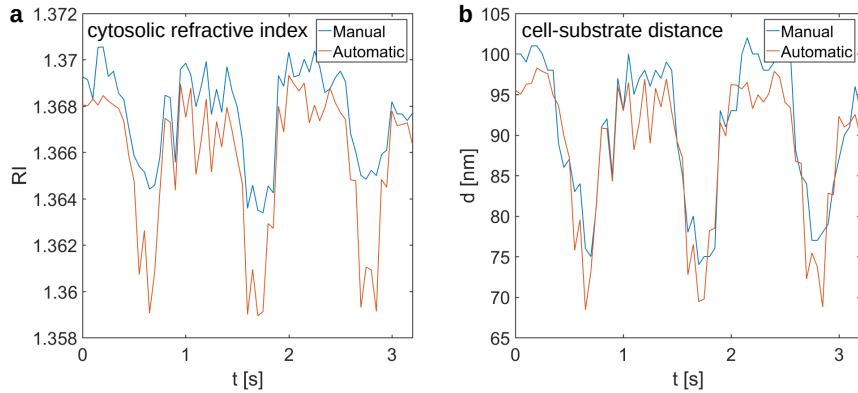


**Figure 5.15:** Single-spot measurement of a beating cardiomyocyte analyzed manually and automatically (analysis method: least squares, Fermi-Dirac pulse,  $T = 10$ ). a) Cytosolic refractive index over time. b) Cell-substrate distance over time. Figure adapted from [16].

In order to evaluate the performance of the automated fitting software *SPRing* when analyzing real data, a test data set was generated from a single-spot recording of a beating cardiomyocyte which was analyzed both automatically and manually (see Figure 5.15). The manual fit was used as a baseline to evaluate precision and accuracy of the automated fit (see Table 5.1).

As these values correspond to subpixel precision and accuracy for the assumed layer system (see next section), it is justified to use this automated fitting procedure in order to analyze real data.

## 5 SPRM Setup

	Precision $\omega$	Accuracy $\delta$
RI	$ std(RI_{SPRring} - RI_{manual})  = 0.0015$	$ mean(RI_{SPRring} - RI_{manual})  = 0.0019$
d	$ std(d_{SPRring} - d_{manual})  = 3.5 \text{ nm}$	$ mean(d_{SPRring} - d_{manual})  = 2.3 \text{ nm}$

**Table 5.1:**  $\omega_{RI}$ ,  $\omega_d$ ,  $\delta_{RI}$ ,  $\delta_d$ ,  $std$  correspond to the precision of  $RI$ , the precision of  $d$ , the accuracy of  $RI$ , the accuracy of  $d$  and the standard deviation, respectively.

## Limitations of the precision due to pixel size

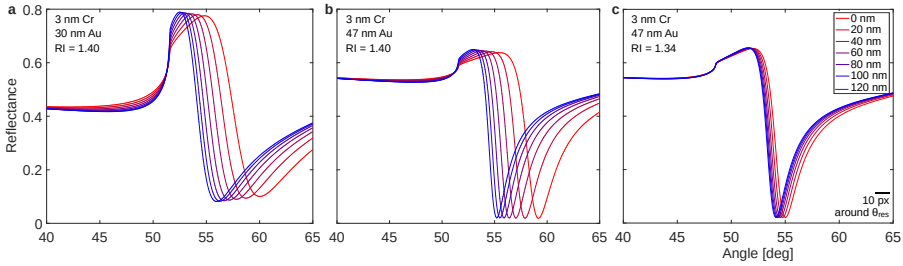


**Figure 5.16:** The precision of the distance measurement depends upon all the layers involved in the sample configuration. This is obvious when comparing the reflectance profiles for different layer thicknesses and different RI. The spectrum of the resonance angles for a fixed range of cell-substrate distances can vary strongly depending on the properties of other layers such as the thickness of the gold layer or the RI of the cytosol. A low cytosolic RI for example results in a relatively narrow angle spectrum (compare (c) and (b)). Thus, the precision of the measurement is lower for cells with a relatively low RI.

The limitation of the distance precision of a real measurement results from the pixel density in the BFP images. In other words, the precision  $\omega_d$  is limited by the angle spectrum captured by a single pixel. Considering the spectrum captured by one pixel around the resonance angle in a sample used for cell culture, this corresponds to  $\sim 0.13^\circ$  per pixel (here calculated for the sample setup shown in Figure 5.16c). If the measurement uncertainty of  $\Delta\theta \hat{=} \pm 1/2 \text{ px}$  is assumed for the detection of the minimum, one can calculate the precision for each sample composition by calculating  $\Delta d = d(\theta_{res} + \Delta\theta) - d(\theta_{res})$  using *SPRring Simulate*.

Cr layer	Au layer	$RI$	$d$	$\omega_d$
3 nm	47 nm	1.40	20 nm	2.7 nm
3 nm	47 nm	1.34	20 nm	13.3 nm

**Table 5.2:** Pixel precision for the sample compositions corresponding to Figure 5.16b and c.

As can be seen from Figure 5.16, the shape of the reflectance curve depends strongly upon the thickness of the layers involved as well as the RI of the cytosol. Therefore, it is not possible to give a single value describing the precision of SPRM cell measurements. The value rather needs to be determined for each sample composition and each cell-substrate distance individually based on simulations. In general, it can be said that for a fixed sample composition the precision decreases (the value for  $\omega_d$  increases) with increasing cell-substrate distance and that the precision increases with increasing RI of the cytosol (compare Figure 5.16b and c).

As an orientation, the limitations of the distance precision for the sample compositions shown in Figure 5.16b, c are given in Table 5.2.

The limitation of the RI precision due to pixel size was evaluated in the same manner. Here, a precision of  $\omega_{RI} = 0.0018$  was determined within the RI range  $RI = 1.33..1.40$ . This value is independent of the intermediate layers as will be shown in detail in section 6.2.

This evaluation of the limits in precision of SPRM cell measurements show that the performance of the setup is currently limited by the pixel per angle density, as the software was previously shown to be able to realize a measurement accuracy of 1.5 nm on average.

In order to improve the performance of the setup, it would therefore be advisable to increase the pixel density. This could be realized by either installing a camera with higher pixel density or by using a second BFP camera in parallel, which could be used to capture only a

part of the BFP. This part could be chosen to be either the area around the resonance angle or the critical angle depending on the experiment. Zooming into the area of the resonance angle would improve the distance measurement while an increased resolution around the critical angle would facilitate the observation of very small changes in the RI of the cytosol making it possible to observe action potentials *in vitro*, non-invasively and without labeling. This suggestion will be presented in detail in chapter 7 (see Figure 7.11).

## 5.5 Further setup elements

In order to correlate the SPRM results with conventional light microscopy, an upright microscope (Zeiss Axiotech) was installed inside of the SPRM setup. Its position is chosen such that the optical axis of the objective mounted at the Axiotech microscope and the optical axis of the TIRF objective coincide. The Axiotech microscope is equipped with a DIC crystal as well as fluorescence filter sets.

The Axiotech microscope can be used to capture overview images of the cultured cells with a lower magnification compared to the SPRM pictures. Simultaneous illumination of the substrate through the Axiotech microscope and the scanning path allows to determine the scanned area even at low magnification because the scattered laser light appears as a bright spot in the overview image. The fluorescence filter sets can be used e.g. for tracking action potentials, if the cells are labeled correspondingly.

An additional imaging mode was facilitated by the installation of the Axiotech microscope: It uses the illumination of the sample through the Axiotech objective. The light which is transmitted through the semi-

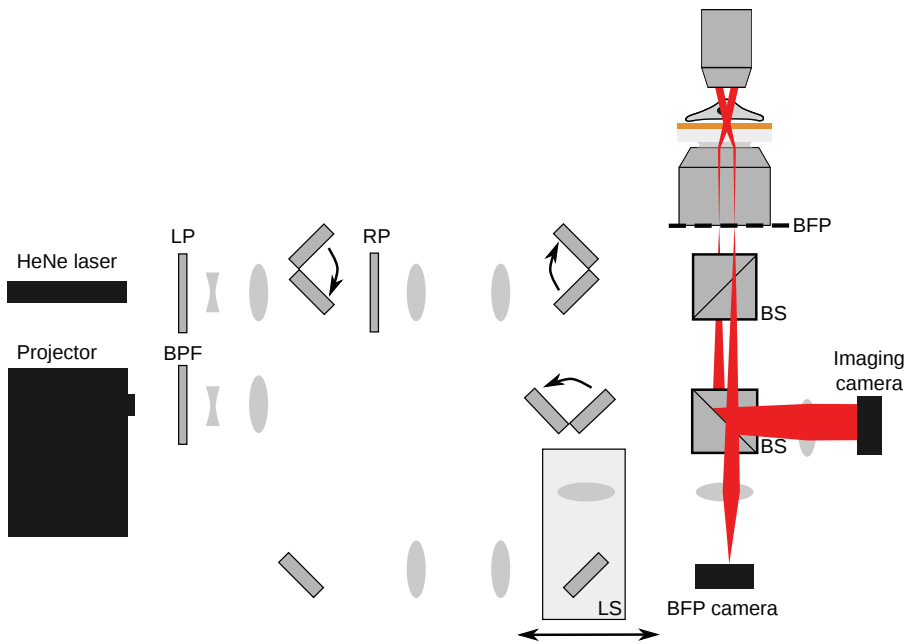


**Figure 5.17:** An upright microscope is used to image the substrate in the conventional way. Additionally, the transmitted light is collected by the TIRF objective of the SPRM setup. This way, the imaging camera can be used to capture a bright-field image of the cell-substrate interface.

transparent gold layer is collected by the TIRF objective and follows the optical path towards the cameras. A bright-field picture is captured by the imaging camera (see Figure 5.17). This mode is very useful, as it allows for the recording of bright-field images of the exact same area, with the same magnification as the SPRM live-imaging pictures. It can e.g. help to distinguish artifacts in the plasmon image caused by small defects in the metal layer from cellular structures. It could also be shown, that this mode is very useful to track the position of organelles which can be correlated with the refractive index maps which is determined based on the scanning data (see chapter 8).



# Validation

As described earlier, the SPRM shall be used to investigate the cell-substrate interface qualitatively and quantitatively. In contrast to the qualitative measurements, the quantitative measurements require a either a validation or a calibration of the system.

This process begins with the most fundamental parameter, the angle of incidence. As described in section 5.4.3, the angle of incidence is calculated by translating the radial distance to the optical axis  $r$  on the BFP into the angle of incidence at the substrate using the Abbe sine condition. Therefore, it needs to be tested whether this condition is indeed satisfied. This is going to be addressed in section 6.1.

Once the angle measurement is validated, one can proceed and continue with the RI measurement. In section 6.2, it will be shown based on simulations, that the used model system is sufficient for a RI validation. Afterwards, the respective measurement series will be presented and the results will be discussed.

In the subsequent section (see section 6.3), different approaches that were taken in order to verify the distance measurement using control samples will be described. The one successful approach will be presented in detail and the potential error sources will be discussed.

In (see section 6.4), the significance of these measurements will be discussed.

## 6.1 Angle validation

As discussed in section 5.4.3, the radial position on the BFP is converted into the angle of incidence during the processing of the scanning data. This calculation is based on the assumption that the objective satisfies the Abbe-sine condition i.e. that the image is not distorted. In order to control if this assumption is satisfied, a specific experiment had to be designed which allows for the generation of a well defined angle spectrum inside the optical path of the objective. This should give rise to an image on the BFP which facilitates the assignment of an angle of illumination to each position on the BFP.

In a first attempt, it was tried to focus laser pointers from the top of the objective through a coverslip and the immersion oil and the front lens onto the BFP. As a result, each laser pointer should generate a bright spot on the BFP. If the incidence angle of the laser pointer could be well controlled, this signal could be used as a calibration signal.

In order to couple in light originating from external laser pointers, two setups were constructed. In the first setup, three laser pointers were arranged around the optical axis of the TIRF objective. The laser pointers were held in position under a fixed angle (see Figure 6.1). The laser light was supposed to pass through the front lens of the objective and exit the objective through the BFP.

The BFP was imaged and the radial positions of the bright spots, which correspond to the positions where the laser light exits the BFP, were measured. Even though this setup was aligned very carefully, the variances of the radial positions of the three lasers reached 28 pixels. As the precision of a validation method needs to be in the order of one pixel, this approach was discarded.

A second setup was proposed which should hold one laser pointer only which would then rotate around the front lens. Unfortunately,

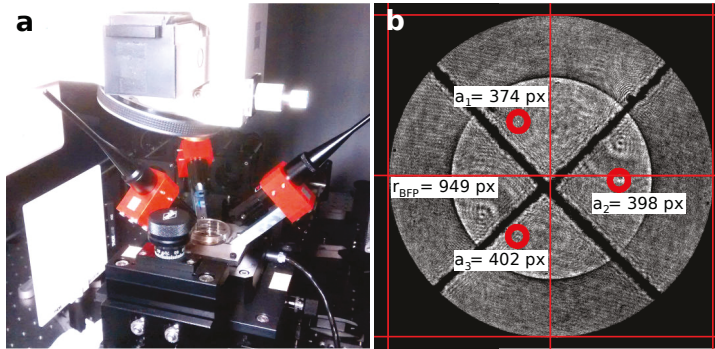


**Figure 6.1:** a) The additional setup holds three laser pointers which point at the front lens of the TIRF objective. The laser light has to travel through the sample before it can reach the front lens. Laser holder built according to design by Hossein Hassani. b) The light of the three last pointers is collected by the objective and appears as three bright spots on the BFP. The distance to the optical axis is measured. Variations of 28 pixels were measured. The red lines have been used to determine the edges of the center of the BFP.

the space such a setup would have occupied was not compatible with the space available on the SPRM setup. Therefore, a much simpler version of a laser pointer holder was created which could be adjusted to many different angles which would have to be measured externally. Alternatively, the setup was thought to illuminating a commercially available transmission grating which was placed in the position of the sample (see Figure 6.2). This should generate a diffraction pattern at the BFP. The positions of the maxima of the diffraction patterns should be calculated and compared to the measured values. Unfortunately, this setup proved to be experimentally inconvenient as it was very difficult to strike the front lens with the laser pointer and to measure the angle in respect to the optical axis. Additionally, the transmission grating had to be brought in contact with the immersion oil and the immersion oil crystallized at its surface and could not be removed easily. Therefore, this approach was abandoned as well.

The third approach did not involve the creation of a new setup but the

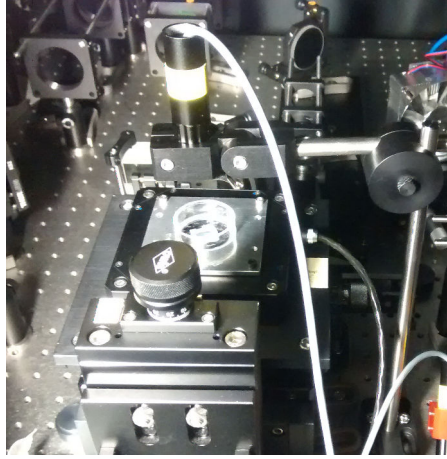


**Figure 6.2:** The laser pointer holder illuminates a transmission grating from the top. The transmission grating is glued to the bottom of a Petri dish which is placed on the sample holder of the SPRM.

generation of a reflection grating with lattice constant  $l$  in the cleanroom. Using a monochromatic light source of wavelength  $\lambda$ , it should give rise to a diffraction pattern at the BFP. Maxima are generated when the optical path difference between light reflected at neighboring grid lines corresponds to a multiple  $m$  of the wavelength in the respective media  $\frac{\lambda}{RI}$  (see [64, ch. 10]):

$$\sin(\theta) = \frac{m\lambda}{RI \cdot l} \quad (6.1)$$

The grating should be used in reflection as the standard conditions of the SPRM setup should be retained. No commercial grating could be used, as these are evaporated on thick glass slides. These slides are thicker than the working distance of the TIRF objective and the refractive index of the glass slides do not match that of the objective either. Additionally, the objective requires an immersion oil which crystallizes easily: Therefore, using a commercial grating upside-down and exposing the grid structure to the immersion oil would probably damage the grating within one experiment.

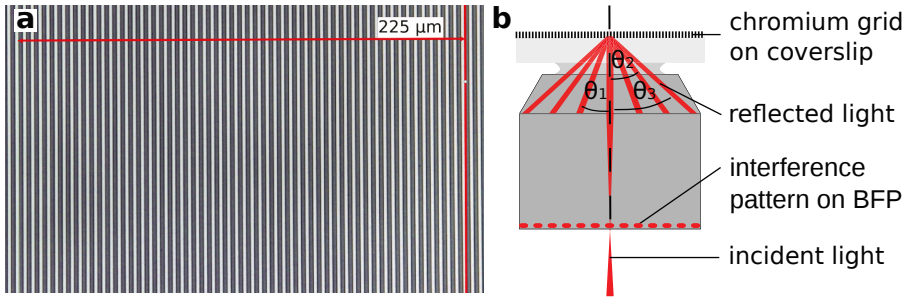


**Figure 6.3:** a) Control image of the custom-made diffraction grating with a lattice constant of  $4\mu\text{m}$  taken with a KEYENCE light microscope. The horizontal, red bar has a length of  $225\mu\text{m}$ . b) Laser light is focused onto the center of the BFP. This results in an illumination of the coverslip with collimated light. The chromium grid reflects the incident light and gives rise to an interference pattern on the BFP.

Therefore, a chromium grid structure was evaporated on one half of a high index coverslip in the cleanroom. The grid structure was designed to have a lattice constant of  $l = 4\mu\text{m}$ . In order to estimate the tolerance of the fabrication, the grid was observed with an optical microscope and the lattice constant was measured by averaging over 57 periods (see Figure 6.3a). This gives a measured lattice constant of  $l_{\text{measured}} = 3.95\mu\text{m}$ . As there is a deviation of  $50\text{nm}$  between the measurement and the production, a lattice constant of  $4\mu\text{m} \pm 0.05\mu\text{m}$  was assumed.

The sample was glued to a Petri dish in order to fit the conventional SPRM sample holder. It was illuminated according to the scheme illustrated in Figure 6.3b. This can be realized using the laser live-imaging mode while the position of the linear stage is chosen such that the light is focused onto the center of the BFP. This results in an illumination of the grid with collimated light. The chromium grid on top of the coverslip reflects the incident light. Imaging the BFP reveals the intensity maxima of the diffraction pattern. As one can see in Figure 6.4a, the intensity of the maxima is weaker at the edges

## 6 Validation

than in the center. In order to be able to determine each individual maximum, the BFP was imaged several times with different exposure times. Additionally, a BFP image is taken in the scanning mode at a position in the second half of the sample (bare glass), (see Figure 6.4b). This allows for the determination of the radius of the BFP by measuring the coordinates of the edge.

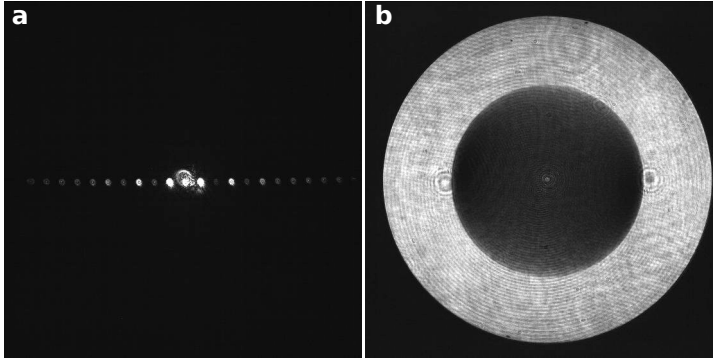


**Figure 6.4:** a) An interference pattern is created on the BFP during illumination of a chromium grid. b) The BFP was imaged in the scanning mode at the bare coverslip surface in order to determine the edges of the BFP.

The centers of the maxima and the edges of the BFP were determined. Taking into account the images with different exposure time, the centers of 22 maxima could be determined. The central maximum correspond to the maximum  $\mathcal{O} = 0$ . The maxima to the right and to the left are numbered subsequently with positive and negative numbers, respectively.

The  $X$  and  $Y$  coordinates as well as their uncertainties were determined in pixels for each maximum. Afterwards, the distance to the central maximum  $d_0$  was determined. The error in  $X$  and  $Y$  was propagated and rounded to two decimals (and therefore appears not to differ from the uncertainty in  $X$ ).

The distance was converted from pixels into mm (not shown) using

the diameter of the BFP ( $d_{BFP} = 1888 \text{ pix}$ , measured from Figure 6.4b) and the diameter of the BFP in mm ( $D_{BFP} = 6.12 \text{ mm}$ , specification provided by the manufacturer) with

$$r = d_0 * D_{BFP}/d_{BFP}.$$

The angle is determined with  $\theta_{exp} = \arcsin\left(\frac{r}{RI \cdot f_{obj}}\right)$  (see Table 6.1). As there is no straightforward error propagation for the arcus sinus functions, the error is estimated according to [65]:

$$\Delta\theta_{exp} = \left| \arcsin\left(\frac{r}{RI \cdot f_{obj}}\right) - \arcsin\left(\frac{r \pm \Delta r}{RI \cdot f_{obj}}\right) \right| \quad (6.2)$$

with  $\Delta r = \Delta d_0 * D_{BFP}/d_{BFP}$ . Due to the  $\pm$  sign, this estimation gives rise to a set of two errors for each angle value, which have been averaged over for convenience.

Now, the experimentally determined angles  $\theta_{exp}$  shall be compared to the theoretical expectations. Therefore,  $\theta_{th}$  is calculated based on Equation 6.1 and the error caused by the inaccuracy of the lattice is estimated in the same manner as before [65]. As one can see from Table 6.1, the values agree within their errors. A plot of these values is given in the appendix Figure 12.1. Due to the small errors, the error bars vanish for most of the values while the markers indicating the positions of the theoretical and experimental values coincide in a plot involving more than one maximum. As the theoretical and experimental values agree with very small deviations which are smaller than the estimated errors, it could be shown, that the objective can be assumed to satisfy the Abbe sine condition. This relation will therefore be used in the further analysis to calculate the illumination angle.

## 6 Validation

$\mathcal{O}$	$X \pm \Delta X$	$Y \pm \Delta Y$	$d_0 \pm \Delta d_0$	$\theta_{exp} \pm \Delta\theta_{exp}$	$\theta_{th} \pm \Delta\theta_{th}$
-10	$152 \pm 6$	$1033 \pm 6$	$882 \pm 6$	$62.67 \pm 0.75$	$62.23 \pm 1.36$
-9	$241 \pm 2$	$1034 \pm 4$	$793 \pm 2$	$53.01 \pm 0.19$	$52.78 \pm 0.94$
-8	$328 \pm 2$	$1035 \pm 2$	$706 \pm 2$	$45.32 \pm 0.16$	$45.06 \pm 0.72$
-7	$417 \pm 1$	$1036 \pm 1$	$617 \pm 1$	$38.42 \pm 0.07$	$38.27 \pm 0.57$
-6	$505 \pm 1$	$1036 \pm 1$	$529 \pm 1$	$32.20 \pm 0.07$	$32.06 \pm 0.45$
-5	$593 \pm 2$	$1036 \pm 2$	$441 \pm 2$	$26.37 \pm 0.13$	$26.26 \pm 0.35$
-4	$682 \pm 2$	$1037 \pm 2$	$352 \pm 2$	$20.77 \pm 0.12$	$20.73 \pm 0.27$
-3	$769 \pm 2$	$1036 \pm 2$	$265 \pm 2$	$15.48 \pm 0.12$	$15.39 \pm 0.20$
-2	$858 \pm 2$	$1036 \pm 2$	$176 \pm 2$	$10.21 \pm 0.12$	$10.19 \pm 0.13$
-1	$946 \pm 3$	$1036 \pm 4$	$88 \pm 3$	$5.09 \pm 0.17$	$5.08 \pm 0.064$
0	$1034 \pm 4$	$1034 \pm 3$	0	0	0
1	$1123 \pm 4$	$1035 \pm 4$	$89 \pm 4$	$5.14 \pm 0.23$	$5.08 \pm 0.064$
2	$1211 \pm 2$	$1035 \pm 2$	$177 \pm 2$	$10.27 \pm 0.12$	$10.19 \pm 0.13$
3	$1299 \pm 2$	$1033 \pm 2$	$265 \pm 2$	$15.48 \pm 0.12$	$15.39 \pm 0.20$
4	$1387 \pm 2$	$1032 \pm 2$	$353 \pm 2$	$20.83 \pm 0.12$	$20.73 \pm 0.27$
5	$1475 \pm 2$	$1031 \pm 2$	$441 \pm 2$	$26.37 \pm 0.13$	$26.26 \pm 0.35$
6	$1563 \pm 2$	$1030 \pm 2$	$529 \pm 2$	$32.20 \pm 0.14$	$32.06 \pm 0.45$
7	$1651 \pm 2$	$1028 \pm 2$	$617 \pm 2$	$38.42 \pm 0.15$	$38.27 \pm 0.57$
8	$1739 \pm 2$	$1027 \pm 2$	$705 \pm 2$	$45.24 \pm 0.16$	$45.06 \pm 0.72$
9	$1826 \pm 2$	$1024 \pm 2$	$792.1 \pm 2$	$52.92 \pm 0.19$	$52.78 \pm 0.94$
10	$1914 \pm 2$	$1021 \pm 2$	$880.1 \pm 2$	$62.43 \pm 0.25$	$62.23 \pm 1.36$
11	$2001 \pm 10$	$1017 \pm 3$	$967.1 \pm 10$	$76.93 \pm 2.60$	$76.72 \pm 3.13$

**Table 6.1:** Angle calibration of the TIRF objective.

## 6.2 Refractive index validation

This section contains a revised and significantly extended version of the supplementary material part on refractive index measurement validation which is part of the publication by E. Kreysing *et al.* “Nanometer-resolved mapping of cell-substrate distances of contracting cardiomyocytes using Surface Plasmon Resonance Microscopy” [16].

Before presenting the refractive index validation measurements, it will be shown that the model system which was studied is suited for this purpose. Therefore, it will first be shown that the position of the critical angle depends upon the refractive index of the last layer within the evanescent field while it is independent of the refractive indices as well as the number of layers between the coverslip and the last layer.

### 6.2.1 Critical angle dependence on last layer

Changes in the composition of a measured sample such as number of layers within the evanescent field, variations in the refractive indices or thicknesses of the layers strongly influence the plasmonic response. This is the reason why the cell-substrate distance can be analyzed with a very high accuracy ( see section 5.4.3). Therefore, it might be surprising that the position of the critical angle is independent of changes in composition and number of layers in between the first (coverslip) and the last layer within the evanescent field. Its position depends solely upon the refractive indices of this first and last layer.

The following simulation will show, that the position of the critical angle of two different sample configurations coincides, if the RI of the last layer in these configurations agree. As the refractive index of

## 6 Validation

the coverslips is constant ( $RI_{CS} = 1.788$ ), its value will not be varied within the simulation.

The sample configurations correspond to a sample used in cell culture, consisting of the following layers: coverslip (CS), 3 nm Cr, 40 nm Au, 80 nm media, 8 nm membrane, cytosol (RI 1.34 -1.40) and a second sample corresponding to a SPRM substrate exposed to a Dimethyl sulfoxide (DMSO)-water mixture: CS, 3 nm Cr, 40 nm Au, DMSO-water mixture (RI 1.34 – 1.40). The simulated reflectance curves show

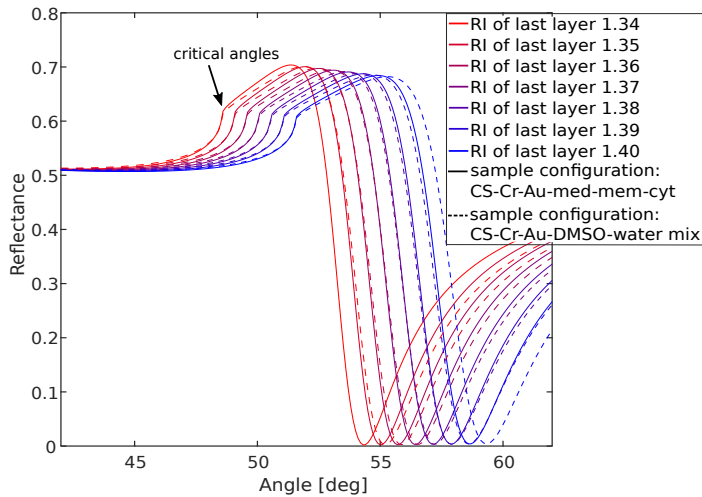


**Figure 6.5:** Reflectance curves for two different sample configurations are simulated: A sample used in cell culture and a sample exposed to a DMSO-water mixture. The critical angles of the two different configurations coincide as long as the refractive index of the last layer involved in the sample configuration coincides. Figure is part of the publication by E. Kreysing *et al.* "Nanometer-resolved mapping of cell-substrate distances of contracting cardiomyocytes using Surface Plasmon Resonance Microscopy" [16].

differences in the shape of the reflectance curves and in the position of the resonance angles (see Figure 6.5). However, this does not apply for the position of the critical angle. If the RI of the last layer in the two

different sample setups agree, the position of the critical angles of the two different sample setups coincide. This shows, that the position of the critical angle is independent of the intermediate layers. Therefore, a RI-validation measurement does not require a sample with the same layer structure as a sample used in cell culture, but it can consist of a smaller number of layers. In section 6.2.2, a RI-validation measurement based on DMSO-water mixtures is shown.

## 6.2.2 Refractive index validation measurements

It was just shown that the position of the critical angle is independent of the intermediate layers (as long as all layers are within the penetration depth of the evanescent field). As the easiest control experiment possible shall be prepared, the number of layers is reduced compared to a cell-substrate setup. Therefore, a standard SPRM sample is used and a liquid with extremely high refractive index is added which can be diluted stepwise with water. DMSO is liquid at room temperature and has a refractive index of  $RI_{DMSO} = 1.4749$  at  $\lambda = 632.8 \text{ nm}$  [66]. The refractive index of the solution can be calculated based on the Lorentz-Lorenz equation.

$$\frac{RI_{ges}^2 - 1}{RI_{ges}^2 + 2} = \sum_i \frac{4\pi N_i \alpha_i}{3} \quad (6.3)$$

Here,  $\alpha$  is the mean polarizability of the respective molecule and  $N$  is the number of molecules per unit volume.

It has been reported that DMSO-water mixtures deviate slightly from the theoretical expectation [67]. The molecular interaction between water and DMSO causes the largest deviation at a mass-ratio of 1:2

## 6 Validation

(DMSO:water) [67]. Therefore, a small deviation between the calculated and the measured values is to be expected.

The literature values used for the polarizability are given by  $\alpha_{DMSO} = 8.00 \text{ \AA}^3$  and  $\alpha_{H_2O} = 1.47 \text{ \AA}^3$  at room temperature [68]. These have been measured at  $\lambda' = 587 \text{ nm}$ . Compared to the light source used in the SPRM experiments, this wavelength mismatch is expected to cause a systematic error. This error is estimated by the dispersion of DMSO within the range of wavelengths:

$$\begin{aligned} RI_{DMSO}(537.0nm) - RI_{DMSO}(632.8nm) &= 1.4772 - 1.4749 \\ &= 0.0023 \end{aligned}$$

In the experimental realization, a standard SPRM sample was filled with solutions of DMSO and water at different concentrations. A single-spot measurement consisting of 50 frames was recorded at each mixing ratio. At first, the sample was filled with 1 ml DMSO and a measurement was taken. Afterwards, the sample was kept in place while adding 1 ml of purified water (Milli-Q) with a pipette while paying attention not to touch the sample. The content of the dish was mixed 20x before another measurement was taken. This procedure was repeated until the volume ratio reached 4:1. Afterwards, the full dish was carefully aspirated dry and washed before it was filled with 1.8 ml water and 200  $\mu\text{l}$  DMSO, mixed carefully and measured. After adding the last 2 ml water and careful mixing, another measurement was taken. The sample was washed again and pure water was measured.

Each measurement series was analyzed individually. The metal layer were set to constant values while the critical angle was varied. The uncertainty in the determination of the critical angle was determined to one pixel which results in a statistical error of  $\Delta RI_{exp} = 0.0018$ . Unfortunately, the first measurement (100% DMSO) could not be analyzed

due to noise in the area of the critical angle and therefore this measurement point had to be discarded. The analyzed RI as well as the expected theoretical values were plotted as a function of the concentration. As one can see in Figure 6.6, the simulated values are slightly higher compared to the measurements. This is expected because the value for the polarizability was measured at a smaller wavelength. The deviation for pure water is smaller compared to higher DMSO concentrations. This deviation from the Lorentz-Lorenz equation was described earlier and was therefore also expected. Despite these expected deviations, most of the experimental values lie within the estimated RI range. In

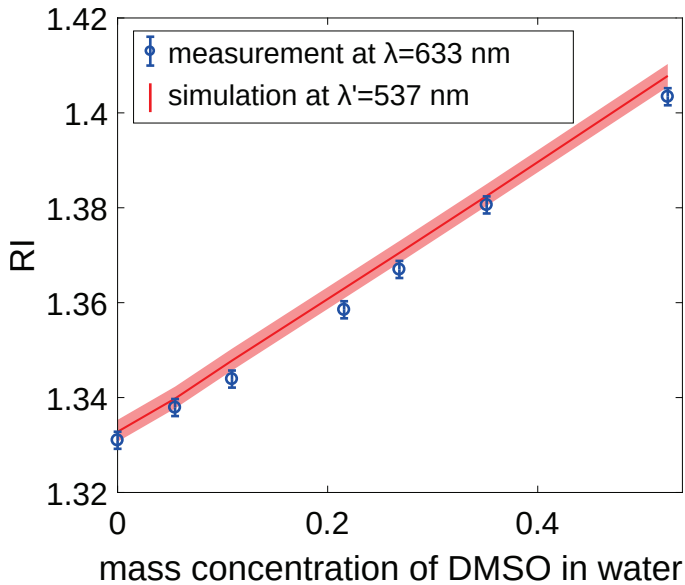


**Figure 6.6:** Measurement and simulation of the refractive index of a DMSO-water mixtures at different concentrations. The simulated values were calculated based on the polarizability of DMSO at  $\lambda' = 537 \text{ nm}$  while the experiment has been carried out at  $\lambda = 633 \text{ nm}$ . The pink area represents the range in which the measured RI values could be expected when the wavelength mismatch is taken into account.

summary, it could be shown in this experiment, that the refractive index measurement with the SPRM is a suitable method over the entire RI

range that can be expected within cell measurements ( $RI : 1.34 - 1.4$ ).

### 6.3 Distance validation

The idea of a distance validation measurement is to measure a sample with a well defined structure. There are two fundamentally different ways to approach this task. The first approach can be realized by the deposition of an additional layer of a suitable material with a controllable thickness on SPRM samples and measure the thickness of this layer in an SPRM scan. The second approach can be realized by placing an object with a well defined structure and a suitable material on an SPRM sample and measure the cleft between the gold surface and the object. For this approach, the easiest solution would be to find a sphere of a suitable size and material, as one does not have to consider different possible orientations of the object on the substrate.

The difficulty in both approaches is to devise a model system which can be measured with the SPRM. The limiting factor is the RI of the involved materials. Constructing a model system from solid materials, which usually have a high RI compared to cells, the corresponding reflectance curves show high resonance angles (outside of the captured angle spectrum) which handicap the analysis of the reflectance curve.

Another difficulty with the first method lies in depositing very thin an homogeneous layers on top of the gold layer. One possibility is to deposit silicon dioxide layers of variable thickness on top of the SPRM samples. As silicon dioxide does not adhere well to gold, this approach needs an additional adhesion layer such as chromium. It was decided to use  $10\text{ nm}$ ,  $20\text{ nm}$  and  $30\text{ nm}$  of  $\text{SiO}_2$ . A collaborator, produced the entire SPRM samples including the  $\text{SiO}_2$  layers. The

sample configuration was planned to be 2 nm Cr, 40 nm Au, 2 nm Cr, 10 nm; 20 nm; 30 nm SiO<sub>2</sub>. Each sample configuration was produced three times.

Unfortunately, the measurements could not be analyzed because the critical angle could not be detected. This happens, if the thickness of the gold layer exceeds  $\sim 70$  nm, since the maximum in the reflection curve gets flattened with increasing thickness of the gold layer. As the production of such samples is very expensive, this approach was discarded.

As an alternative, cylindrical and spherical objects were measured. Optical fibers with a polymer cladding with a low RI ( $RI_{clad} = 1.4$ ) which corresponds to the cytosolic RI were purchased. Unfortunately, the optical fibers were additionally wrapped in a plastic coating which could only be removed with a specific tool. However, removing the coating and cutting/breaking the fiber into very small objects which could be observed in the SPRM always caused scratches in the polymer cladding or even entire dissolution.

The next approach was to use microlenses. Which was successful and will be described in the next section.

#### 6.3.1 Measurement of microlenses

Spherical microlenses with a diameter of  $D = 500 \pm 2.5 \mu\text{m}$  were purchased. The lenses consist of fused silica which has a literature RI of  $RI_{silica}(\lambda = 633\text{nm}) = 1.4570$  [69]. The reflectance profile does not show a plasmon resonance angle within the captured angle spectrum, if the sphere is placed directly on the SPRM sample. But it shows an analyzable reflectance curve if the gap between the gold surface and the sphere is filled with water or ethanol. As these lenses have

## 6 Validation

been found to be hydrophobic, a bead was placed in 100% ethanol with  $RI_{ETOH}(\lambda = 633nm) = 1.3604$  [70] and the contact area was scanned.

The data extraction showed an extremely noisy average reflectance curve (see Figure 6.7 a). The noise is assumed to be caused by the laser light which is transmitted through the gold layer and reflected within the sphere before it exits the bead and thus disturbed the SPRM measurement. Nevertheless, the data was processed. As it is impossible

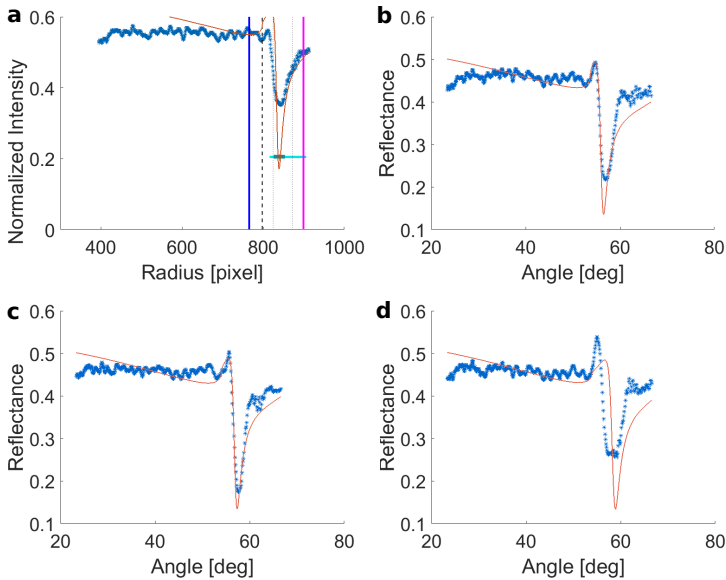


**Figure 6.7:** Reflectance curves of the microlens. a) The initial manual fit could not be realized by optimizing the overlay of the simulated curve and the measured data because the data is very noisy. Therefore, the initial fitting had to be based on guessing. b-d) The automated fit of the individual reflectance curves shows bad overlays for some of the curves (especially in (d)).

to fit a model to the extremely noisy averaged curve (see Figure 6.7 a), the analysis procedure of the data was more difficult than usual. The initial fitting of the model was based on guessing. Once the analysis was completed, the fits of the reflectance curves corresponding to the

individual BFP images were judged. Based on these insights, the initial manual fitting was repeated and the layer structure was adapted accordingly. This procedure was repeated until the fit of the reflectance curves of the individual BFP images showed good agreement with the data. The best fit was achieved for 5 nm Cr, 56 nm Au, 95 nm ETHO.

However, as also the individual profiles are very noisy (see Figure 6.7 b-d), it is surprising, that the determined distance profile follows a spherical shape. In Figure 6.8, one can see the analyzed distance profile (solid surface plot) as well as the simulation of an ideal sphere with diameter  $D = 500 \mu\text{m}$  (plotted as a mesh structure). The position of the simulated sphere has been adjusted manually.

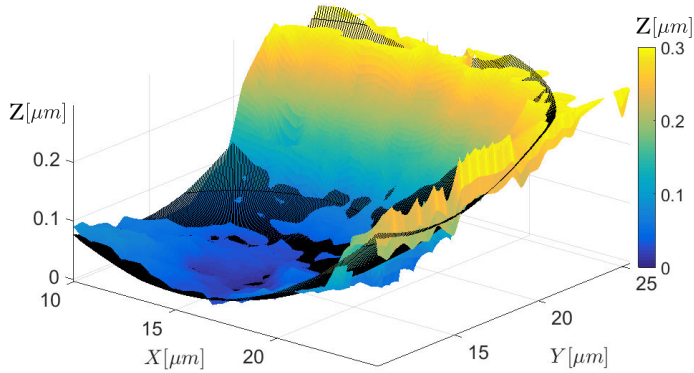


**Figure 6.8:** Section of the analyzed Z-profile of the microlens in ethanol (solid profile) and simulated curve of an ideal sphere with a diameter of  $500 \mu\text{m}$ .

In order to determine the deviation of the measured distance  $Z_{exp}$  profile and the shape of an ideal sphere  $Z_{sim}$ , the difference  $\Delta Z = Z_{exp} - Z_{sim}$  is calculated. Subsequently, the distance profile is sliced horizontally into 30 slices and the average  $\Delta Z$  is determined for each slice.  $\Delta Z$  as well as the standard deviation are plotted against the Z-value of an ideal sphere (see Figure 6.9). The average deviation is

## 6 Validation

relatively small ( $\sim 20 \text{ nm}$ ) for  $Z$ -values up to  $\sim 200 \text{ nm}$  and exceeds relatively high values around  $250 \text{ nm}$  for  $Z$ -values around  $Z = 500 \text{ nm}$ . It can also be observed, that the standard deviation increases strongly for  $Z$ -values larger than  $50 \text{ nm}$ .

In case of an ideal measurement, plotting  $Z_{exp}$  against the simulated values  $Z_{sim}$  gives a straight line with slope  $s = 1$  which passes through the origin (see blue line in Figure 6.10). For this measurement, an absolute shift of the curve to higher values is found. For  $Z_{exp} < 200 \text{ nm}$  the measured curve is parallel to the ideal curve for  $Z_{exp} > 200 \text{ nm}$ , the curve does not follow the expected linear behavior anymore and the standard deviation becomes relatively large.

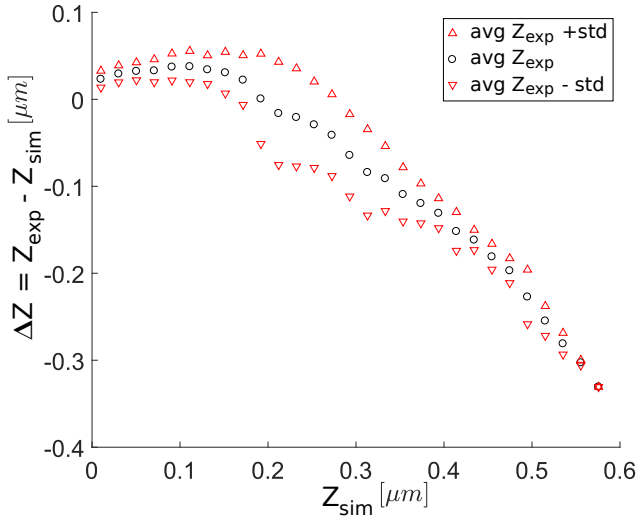


**Figure 6.9:** The deviations between the measured and the expected distance are plotted as a function of the expected distance. This shows a systematic shift towards higher values for small distances. Additionally, the distance measurement can be seen to fail for large values, where the distances are strongly underestimated.

The observed deviation between the measured and the ideal profile can have multiple reasons. The non-ideal modeling of the initial, manual

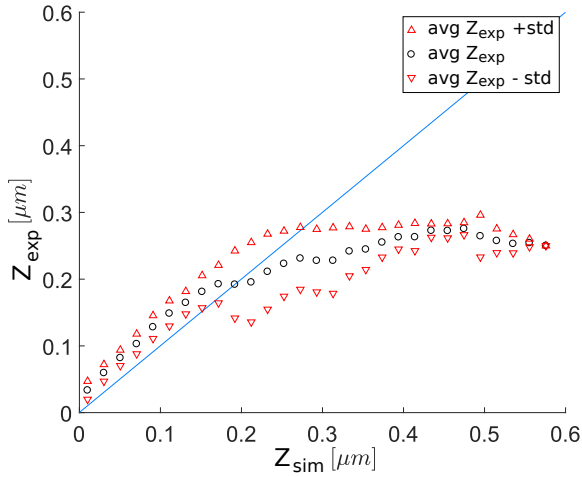


**Figure 6.10:** The experimentally measured distances are plotted against the expected values. In case of a perfect measurement, the experimental values were expected to lie on the blue line. The absolute shift to higher values shows the systematic error while the strong deviation for values larger than  $d = 200 \text{ nm}$  give an estimate for the inaccuracy of the method for high distances.

fitting which was described earlier can lead to inaccurate distance estimations as the metal layers might not be estimated correctly. During the automated fitting, the noise around the critical angle can result in errors in the estimation of the RI of the sphere and thus influence the distance calculation as the model assumed for this scanning point deviates then from the reality. Noise around the resonance angle directly leads to errors in the distance calculation. Other error sources are the manual placing of the ideal sphere in the coordinate system as well as the fabrication tolerances of the microlens which are not taken into account in the modeling.

The absolute shift of the curve towards higher values could be caused e.g. by a non-ideal manual fitting. This would not be surprising, due to the problematic fitting procedure for this measurement as described earlier.

## 6 Validation

The strong deviations for Z-values larger than 200 nm might be caused by the finite penetration depth of the evanescent field. Another possible reason is the decreasing sensitivity of the measurement with increasing distances as the change in the resonance angle decreases with growing distances (e.g.  $|\theta_{res}(d = 10 \text{ nm}) - \theta_{res}(d = 5 \text{ nm})| \gg |\theta_{res}(d = 210 \text{ nm}) - \theta_{res}(d = 205 \text{ nm})|$ ). If the changes in the resonance angle get smaller, than detectable by the BFP camera (smaller than a pixel), an increase in the distance cannot be resolved. As a result, measurements taken at higher distances are assigned a smaller value in the analysis.

However, this gives a good estimate for maximum measurable distance. As an orientation for the other measurements which will be shown in this thesis, one should keep in mind that measured Z-values larger than 200 nm are likely deviate strongly from the real values.

In the end, the RI profile corresponding to this distance validation shall be shown (Figure 6.11). This profile shows values between 1.44 and 1.46 in the contact area which agree with the literature values for fused silica. In this contact area, no systematic shift in the measured values from the center to the periphery is observed. This shows that the RI measurement of the last layer within the evanescent field is reliable for relatively large distances compared to the distance measurement.

This can be explained by the fact that the penetration depth of an evanescent field is a function of the incidence angle. For a simple interface between a substrate with RI  $n_s$  and media with the RI  $n_m$ , the penetration depth can be calculated by

$$d_p = \frac{\lambda}{4\pi} (n_s^2 \sin^2 \theta_i - n_m^2)^{-1/2} \quad (6.4)$$

[71]. Even though the setup of an SPRM sample is more complex, this simple model helps to interpret the results of this experiment. Figure 6.12 shows that the theoretical model for the penetration depth

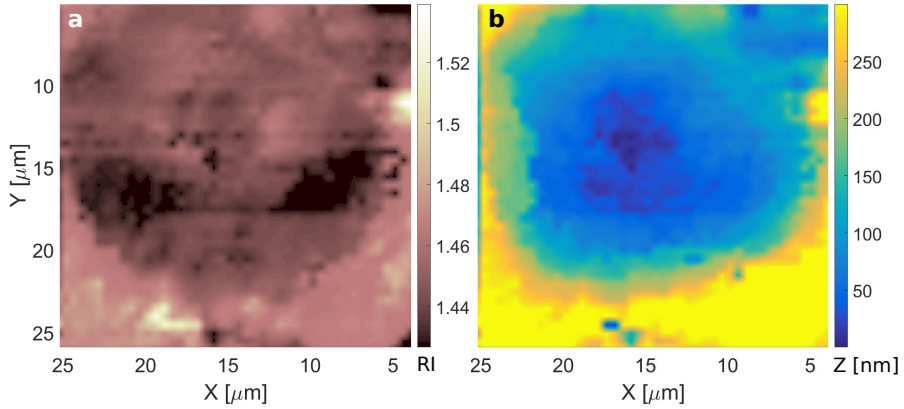


**Figure 6.11:** The RI profile of the measured sphere shows that the RI measurement is reliable even for large distances. a) RI profile of the sphere. The RI values vary non-systematically within the contact area. b) Distance profile of the same scanning area.

diverges at the critical angle. Assuming a similar behavior of the evanescent field, which is created at the SPRM sample interface, a larger penetration depth around the critical angle compared to the resonance angle would explain why the RI profile gives good results for the sphere measurement even at high distances while the distance measurement fails.

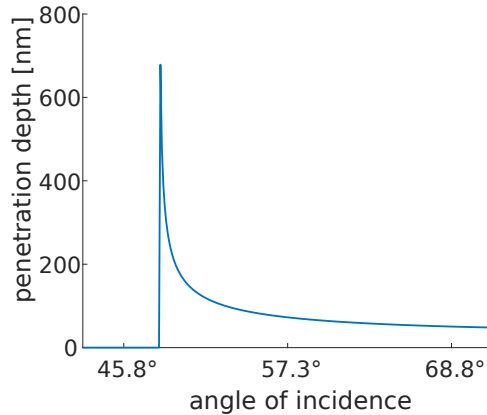


**Figure 6.12:** The penetration depth at the interface between the substrate with  $n_s = 1.788$  and a media with  $n_m = 1.335$  has been simulated numerically. The curve shows that the penetration depth diverges at the critical angle and decreases for higher angles. The peak height around the critical angle depends on the number of simulated points and reaches higher values for a higher density of simulated points.

## 6.4 Discussion

In this chapter, validation measurements for the angle calculation, the RI measurement and the distance measurement were shown.

Based on the generation of diffraction pattern, it could be verified that the used objective satisfies the Abbe sine condition. Therefore, it is appropriate to calculate the incident angle based on this equation within the analysis.

The refractive index measurement could be validated based on a measurement series of a DMSO-water mixtures with variable mixing ratio. The measured values agree mostly with the theoretical values within their respective errors. Small deviations between theory and experiment could be explained by the insufficient description of the physical system by the Lorentz-Lorenz equation. These deviations are well described in literature and were to be expected. Therefore, the RI mea-

surement is not expected to introduce systematic errors in the distance calculation in the cell-substrate distance measurements.

The distance validation was the most tricky task among the validation experiments. Several approaches were tried unsuccessfully. In the end, a fused silica microlens could be measured successfully. Even though the internal reflections in the spherical lens lead to extremely noisy signals, a distance profile could be determined. The profile follows the shape of a sphere for distances smaller than  $200\text{ nm}$ . A total shift of the data of  $\sim 20\text{ nm}$  was found which is believed to be caused by the extreme noise which handicapped the analysis procedure. For distances larger than  $200\text{ nm}$ , very strong deviations were found which can be explained by the finite penetration depth of the evanescent field. This is an important finding because it shows that analysis results which show distances of  $200\text{ nm}$  or higher are likely to have large errors. Therefore, if higher distances are analyzed, those results should be examined with caution.



# Cardiomyocyte experiments

# 7

In this chapter, SPRM measurements at the cell-substrate interface of contracting cardiomyocytes will be described. The motivation of these experiments was to show, that SPRM cannot only be used to determine the cell-substrate distance of comparatively static cells, but that SPRM can also be used to study the movements of the basal cell membrane. Therefore, a qualitative imaging which allows for the observation of cellular dynamics of the cardiomyocytes is shown first. In these widefield images, certain cellular structures were observed. In order to identify these structures, the live-imaging SPRM was be correlated with fluorescence imaging based on immunostainings.

In order to show that the dynamics could also be studied quantitatively, new scanning modes, which allow for the recording of multiple BFP images per scanning point had to be implemented. These modes have been introduced in section 5.4.2.

During my first experiments with contracting cardiomyocytes, it was found that the refractive index was changing with the contraction frequency of the cells. Therefore, a second new set of experiments was designed, which allowed me to correlate the dynamics in the cytosolic refractive index as well as the cell-substrate distance with a fluorescent calcium imaging using Fluo-4. These experiments showed, that the observed dynamics in the SPRM signals strongly correlate with the action potentials.

For the experiments, which will be shown within this chapter, iPSC derived cardiomyocytes were cultured on fibronectin-coated (see section 11.2.1) SPRM substrates according to the protocol described in section 11.3.

This chapter contains revised and extended parts of the publication by E. Kreysing *et al.* “Nanometer-resolved mapping of cell-substrate distances of contracting cardiomyocytes using Surface Plasmon Resonance Microscopy” [16].

# 7.1 Experimental

Most of the experimental details have been introduced in chapter 5. Regarding the single-spot measurements, additional measurement and analysis techniques had to be established to allow for correlative SPRM and fluorescent calcium imaging. These specific methods will be explained in this section. The experimental procedure regarding the live-imaging and the time-dependent area scan can be found in chapter 5.

In order to correlate the SPRM signals with the action potentials of the cardiomyocytes, I decided to record the SPRM measurement in parallel with a fluorescent calcium imaging as the action potential causes an intracellular calcium release and therefore causes a rise in the fluorescence signal after each action potential. I chose to use the calcium indicator *Fluo-4*, because the maxima of the excitation wavelength  $\lambda_{ex} = 494 \text{ nm}$  and emission wavelength  $\lambda_{em} = 516 \text{ nm}$  are smaller than the wavelength of the SPRM laser [26]. This is of great importance, as a significant part of the excitation light is transmitted through the semi-transparent SPRM samples and collected by the TIRF objective. In order not to interfere with the SPRM measurements, the excitation and emission light need to be filtered out.

In order to conduct these fluorescence measurements with the upright microscope introduced in section 5.5, it had to be equipped with a

suitable light source, a filter set corresponding to the excitation and emission wavelength of the fluorescent dye, a very sensitive, high-speed camera and a high NA objective. An HBO lamp was chosen as this provides a high light intensity if the light bulb is replaced on a regular basis. The *Zeiss filter set 10* allows for an excitation of the dye as well as transmission of the emitted light to the camera [72]. An *Andor Zyla 4.2* camera and a 63x objective with  $NA = 1.0$  guaranteed a high luminous efficiency. Additionally, *Zeiss filter set 15* was installed in the filter bench next to the *Zeiss filter set 10*. *Zeiss filter set 15* consists of a band-pass filter with a central wavelength of  $\lambda_{cent} = 546 \text{ nm}$  which should avoid the excitation of the Fluo-4 while exciting the auto-fluorescence of the markers on the substrate and a long pass filter with a cut-on wavelength of  $\lambda_{co} = 590 \text{ nm}$  which allows for the transmission of the SPRM laser light (see Figure 7.1). To avoid disturbances of the SPRM signal by excitation light of the upright microscope, I also installed a long-pass filter with a cut-on wavelength of  $\lambda_{co} = 590 \text{ nm}$  in front of the BFP camera.

The SPRM signals were captured at a rate of  $50 \text{ fps}$  while the calcium imaging was recorded with  $100 \text{ fps}$ . Recording with these high frame rates required the use of two computers. In order to guarantee a temporal correlation of the signals, optical time stamps needed to be set. The recording procedure including the time stamps was realized as follows: First, the filter bench was shifted to an intermediate position between filter set 10 and 15 which resulted in a complete blocking of the HBO light within the illumination light path of the upright microscope.

A SPRM single-spot measurement was started. After a recording for 60 seconds, the recording of the *Zyla* camera was started. Afterwards, the filter bench was shifted and filter set 15 was set in place which does not excite the Fluo-4 and transmits the laser light from the SPRM, thereby indicating the scanning spot on the semi-transparent sample. Thus, a short mechanical occlusion of the laser source with a piece

## 7 Cardiomyocyte experiments

of paper appears in both measurements and serves as a time stamp. Afterwards, filter set 10 is moved in position. After another 60 seconds, this procedure is repeated in order to set a second time stamp.

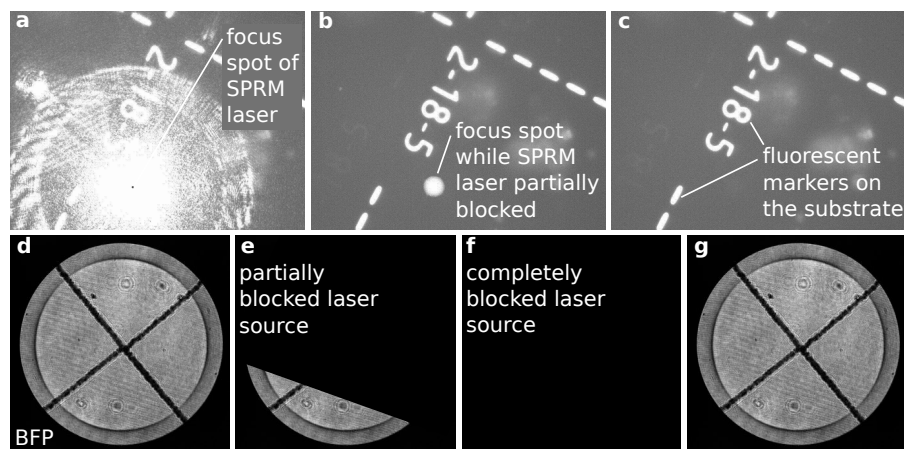


**Figure 7.1:** Time stamps in calcium imaging and SPRM a) The substrate is imaged with filter set 15 which allows for the excitation of the auto-fluorescence of the photoresist-based markers on the substrate. The fluorescent markers help to find the correct focus plane using the upright microscope. The laser spot created by the SPRM illumination is transmitted. b) Partial occlusion of the laser source allows for a better localization of the focus spot. c) The first picture with a complete occlusion of the laser source is used as a time stamp in the calcium imaging. d-g) BFP images before and after occluding the laser source. d) last unblocked image e) first partially blocked f) first completely blocked image - used as a time stamp. e) first unblocked BFP image.

The time stamps were located manually in each measurement. Afterwards, the measurements before and in between the time stamps were analyzed. For the SPRM signals, the analysis procedure described in section 5.4.3 was followed while the analysis of the fluorescence signals was carried out using the camera software *AndorSolis*. Choosing the ROI graphically, *AndorSolis* integrates the intensity over this area and generates an output table which contains the integrated number of counts detected by the camera for each frame within the ROI. As the ROI, I chose the region corresponding to SPRM illumination area.

## 7.2 Live-imaging of cardiomyocytes

The live-imaging mode can be used to observe the cell-substrate interface in real-time. Dynamics at the interface can be easily observed as changes in the intensity in the cell-substrate contact areas. Here, the live-imaging mode was used to localize contracting cardiomyocytes.

First, the radius of the arcs which were projected on the BFP were adjusted: The radius of the arcs was chosen such that the illumination angle at the substrate interface corresponded to the resonance angles while the arc opening angles were chosen such that the contrast in the live-imaging mode was optimized. Figure 7.2a shows the projected arcs which were imaged using the BFP camera while the setup was in the live-imaging mode.

The live-imaging camera was observed while manually changing the lateral position of the sample holder. When a singular cell was found, it was observed and checked for periodical changes which indicate cellular dynamics such as cell contraction. Afterwards, a video was taken in the live-imaging mode which was post-processed as described in section 5.3.2. In the video, one can see periodical changes at the majority of the cell-substrate interface. From this video, I identified one frame which corresponds to the relaxed state of the cell (see Figure 7.2b) and one frame which corresponds to the contracted cell (see Figure 7.2c) and calculated the difference between the non-processed frames by a pixelwise subtraction. The areas with the strongest changes in the plasmon resonance angle appear as white areas in Figure 7.2d.

The observed periodic changes in the live-imaging mode result from a change in the plasmon resonance angle. This can be caused either by a change in the intracellular RI, by a change of the cell-substrate distance (see Figure 5.13), or by a combination of both changes.

## 7 Cardiomyocyte experiments

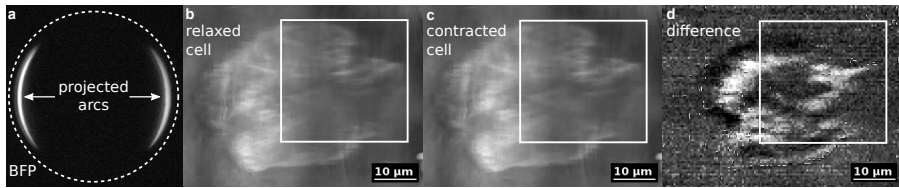


**Figure 7.2:** Projector based live-imaging of a cell-substrate interface of a contracting cardiomyocyte. a) Two arcs are projected on the BFP. b) A live-image of the cell-substrate interface of a cardiomyocyte is recorded in the resting phase (image is post processed for background correction). c) The cell is imaged during the contraction phase (image is post processed). d) The difference between the non-processed images corresponding to (b) and (c) is determined pixelwise. This figure is part of the publication by E. Kreysing *et al.* “Nanometer-resolved mapping of cell-substrate distances of contracting cardiomyocytes using Surface Plasmon Resonance Microscopy” [16].

As it is not possible to separate these influences in the live-imaging mode, the live-imaging mode can yield only qualitative information on the cell-substrate interface. In order to determine the cell-substrate distance and the cytosolic refractive index quantitatively, the entire angular spectrum needs to be analyzed. Therefore, single-spot measurements as well as time dependent area scans were recorded and analyzed which will be presented in section 7.3 and section 7.4.

It is striking that live-imaging pictures show a stripy structure at the cell-substrate interface. In order to understand the origin of these structures, a correlation of a cardiomyocyte in the live-imaging mode and fluorescent confocal microscopy images after specific labellings and immunostaining were performed.

## 7.2.1 Correlation of live- and confocal imaging after labeling

The specific labellings as well as the immunofluorescence stainings have been carried out under guidance of Nico Hampe whereas the fluorescence images have been taken with a confocal microscope by Nico Hampe.

First, a sample with cardiomyocytes has been imaged in the SPRM live-imaging mode. Similar stripy structures as in Figure 7.2 were found (see Figure 7.3a, b). The positions of the cell was clearly identified with the help of the unique markers made from photo resist. After the live-imaging, the sample was chemically fixated, and cellular structures were marked by primary antibodies and fluorescently labeled secondary antibodies as well as by specific dyes according to the protocol presented in (see section 11.6).

The antibodies marked the positions of vinculin and  $\alpha$ -actinin while actin and the nucleus were labeled with specific dyes. Vinculin is present in integrin-ECM bindings and therefore indicates the positions of focal adhesions as well as in costameric adhesions (see Figure 7.3d and section 2.3). Actin forms filaments which are one of the major components of the cytoskeleton of cardiomyocytes while  $\alpha$ -actinin is present in the Z-disks which are connected to the actin filaments (see section 2.4.2). In costameric adhesions, adapter proteins link integrins to the Z-disks. Thus, all of these proteins can be involved in the cell-substrate adhesion.

The observed structures in the vinculin staining (see Figure 7.3d) appear to be smaller than the stripy structures in the live-imaging mode (see Figure 7.3b). In contrast, the actin and  $\alpha$ -actinin stainings reveal the structure of the cytoskeleton which shows many elongated fiber-like structures close to the top edge of the cell (see Figure 7.3e, f). As

## 7 *Cardiomyocyte experiments*

these structures are connected to the cell-substrate adhesion complexes while they are not expected to lie flatly on the basal cell membrane (see Figure 2.8), it is likely, that these protein structures are only found partially within the evanescent field. This would explain why the stripy structures observed in the live-imaging are elongated compared to the positions of vinculin molecules but not as elongated as the filaments observed in the actin staining.

In Figure 7.3g, the fluorescent channels were merged, showing all the discussed protein structures at the same time. This image was desaturated and combined with the corrected live-image. For this purpose, the SPRM image was colorized in blue and pasted on top of the fluorescence image. As the opacity of the SPRM layer was reduced, it is possible to see overlapping structures in the combined image (see Figure 7.3c). This suggests that the observed structures in the SPRM are caused by a combination of different protein complexes which can be found close to the cell membrane.

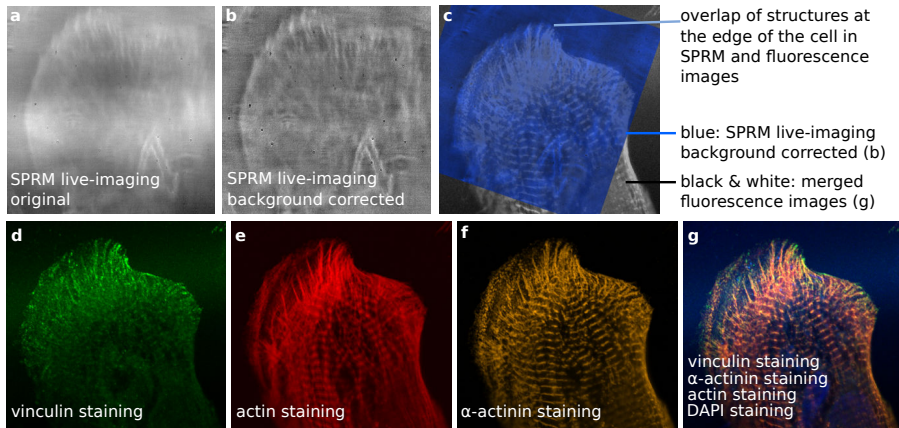


**Figure 7.3:** Correlation of the live-images and the cellular structures resolved by a confocal microscope after specific labellings as well as immunostaining. a) The original live-image shows a stripy structure and background noise due to the inhomogeneous projector-illumination. b) After elimination of the background pattern using a shadow mask, the stripy structures appear more distinct. c) The corrected live-image has been colorized in blue and combined with a fluorescence picture (see g). A reduced opacity of the live-image allows for determination of coinciding structures. d-f) Specific labeling as well as immunofluorescent stainings reveals the positions of proteins involved in the cell adherence. d) Vinculin coincides with focal- and costameric adhesions. e) Actin filaments partially connect to the cell-substrate junctions. f)  $\alpha$ -actinin is present in the Z-disks and can be involved in costameric adhesions. g) Merging of all fluorescence channels (including DAPI) shows the strongest overlap with the structures observed in the live-imaging mode (see c).

## 7.3 Single-spot measurements

This section contains a revised and extended version of the results section of the publication by E. Kreysing *et al.* “Nanometer-resolved mapping of cell-substrate distances of contracting cardiomyocytes using Surface Plasmon Resonance Microscopy” [16].

The single-spot measurements of contracting cardiomyocytes were used to determine the cell-substrate distance and the cytosolic refractive index as a function of time. Fluorescent calcium imaging (see section 11.3.2) is used in parallel to confirm that the dynamics in the

distance and refractive index are induced by action potentials.

Figure 7.4a shows the fit to the average data of a single spot measurement. The thicknesses of the metal layers of the model-system were determined to be  $3.6\text{ nm}$  Cr and  $43\text{ nm}$  Au via manual fitting. Afterwards, the refractive index and the cell-substrate-distance were found automatically as a function of time (see section 5.4.3).

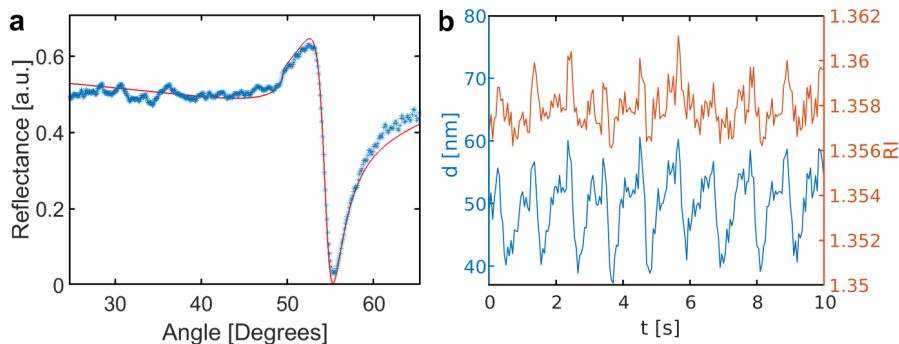


**Figure 7.4:** a) An initial fit of the multilayer system to the average data is applied manually. (Here: Cr:  $3.6\text{ nm}$ , Au:  $43,0\text{ nm}$ , media:  $53,0\text{ nm}$ ) Afterwards, the automated optimization algorithm tracks the values for  $RI$  and  $d$  over time. b) The results of a single-spot measurement of a contracting cardiomyocyte show periodic changes in both parameters. This figure is part of the publication by E. Kreysing *et al.* “Nanometer-resolved mapping of cell-substrate distances of contracting cardiomyocytes using Surface Plasmon Resonance Microscopy” [16].

Figure 7.4b shows a section of the results for  $RI$  and  $d$  as a function of time. The two parameters show a periodic behavior with  $d$  exhibiting distinct minima occurring at a frequency of  $0.94\text{ Hz}$ . Occasionally, the distance signal shows a strong overshoot before it decreases again. The distance was found to vary between  $35\text{ nm}$  and  $60\text{ nm}$  with peak-to-peak changes of around  $20\text{ nm}$ .  $RI$  shows strong peaks (peak-to-peak between  $0.002$  and  $0.004$ ) appearing simultaneously with the overshoots in the distance. A fluorescent calcium imaging allows for the tracking of action potentials (see Figure 7.5a, b) and correlation with the SPRM

measurements. In Figure 7.5c an overlay of the measurement shown in Figure 7.4b and the fluorescence intensity resulting from a calcium imaging (Fluo-4) is shown.

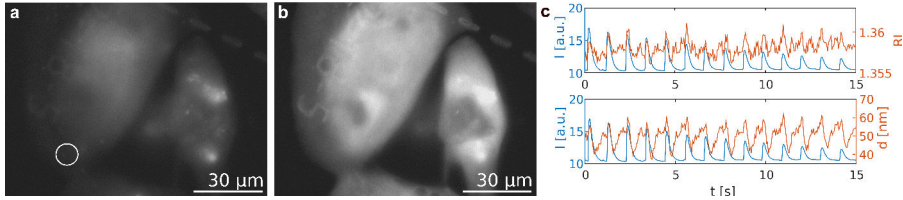


**Figure 7.5:** A fluorescent calcium imaging allows for the correlation of the SPRM signals with the action potential-triggered calcium release. a) At rest, the calcium imaging shows a low fluorescence. The circle indicates the position of the single-spot measurement. b) The fluorescence is increased due to the calcium release. c) Simultaneously recorded calcium imaging and single-spot measurements reveal the same periodicity of the signals.  $d$  decreases immediately after the fluorescence peak as expected. This figure is part of the publication by E. Kreysing *et al.* “Nanometer-resolved mapping of cell-substrate distances of contracting cardiomyocytes using Surface Plasmon Resonance Microscopy” [16].

A strong correlation of the peaks in the refractive index and the intensity of the fluorescence can be observed while the cell-substrate-distance decreases shortly after the peak in fluorescence. The delay  $\Delta t$  between the fluorescence maximum and the start of the decrease in distance has been averaged over 10 periods with  $\Delta t = 87 \text{ ms}$  with a systematic error of  $\pm 50 \text{ ms}$ , which is in the expected range for the time delay between the calcium signal and the cell contraction for iPSC derived cardiomyocytes [73]. Therefore, the minima in the cell-substrate-distance are assumed to be caused by the contraction of the cell.

The systematic error in the temporal correlation is caused by the non-synchronous recording of the SPRM camera and the fluorescence camera. As the temporal correlation of the signals is based on optical time stamps, the maximal systematic error occurs when the shift between the time stamps in the two measurements corresponds to one frame

## 7 Cardiomyocyte experiments

of the slower camera. As the discussed measurement was recorded with  $20\text{fps}$ , the systematic error is estimated to be  $50\text{ms}$ . While the accuracy in the distance measurement of perfectly, noise-free data was determined to  $1.5\text{nm}$  (see section 5.4.3), the accuracy of this measurement was determined by comparing the results of a completely manual fitting with the results of the automatic process (see section 5.4.3) and determined to be  $2.3\text{nm}$  (see section 5.4.3).

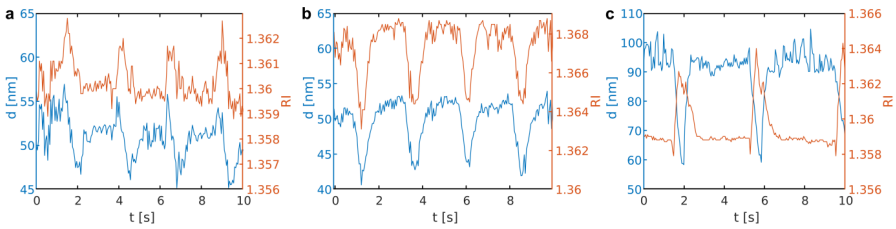


**Figure 7.6:**  $d$  decreases when the cell contracts while the behavior of  $RI$  depends on the position of the measurement. The two signals have been observed to behave entirely different (a), in a parallel (b) or in an antiparallel (c) manner. This figure is part of the publication by E. Kreysing *et al.* “Nanometer-resolved mapping of cell-substrate distances of contracting cardiomyocytes using Surface Plasmon Resonance Microscopy” [16].

The behavior of  $d$  follows a simple pattern, whereas the behavior of  $RI$  differs between measurements taken at different spots. In Figure 7.6a, b, measurements at different spots at the cell substrate interface of different cells are shown. It is striking, that the shape of  $d$  is quite similar in all the measurements except for occasional overshoots of the signal. The shape of the  $RI$ -signal in contrast can differ fundamentally from one position to another. There are positions at which  $RI$  increases directly before the minimum in  $d$  occurs (see Figure 7.6a), positions where the two variables vary in parallel (see Figure 7.6b) and positions where the two variables show an antiparallel behavior (see Figure 7.6c). In cells as complex as cardiomyocytes, there are multiple reasons which can result in such a behavior as will be discussed later.

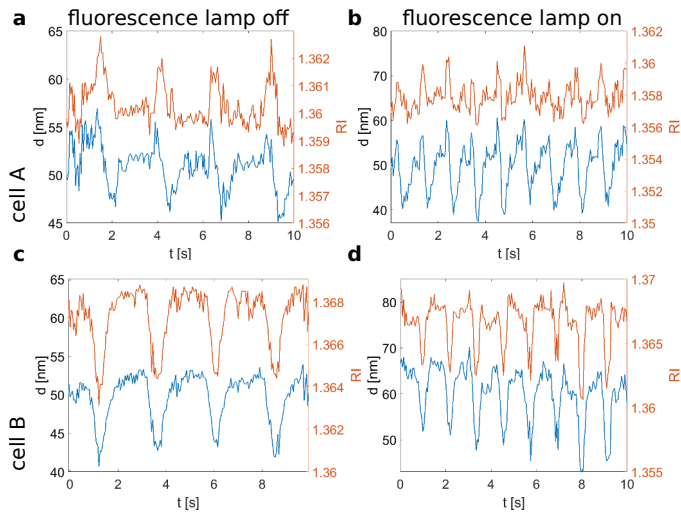


**Figure 7.7:** Measurements directly before (a, c) and during the fluorescent calcium imaging (b, d) show the effect of phototoxicity. In cell A and cell B, the contraction frequency was increased by a factor of 2.

In Figure 7.7, the strong influence of the fluorescence imaging on the cellular behavior is shown. Figure 7.7a, c show a measurement interval of cell A and cell B, respectively. These intervals are part of the first 60 seconds of the single-spot measurement, before the first time stamp, during which the fluorescence excitation light was blocked. Figure 7.7b, d show the measurement of cell A and cell C during illumination with the excitation light directly after the first time stamp. Interestingly, an increase by a factor of 2 in the periodicity of the distance signals is observed in both cells.

## 7.4 Time dependent area scan

This section contains a revised and significantly extended version of the results section of the publication by E. Kreysing *et al.* "Nanometer-

## 7 Cardiomyocyte experiments

resolved mapping of cell-substrate distances of contracting cardiomyocytes using Surface Plasmon Resonance Microscopy” [16].

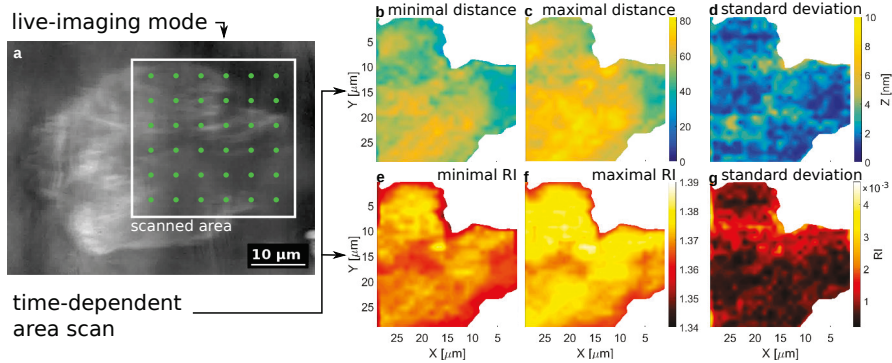


**Figure 7.8:** For the analysis of  $RI$  and  $d$  along the entire interface 870 scanning points were combined. a) The scanning area (white frame) was defined in the live-imaging mode. b) The minimum cell-substrate distance is interpreted as the state of the contracted cell while the maximum distance (c) is interpreted as the relaxed state of the cell. d) The standard deviation is used as a measure for the membrane dynamics. The refractive index profile varies between the minimum values shown in (e) and the maximum values (f). g) The standard deviation indicates the  $RI$  dynamics. For scanning parameters see section 12.2.1. Figure adapted from [16]

As shown in the last section, single-spot measurements can give insights into the cellular behavior at one scanning point at the cell substrate interface. Time-dependent area scans in contrast give information about the cellular behavior along the entire cell-substrate interface by combining large numbers of single-spot measurements. The results of the area-scan shown in Figure 7.8 have been combined from 870 scanning points. The scanned area of  $29 \times 30 \mu\text{m}$  is marked in a live-image of the respective cell (see Figure 7.8a).

$RI$  and  $d$  are analyzed at each scanning point in the same manner as in the single-spot measurements. The combination of the results of all the scanning points allows for the reconstruction of the refractive index profile as well as the 3D structure of the basal cell membrane.

As shown in section 7.3, the cell-substrate distance was always found to show relatively stable plateaus interrupted by distinct minima. Therefore, the maxima are interpreted as the relaxed state of the cell and the minima as the contracted state of the cell.

Based on this assumption, the minimum and the maximum cell-substrate distance determined at each scanning point of the time-dependent area scan are combined to reconstruct the topography of the basal cell membrane in the contracted and the relaxed state, respectively (see Figure 7.8b, c). The standard deviation at each point represents a measure for the membrane dynamics. In the relaxed state, the cell-substrate distances are distributed between 10 *nm* and 80 *nm* with membrane dynamics (standard deviation) between 1 *nm* and 10 *nm*. In order to get a better understanding of these dynamics, which are most likely caused by cell-contractions, an animated 3D video model of the basal cell membrane was generated (section 11.7.3).

Figure 7.8e - g show the cytosolic refractive index maps at their minimal value, maximal value, and the standard deviation, respectively. The measured cytosolic RI varies between 1.36 and 1.39 which is in the expected range [63].

When the areas with the highest standard deviation in the two variables are combined (see Figure 7.8g and d), they show a strong correlation with the observed dynamics in the live-imaging (see Figure 7.2d).

Figure 7.9 shows the results of a second time-dependent area scan recorded from another sample. Here, the cardiomyocytes did not grow as singular cells but were found in clusters. Therefore, an area inside a cell-cluster was investigated first in the live-imaging mode (see Figure 7.9e), afterwards in a time-dependent area scan (see Figure 7.9b-d, f-h) and eventually after the staining (see section 11.6) with a confocal microscope (see Figure 7.9a).

## 7 Cardiomyocyte experiments

The confocal image (see Figure 7.9a) shows that the recorded area contains parts of the cell-substrate interface of two neighboring cells. After the fixation and the stainings, a gap was apparent between the two cells when focusing at the cell-substrate interface. The structures observed in the live-images agree with this finding (see Figure 7.9e).

The minimum refractive index profile shows an area with a refractive index around 1.335 in the same area. This value correspond to the RI of the culture media. In the maximum RI profile though, this area is narrowed (see Figure 7.9g). The refractive index fluctuations are shown to be significantly higher in this intermediate area compared the other areas at the interface.

As the analysis of the cell-substrate distance is based on the assumption that the layer system corresponds to the sample structure at the interface of a cell, areas which are not covered by a cell result in unreliable distance measurements. In those areas around the cleft,  $d$  varies between  $20\text{ nm}$  and  $70\text{ nm}$  which is comparable to the cell observed in the first area scan. The standard deviation reaches from  $0\text{ nm}$  to  $6\text{ nm}$  at the interface which is comparable to the first scan as well.

The fluorescence image shown in Figure 7.9a is part of a Z-stack which has been recorded with a confocal microscope. Looking deeper into the cell-cluster, the adherens junctions which connect the actin-fibers of the neighboring cells (see section 2.3) become visible (see Figure 7.10).

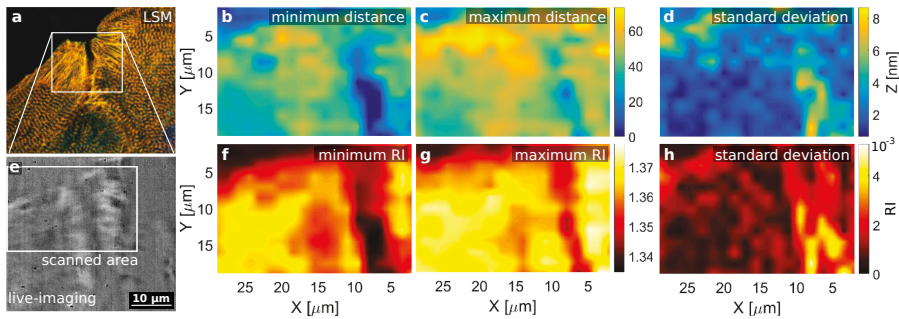


**Figure 7.9:** Results of an area scan at the interface of two neighboring cells reveal the dynamics of the cleft between the cells. a) A fluorescence image of the fixated and stained cells shows a cleft between the cells. Here, actin,  $\alpha$ -actinin, vinculin and the nuclei were stained and imaged. The same cleft was observed in the live-image of the interface (e). b-d) The results of the scan reveal distances between 20 *nm* and 70 *nm* with a standard deviation of up to 6 *nm* (All values assigned to the cleft are neglected.). f-h) The refractive index profiles vary between 1.35 and 1.38 with a standard deviation in the order of magnitude of 0.001. It is striking that the cleft, which can be clearly identified in (f) as those areas with  $RI = 1.335$  narrows due to the cellular dynamics (g). For scanning parameters see section 12.2.1.

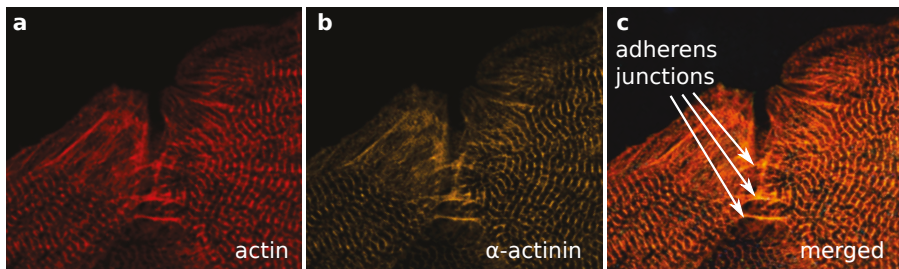


**Figure 7.10:** The confocal fluorescence imaging reveals the existence of adherens junctions when focused at the center of the cells. These connections were not visible when focusing at the interface (see Figure 7.9a). a) Actin filaments of the cell cluster. b) Z-disks in the cell cluster. c) Merged fluorescence channels.

## 7.4.1 Discussion

In the live-imaging mode, strong changes in some areas at the cell-substrate interface are observed. As this mode only allows for a qualitative observation, the influence of the two variables  $RI$  and  $d$  cannot be separated. But the areas of the strongest dynamics of the resonance angle can be identified.

The observation of changes in the SPRM live-imaging during electrical activity of other cell types has been published recently in other works. Here, the electrical activity of HeLa cells [74] and neurons [75] was correlated with a changes in the live-imaging. These observations are in agreement with the experiments described in this thesis and the change of the cytosolic ion concentration is mentioned. In both publications, the changes in the calcium concentration are assumed to increase the cytosolic refractive index directly. Further effects like the change in osmotic pressure which is thereby induced and which in turn leads to water influx across the membrane which would decrease the cytosolic refractive index are not discussed. Instead [75] explains the changes in the plasmonic response with an impedance coupling. As the cell-substrate distances observed in the experiments in this chapter are in the range of  $20\text{ nm}$  to  $80\text{ nm}$  while the Debye length is estimated to  $0.5\text{ nm}$  for the employed experimental conditions, the effect is expected to play a minor role.

It was pointed out earlier (see section 5.4), that the resonance angle of each spot at the cell-substrate interface depends on both, the cell-substrate distance and the refractive index of the cytosol. Consequently, areas with a good cell adhesion as well as areas with optically dense structures near the cell membrane (protein structures and filaments) are expected to appear as bright structures in the live-imaging.

The observed stripy structures at the interface have been correlated

with a fluorescent imaging based on the specific labellings and immunostainings (see section 7.2.1). It could be shown that the size of the areas found in the vinculin fluorescence images does not show sufficient agreement with the structures in the live-imaging. The overlay of the entire stained proteins with the live-imaging showed a good agreement regarding the stripy structures at the front edge of the cell. Therefore, it is assumed that the filaments and possibly also the Z-bands are partially found within the evanescent field of the SPRM and thus contribute to the change in the plasmonic response.

In the single-spot measurement, strong fluctuations of the distance and the RI were observed. At different spots at the cell substrate interface, the distance signal shows similar behavior. Relatively long plateau phases at high distance values are interrupted by sharp minima which occur after the peaks of the fluorescent calcium imaging which indicate cellular action potentials. Therefore, it is assumed that the minima are indeed caused by the contraction of the cell, which is known to follow the action potential in cardiomyocytes. The RI changes with the same periodicity as the distance but shows a less predictable behavior. This might be a result of many different changes within the cell after the action potential and during the contraction.

The action potential triggers an intracellular calcium release (see section 2.4.2). As simulations suggest, this can increase the calcium concentration locally by up to  $2\text{ mM}$  [76] whereas the increase of the ion concentration caused directly by the action potential is orders of magnitude smaller (see section 7.4.2). The effect of the increased ion concentration on the refractive index can be calculated by the Lorentz-Lorenz equation. As shown in section 7.4.2 the resulting change of the RI is three orders of magnitude smaller than the changes observed in the measurement. Taking into account that the change in ion concentration changes the osmotic pressure which in turn results in a water influx, the change in the refractive index could be estimated to  $\Delta Ri = 0.0005$

## 7 *Cardiomyocyte experiments*

(see section 7.4.2), which is one order of magnitude smaller than the observed changes. This value is by a factor 3 smaller than the precision in the RI measurement which was reached with the current setup (see section 5.4.3) when capturing the entire BFP. Zooming into the area around the critical angle promises to resolve the changes in the RI caused directly by the water influx. Measuring this effect would also give an alternative explanation for the observations shown in [74] and [75].

Apart from the changes in the RI caused by the changes in the ion and water concentration in the cytosol, the cell undergoes morphological changes during its contraction (see section 2.4.2). This changes the cell-substrate distance but it also influences the positions of cellular structures such as filaments and cell organelles. As those structures can vary strongly in their RI, it is to be expected, that organelles or other structures which are pushed into or out of the evanescent field change the RI signal in the single-spot measurements. Generally, the values found for the cytosolic RI are in good agreement with the literature [63].

In the time-dependent area scans, the dynamics could be measured pointwise and combined into mappings which show the dynamics of both variables along the entire cell-substrate interface. Even though the results show that the cells tend to keep relatively high cell-substrate distances, this does not indicate poor cell adhesion but on the contrary shows that the cell adhesion proves to be very stable even under high mechanical stress.

An interesting observation in the second area scan could give insights into the behavior of a cluster of cells. While the live-image and the fluorescence image of the cells at the interface first gave the impression that the cells were separated by a cleft, the refractive index profile showed strong deviations in this area. This is an indicator that also the

cleft is highly dynamic, meaning that the cells are likely to be connected to each other in a distance from the substrate which is larger than the evanescent field.

Using the confocal microscope to focus deeper into the cell cluster, actin filaments were found which connect the cytoskeleton of the neighboring cells across the cleft. These junctions are well described in the literature and known as adherens junctions [18, ch. 19]. During the cell contraction, myosin heads move along the actin filaments while the actin filaments are pulled on. Therefore, it is likely, that the parts of both cells are being pulled towards the cleft during a contraction and thus move into the evanescent field over the area which has been identified as a cleft before. These results show how area scans can give insights into intra- as well as inter-cellular behavior and that this technique might be interesting for a variety of applications. Especially the combination of the measurement of changes in the cell morphology and the refractive index seems to be a good platform for the investigation of neuro-degenerative diseases as e.g. an accumulation of plaques, as well as changes in the spontaneous activity of a neuronal network and changes in the cell morphology could be observed non-invasively with only small modifications of the setup. For instance the temporal resolution would have to be increased by the use of a high-speed camera recording the BFP images and the angle resolution needs to be improved by using either a camera with a higher pixel density or by increasing the magnification of the BFP optically.

One possible realization is shown in Figure 7.11. Here, an additional beam splitter is introduced which makes it possible to install an additional recording path for a second BFP camera. I suggest to use a high speed camera in this light path and increase the magnification of the BFP. The magnification can be chosen such that only a part of the BFP is recorded while the other BFP camera records the entire BFP, as usual. This would have two advantages: The angle resolution and therefore

the RI resolution would be increased as this is limited by the imaged angle range per pixel of the camera. If combined with one image of the current BFP camera, one could record only a small area of the BFP with the high-speed camera. This would reduce the size per image and make it possible to image at higher rates because the rate of these cameras decreases with an increasing number of recorded pixels.

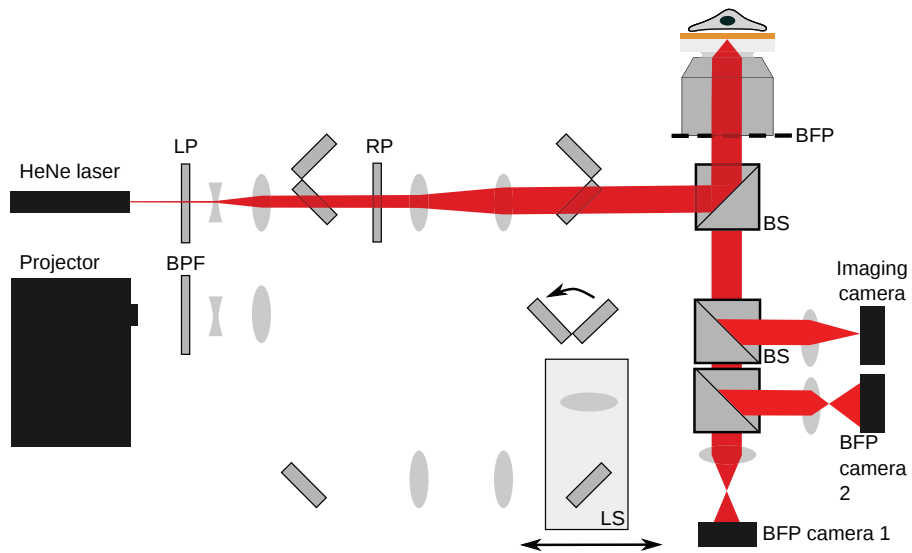


**Figure 7.11:** Suggested modification of the setup. An additional high speed camera which images a fraction of the BFP would allow to increase the temporal resolution (important for measurements of neuronal action potentials) and the angle resolution and therefore the RI sensitivity.

## 7.4.2 Calculations of changes in the RI

### Refractive index changes caused by calcium release

In this section, it shall be briefly discussed, which influence the changes in ion concentration can result in.

First, the refractive index of a aqueous solution is calculated based on the Lorentz-Lorenz equation (see Equation 6.3). The solution is assumed to contain the same concentration of ions as cardiomyocytes. The values for the ion concentrations of calcium, sodium, potassium, and chloride have been taken from [17]. For the sake on simplicity, protein structures in the cytosol are neglected, as their amount does not change during the action potential. The polarizabilities of the different ions types have been found in [77] and need to converted from  $\text{\AA}^3$  to  $Fm^2$ .

Inserting the values for the polarizabilities in Equation 6.3, one obtains  $RI_{sol} = 1.335802$ . An increase of the calcium concentration by  $2 mM$  results in an increase of the RI by  $4 \times 10^{-6}$ . This value is four orders of magnitude smaller than the changes observed in the single-spot measurements. Therefore the direct influence of the change in the ion concentration on the RI of the cytosol can be neglected.

### Refractive index changes caused by ion flux during the action potential

The membrane capacitance is assumed to be  $C = 10^{-2} F/m^2 \cdot A$  (with  $A$  = membrane area) [78] while the voltage difference is estimated to be  $110 mV$ . Using  $Q = C \cdot U$ , the number of ions which are crossing the membrane in the area  $A$  can be calculated. In order to estimate

the number of ions crossing the membrane within the evanescent field during an SPRM measurement, the membrane area  $A$  is assumed to correspond to the illumination spot with a diameter of  $\sim 200 \text{ nm}$ . The number of ions crossing the membrane is determined to 216 ions. This would cause an instantaneous change of the osmolarity within the evanescent field (here, the penetration depth is estimated to be  $200 \text{ nm}$  (based on the experiment shown in section 6.3) while a cell-substrate distance of  $100 \text{ nm}$  is assumed (compare distance measurements shown in Figure 7.8)) in the range of  $10^{-5} \text{ mM}$  if no diffusion is taken into account. Comparing this value to the increase of calcium after a calcium burst, it is found, that the effect of the action potential itself is five orders of magnitude smaller. Therefore, the effect on the refractive index can be neglected.

### **Refractive index changes caused by water influx due to osmotic pressure**

Changes in the osmotic pressure can result in a change of the cell volume as described in [79]. Based on the values given in [76], one can expect local changes of the calcium concentration of around  $2 \text{ mM}$  after a calcium release from the SR. Compared to the intracellular ion concentration shown in Figure 2.4, this causes the intracellular ion concentration to change by around 1% (regarding the intracellular space except for the SR). This in turn causes a water influx due to osmotic pressure of around 1%. An increase of the water content by 1% causes the RI of the cytoplasm to drop from its maximum value (assume  $RI_{max} = 1.38$  and  $RI_{H2O} = 1.33$ ) by  $\Delta RI_{cytoplasm} = RI_{max} - (0.99 * RI_{max} + 0.01 * RI_{H2O}) = 0.0005$ .

# Neuron experiments

This chapter will mainly focus on correlation experiments of SPRM and FIB-SEM.

SPRM is a powerful technique to investigate the cell-substrate distance in a non-invasive and label-free manner *in vitro*. As the light intensity used for SPRM measurements is weak ( $\ll 1 \text{ mW}$ ) and cells have survived weeks after the measurements, it seems reasonable to believe that the measurement technique itself does not introduce major artifacts. This is a great advantage compared to other techniques such as FIB-SEM which is commonly used for the investigation of the cell-substrate interface while it involves extensive preparation procedures.

Combining the two techniques, it is possible to get an insight into the artifacts which might be introduced by chemical fixation as well as heavy-metal stainings and resin embedding.

This chapter will also present the results of the first experiments regarding the tracking of cell organelles, the investigation growth cone dynamics, and tracking of the action potentials of neurons. This provides an outlook regarding the range of applications of the technique.

## 8.1 Correlation of SPRM with FIB-SEM

This section describes the experiments which have been carried out in order to quantify the effect of chemical fixation on the cell-substrate distance and the refractive index. Subsequently, the SPRM results are

correlated with FIB based investigation of the interface which have been executed on the same cells afterwards. Therefore, heavy metal stainings with Osmium tetroxide and Uranyl acetate as well as a resin embedding were executed according to protocol (see section 11.5.2) by Silke Seyock. The FIB processing has been carried out by Elke Brauweiler-Reuters and the STEM images have been recorded by Dr. Elmar Neumann and Elke Brauweiler-Reuters.

### 8.1.1 Experimental

Cortical neurons of 18 day old Wistar rat embryos were isolated and cultured (see section 11.4) on poly-L-lysine (PLL) coated SPRM substrates (see section 11.2.2). The cells were investigated with the SPRM on DIV7. Therefore, the projector live-imaging mode was used to localize cells with a good contrast. Afterwards, live-images as well as bright field images and DIC-images were recorded (see Figure 8.1). The DIC-images were taken with the upright microscope which is equipped with a 20x objective. Thus, the DIC images were recorded with a wider FOV compared to the other modes. This guarantees the recording of the substrate markers close to the investigated cell and allows for locating the same cell later again.

Following the live-imaging, the SPRM mode was switched to the scanning mode to measure the cell. The entire procedure was repeated for 4 cells per sample. Subsequently, the sample has been washed three times with 37°C warm Phosphate-buffered saline (PBS) with same osmolarity as the culture media, fixated with glutaraldehyde and washed again three times with PBS (see section 11.5.1). Afterwards, the samples were kept in PBS. If the measurement could not be repeated directly after the fixation, the cells were kept at 4°C over night. Finally, measurements of the previously scanned cells were repeated with the same parameters

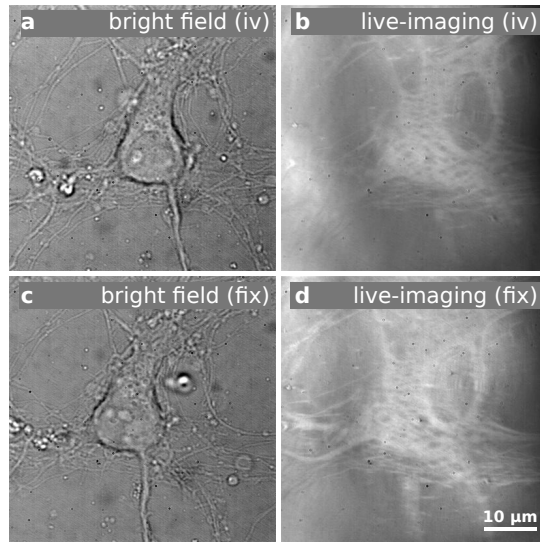


**Figure 8.1:** Imaging the same neuron *in vitro* and after fixation reveals changes at the cell-substrate interface. The mesh-like structure which is seen in the live-imaging shows a stronger contrast compared to its surrounding than *in vitro*. a, c) A neuron is imaged in the in the bright field mode *in vitro* and after fixation, respectively. b, d) The same neuron is imaged in the live-imaging mode *in vitro* and after fixation, respectively.

as in the *in vitro* measurements.

Following the SPRM measurements, the samples were prepared for FIB. Therefore, the cells were stained with Osmium tetroxide and Uranyl acetate (see section 11.5.2). Afterwards, a resin embedding was performed and the samples cured at 60°C over night.

As the SPRM substrates had been glued to polystyrene Petri dishes in order to be used in cell culture, they had to be cut out of the dish before they could be processed further. Therefore, a metal scalpel was heated with a Bunsen burner until the blade glowed. The glowing blade was used to partially cut, partially melt the substrates out of the polystyrene surrounding. These cut samples were glued to specific aluminum SEM holders using silver glue. Covering also the edge of the sample surface

with the glue allows a conductive contact between the sample surface and the aluminum holder to be established. Afterwards, the samples have been sputtered with a platinum layer for 30 s using a current of 30 mA (Balzer SCD004). The additional platinum layer avoids strong charging effects which would result in a low image contrast in the SEM images otherwise.

Afterwards, the samples were investigated with the FIB-SEM system (Fei, Helios NanoLab 600i). When a cell was localized, an additional thin platinum layer was deposited on the ROI via electron beam induced deposition (EBID). This layer protects the sample from damages caused by the ion source. Before the FIB sectioning was started, a several micrometer thick platinum layer was deposited on the ROI using ion beam induced deposition (IBID) in order to stabilize the sample during the sectioning process.

After finishing the FIB sectioning, the cross section was investigated with an SEM. For the investigation with a scanning transmission electron microscope (STEM) or a transmission electron microscope (TEM), a lamella was cut out of the center of the cell and soldered to a specific TEM sample holder.

### 8.1.2 Analysis

First, the scanning data was analyzed using the software *SPRing* according to the procedure described in section 5.4.3. Within this procedure, there are many parameters which need to be chosen individually for each scan, like the opening angle of the areas which are considered during the extraction of the reflectance profiles from the BFP images, the minimal and maximal radius on the BFP which should be considered in the manual fitting procedure, the thicknesses and RI of each layer

involved in the multilayer system, and the parameters and method used in the automated fitting. It is important that the same parameters were used in the analysis of the scans before and after the fixation. As the chosen parameters often work for one but not for both data sets, this procedure had to be repeated usually between 5 and 10 times for each pair of scans until working parameters were found.

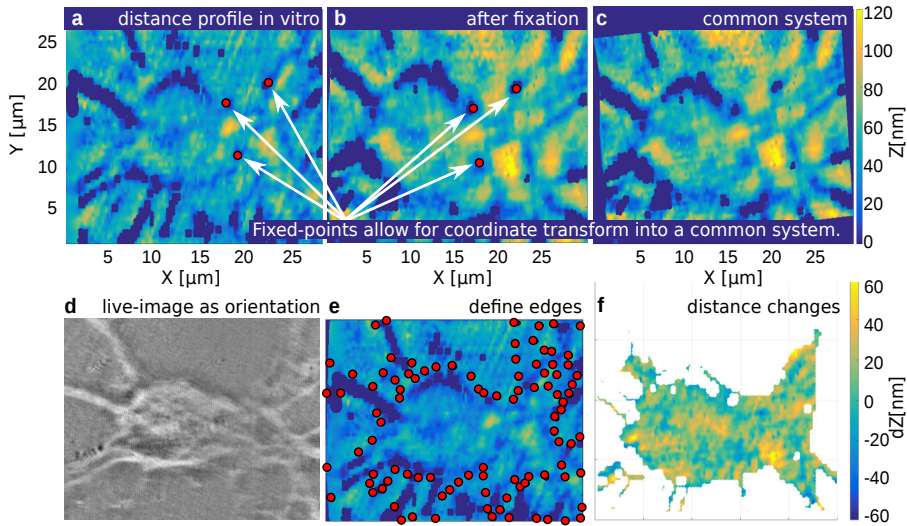


**Figure 8.2:** The *MATLAB* script allows for the calculation of the difference in the cell-substrate distance caused by chemical fixation. First, it shows the distance profiles (a) and (b) and asks for graphical input of three salient points which can be found in both profiles. A coordinate transform of the distance profile after fixation transforms this profile into the system of the distance profile scanned *in vitro*. With help of the live-image (d), the outline of the cell can be identified and passed over to the script via graphical input (e). f) The distance change is calculated for each scanning point and the surrounding of the cell is cut. (The live-image is background corrected and spots on the focus plane have been removed.)

As the samples were fixated inside a chemical hood in between the first and the second measurement, the orientation of the sample on the SPRM setup was altered. Consequently, the scanning results have to be aligned with respect to each other before the cell-substrate distances

## 8 Neuron experiments

measured *in vitro* and after fixation can be compared. Therefore, I wrote the *MATLAB* script *Align and compare* (see section 11.7.5), which loads the scanning results of both scans for one cell. It produces a graphical output of the distance profiles and asks the user to identify the same three salient points in the two distance profiles. These three points have to be chosen via graphical input (see Figure 8.2a, b). Based on the position of these points, a coordinate transform is performed which transforms the data set of the fixated cell into the coordinate system of the *in vitro* scan (see Figure 8.2c). Afterwards, the user is asked to define the borders of the cell. Here, a live-image or a bright field image can be helpful for orientation. The edge is defined via graphical input and the script defines a polygon connecting all of these chosen points. Subsequently, only the area inside the polygon is considered within the distance profiles. Afterwards, the software determines the difference in the distance profiles pointwise. The resulting distance changes are plotted as a color-coded 2D plot (see Figure 8.2f).

For a better visualization of the distance shifts, two other plotting methods are implemented. In the first method, the user defines two points at the cell-substrate interface and the software plots the cell-substrate distance before and after the fixation as a cut through these two points (see Figure 8.3). The other visualization of the distance is implemented

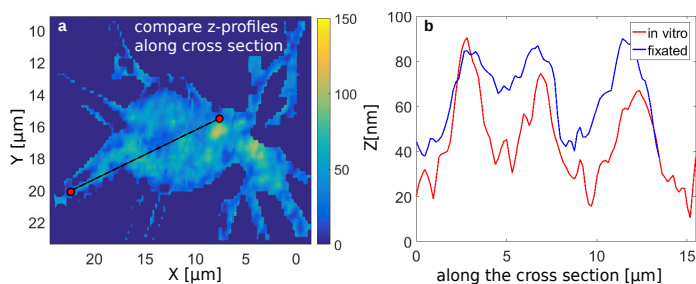


**Figure 8.3:** The user defines two points via graphical input (a). A cross section of the distance profile of the cell is generated between these two points for the situation *in vitro* and after the fixation (b).

using box-plot-diagrams (see Figure 8.5). As the corresponding toolbox in *MATLAB* was not available, the relevant data was saved as .txt-files. Thus, the distance shift at each scanning point was imported in python and plotted as violin-plots which will be shown in the next section.

Within the analysis procedure, not only the distance profiles were subtracted from one another but the shift in the RI was determined in the same manner. The results are also visualized using violin plots. The results regarding both variables will be shown in the next section.

### 8.1.3 SPRM measurements

In this section, the changes of the cell-substrate distance and the RI of the cytosol caused by chemical fixation are evaluated quantitatively. Afterwards, images of the cross sections at the interfaces using FIB-S(T)EM are presented and compared with the SPRM results.

Approximately 100 cells have been measured with SPRM before and after chemical fixation. 10 cells have been successively analyzed according to the procedure described in section 8.1.2. Figure 8.4 shows the evaluation of the distance profiles along the cross sections of three cells. This analysis reveals that the shape of the distance profile remains relatively stable while local changes can result in strong deviations (see Figure 8.4f). While this representation gives information about the changes at specific areas of the cell-substrate interface, it does not provide insight into the overall changes induced by the fixation. Especially in order to evaluate systematic shifts of the data, a box-plot representation of the data can be very informative.

Therefore, the distribution of the distance shifts  $\Delta Z$  at the entire interface is visualized in Figure 8.5a. The underlying light-blue violin plots represent the estimated probability density function which is based on

## 8 Neuron experiments

the measured data. The measurements of two cells show strong shifts of the median ( $> 10 \text{ nm}$ ) while the other 8 cells show lower changes. The shifts do not appear to follow a systematic behavior regarding their directionality as the medians scatter around  $\Delta Z = 0$ .

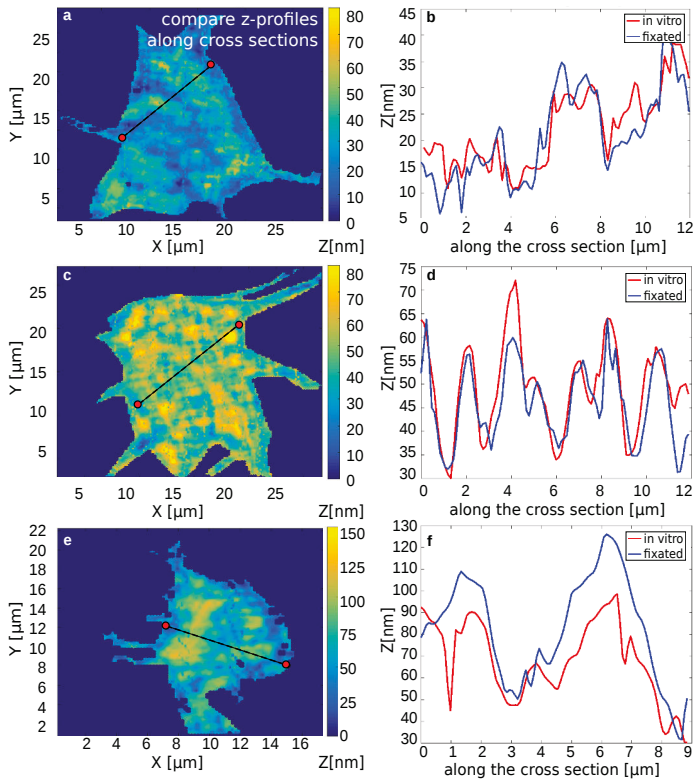


**Figure 8.4:** Comparing the distance profiles before and after the fixation reveals local changes with random directionality while the shape of the distance profiles remains globally similar. Local changes in the distances reach up to  $50 \text{ nm}$ . The cell-substrate distances along the cross sections defined by the dashed lines in (a), (c), (e) are evaluated *in vitro* and after the fixation (b), (d), (f).

Interestingly, a systematic shift is found in the cytosolic RI for the same cells (see Figure 8.5b). Except for two cells, the cytosolic RI shifted systematically to higher values. As an example, the refractive index

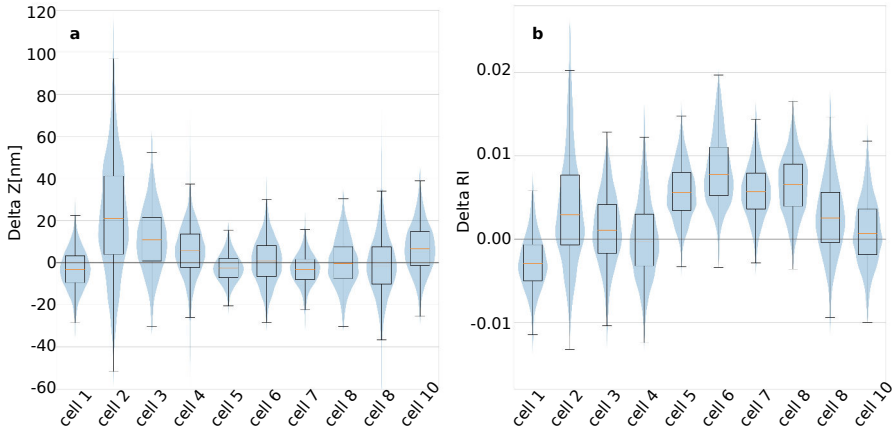


**Figure 8.5:** The changes in the cell-substrate distance as well as the RI of the cytosol have been evaluated for each scanning point for 10 cells. a) Cell 2 and cell 3 show significant changes in the cell-substrate distance towards higher values. The remaining cells show random changes at many scanning points while the average distance is relatively constant. b) The refractive index of the cytosol shifts systematically towards higher values due to the chemical fixation.

profiled before and after the fixation are shown in Figure 8.6 for one cell. These shifts are not going to be discussed further in this section but they will be referred to in section 8.1.4, while discussing possible reasons for the changes in both variables.

In a next step, the distance profiles found in the SPRM measurements will be compared with the pictures which were recorded at the cell-substrate interface using FIB-SEM and STEM. In Figure 8.7a, d, the distance profiles of two cells are shown *in vitro*. The dashed line indicates the cross section which is the basis for the determination of the distance profiles shown in (b) and (e). These cross sections have been chosen at the same position and with the same directionality as the FIB cuts shown in (c) and (f). These images have been taken with the SEM directly after sectioning the cell with FIB. Due to the heavy metal stain-

## 8 Neuron experiments

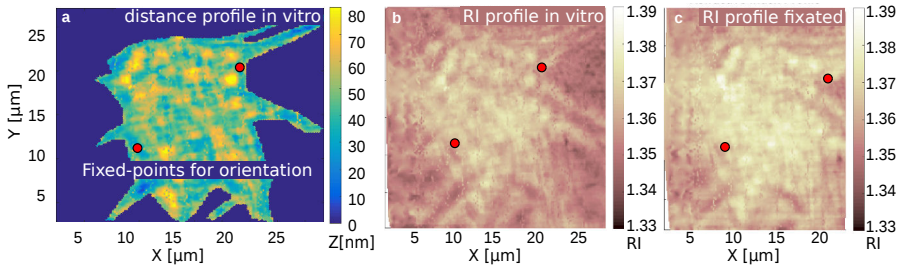


**Figure 8.6:** The RI shifts systematically towards higher values due to the chemical fixation. a) Distance profile of a cell *in vitro*. Two fixed points are marked as an orientation. b) The RI profile is shown *in vitro*. The same points are marked in the profile as in (a). c) The RI profile shows higher values after the fixation.

ings, it is possible to identify cellular structures such as the nucleus as well as a nucleolus (c). Round cavities are found along the interface of the cell. These cavities are filled with material which appears relatively dark in the SEM images. As its color coincides with the resin which is found on top of the cell, it seems reasonable to assume that these cavities are filled with resin. Based on these SEM images, it is difficult to get further insights into the origin of the cavities. Thus, the cell shown in (c) was imaged with a Fei Magellan 400 SEM which additionally allows for scanning transmission electron microscopy (STEM), promising a higher spatial resolution. It was also tried to image the cell-substrate interface with a classical transmission electron microscope. As both methods work in transmission, a thin lamella (thickness  $\sim 100$  nm) had to be cut from the center of the cell and soldered to a specific TEM grid.

The Magellan microscope was used with two different detectors. The vCD detector was used to capture those electrons which were backscattered. Here, the resin which is not stained appears dark while structures which were stained with heavy metals leading to an effective electron scattering appear bright (see Figure 8.8d). The STEM II detector was

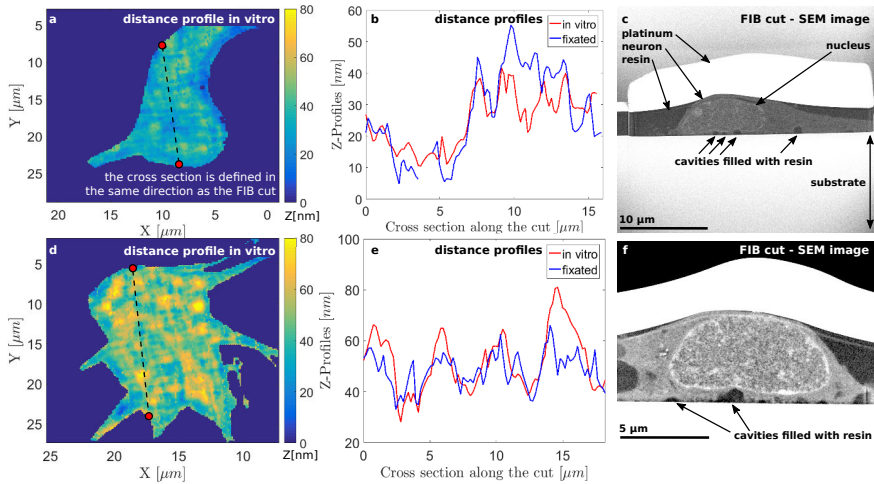


**Figure 8.7:** The distance profile of two cells are shown in (a) and (d). The distance has been evaluated along the cut shown by the dashed line. b, e) Distance profiles along the cross section before and after fixation. The cross sections have been chosen at the same positions as the FIB cuts which are shown in (c) and (f), respectively.

used to detect the electrons in transmission. Here, the stained areas such as the cell membrane appear dark, the unstained resin appears bright and the vacuum appears white (see Figure 8.9). While it is easier to identify cellular structures using the vCD detector, the cell membrane can be identified more easily using the STEM II detector.

In Figure 8.9a, b, the lamella is shown before it was imaged with the TEM whereas images (c) and (d) were recorded with the Magellan microscope after the TEM imaging. Due to a strong mechanical shock, when installed at the TEM, the cell lost the contact to the substrate along the entire interface except for the edges (see appendix, Figure 12.2). Fortunately, the lamella disintegrated cleanly at the interface between the resin and the gold surface. Therefore, the interface could still be investigated by imaging the membrane and the resin which filled the cleft between the cell and the substrate.

## 8 Neuron experiments

In Figure 8.9a, the membrane is shown to be attached to the substrate in large areas while small cavities are found in other areas. In (a) and (c), the contrast between the cytosol and the resin is relatively strong. The separation between intracellular space and extracellular space appears distinct. In (b), a large oval structure which resembles a vacuole is found near the membrane. It cannot be told with certainty whether the compartment is closed or whether the cell membrane is torn. In (d), a large cavity is found which is not clearly distinct from the intracellular space. The edge of the cytosol appears fuzzy and small structures are found within the bright areas which are interpreted as the resin.

Figure 8.10 shows a stitching of four TEM images along the cell-substrate interface. The vacuum cleft is well visible while the contrast between the resin and the cytosol is so poor that the membrane cannot be resolved at most positions at the interface.

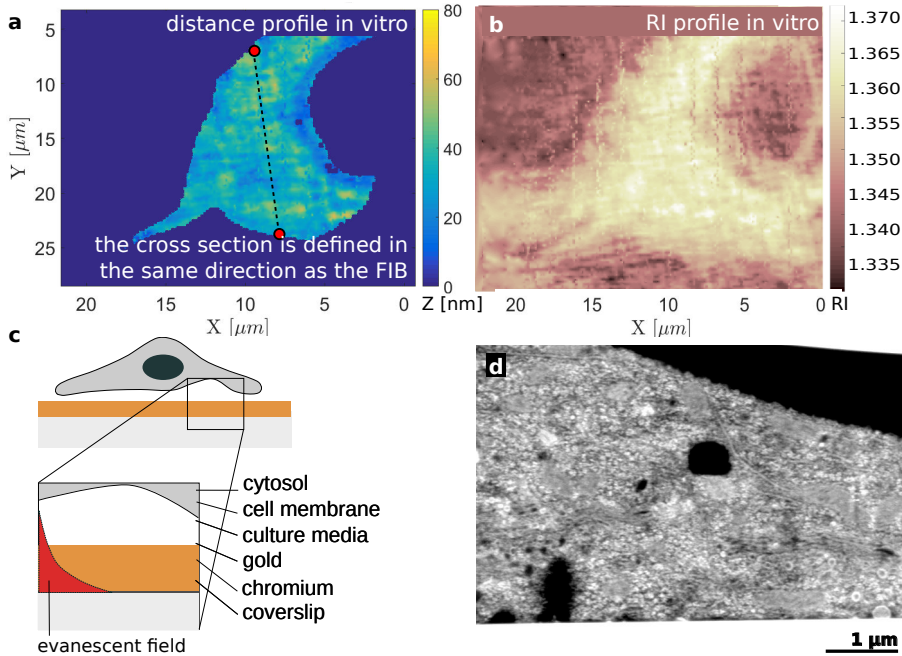


**Figure 8.8:** Are the cavities observed in the S(T)EM images artifacts caused by the fixation and embedding process? a) The distance profile from the SPRM measurement shows distances smaller than  $60\text{ nm}$ . b) The RI profile at the cell-substrate interface shows values for the RI between 1.35 and 1.37. c) The penetration depth of the evanescent field is in the order of magnitude of  $100\text{ nm}$ . The RI measured in a SPRM scan corresponds to the RI of the last layer within the penetration depth. If the evanescent field does not penetrate the cytoplasm because the cell-substrate distance is too high, the measured RI is expected to correspond to the RI of the culture media. In (b), those areas are not found within the cell-substrate adhesion area but only in the surrounding. Therefore, the cavities observed in the FIB-S(T)EM are likely to correspond to fixation artifacts. d) An image taken with the vCD detector at the STEM microscope reveals a large cavity at the interface when the cell was cut along the dashed line shown in (a).

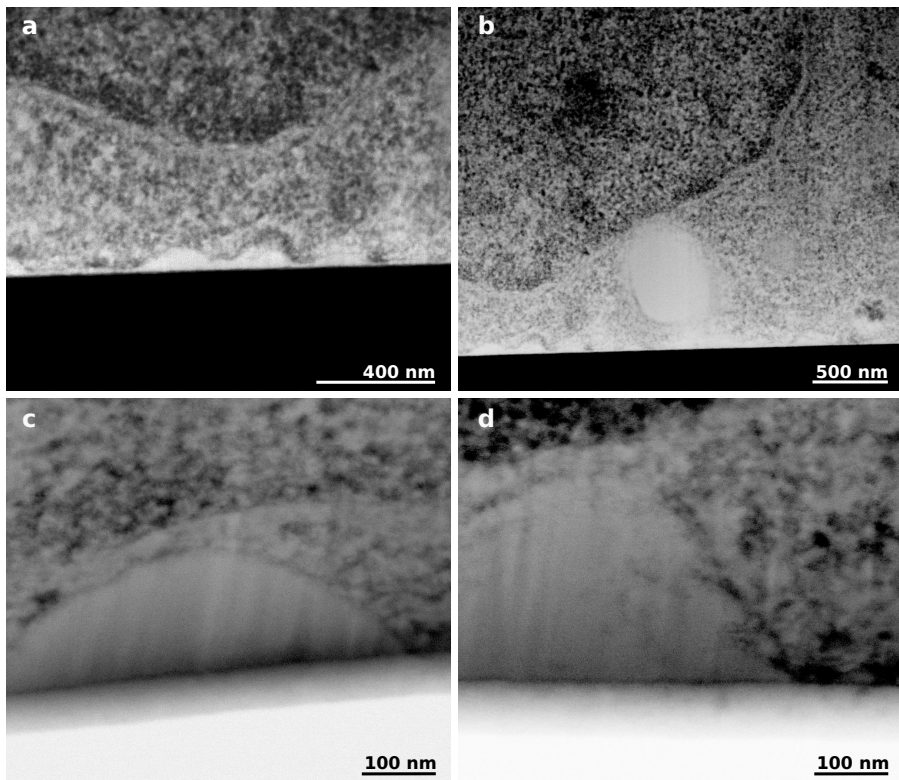


**Figure 8.9:** Images (a)-(d) show close-up recordings of cavities found at the cross section shown in Figure 8.7c. Here, the interface is imaged with a scanning transmission electron microscope (STEM) which allows for resolving more details. (a) Several neighboring cavities at the interface next to an area of relatively tight contact. (b) A large resin-filled vacuole-like structure at the interface is mostly enclosed. It cannot be told with certainty, if the membrane is torn at on position at the interface. (c) The cavity seems well confined. A rather high contrast suggests that the membrane might still be intact. (d) The cavity is larger compared to (c). The edges are rather fuzzy. The cavity is not as homogeneous as in (c), but there are structures which suggest that the membrane might be torn.

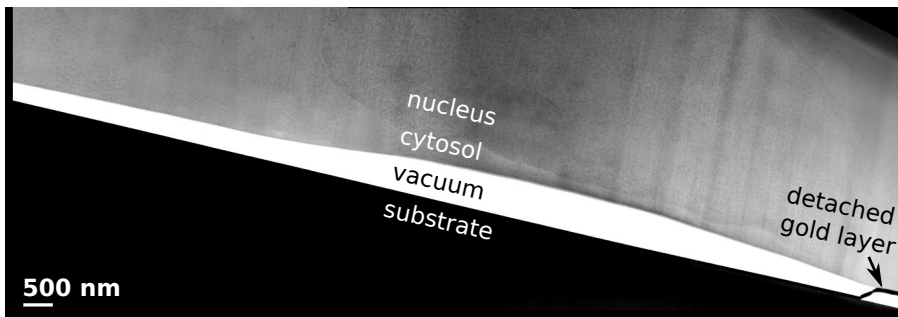


**Figure 8.10:** The TEM image of the lamella shows a rather poor contrast. It is difficult to resolve the cell membrane. Only the nucleus can be easily identified. The cleft between the gold surface and the resin which was caused by a mechanical shock while mounting the sample is clearly visible along the entire interface. Only at the right edge, one can see, that the gold layer detached from the substrate as well.

## 8.1.4 Discussion

In the experiments, it was shown that the cell-substrate distance as well as the RI of the cytosol are altered during the standard protocols applied for preparing the cells for electron microscopy. The SPRM measurements could only be performed before and after the chemical fixation as the subsequent preparation steps involve staining with radioactive and very toxic substances which need to be handled with special care. Afterwards, the samples cannot be brought into the ordinary labs for further investigation.

In the following paragraphs, the changes introduced by chemical fixation will be discussed separately from the artifacts which might have been introduced during the subsequent preparation.

Afterwards, the differences between the SPRM results and the FIB images as well as possible reasons for the differences will be discussed. This involves the possibility that certain artifacts might have arisen after the chemical fixation.

### Fixation induced artifacts

In order to get a better understanding of how the chemical fixation can change the cell-substrate distance, it is necessary to understand the cell-adhesion under physiological conditions. The cells are cultured on substrates which have been coated with PLL which is positively charged under physiological conditions. Electrostatic interaction between the positively charged coating and the negatively charged acidic side chains (e.g. glutamic acid or aspartic acid) of the membrane proteins mediate a stable cell-substrate adhesion [18, ch. 3]. Only a fraction of the membrane proteins creates such bonds with the polypeptides within the substrate-coating. The charged proteins which are not in-

volved in the membrane adhesion, are hydrated by the water molecules found within the culture media.

Using glutaraldehyde to fixate the cells, amino groups of close polypeptides are linked to one another. As a result, the membrane proteins can be crosslinked with the coating molecules but it also applies to intracellular protein structures present in cell organelles or the cytoskeleton. Glutaraldehyde binds covalently to the amino acids of close polypeptides. As a result, the former ionized amino groups lose their charges and the three binding partners form a neutral complex. This changed charge distribution might lead to a change in the tertiary structure of the proteins. As the former ionized amino groups lost their charges which caused a hydration of the proteins before the crosslinking, this might explain a locally reduced water concentration. As most processes evolve in a manner which favors energetically lower states, the fixation process might change the cell-substrate binding accordingly. Since covalent bonds are much stronger than electrostatic bonds, the cell-adhesion complexes can be expected to alter during the fixation. Changes in the membrane proteins regarding the tertiary structure as well as the hydration, are likely to affect the cell-substrate distance. Additionally, a change in the hydration of the proteins would explain the increase of the cytosolic RI because the RI of water ( $\sim 1.3$ ) is much lower than the RI of proteins ( $\sim 1.5$ ).

Changes in the intracellular protein structures might alter the polarizability of the proteins directly or by reducing the hydration of said structures. Both processes might result in a change in the RI of the actin cortex of the cells. Such a process would not only explain why the average RI in the RI profiles shows increased values after the fixation but assuming that the mesh-like structures which are observed in the live-imaging (see Figure 8.1) are caused by the actin-cortex, an increase in the RI would explain the enhanced contrast between the mesh and the surrounding after the fixation.

In order to analyze whether the observed structures correspond to the actin cortex, a correlation of SPRM and fluorescent confocal microscopy after a specific immunostaining of the actin would be advisable.

### Comparison FIB and SPRM

Comparing the distance profiles measured with SPRM with the S(T)EM images, it is striking, that the distances found in SPRM do not exceed  $80\text{ nm}$  while the S(T)EM images show resin-filled cavities with a height of  $h > 200\text{ nm}$ . This allows for three different explanations.

The first one would be, that the cavities have been present already *in vitro*, but they are not resolved by the SPRM. In this explanation, it needs to be considered, that the maximum scanning resolution is limited by the diffraction limit to  $\sim 200\text{ nm}$ . Consequently, the result for each scanning point is averaged over a spot with a diameter of  $\sim 200\text{ nm}$ . However, the scanning resolution also depends on the distance between the scanning points. This was set to  $250\text{ nm}$  in order to save time during the experiment. Due to the large number of cavities at the interface, it appears unrealistic that none of these cavities was matched relatively close to their center by a scanning point during the scan of the entire interface of multiple cells.

The second explanation involves a mismatch of the data and the model. The cell-substrate distance can only be determined correctly, if all the layers involved in the multilayer-system (coverslip, Cr, Au, media, membrane, cytosol) are penetrated by the evanescent field. For scanning points with a larger cell-substrate distance than the penetration depth of the evanescent field, the determined distance would not reflect the reality. If such a situation would occur, the RI profile of the cell would show a the RI value of the media ( $RI_{media} \sim 1.335$ ) as this would represent the last layer within the evanescent field. Here, it needs to

be considered, that the penetration depth around the critical angle is larger than around the resonance angle (see section 6.3.1). In order to be able to give a final judgment regarding this theory, the penetration depth around the critical angle needs to be measured and this value needs to be compared to the size of the cavities found in the S(T)EM images.

The third explication why the large cavities are not found in the SPRM analysis but only in the FIB sectioning is that the cavities developed after the SPRM measurement of the fixated cells. As the successive preparation is quite extensive, there are many steps which might potentially damage the cell membrane. One of them is the extensive washing with ethanol which might dissolve the membrane even though in theory, the lipid structure should have been fixated by the use of osmium tetroxide before. An indication for this theory is the observation of stained fragments inside some of the cavities and fuzzy edges in the STEM images where the cell membrane would be expected.

### **Conclusion**

It has been observed that the chemical fixation induces changes at the cell-substrate interface while even stronger alterations of the morphology might be caused by the subsequent preparation. The lack of scanning points with low RI in the SPRM results suggests that the cavities did either not exist *in vitro* or that the cell-substrate distances at some scanning points were larger than the penetration depth of around the resonance angle but smaller than the penetration depth around the critical angle.

In order to be sure whether the large cavities developed during the preparation or whether they existed before and the SPRM analysis failed to resolve them, it seems reasonable to repeat the experiments

shown here with a different optical method. FLIC has been used to investigate of the neuron-substrate interface but as the lateral resolution has not exceeded  $900\text{ nm}$  in these experiments, only cavities much larger than those observed in the presented experiments would be resolved [33], [11]. As MIET reaches a lateral resolution comparable to SPRM (around  $\sim 200\text{ nm}$ ), this might be a good alternative.

However, the observed alterations due to the cell preparation suggest, that the investigation of the cell-substrate interface according to the protocol used here might be not as preservative as expected. This could have been caused by a large variety of influences. As the samples were all prepared at the same time, it is not possible to tell whether it is typical to find these large cavities or whether this might have been caused by a specific step in the extensive preparation or whether any of the chemicals might have been contaminated or were too old.

In conclusion, it could be shown that is possible to correlate SPRM and FIB. The differences which were found with the two different techniques indicate that SPRM can be used to identify artifacts which might occur during the preparation and show in the FIB-S(T)EM images. This emphasizes to be careful while interpreting FIB-S(T)EM images as even the chemical fixation has been shown to introduce artifacts. Therefore, when it comes to estimating the cell-substrate distance *in vitro*, non invasive optical methods might be considered a valuable alternative to FIB-S(T)EM.

## 8.2 Other experiments with neurons

### 8.2.1 Measurement of cell organelles

The focus of the experiments shown so far was on the morphology of the cell and local changes in the RI and the distance. In this section, it shall be shown that the RI of the cytosol is a valuable information which can provide insights into the intracellular structure. As an illustration of this, it shall be shown that the lateral resolution of the SPRM is sufficient for the detection of the position of cell organelles.

In order to find out whether the RI profile can provide information regarding the positions of the cell organelles, many area scans of neurons cultured on PLL-coated substrates and recorded at different *DIVs* have been analyzed. It was found, that most of the RI profiles are rather homogeneous (see Figure 7.8, Figure 8.6 and Figure 8.8b). Here, it is not possible to identify the positions of cell organelles within the soma. However, two scans of neurons of different age (*DIV* 3 and *DIV* 10) were recorded which allow for a good correlation of the positions of cell organelles in bright field images and the RI profiles.

Figure 8.11a shows a phase contrast image taken after scanning which reveals the position of the nucleus. Its position is also clearly visible in the RI profile as an area with a low refractive index with  $RI_{nucleus} \sim 1.335$  while the rest of the soma is shown to have a higher RI of around  $RI_{cytosol} \sim 1.36$  (see Figure 8.11b). It needs to be mentioned, that the distance profile shows distances of  $d = 0 \text{ nm}$  in the area corresponding to the low RI (see discussion part for possible reasons).

A similar observation could be made in a measurement of a neuron at

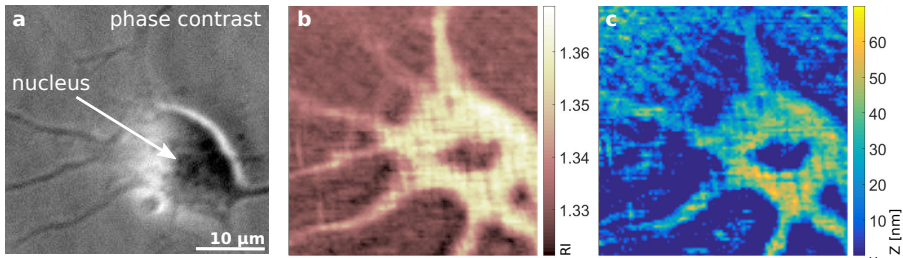


**Figure 8.11:** Measurement of a cortical rat neuron on *DIV 10* cultured on PLL. a) A phase contrast image taken after the measurement outside of the SPRM setup allows for the identification of the nucleus. b) The nucleus appears in the RI profile as it has a lower RI than the cytosol (see [63]) and as it lies within the penetration depth of the evanescent field. c) The determination of the distance profile fails at the position of the nucleus because the simulated multilayer system does not correspond to the reality.

*DIV 3* (see Figure 8.12). Subfigure (a) shows an image recorded in the bright field mode in the SPRM setup (see section 5.5) and allows for the identification of cell organelles (e.g. A-D). The RI profile shown in subfigure (b) reveals the RI of these structures. While the organelles which appear as dark structures in the bright field image (structures A and C) are assigned low RI values, the organelles which appear as bright structures in the bright field image (B and D) are assigned high RI values in the RI profile. As in the first measurement, distances of  $0\text{ nm}$  are assigned to some areas in the distance profile, e.g. at the position of the organelle labeled with A.

## Discussion

In the two measurements presented in this section, it could be shown, that the position of cell organelles observed in the bright field mode or the phase contrast microscope could be correlated with the RI profiles.

Figure 8.11a reveals the position of the nucleus, which could be corre-

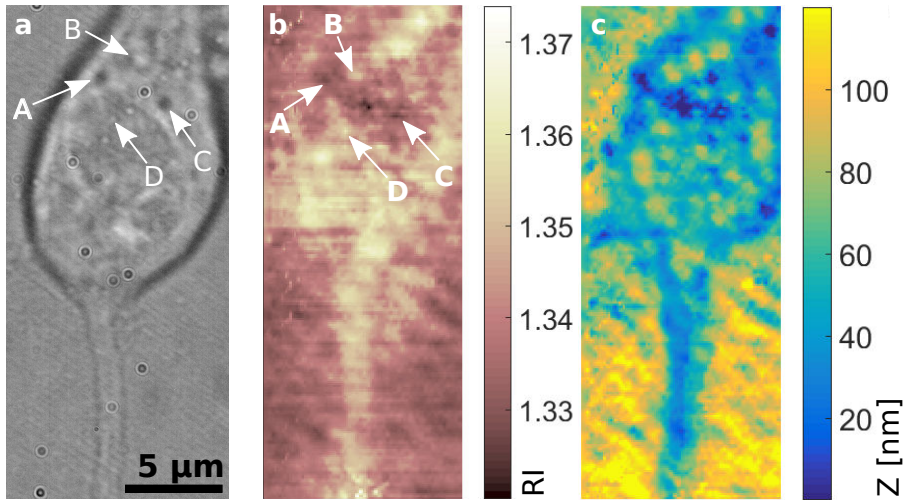


**Figure 8.12:** Measurement of a cortical rat neuron on *DIV 3* cultured on PLL.

lated with a large structure appearing in the RI profile with a lower RI than the remaining soma. Even though it seems contra-intuitive, it is well described, that the nucleus has a lower refractive index than the surrounding cytoplasm [63].

While this finding suggests that the RI measurement of the last layer within the evanescent field works well, the distance profile shows an analyzed distance of  $0\text{ nm}$  in the same area (see Figure 8.11c). This suggests that the distance calculation fails at the position of the nucleus (see section 2.3 for minimum expected distances). The failure of the distance determination is a logical consequence of the mismatch between the multilayer system consisting of six distinct layers (coverslip, Cr, Au, culture media, membrane and cytoplasm), which is assumed during the data analysis and the real situation because apparently also the nucleus (including its membrane) is found within the evanescent field. In order to calculate the cell-substrate distance in this area, an accurate knowledge of the RI and the thicknesses of the additional layers would be required. The area containing the nucleus would have to be analyzed

separately from the rest of the scan. However, this would require an adaptation of the layer structure at each scanning point, which would imply a great effort and seems currently unrealistic.

Similar observations were made in the second measurement. Here, small cell organelles could be localized in the brightfield mode and their positions could be correlated with the RI profile. Showing that the measurement of the RI of these small organelles is possible with SPRM proves that the spatial resolution is sufficient to provide insights into cellular properties of structures with a diameter of  $\sim 200\text{ nm}$ . Such structures are difficult or maybe even impossible to analyze quantitatively *in vitro* with other techniques. This shows, that the RI measurement of SPRM is a very powerful tool and has a large potential to answer biological questions without disturbing the cell.

As mentioned before, most of the RI profiles measured at the neuron-substrate interface show a very homogeneous cytosolic RI (see Figure 7.8, Figure 8.6 and Figure 8.8b). These two measurements shown here are exceptional on that score. Trying to understand this fact, the cellular structure of neurons needs to be considered. Like most adherent cell types, neurons possess a rich actin cortex [80] which is organized in a mesh-like manner. This actin cortex covers the entire inner side of the cell membrane. Its thickness can vary between different cell types. Due to the small number of studies [81, 82], this thickness is still unknown for many cell types. It could be determined to  $\sim 200\text{ nm}$  for HeLa cells [81]. As no concrete values for cortical neurons are found in the literature, a thickness of around  $200\text{ nm}$  shall be assumed here.

As discussed before, the penetration depth of the evanescent field depends upon the angle of incidence and cannot be determined accurately. The distance measurement of the glass bead suggests a penetration depth in the range of  $150 - 200\text{ nm}$  around the resonance angle and a higher but unknown value around the critical angle (see

section 6.3.1). As the measured cell-substrate distances are usually in the range of 40 – 150 *nm*, an actin cortex with a thickness of  $\sim 200$  *nm* might occupy those parts of the cytosol which are found within the evanescent field around the critical angle.

As cell organelles which are larger than the mesh-size of the actin cortex might be kept in a certain distance from the membrane by the actin cortex, this could explain why the RI profiles are usually rather smooth and positions of cell organelles are only rarely revealed. On the one hand, this would limit the investigation of cell organelles to a small ratio of cells for the used cell type (maybe, the situation differs for other cell types). On the other hand, this situation would allow for a rather accurate determination of the cell-substrate distance in most cells.

As this discussion is based on assumptions regarding the penetration depth around the critical angle as well as the thickness of the actin cortex in neurons, it would be helpful to characterize these two values accurately.

However, these experiments give important insights for the interpretation of all the distance profiles: If strong spatial variations are observed in the RI profiles, the distance profiles need to be handled with care because they are likely to be inaccurate as the modeled layer system probably does not describe the real situation in the cell.

### **8.2.2 Measurement of growth cones**

All the cell measurements shown before have been taken in the contact areas of the soma. Here, it shall be discussed whether SPRM is also suited to measure the interaction of neuronal growth cones with the substrate. In order to answer this question, cortical neurons have been

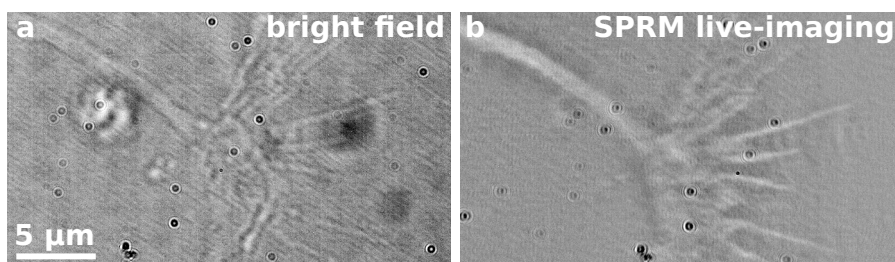


**Figure 8.13:** A neuronal growth cone has been observed in the bright field mode (a) and in the SPRM live-imaging mode (b). The background of the picture has been corrected using a shadow mask. The scanning results for the same growth cone are presented in Figure 8.14.

cultured on PLL-coated SPRM substrates and have been measured at *DIV 3*.

When a neuronal growth cone was found, it was imaged in the bright field mode as well as the SPRM live-imaging mode (see Figure 8.13). In the bright field mode, the contrast is very poor and even after adapting the dynamic range of the image, it is difficult to identify the outline of the growth cone. The dendrite and the filopodia (the finger-like structures) can be observed while the lamellipodia (the sheet-like structure between the filopodia) are not clearly visible. The SPRM live-image shows a much better contrast. Here, it is easy to identify the filopodia as well as the lamellipodia, because both of these structures represent contact areas between the cell and the substrate and therefore shift the resonance angle compared to the bare substrate around the growth cone.

Following these qualitative measurements, area scans were taken for a quantitative analysis of the growth cone-substrate interface. The first scan included a part of the dendrite and its growth cone. Subsequently, three additional measurements were taken exclusively at the growth cone-substrate interface. As the scanning time for this small area took three minutes and the scans were recorded directly one after another,

the changes which occur from one scan to another correspond to the dynamics at the interface within these three minutes.

The resulting RI and distance analysis are shown in Figure 8.14. In the RI profiles, the filopodia as well as the lamellipodia are well resolved. It is striking that the RI of some filopodia and the dendrite have been analyzed to have a lower refractive index than the surrounding media and even lower than water with  $RI_{dendrite} \sim 1.325$  (see Figure 8.14a). Other structures within the growth cone are assigned higher values reaching up to  $RI_{growthcone,max} = 1.350$ . Around the growth cone, a RI of  $RI_{media} = 1.335$  is measured which corresponds to the expected value for the surrounding media. The RI profiles show small changes over time.

In the distance measurements, large areas at the interface of the dendrite and at the growth cone which are analyzed to have  $0\text{ nm}$  distance to the surface. Nevertheless, some areas (e.g. the filopodia) show changes in the analyzed distances.

## Discussion

The dynamics which are observed in the distance and the refractive index profiles are likely to be caused by the dynamics of the growth cone which is known to explore its surrounding by tapping at the surrounding surfaces using the filopodia and eventually increase the contact or retracting the finger-like structures (see section 2.4.1).

The RI values measured in the dendrite and partially in the filopodia are surprisingly low. As the values are even lower than the RI of water, the possibility that the data analysis failed should be considered. As the analysis of the surrounding of the cell is exactly in the expected

range, it is unlikely that the problem is caused by noise or the quality of the SPRM substrate.

A possible error source might be caused by the structure of the probed sample and its deviation from the multilayer system since growth cones are relatively thin compared to the soma of a cell. The height of the leading edge of the growth cone is expected in the range of 200 – 400 nm [83]. This implies, that there might be areas in which the evanescent field does not only penetrate the cytosol but maybe even the upper membrane and the culture media above the cell. In this case, the real layer structure in these areas differs from the assumed structure. Thus, the shape of the reflectance curve changes. The slope after the critical angle might change and therefore, the fitting algorithm used to determine the position of the critical angle might fail.

In order to understand the origin of the low RI values, it should first be checked, whether the critical angle is found correctly at the respective positions which is unfortunately not possible with the current analysis software.

Due to the probable mismatch of the assumed and the real layer structure, it is not surprising that distances of 0 nm occur in large areas of the scan. Generally, one would expect that the presence of proteins in the membrane would always introduce a non-zero distance to the substrate.

In conclusion, it should be said that scanning SPRM can be used to visualize dynamics of the growth cone. The analysis and interpretation of the measured data is nontrivial and requires a more detailed understanding of the analyzed sample. Since the growth cone might be thinner than the penetration depth, the thickness of the cytoplasm as well as its RI would have to be known in order to analyze the system correctly. Here, it also needs to be taken into account that the penetration depth depends on the angle of incidence. Thus, the number of

penetrated layers might differ around the critical angle and around the resonance angle. This might make it necessary to assume different layer structures for the fitting of different parts of the reflectance curve.

## 8 Neuron experiments

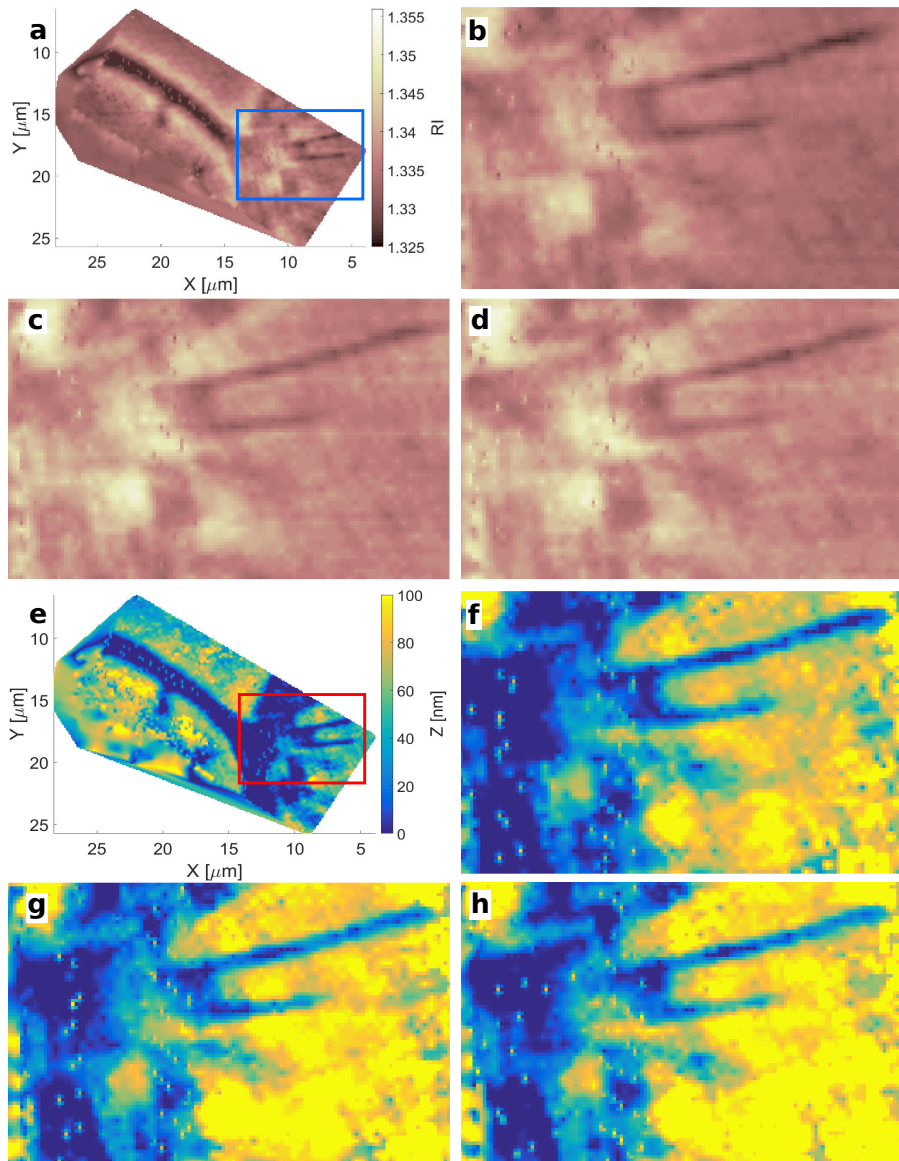


**Figure 8.14:** Subsequent scans of the same growth cone can reveal its dynamics. The RI profile and the distance profile of a dendrite and its leading growth cone are shown in (a), (e), respectively. A small area of the growth cone has been scanned three more times. The resulting RI profiles are shown in (b-d) and the corresponding distance profiles in (f-h). The time between the recordings was  $\sim 3 \text{ min}$ . The many point-like structures which appear in the RI and more obviously in the distance profiles are caused by a measurement issue explained in section 9.1.3.

### 8.2.3 Failed measurement series

In this section, I want to describe two other measurement series with neurons which have been started but could not be finished due to technical problems.

#### Measurement of neurons over several days

This measurement series was conducted in order to determine the development of the cell-substrate distance over time. Cortical neurons were cultured on PLL-coated SPRM substrates and the same cells were measured on *DIV 0*, *DIV 1*, *DIV 3* and *DIV 7*.

Cells with a good contrast in the SPRM live-imaging were localized  $\sim 5 h$  after plating. Afterwards, images were recorded in the live-imaging mode, the bright field mode and with the upright microscope. Due to the photoresist markers on the substrate, the position of the respective cells could be clearly identified.

The chosen cells were scanned at *DIV 0*. The parameters, which are characteristic for a measurement were defined prior to the first measurement and were kept constant for all subsequent measurements. The entire measurement procedure was repeated for the same cells on the indicated days.

Unfortunately, the radial polarizer which was used during these experiments did not provide exactly radial polarized light. Therefore, it was not possible to fit the reflectance curves and the data could not be analyzed.

I highly recommend this experiment be repeated, as it might give insights into the question how the cells secrete their extracellular matrix and thereby change the cell-substrate distance. This could be of great

import for the extracellular recording of action potentials with MEAs or FETs.

When repeating these experiments, one needs to take care that all the parameters which can be set in both the data extraction and in the data analysis software are set to the same values, as even small changes can result in changed distance values. The software described in section 8.1 could be used to determine the changes in the cell-substrate distance.

### 8.2.4 Time series of neurons

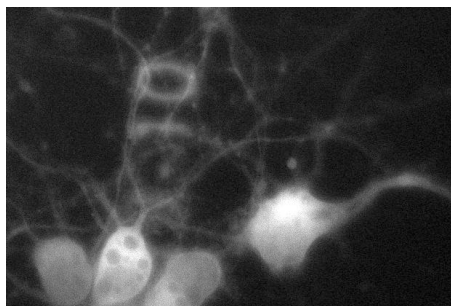


**Figure 8.15:** Cortical neurons have been transfected with GCaMP and imaged with the upright fluorescence microscope while recording a single spot measurement with the SPRM

This measurement series was started in order to investigate whether or not action potentials in neurons can be measured with SPRM. For this neurons were cultured on PLL-coated SPRM substrates.

In order to manipulate the cells to express GCaMP, a calcium indicator containing green fluorescent protein (GFP) [84], Timm Hondrich executed a viral transfection of the cells (see section 11.4). The advantage of using GCaMP instead of Fluo-4 which was used in the cardiomyocyte experiments (see chapter 7) is that GCaMP can be found in the cell

membrane after the transfection while the surrounding media is not affected. This reduces the background fluorescence.

The setup has been prepared for the experiments in the same manner as for the cardiomyocyte experiments (see chapter 7). Additionally, the ND filter which is usually used to reduce the laser light intensity in the setup has been removed in order to reduce the exposure time for each BFP image.

First, an adhering area at the cell-substrate interface was localized in the live-imaging. Afterwards, a single spot measurement was started. After 60 seconds, the Andor camera recording was started. The first time step was set in the same manner as described in chapter 7. Afterwards the cell was exposed to the excitation light. After another minute, a second time stamp was set.

Afterwards, the measurement series were supposed to be analyzed and potential changes in the RI signal or in the distance signal were supposed to be correlated with the fluorescence intensity.

Unfortunately, several problems occurred during the experiment. The upright microscope is installed on a X-Y-stage which broke during the day of the experiment so that the position of the microscope could not be fixed anymore, but it was moving when the filter bench was moved in order to set the time steps. Additionally, none of the recorded fluorescence measurements showed significant changes in the fluorescence intensity that one would expect during an action potential.

I strongly recommend this experiment be repeated. If a correlation in the RI change and a peak in the fluorescence could be found, this would finally explain why several groups have observed changes in the plasmon resonance angle during electrical activity of the cells [74, 75]. So far, this has always been explained by an impedance coupling. As the cell-substrate distances that have been presented in this thesis are

## *8 Neuron experiments*

orders of magnitude higher than the Debye length (see section 7.4.1), this explanation seems rather unlikely.

Before repeating this experiment, I suggest to modify the setup as shown in Figure 7.11 in order to improve the temporal resolution and the RI sensitivity.

# Discussion

## 9.1 Development of the technique

### 9.1.1 What has been done?

In this thesis, an improved SPRM setup was developed containing several new imaging modes. The projector based live-imaging allows for resolving of small cellular structures such as costameric adhesion areas in cardiomyocytes as well as thin dendrites in neurons which was not possible with the original laser-based live-imaging mode due to strong speckle noise. The improved live-imaging allows for the observation of larger cell types due to the increase of the FOV from  $35 \times 35 \mu m$  to  $50 \times 50 \mu m$ .

Thanks to the establishment of several image correction algorithms, inhomogeneous background illumination in the projector-live imaging can be easily compensated for.

The newly introduced bright field mode allows imaging of the exact same FOV as the SPRM live-imaging mode which helps with the interpretation of the live-images as well as the scanning results e.g. by correlating the positions of cell organelles in the bright field mode and the RI profile obtained from the scanning mode.

In order to study cell dynamics, new acquisition modes have been established for the scanning SPRM: the single-spot measurement and the time dependent area scan. These two new modes have been shown to be a powerful tool for the study of the dynamics at the interface of beating cardiomyocytes.

To combine the dynamic SPRM scans with an established method for characterizing action potentials, an additional fluorescence microscope has been built into the setup and an experimental procedure to set time stamps into both measurements simultaneously was established. This facilitates the correlation of the new SPRM techniques with a well established procedure.

In order to improve the accuracy of the distance measurements in scanning SPRM, the analysis routine was completely redesigned with a separated analysis of the RI and the cell-substrate distance. This could be shown to improve the accuracy in the distance measurement by a factor of 25. As a result, the distance measurement reaches an accuracy of up to  $1.5\text{ nm}$  in a cell measurement.

In order to validate the experimental results, many different validation experiments have been shown. First, the angle measurement was verified based on the generation of an interference pattern inside the objective. Afterwards, the RI measurement could be validated by the measurement of mixtures of DMSO and water in different ratios. And finally, the distance measurement could be validated through the measurement of a silica bead. Based on this experiment, it was possible to estimate the limits for the distance measurements to  $\sim 200\text{ nm}$ , while the RI measurement seems to work even at larger distances. This could be shown to be caused by different penetration depth for different incident angles.

The design of SPRM chips with unique markers which allow for a clear identification of each position on the chip, has been shown to facilitate the correlation of SPRM with FIB measurements of the same cells.

## 9.1.2 What remains to be done?

Regarding the interpretation of the analysis results, it would be helpful to redesign the analysis software in such a way that the individual reflectance profiles would be accessible for each scanning point. Storing these reflectance profiles for each image during the analysis would increase the volume of the output-files enormously. Therefore, it might be a good alternative to implement a routine which allows the user to click on the point of interest within the analyzed RI profile or distance profile and based on this graphical input, the software would repeat the analysis of this point and create the reflectance profile for this scanning point.

In order to be able to interpret the analyzed data correctly, it would be necessary to characterize the penetration depth as a function of the incidence angle. The simulation as well as the measurements in section 6.3 suggest that the penetration depth around the critical angle is much higher than at the resonance angle. While the penetration depth around the resonance angle could be estimated to  $150 - 200 \text{ nm}$ , it was not possible around the critical angle based on this measurement because the sphere-substrate distance was too low within the scanned area. Scanning a microlens with smaller diameter and therefore larger sphere-substrate distances within the scanning area could solve this issue.

Another approach, which might result in less noisy signals is based on using optical glue. For this purpose, one could deposit a thin layer of optical glue with the same RI as the cytosol (e.g. NOA136) on an SPRM sample. Either different amounts of glue could be spincoated on different SPRM samples in order to realize glue layers of different but homogeneous thicknesses or a relatively thick layer of optical glue could be deposited on a substrate and a sphere could be placed on top of it during the curing process. In order to avoid internal reflections

in the SPRM measurements, the sphere would have to be removed after curing. Therefore, the sphere would need to be coated in such a way, that it does not stick to the glue itself. In order to produce such a sample, it needs to be considered, that the mentioned optical glues require specific conditions for curing (oxygen-free atmosphere as well as exposure to UV light).

In order to measure action potentials of neurons, the setup would need to be complemented by an additional high-speed camera as described in chapter 7. After each alignment of the setup, the positions of the cameras would have to be calibrated by measuring a well defined signal such as the diffraction pattern as described in section 6.1.

Maybe, it could be helpful to complement the setup with a second laser light source with a different wave length in order to analyze the data with higher accuracy. The data analysis would then require the fitting two different profiles and could therefore decrease the ambiguity of this process, because the fitting of the reflectance curves is not always very clear as the curves are often noisy.

### 9.1.3 Problems and issues

#### Problems in sample production

In the beginning of this work, most of the samples revealed defects in the gold layer when exposed to an aqueous media (see appendix, Figure 12.3). These samples were produced with titanium as the adhesion layer. The samples became more stable when the titanium layer was changed for a chromium layer.

It has been found, that chromium layers have a high surface roughness ( $\sim 20\text{ nm}$ ) when the chromium is deposited through evaporation.

Therefore, the deposition of the chromium layer was changed to a sputter deposition. Here, chromium layers of 3 nm can be produced with a surface roughness of  $< 1$  nm. Afterwards the gold layer is evaporated according to protocol described in section 11.1.2. After establishing this protocol, most of the chips were stable even over weeks in cell culture. However, for unknown reasons sometimes an entire batch of chips shows small defects in the surface and is therefore not stable in culture.

In general, substrates should be used within two weeks after production because the gold detaches under normal atmosphere after a couple of weeks.

In some area scans, strong deviations of the reflectance profiles have been found. This can be caused by inhomogeneities of the gold layer within the measured area which compromises the fit-quality.

### **Problems during the cell culture**

It was observed that the neurons did not attach well for culture times longer than one week on the SPRM substrates, when PLL aliquots were used which were previously frozen. As the number of observed samples is not high enough, this could just be a coincidence. However, when the samples have been coated according to the protocol described in section 11.2.2, which was established for the gold-surfaces, most of the cells stayed attached (culture times of up to 6 weeks were successful).

It has been observed that many cells detach during experiments when the lid of the dish was not sealed with parafilm. This is expected to be caused by the evaporation of the culture media and successive changes in the osmolarity of the media.

## **Problems during the measurements**

The point-like structures which are observed in the RI as well as the distance profiles (see e.g. Figure 8.14) are caused by a problem in the recording routine. The scanning routine is supposed to take one BFP image at each scanning point in each scanning row. When one row has been finished, the stage moves to the starting point in the next row. As it is always scans from left to right, the stage needs to move across the entire ROI before starting the measurement of the next row. Unfortunately, it continues recording while moving across the ROI. This causes additional BFP images taken during the movement of the stage and result in the points scatter through the plots. This could be solved with improved path planning and/or better coordination between microstage and data capture.

## **Problems in the analysis**

During the analysis, there are many different parameters which need to be set manually for each data extraction, fitting of the average data and the optimization algorithm. It is very important to consider that each of these parameters can potentially change the analyzed RI values and distances. Therefore, it is important to check each of the saved single-point reflectance curves for the fitting quality and adapt the fitting parameters accordingly afterwards. This can mean, that a scan needs to be analyzed more than 10 times in a row before a good fit is found.

Therefore, it might be helpful to find reliable fitness criteria and improve the fitting algorithm regarding its speed, transparency and role in the analysis process.

## Problems in understanding of the system

As mentioned before, the interpretation of the growth cone measurements is not yet possible because the reflectance profiles for the critical areas are not accessible in the current version of the analysis tools. It needs to be kept in mind, that the analysis of such a thin cellular structure might stay impossible as the thickness of the growth cone might be lower than the penetration depth.

### 9.1.4 Comparison with other techniques

In this section SPRM will be compared to the other optical methods which are used to characterize the cell-substrate interface (see chapter 3).

In order to enable an intuitive comparison of the methods without repeating the working principles, advantages, disadvantages and limitations, the comparison is reduced to a small number of criteria. These criteria have been chosen to be the lateral and axial resolution, whether or not a technique facilitates the resolution of intracellular structures and the dynamics of the cells, and whether or not it works in vitro and label-free. Table 9.1 allows for the comparison of all the methods presented in chapter 3 and SPRM regarding these criteria at one glance. If there is any limitation to the methods which is not covered by the chosen criteria, this limitation is listed separately.

The table shows that SPRM is the only method which satisfies all the chosen criteria. Regarding the lateral resolution, SPRM is only surpassed by FIB-S(T)EM while the axial resolution of SPRM is higher than the axial resolution of FIB-S(T)EM. However, it is possible to resolve small adhesion areas and cavities at the cell-substrate interface with FIB-S(T)EM, which would be averaged out in SPRM analysis. At

## 9 Discussion

method	XY-res	Z-res	ICS	dyn	iv	lf	limitations
RICM	DL	4 nm	-	✓	✓	✓	knowledge of RI necessary
FLIC	0.9 $\mu m$	0.61 nm	-	✓	✓	-	assuming constant distance
	2.5 $\mu m$	0.31 nm	-	✓	✓	-	over several fields
	6 $\mu m$	0.06 nm	-	✓	✓	-	
MIET	200 nm	3 nm	-	✓	✓	-	
FIB	$\sim 10 nm$	$\sim 10 nm$	✓	-	-	-	extensive preparation
SPRM	$\sim 190 nm$	$> 1.5 nm$	✓	✓	✓	✓	only well defined at soma

**Table 9.1:** Comparison of different optical techniques for the investigation of the cell-substrate interface. Abbreviations: res: resolution; ICS: resolution of intra cellular structures; dyn: resolution of cell dynamics; iv: *in vitro*; lf: label-free

the same time, potential artifacts which might be introduced by the extensive preparation for FIB need to be taken into account.

As the axial resolution of SPRM strongly depends upon the details of the sample composition, it is impossible to compare its axial resolution to those of the other techniques. In the best-case scenario, SPRM can reach an axial resolution of 1.5 nm with the current setup. In contrast to the other techniques, its resolution decreases strongly with increasing cell-substrate distance. This resolution is currently limited by the pixel density of the recording camera and can be increased by an optical zoom-in (see section 5.4.3).

Even at its optimal resolution, SPRM can be surpassed by FLIC. Due to its low lateral resolution FLIC might give better results regarding the measurement of the distances of very homogeneous interfaces, but SPRM might give more accurate results in case of a curved cell-membrane as its lateral resolution is much higher.

MIET has a comparable lateral and axial resolution to SPRM at its sweet-spot, but it cannot resolve intracellular structures and requires labeling which might alter the cell behavior and is therefore not as well suited for long-term investigations as SPRM.

RICM is the only other label-free technique but its accuracy depends in a similar manner upon the knowledge of the RI of the last layer as SPRM. Therefore, the given axial resolution can only be reached for very simple sample setups (buffer-filled vesicles) or if one can realize the combination with a different technique which facilitates the simultaneous measurement of the cellular RI at the interface with a high lateral resolution.

It shall be pointed out again, that SPRM is only well defined if the thickness of the cytosol in the layer structure is larger than the penetration depth within the entire angle spectrum. SPRM shows obvious problems in the analysis of the cell-substrate distance of thin cellular structures such as dendrites and growth cones. Even though FLIC has been used to analyze neuronal growth cones [11], the accuracy in the distance measurement might be affected when studying very thin structures because the interaction between the dye molecules and the excitation light might not be limited to the basal cell membrane but the dye molecules in the upper cell membrane might also contribute to the signal. The same concern shall be expressed regarding the study of growth cones with MIET. As RICM shows problems in the accurate analysis of the cell-substrate distance if the RI of the cytosol is unknown, this technique does not provide a solution to the problem either unless combined with a RI measurement.

In conclusion, it can be said, that SPRM is the only method which satisfies all the criteria which were defined for the study of the cell-substrate interface: label-free, *in vitro*, with nanometer accuracy and suitable for long-term studies. It even allows for the study of cell dynamics and intracellular structures which lie in the evanescent field. It would be advisable though to improve its axial resolution using a different recording path.

Compared to FIB-S(T)EM, it shows many advantages because it works

in vitro and does not require extensive preparation of the samples. But the lateral resolution of SPRM is a draw-back compared to FIB. Therefore, the correlative SPRM-FIB-STEM measurements are very valuable. They allow the artifacts, which might have been introduced by the preparation protocols to be determined, but also allow for the visualization of small adhesion structures or cavities at the cell-substrate interface which are averaged out in SPRM distance profiles.

## 9.2 Biological measurements

### 9.2.1 What has been measured?

In this thesis, it has been shown, that the dynamics of the cell-substrate distance as well as the intracellular RI can be measured at single points or along the entire cell-substrate interface of cardiomyocytes. The measured signals could be correlated with fluorescence calcium imaging which proves that the origin of these measured dynamics is indeed caused by action potentials.

As a result of the time-dependent area scans not only 3D plots of the basal cell membrane are generated but the 3D representation has been animated based on the scanning results. This visualization helps to get an intuitive understanding of the effects of the cell contraction on the membrane distance.

The structures at the interface of said cardiomyocytes observed in the live-imaging mode could be correlated with the positions of costameric adhesion sites and filaments of the cytoskeleton due to immunostaining.

Apart from the dynamics measurements, SPRM was used to determine the effect of chemical fixation on the cell-substrate distance at the neuronal membrane. Additionally, these measurements were correlated with FIB allowing artifacts introduced by the cell preparation to be identified for the first time.

From the measurement of a neuronal growth cone it could be seen that accurate distance measurements are limited to the soma of cells as the multi-layer structure which is assumed in the analysis procedure describes an infinitely thick cytosolic layer. Therefore, measurements of thin cellular structures are not possible without risking large errors.

### 9.2.2 What could be measured in the future?

Without any modification of the setup, it is possible to investigate the cell-substrate distance as a function of time. This means that by measuring the same cells on subsequent days, it would be possible to determine whether or not the cell-substrate distance increases due to the secretion of extracellular matrix and how much. This would be of great interest for the field of bioelectronics where the cell-substrate distance is one of the bottle necks towards a good extracellular recording of action potentials. It would also give insights into the development of cell-substrate contacts (e.g. focal adhesion points) over time.

In order to understand the origin of the mesh-like structures which are found in the live-imaging, it might be a good idea to correlate SPRM with confocal fluorescence imaging for neuronal cells. A Z-stack measurement taken with a confocal microscope after a specific immunostaining of actin might give insights into the structure of the actin cortex.

Another interesting application of the technique is the study of biomimetic approaches in order to reduce the cell substrate distance. For this the substrate could be coated by a combination of a lipid bilayer and specific membrane proteins which enable the establishment of cell adhesion complexes resembling cell-cell contacts *in vivo*. This approach is called “artificial synapse” and is of great interest to the field of bioelectronics as it is unclear whether or not such an approach could reduce the cell-substrate distance.

By adding a high speed camera to the setup as suggested in Figure 7.11, one could study whether or not the action potentials influence the RI of the cytosol in neurons or if they influence the cell-substrate distance by cellular swelling. These insights would be very valuable for the field of SPRM, where the origin of the shift in the resonance angle during electrical activity cells has been speculated about for the past decade. Also, investigating the spontaneous activity of neuronal networks label-free and non-invasively in long-term experiments would be of enormous value for many biological and medical questions. In the area of Alzheimer’s disease, SPRM could be very helpful for the study of spontaneous activity, as well as the morphology and the intracellular RI before and after the exposure to Amyloid beta in order to understand how neurons react to the presence of these proteins and the building of fibrils at the membrane.

# Abbreviations

**BFP** Back focal plane

**CaM** Calmodulin

**DIV** Day *in vitro*

**ECM** Extracellular matrix

**FIB** Focused ion beam (sectioning)

**FLIC** Fluorescent interference contrast microscopy

**FOV** Field of view

**fps** Frames per second

**FRET** Förster resonance energy transfer

**GCaMP** A specific, genetically encoded calcium indicator

**GFP** Green fluorescent protein

**MIET** Metal induced energy transfer

**NA** Numerical aperture

**PALM** Photo-activated localization microscopy

**PLL** Poly-L-Lysine

**PBS** Phosphate-buffered saline

**RI** Refractive index

**RICM** Reflection interference contrast microscopy

**ROI** Region of interest

## *10 Abbreviations*

**RT** Room temperature

**SEM** Scanning electron microscopy

**SERCA** Sarco/endoplasmic reticulum Ca<sup>2+</sup>-ATPase

**SPR** Surface plasmon resonance

**SPRM** Surface plasmon resonance microscopy

**STEM** Scanning transmission electron microscopy

**STORM** stochastic optical reconstruction microscopy

**TEM** Transmission electron microscopy

**TMM** Transfer matrix method

# Protocols

## 11.1 Sample production

### 11.1.1 Chip design

The unique markers on the substrate which allow for the identification of each position on the substrate are made from photoresist. Therefore, a mask was designed which allows for the partial development of the photoresist (see Figure 11.1). The structure of the mask was coded in *LUA* (see section 11.7.1). The development protocol is given in section 11.1.2.

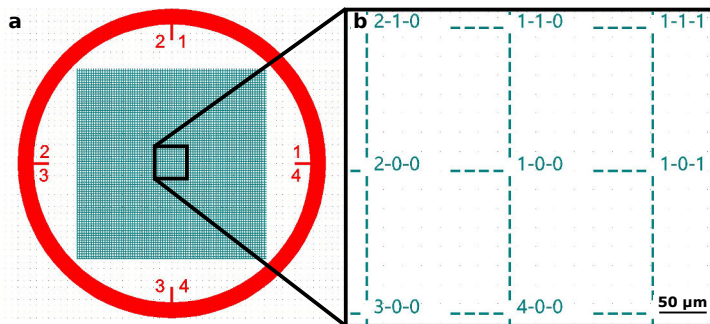


**Figure 11.1:** Mask for the markers made from photoresist. a) The mask shown here consists of a grid with unique markers representing a coordinate system. The quadrants are labeled from 1 to 4 counter clockwise. b) The coordinate system is organized in the following way: quadrant - row - column (counting from the center outwards). This coordinate system allows for identification of the position of each cell cultured on the substrate.

## 11.1.2 Layer deposition

### Cleaning of substrates

Protocol established and executed by Michael Pömpers

Used substrates: High index coverslips (Olympus, HIGH INDEX-CG)

Clean substrates with ethanol, acetone and isopropanol (5 min each).

O<sub>2</sub>-plasma cleaning

machine: Barrel Reactor TePla Gigabatch 310M

parameters: 200 W, 50 sccm, 5 min

Create N<sub>2</sub>-atmosphere in the sample box and weld in plastic foil.

### Chromium deposition

Protocol established and executed by René Borowski, PGI-7

3 nm Cr sputtered

machine: Leybold Univex 450C

parameter: 300 W DC, 60 sccm Argon ( $2.1 \cdot 10^{-2}$  mBar), 5.3 s

### Gold deposition

Protocol established and executed by Michael Pömpers

Gold evaporation directly after the chromium deposition

machine: PLS-570

parameters: 38nm Au

### Lithography

Protocol established and executed by Michael Pömpers

Baking of samples 5 min, 130°C

Spincoating: AZ5214E: 4000 rpm

Baking of samples 1 min, 110°C

Mask Aligner MA4: 2.3 s, 75 mW/cm<sup>2</sup>, hard contact

machine: Süss MA/BA 8

Development: MIF326, 45 s, stop in DI-water ~ 5 min until guide value > 10 MOhmcm

Baking of samples 10 min, 135°C

Create N<sub>2</sub>-atmosphere in the sample box and weld in plastic foil.

### 11.1.3 Sample assembly

Mix the two components of the adhesive (EPO-TEK® 302-3M) in ratio 1:0.45 in a tube.

Vortex the mixture for 5 min.

Turn the polystyrene dish upside down.

Use a toothpick to apply small droplets of glue all around the opening.

Spread the glue over the surface.

Carefully pick up a substrate with tweezers.

Place the substrate (gold facing the glue) over the center the hole.

If the amount of glue is right, the substrate can now be slid easily within the glue.

Slide and rotate the substrate a bit in order to spread the glue homogeneously within the cleft.

Make sure that the center of the substrate never gets in contact with the glue.

Leave the sample for curing turned upside down for a day.

Use the substrates for measurements within 2 weeks, if possible (gold detaches over time).

When all the steps are completed, the sample should look as shown in Figure 11.2.

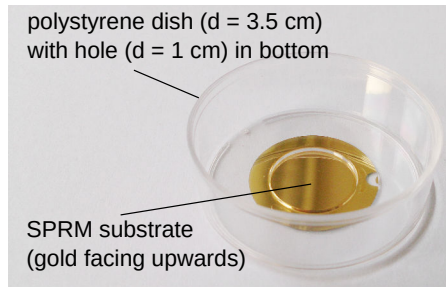


**Figure 11.2:** SPRM chip is glued with medical epoxy to the bottom of the polystyrene dish.

## 11.2 Coatings

### 11.2.1 Fibronectin coating

For coating, dilute Fibronectin in PBS w/o Ca (1:100).

Incubate 1 ml of coating solution for 1h at RT.

Aspirate most of the solution (just keep the bottom of the dish covered).

Wash with PBS w/o Ca once.

Aspirate most of the solution.

Plate cells directly afterwards.

### 11.2.2 PLL coating

The PLL powder is stored at  $-20^{\circ}\text{C}$  until aliquots are prepared.

For the aliquots, 1 mg PLL is dissolved in 1 ml MilliQ, and stored at  $4^{\circ}\text{C}$  afterwards.

For coating, dilute PLL in MilliQ (1:100).

Incubate 1 ml of coating solution for 1h at RT.

Aspirate most of the water (just keep the bottom of the dish covered).

Add 2 ml HBSS.

Keep at 4°C over night.

Replace HBSS by 1.5 ml neurobasal media.

Keep sample in the incubator before cells are plated.

## 11.3 Cell culture of cardiomyocytes

Cor.4U cells are cardiomyocyte-like cells which are differentiated from human induced pluripotent stem cells (iPSC). These cells have been purchased as in frozen vials from Axiogenesis AG with specific culture media.

### 11.3.1 Thawing, plating, maintenance

The protocol has been established and published by Axiogenesis AG. The only adaptation of the protocol is adding 10  $\mu$ L Gentamicin, (from Sigma, G1397) per 10 mL media. Pipette 3 ml media in “tube A” and 1 mL media “tube B”.

Warm tubes A and B to 37°C.

Transfer the frozen vial quickly from liquid nitrogen directly to a water bath at 37°C.

Thaw the cells until only a small ice clump is visible ( $\sim 2$  min).

Spray the vial with ethanol and bring it into the cell culture bench.

Pipette the cell suspension into tube A.

Rinse the vial with the content of tube B and add it to tube A.

Plate the cells directly on the fibronectin coated SPRM substrates.

## Maintenance

Replace the media every 3 days completely with 2.5 *mL* warm culture media.

### 11.3.2 Calcium imaging of cardiomyocytes

Add Fluo-4, AM to the culture media in the dish, achieving a final concentration of 4  $\mu$ M.

Cover the sample with aluminum foil to protect from light.

Incubate for 20 min before imaging.

## 11.4 Cell culture of neurons

### Culture media

10 *mL* Neurobasal Medium (from Life Technologies, 21103049)

100  $\mu$ L B-27 supplement (from Life Technologies, 17504044)

25  $\mu$ L L-Glutamine (from Life Technologies, 25030024)

10  $\mu$ L Gentamicin, (from Sigma, G1397)

### Maintenance

200 000 primary neurons are suspended in 1 *mL* and added to the 1.5 *mL* media which was added to the substrate in advance (see section 11.2.2).

Replace the entire media 3h after plating.

Replace half the volume of the media each 3 or 4 days (alternating).

## SPRM measurements

Seal the lid of the sample with parafilm as soon as the cells are taken out of the incubator to prevent evaporation of the culture media.

### **For long-term measurements:**

If neurons need to go back into the incubator after an SPRM measurement, an additional media change is done after each measurement. After this adaptation of the cell culture protocol, the number of cells surviving the long-term measurement series increased. The idea was to reduce the number of dead cells in the culture because it could be observed that some of the cells detached from the substrate during the experiments.

## Transfection

The protocol was executed by Timm Hondrich.

Cells have been transfected with rAAV9 Syn.GCaMP6f.WPRE.SV40 on DIV 3 with an end concentration of  $\sim 1.44 * 10^{10}$  genome copies (GC)/mL.

In detail, 1  $\mu$ L of rAAV9 Syn.GCaMP6f.WPRE.SV40 with a titer of  $3.6 * 10^{13}$  GC/mL was mixed with 2.5 mL Neurobasal medium containing additional 1% B27 supplement, 0.25% Glutamin and 0.1% Gentamicin (NB+).

On DIV 3, the culture medium was replaced entirely with this freshly prepared mixture.

On DIV7, the medium was again exchanged entirely with 2.5 mL of fresh NB+ medium.

## 11.5 Preparation of samples for FIB

### 11.5.1 Fixation with glutaraldehyde

Wear gloves throughout the entire protocol and work under the chemical hood. Collect the liquid and the solid waste separately.

Dissolve 640  $\mu\text{L}$  glutaraldehyde in 10  $\text{mL}$  PBS.

Warm the solution until it becomes homogeneous.

Warm 10  $\text{mL}$  PBS.

Wash samples 3x with warm PBS (make sure it does not dry out).

Aspirate the PBS, add glutaraldehyde solution to the sample.

Incubate for 30 *min*

Aspirate the solution and wash 3x with PBS.

Fill each sample with 3  $\text{mL}$  PBS, seal the lid with Parafilm.

Keep at 4°C in the fridge.

### 11.5.2 Heavy metal staining and resin embedding

The entire preparation of the fixated cells for the FIB-SEM investigation was executed by Silke Seyock according to the following protocol.

Staining with Osmium and Uranylacetate

- Rinse two times with MilliQ
- Add 1% OsO<sub>4</sub> (stock: 2%) in Cacodylate buffer, leave for 2 h on ice
- Rinse 5x with MilliQ, 2 min each
- Leave in 1% Tannic acid (0.1 g in 10 ml MilliQ) for 30 min at RT
- Rinse 5x MilliQ, 2 min each

## 11.5 Preparation of samples for FIB

- Leave samples overnight in 2% Uranylacetate at 4°C
- Rinse 5x MilliQ, 2 min each

### Resin recipe (prepare fresh)

- mix 20 ml DDSA with 12.5 ml of EPON 812
- mix 17.3 ml MNA with 15.2 ml of EPON 812
- mix 32.5 ml of both solution together
- add 1.3 ml of DMP30
- stir for 1 h

### Ethanol Dehydration

- 5 min 10% EtOH
- 5 min 30% EtOH
- 5 min 50% EtOH
- 15 min 70% EtOH
- 5 min 90% EtOH (3x)
- 5 min 95% EtOH (3x)
- 5 min 100% EtOH

Pause step: parafilm, 4°C for max. 2 week

### Resin embedding

- EtOH (3) : Resin (1) 3h at RT (e.g. 15ml EtOH: 5ml Resin)
- EtOH (2) : Resin (1) 3h at RT
- EtOH (1) : Resin (1) overnight at RT
- EtOH (1) : Resin (2) 3h at RT
- EtOH (1) : Resin (3) 3h at RT
- Pure Resin 3h at RT
- Tilt the well, let the resin settle down and take the sample carefully
- EtOH splash over the sample (crucial step) with a plastic pipette; from

the sides of the dish

- Put immediately the sample in the oven at 60°C, at least for 12 h

## 11.6 Fixation and staining for immunofluorescence

### 11.6.1 Fixation and staining

- Wash with CB at 37°C (section 11.6.3)
- Fixate with 3, 7% Formaldehyde in CB, at 37°C. Incubate for 20 *min*
- Wash with 30 *mM* Glycine in CB at room temperature (RT); 5 *min*
- Breaking of the membrane: 1 – 3% TritonX100-solution in CB. Incubate for 2 – 3 *min* at RT
- Wash with CB at RT. Incubate for 5 *min*
- Blocking of unspecific binding sites with 5% milk powder in CB. Incubate 30 – 45 *min* at RT
- Primary antibody: AB 1:100 to 1:200 in CB + 1% milk powder. Incubate 45 *min* at RT (200 – 300  $\mu$ L)
- Washing 3x with 1 – 2% milkpowder in CB. Incubate 5 *min* each time
- Sekundary antibody: 1:100 to 1:200 in CB + 1% milkpowder. Incubate for 45 *min* at RT (200 – 300  $\mu$ L)
- Washing 3x with CB at RT. Incubate for 5 *min* each time

## 11.6.2 Antibodies and additional stainings

### For staining of $\alpha$ -Actinin:

Primary antibody:

Monoclonal Anti- $\alpha$ -Actinin (Sarcomeric) antibody produced in mouse clone EA-53

Secondary antibody:

Cy3 antimouse produced in goat, 546 nm (excitation)

### For staining of vinculin:

Primary antibody:

Anti-vinculin produced in rabbit

Secondary antibody:

Anti-rabbit Alexa 488 produced in chicken, 488 nm

### For staining of actin:

Alexa Fluor<sup>TM</sup> 633 Phalloidin, 633 nm

### For staining of the nucleus:

DAPI, 358 nm

## 11.6.3 CB Buffer

CB buffer was prepared by Nico Hampe according to the following protocol:

150 mM NaCl

5 mM MgCl<sub>2</sub>

5 mM EGTA

5 mM Glucose

10 mM MES 2-(N-morpholino)ethanesulfonic acid (pH 6,1)

1000 mg Streptomycin for 1L buffer

Store at 4°C

## 11.7 Scripts

### 11.7.1 Grid markers on chips

The mask consists of four quadrants which have been coded separately in LUA and merged in CLEWIN.

First, a symbol was defined in CLEWIN, which consists of the basic unit of the grid (dashed lines in X- and Y-direction). The dimensions of this basic unit are  $150\ \mu\text{m} \times 150\ \mu\text{m}$ . This symbol is defined as *box150*, which is used in the LUA script afterwards.

Quadrant 1:

```
width = 150
height = 150

n_rows = 40
n_cols = 40

transform = identity();

n = 0
for irow=0,n_rows do
  for icol=0,n_cols do
    str = string.format("1-%d-%d", irow, icol)
    text(str, transform)
    symbol("box_150", transform)
    transform = translate(transform, width, 0)
  end
  transform = translate(transform,
                        -(n_cols+1) * width,
                        height)
end
```

The code was slightly adapted for the other three quadrants.

## 11.7.2 Background correction

In order to reduce the inhomogeneous background illumination in the live-imaging video of a beating cardiomyocyte, a mean background image was generated and subtracted pixelwise from each frame. The mean background image was generated by averaging over several images, which were recorded while moving the sample laterally.

```
#!/bin/bash
#
# Subtract mean from video, increase contrast

INPUT=$1
OUTPUT=${INPUT%.*}

# Extract all frames from video and determine mean
ffmpeg -i $INPUT frames_%d.png
convert frames_*.png \
        -evaluate-sequence mean \
        mean.png

# Subtract mean from video
ffmpeg -i $INPUT -i mean.png \
        -filter_complex \
        "blend=all_mode='difference128'" \
        -r 25 -f mpeg -vcodec mpeg1video \
        -qscale:v 5 -y \
        ./"$OUTPUT"_subtracted.mpg
```

## 11 Protocols

```
# Equalize contrast of subtracted video
ffmpeg -i "$OUTPUT"_subtracted.mpg \
  -filter_complex "eq=contrast=2" \
  "$OUTPUT"_subtracted_contrast.mpg

# Place videos side by side for comparison
ffmpeg -i $INPUT \
  -i "$OUTPUT"_subtracted_contrast.mpg \
  -filter_complex \
    "[0:v:0]pad=iw*2:ih[bg]; [bg][1:v:0]overlay=w" \
  "$OUTPUT"_comparison.mpg

# tidy up
rm frames_*.png
```

### 11.7.3 Animation of contracting cardiomyocyte

First, this script was executed generating images of the 3D-SPRM profile of a beating cardiomyocyte from different perspectives and different states during the contraction. Afterwards, these pictures were sorted by hand and merged to a video using FFmpeg.

```
close all
%Read the dat file containing x-y-and n (x,y,ri)
  information and read each of the
%columns seperately
RIdata = importdata('\material analysis\
  n_max_central.dat');
x = RIdata(:,1);
```

```

y = RIdata(:,2);
ri = RIdata(:,3);
%generare a grid in x-y plane
[X , Y] = meshgrid(min(x):.1:max(x) , min(y):.1:max
    (y));
RI = griddata(x, y, ri , X , Y , 'natural');
%Read the dat file containing x-y-and Zs (Zmin,
    Zaverage - std, Zaverage, Zaverage+std, Zmax)
    information and read each of the
%columns seperately
threeDdata = importdata('\distance profiles\
    d_stats_central.dat');
Zmin = threeDdata(:,3);
Zavminusstd = threeDdata(:,4);
Zav = threeDdata(:,5);
Zavplusstd = threeDdata(:,6);
Zmax = threeDdata(:,7);
Zavgrid = griddata(x , y , Zav , X , Y , 'natural')
    ;
Zmaxgrid = griddata(x , y , Zmax , X , Y , 'natural
    ');
Zmingrid = griddata(x , y , Zmin , X , Y , 'natural
    ');
Zavminusstdgrid = griddata(x , y , Zavminusstd , X
    , Y , 'natural');
Zavplusstdgrid = griddata(x , y , Zavplusstd , X ,
    Y , 'natural');

%make a series of plots with steps of 1 degree
    rotation. For better
%understanding of the profile, use lines

```

## 11 Protocols

```
for m = 1:180
    figure
    contour3(X,Y,Zmaxgrid,100)
    colormap(flipud(parula))
    az = 140 + m;
    el = 69;
    xlabel(['$X \lbrack \mu m \rbrack $'],'
           interpreter','latex', 'FontSize', 16)
    ylabel(['$Y \lbrack \mu m \rbrack $'],'
           interpreter','latex', 'FontSize', 16)
    zlabel(['$Z \lbrack n m \rbrack $'],'
           interpreter','latex', 'FontSize', 16)
    zlim([60 200])
    view(az, el);
    hold on
    contour3(X,Y,Zmaxgrid,100)
    hold off
    saveas(gcf,strcat('O:\Arbeits Gruppen\
                     Neuroelectronics\People\Kreysing_Eva\
                     Experiments\SPRresults\SPRDATA_160518\
                     output_2017-09-26_11-23-55 (160518_153729)\
                     threeDfigures\' , num2str(m), 'max.png'), '
           png');
    close(gcf)
end

close all
%Generate plots for demonstration of the cell
    beating Zmin
figure
```

```

contour3(X,Y,Zmingrid,100)
colormap(flipud(parula))
az = 140;
el = 69;
zlim([60 200])
view(az, el);
xlabel(['$X \lbrack \mu m \rbrack $'],'interpreter',
      ', 'latex', 'FontSize', 16)
ylabel(['$Y \lbrack \mu m \rbrack $'],'interpreter',
      ', 'latex', 'FontSize', 16)
zlabel(['$Z \lbrack n m \rbrack $'],'interpreter',
      ', 'latex', 'FontSize', 16)
hold on
%contour3(X,Y,Zmaxgrid,100)
%hold off
saveas(gcf, strcat('O:\Arbeits Gruppen\
  Neuroelectronics\People\Kreysing_Eva\Experiments
  \SPRresults\SPRDATA_160518\output_2017-09-26_11
  -23-55 (160518_153729)\threeDfigures\', 'min.png
  '), 'png');
close(gcf)

%Generate plots for demonstration of the cell
  beating Zav-std
figure
contour3(X,Y,Zavminusstdgrid,100)
colormap(flipud(parula))
az = 140;
el = 69;
zlim([60 200])
view(az, el);

```

## 11 Protocols

```
xlabel(['$X \lbrack \mu m \rbrack $'],'interpreter',  
      ', 'latex', 'FontSize', 16)  
ylabel(['$Y \lbrack \mu m \rbrack $'],'interpreter',  
      ', 'latex', 'FontSize', 16)  
zlabel(['$Z \lbrack n m \rbrack $'],'interpreter',  
      ', 'latex', 'FontSize', 16)  
%hold on  
%contour3(X,Y,Zmaxgrid,100)  
%hold off  
saveas(gcf, strcat('O:\Arbeits Gruppen\  
      Neuroelectronics\People\Kreysing_Eva\Experiments  
      \SPRresults\SPRDATA_160518\output_2017-09-26_11  
      -23-55 (160518_153729)\threeDfigures\',' '  
      avminstd.png'), 'png');  
close(gcf)  
  
%Generate plots for demonstration of the cell  
      beating Zav again  
figure  
contour3(X,Y,Zavgrid,100)  
colormap(flipud(parula))  
az = 140;  
el = 69;  
zlim([60 200])  
view(az, el);  
xlabel(['$X \lbrack \mu m \rbrack $'],'interpreter',  
      ', 'latex', 'FontSize', 16)  
ylabel(['$Y \lbrack \mu m \rbrack $'],'interpreter',  
      ', 'latex', 'FontSize', 16)  
zlabel(['$Z \lbrack n m \rbrack $'],'interpreter',  
      ', 'latex', 'FontSize', 16)
```

```

%hold on
%contour3(X,Y,Zmaxgrid,100)
%hold off
saveas(gcf, strcat('O:\Arbeits Gruppen\
    Neuroelectronics\People\Kreysing_Eva\Experiments
    \SPRresults\SPRDATA_160518\output_2017-09-26_11
    -23-55 (160518_153729)\threeDfigures\' , 'av.png'
    ), 'png');
close(gcf)

%Generate plots for demonstration of the cell
    beating Zav+std
figure
contour3(X,Y,Zavplusstdgrid,100)
colormap(flipud(parula))
az = 140;
el = 69;
zlim([60 200])
view(az, el);
xlabel(['$X \lbrack \mu m \rbrack $'],'interpreter',
    ', 'latex', 'FontSize', 16)
ylabel(['$Y \lbrack \mu m \rbrack $'],'interpreter',
    ', 'latex', 'FontSize', 16)
zlabel(['$Z \lbrack n m \rbrack $'],'interpreter',
    ', 'latex', 'FontSize', 16)
%hold on
%contour3(X,Y,Zmaxgrid,100)
%hold off
saveas(gcf, strcat('O:\Arbeits Gruppen\
    Neuroelectronics\People\Kreysing_Eva\Experiments
    \SPRresults\SPRDATA_160518\output_2017-09-26_11

```

## 11 Protocols

```
-23-55 (160518_153729)\threeDfigures\', '
avplusstd.png'), 'png');
close(gcf)

%Generate plots for demonstration of the cell
beating Zmax
figure
contour3(X,Y,Zmaxgrid,100)
colormap(flipud(parula))
az = 140;
el = 69;
zlim([60 200])
view(az, el);
xlabel(['$X \lbrack \mu m \rbrack $'],'interpreter',
', 'latex', 'FontSize', 16)
ylabel(['$Y \lbrack \mu m \rbrack $'],'interpreter',
', 'latex', 'FontSize', 16)
zlabel(['$Z \lbrack n m \rbrack $'],'interpreter',
', 'latex', 'FontSize', 16)
saveas(gcf, strcat('O:\Arbeits Gruppen\
Neuroelectronics\People\Kreysing_Eva\Experiments
\SPRresults\SPRDATA_160518\output_2017-09-26_11
-23-55 (160518_153729)\threeDfigures\', 'max.png
'), 'png');
close(gcf)
```

## 11.7.4 SPRM profile cuts along the entire interface

First, this script was executed generating images representing cuts through the 3D-SPRM profile. The outline of the basal cell membrane is represented by scatter plots for each cut. The color code of the scatter points represents the RI of the cytoplasm. Afterwards, these pictures were merged to a video using FFmpeg, giving the impression of a cell-substrate interface being cut slice by slice.

```
clear all
close all
% define width and depth of the data first
xwidth = 26;
ydepth = 45;
%Read the dat file containing x-y-and n (x,y,ri)
    information and read each of the
%columns seperately
RIdata = importdata('\material analysis\
    last_n_central.dat');
x = RIdata(:,1);
y = RIdata(:,2);
ri = RIdata(:,3);
%generate a grid in x-y plane
[X , Y] = meshgrid(min(x):.1:max(x) , min(y):.1:max
    (y));
RI = griddata(x, y, ri , X , Y , 'natural');
%Read the dat file containing x-y-and Zs (Zmin,
    Zaverage - std, Zaverage, Zaverage+std, Zmax)
    information and read each of the
%columns seperately
```

## 11 Protocols

```
threeDdata = importdata('\distance profiles\  
    distance_profile_central.dat');  
x2 = threeDdata(:,1);  
y2 = threeDdata(:,2);  
Z = threeDdata(:,3);  
Zgrid = griddata(x , y , Z , X , Y , 'natural');  
  
%3D cell and RI color coded;  
for m = 1: 90  
figure  
rimin = min(ri);  
rimax = max(ri);  
scatter3(x,y,Z, 80, ri, 'filled')  
az2 = -115 + m;  
el2 = 69;  
zlim([0 300])  
view(az2, el2);  
colormap(parula)  
colorbar  
caxis([rimin rimax])  
xlim([5 20])  
ylim([5 22])  
% Add title and axis labels  
title('refractive index per point')  
saveas(gcf, strcat('O:\Arbeits Gruppen\  
    Neuroelectronics\People\Kreysing_Eva\Experiments  
    \SPRresults\170613-21_fixation_experiment\  
    output_2017-09-10_20-34-30 (170616_170305_2-6-9-  
    cell)\Three_d_representation\', '69degree0RI3D',  
    num2str(m), '.jpg'), 'jpg');  
close(gcf)
```

```

end

%generate a scatter plot for each y slice
%assign a color to each RI value (use ri min and
    max of the hole data set
%and keep constant boundaries for the other axis ->
    xlim and y-lim )
for m = 1:xwidth
    rimin = min(ri);
    rimax = max(ri);
    figure
    xplotm = x2([1+((m-1)*xwidth): (xwidth+(m-1)*xwidth
        )]);
    Zplotm = Z([1+((m-1)*xwidth): (xwidth+(m-1)*xwidth)
        ]);
    c = ri([1+((m-1)*xwidth): (xwidth+(m-1)*xwidth)]);
    scatter(xplotm,Zplotm,80,c,'filled')
    xlim([0 22])
    ylim([0 300])
    colorbar
    caxis([rimin rimax])
    saveas(gcf, strcat('O:\Arbeits Gruppen\
        Neuroelectronics\People\Kreysing_Eva\
        Experiments\SPRresults\170613-21
        _fixation_experiment\output_2017-09-10_20-34-30
        (170616_170305_2-6-9-cell)\
        Three_d_representation\', num2str(m), '
        RIprofile.jpg'), 'jpg');
    close(gcf)
end

```

## 11.7.5 Align and compare distance profiles

This script uses the function `absor` published by user *Matt J* on the MathWorks File Exchange<sup>1</sup> which correlates two coordinate systems by a coordinate transformation based on Horn's method [85].

```
clear all
close all
addpath(pwd)
top_level_folder = 'G:\201711-201802_fixations\SL';
%variable for tracing the run
cd(top_level_folder);
run = 'test_1';

folders = {'test'};

delta_all = [];

for k = 1 : length(folders)
    folder = folders{k}
    cd(top_level_folder);
    cd(folder);
    mkdir(pwd, run);
%load cut zprofile from 2 scans
%plot both profiles
%plot individual profiles
%choose points
%save points
```

---

<sup>1</sup><https://de.mathworks.com/matlabcentral/fileexchange/26186-absolute-orientation-horn-s-method>

```

%%%%%%%%%%%%%%%%%%%%%%%%%%%%%%%%%%%%%%%%%%%%%%%%%%%%%%%%%%%%%%%%%%%%%%%% loading data
    %%%%%%%%%%%%%%%%%%%%%%%%%%%%%%%%%%%%%%%%%%%%%%%%%%%%%%%%%%%%%%%%%%%%%%%%%
% configure filepaths
pwd
rifile = fullfile(pwd, '\fixated\RI profile\n_avg.
    dat')
zfile = fullfile(pwd, '\fixated\Z profile\
    z_avg_fix_in_range.dat');
rifile_iv = fullfile(pwd, '\invitro\RI profile\
    n_avg.dat');
zfile_iv = fullfile(pwd, '\invitro\Z profile\
    z_avg_iv_in_range.dat');
gridresolution = 0.05;
low_gridresolution = 0.05;

% load data fixated cell
[x_grid, y_grid, zprofile, x_raw_fix, y_raw_fix,
    z_raw_fix] = load_zprofile(rifile, zfile,
    gridresolution);
% % load data _iv cell
[x_grid_iv, y_grid_iv, zprofile_iv, x_raw_iv,
    y_raw_iv, z_raw_iv] = load_zprofile(rifile_iv,
    zfile_iv, gridresolution);
% % load data _iv cell low resolution
[x_grid_iv_lr, y_grid_iv_lr, zprofile_iv_lr,
    x_raw_iv, y_raw_iv, z_raw_iv] = load_zprofile(
    rifile_iv, zfile_iv, low_gridresolution);

%%%%%%%%%%%%%%%%%%%%%%%%%%%%%%%%%%%%%%%%%%%%%%%%%%%%%%%%%%%%%%%%%%%%%%%% plot overview
    %%%%%%%%%%%%%%%%%%%%%%%%%%%%%%%%%%%%%%%%%%%%%%%%%%%%%%%%%%%%%%%%%%%%%%%%%

```

## 11 Protocols

```
% plot both z-profiles at the same time
figure;
subplot(1,2,1)
xlims_iv = [min(x_grid_iv) max(x_grid_iv)];
ylims_iv = [min(y_grid_iv) max(y_grid_iv)];
imagesc(xlims_iv,ylims_iv,zprofile_iv)
colormap(parula);
caxis([0 80]);
set(gca, 'Xdir', 'reverse');
xlabel(['X  $\backslash\lbrack \mu \text{ m } \rbrack \text{\$}$ '],'interpreter'
, 'latex', 'FontSize', 16);
ylabel(['Y  $\backslash\lbrack \mu \text{ m } \rbrack \text{\$}$ '],'interpreter'
, 'latex', 'FontSize', 16);
title(['Distance living cell'],'interpreter','latex'
, 'FontSize', 16);
%[x, y] = getpts;
subplot(1,2,2)
xlims = [min(x_grid) max(x_grid)];
ylims = [min(y_grid) max(y_grid)];
imagesc(xlims,ylims,zprofile)
colormap(parula);
caxis([0 80]);
set(gca, 'Xdir', 'reverse');
xlabel(['X  $\backslash\lbrack \mu \text{ m } \rbrack \text{\$}$ '],'interpreter'
, 'latex', 'FontSize', 16);
ylabel(['Y  $\backslash\lbrack \mu \text{ m } \rbrack \text{\$}$ '],'interpreter'
, 'latex', 'FontSize', 16);
title(['Distance profile fixated cell'],'
interpreter','latex', 'FontSize', 16);
```

```

%%%%%%%%%%%%%%%%%%%%%%%%%%%%%%%%%%%%%%%%%%%%%%%%%%%%%%%%%%%%%%%%%%%%%%%%%% ploygone markers
    in vitro %%%%%%%%%%%%%%%%%%%%%%%%%%%%%%%%%%%%%%%%%%%%%%%%%%%%%%%%%%%%%%%%%%%%%%%%%%%
figure;
xlims_iv = [min(x_grid_iv) max(x_grid_iv)];
ylims_iv = [min(y_grid_iv) max(y_grid_iv)];
imagesc(xlims_iv,ylims_iv,zprofile_iv)
colormap(parula);
caxis([0 80]);
set(gca, 'Xdir', 'reverse');
xlabel(['X $\lbrack \mu m \rbrack $'],'interpreter'
, 'latex', 'FontSize', 16);
ylabel(['Y $\lbrack \mu m \rbrack $'],'interpreter'
, 'latex', 'FontSize', 16);
zlabel(['Z $\lbrack nm \rbrack $'],'interpreter','
    latex', 'FontSize', 16);
title(['Define polygone'],'interpreter','latex', '
    FontSize', 16);
[x_poly,y_poly] = getpts;
hold on
scatter(x_poly, y_poly, ...
        'MarkerFaceColor',[1 0 0],'MarkerEdgeColor'
        ,[0 0 0],'LineWidth',2)
filenamefig = fullfile(pwd, run, strcat(folder, '
    _d_avg_polygone_marker.fig'));
saveas(gcf, filenamefig);
filename = fullfile(pwd, run, strcat(folder, '
    _d_avg_polygone_marker.png'));
saveas(gcf, filename);
in = inpolygon(x_raw_iv', y_raw_iv',x_poly', y_poly
    ');

```

## 11 Protocols

```
% set parts outside of the polygone to NaN
[row, col] = find(in == 0);
idx = sub2ind(size(z_raw_iv), row, col);
z_in_poly = z_raw_iv;
z_in_poly(idx) = NaN;
three_d_cut = [ x_raw_iv, y_raw_iv, z_in_poly];
% create a grid
[x_grid_iv, y_grid_iv] = create_common_meshgrid(
    xlims_iv, ylims_iv, gridresolution);
[z_poly] = create_zprofile(x_raw_iv, y_raw_iv,
    z_in_poly, x_grid_iv, y_grid_iv);
figure;
surf(x_grid_iv, y_grid_iv, z_poly, 'LineStyle', '
    none');
colormap(parula);
caxis([0 80]);
set(gca, 'Xdir', 'reverse');
az = 180 ;
el = 90;

%%%%%%%%%%%%%%%%%%%%%%%%%%%%%%%%%%%%%%%%%%%%%%%%%%%%%%%%%%%%%%%%%%%%%%%% markers in
    fixated cell %%%%%%%%%%%%%%%%%%%%%%%%%%%%%%%%%%%%%%%%%%%%%%%%%%%%%%%%%%%%%%%%%%%%%%%%%
% plot z-profile fixated cell
% choose points with the cursor and store them in
    Matrix A
% plot A in the image and save it as png
figure;
xlims = [min(x_grid) max(x_grid)];
ylims = [min(y_grid) max(y_grid)];
imagesc(xlims, ylims, zprofile)
colormap(parula);
```

```

caxis([0 80]);
set(gca, 'Xdir', 'reverse');
xlabel(['X $\lbrack \mu m \rbrack $'], 'interpreter'
, 'latex', 'FontSize', 16);
ylabel(['Y $\lbrack \mu m \rbrack $'], 'interpreter'
, 'latex', 'FontSize', 16);
title(['Fixated cell - choose salient points'], '
interpreter', 'latex', 'FontSize', 16);
[x, y] = getpts;
hold on
A = [x'; y'];
scatter(x, y, ...
'MarkerFaceColor', [1 0 0], 'MarkerEdgeColor', [0
0 0], 'LineWidth', 2)

filename_fix = fullfile(pwd, run, strcat(folder, '
_d_avg_fix_marker.png'));
saveas(gcf, filename_fix);
filename_fix_fig = fullfile(pwd, run, strcat(folder
, '_d_avg_fix_marker.fig'));
saveas(gcf, filename_fix_fig);

%%%%%%%%%%%%%% markers in vitro
%%%%%%%%%%%%%%
% same procedure for in vitro cell
figure;
xlims_iv = [min(x_grid_iv) max(x_grid_iv)];
ylims_iv = [min(y_grid_iv) max(y_grid_iv)];
imagesc(xlims_iv, ylims_iv, zprofile_iv)
colormap(parula);
caxis([0 80]);

```

## 11 Protocols

```
set(gca, 'Xdir', 'reverse');
xlabel(['X $\lbrack \mu m \rbrack $'], 'interpreter'
, 'latex', 'FontSize', 16);
ylabel(['Y $\lbrack \mu m \rbrack $'], 'interpreter'
, 'latex', 'FontSize', 16);
zlabel(['Z $\lbrack nm \rbrack $'], 'interpreter', '
latex', 'FontSize', 16);
title(['In vitro - choose the same points, same
order'], 'interpreter', 'latex', 'FontSize', 16);
[x_iv, y_iv] = getpts;
B = [x_iv'; y_iv'];
hold on
scatter(x_iv, y_iv, ...
'MarkerFaceColor', [1 0 0], 'MarkerEdgeColor'
, [0 0 0], 'LineWidth', 2)
filename = fullfile(pwd, run, strcat(folder, '
_d_avg_iv_marker.png'));
saveas(gcf, filename);
filenamefig = fullfile(pwd, run, strcat(folder, '
_d_avg_iv_marker.fig'));
saveas(gcf, filenamefig);

%%%%%%%%%%%%%%%%%%%%%%%%%%%%%%%%%%%%%%%%%%%%%%%%%%%%%%%%%%%%%%%%%%%%%%%%%% apply absor
%%%%%%%%%%%%%%%%%%%%%%%%%%%%%%%%%%%%%%%%%%%%%%%%%%%%%%%%%%%%%%%%%%%%%%%%%%
% apply absor function which finds the translation
and rotation between
% the images and transform the coordinates of the
scan of the fixated
% cell accordingly
[regParams, Bfit, ErrorStats] = absor(A, B);
```

```

% create a matrix containg x, y values representing
    the
% homogenous coordinates necessary for the absor
    script
xy_fixed = [x_raw_fix.';...
            y_raw_fix.'];
xy_fix_transf = regParams.R*xy_fixed + regParams.t;
% create a x-y-z matrix containing the transformed
    data in the original matrix format
% and save the transformed data (matrix) as a dat
    file
xyz_fix_transf = [xy_fix_transf(1,:).',...
                  xy_fix_transf(2,:).',...
                  z_raw_fix];
x_fix_transf = xy_fix_transf(1,:).';
y_fix_transf = xy_fix_transf(2,:).';
datname = fullfile(pwd, run, strcat(folder, '
    _xyz_fix_transf.dat'));
dlmwrite(datname, xyz_fix_transf);

% %%%%%%%%%%%%%%%%%%%%%%%%%%%%%%%%%%%%%%%%%%%%%%%%%%%%%%%%%%% plot mapped
    fixated cell %%%%%%%%%%%%%%%%%%%%%%%%%%%%%%%%%%%%%%%%%%%%%%%%%%%%%%%%%%%
% % create a grid, so that we can plot the cell in
    the transformed area
[x_grid_trans, y_grid_trans] =
    create_meshgrid_from_matrix(xy_fix_transf,
    gridresolution);
z_profile_trans = griddata(xy_fix_transf(1,:).',
    xy_fix_transf(2,:).', z_raw_fix, x_grid_trans ,
    y_grid_trans , 'natural');

```

## 11 Protocols

```
[x_grid_trans_lr, y_grid_trans_lr] =
    create_meshgrid_from_matrix(xy_fix_transf,
        low_gridresolution);
z_profile_trans_lr = griddata(xy_fix_transf(1,:).'
    , xy_fix_transf(2,:).' , z_raw_fix,
    x_grid_trans_lr , y_grid_trans_lr , 'natural');

%%%%%%%%%%%% generate overlapping grid & plot z-
            difference %%%%%%%%%%%%%
% set two markers for defining the range of the
            accepted area

figure;
xlims_trans = [min(x_grid_trans) max(x_grid_trans)
    ];
ylims_trans = [min(y_grid_trans) max(y_grid_trans)
    ];
imagesc(xlims_trans,ylims_trans,z_profile_trans)
colormap(parula);
caxis([0 80]);
set(gca, 'Xdir', 'reverse');
xlabel(['X $\lbrack \mu m \rbrack $'], 'interpreter'
    , 'latex', 'FontSize', 16);
ylabel(['Y $\lbrack \mu m \rbrack $'], 'interpreter'
    , 'latex', 'FontSize', 16);
title(['Define the evaluation range for delta Z -
            choose two points'], 'interpreter', 'latex', '
            FontSize', 16);
[x, y] = getpts;
hold on
C = [x'; y'];
```

```

scatter(x, y, ...
        'MarkerFaceColor',[1 0 0], 'MarkerEdgeColor',[0
            0 0], 'LineWidth',2)
filename_fix = fullfile(pwd, run, strcat(folder, '
    _d_fix_grid_marker.png'));
saveas(gcf, filename_fix);
filename_fix_fig = fullfile(pwd, run, strcat(folder
    , '_d_fix_grid_marker.fig'));
saveas(gcf, filename_fix_fig);
xlims_combi = [min(C(1,1), C(1,2)) max(C(1,1), C
    (1,2))];
ylims_combi = [min(C(2,1), C(2,2)) max(C(2,1), C
    (2,2))];
[x_grid_com, y_grid_com] = create_common_meshgrid(
    xlims_combi, ylims_combi, gridresolution);
[zprofile_iv_com] = create_zprofile(x_raw_iv,
    y_raw_iv, z_raw_iv, x_grid_com, y_grid_com);
[z_poly_com] = create_zprofile(x_raw_iv, y_raw_iv,
    z_in_poly, x_grid_com, y_grid_com);
[zprofile_fix_transf_com] = create_zprofile(
    x_fix_transf, y_fix_transf, z_raw_fix,
    x_grid_com, y_grid_com);
filename = fullfile(pwd, run, strcat(folder, '
    _fixated_cell_relation.png'));
saveas(gcf, filename);
filenamefig = fullfile(pwd, run, strcat(folder, '
    _fixated_cell_relation.fig'));
saveas(gcf, filenamefig);
combined_data.grid_x = x_grid_com;
combined_data.grid_y = y_grid_com;
combined_data.z_iv = z_poly_com;

```

## 11 Protocols

```
combined_data.z_fix = zprofile_fix_trans_com;
datname = fullfile(pwd, run, strcat(folder, '
    _combined_data.mat'));
save(datname, 'combined_data');

%%%%%%%%%%%%%%%%%%%%%%%%%%%%%%%%%%%%%%%%%%%%%%%%%%%%%%%%%%%%%%%%%%%%%%%% make cross sections
%%%%%%%%%%%%%%%%%%%%%%%%%%%%%%%%%%%%%%%%%%%%%%%%%%%%%%%%%%%%%%%%%%%%%%%%

% choose two points and save the coordinates
% calculate distance: x_b - x_a and y_b - y_a
% define interval eg delta_xy/n_st (number of steps
    )
% create a vector containing all the x values with
    stepwidth of
% delta_x/n_st : first define a start vector with
    all entries = start value
% and length(vector x_start) = n_st
% now, define a vecor "stepping_vector" that starts
    with a 0 and has the delta x
% stepwidth as each following entry. The
    displacement can be calculated
% x_displacement = cumsum(stepping_vector). X-
    position of all the steps x_all_steps =
% x_start + x_displacement. Same procedure for y
    values.
% for each xy pair, interpolate the z_fix_trans and
    z_iv and plot the cross
% sections

%%%%%%%%%%%%%%%%%%%%%%%%%%%%%%%%%%%%%%%%%%%%%%%%%%%%%%%%%%%%%%%%%%%%%%%% markers cross section in
    vitro %%%%%%%%%%%%%%%%%%%%%%%%%%%%%%%%%%%%%%%%%%%%%%%%%%%%%%%%%%%%%%%%%%%%%%%%%
```

```

figure
xlims_trans_com = [min(x_grid_com) max(x_grid_com)
    ];
ylims_trans_com = [min(y_grid_com) max(y_grid_com)
    ];
imagesc(xlims_trans_com,ylims_trans_com,z_poly)
colormap(parula);
caxis([0 80]);
set(gca, 'Xdir', 'reverse');
xlabel(['X $\lbrack \mu m \rbrack $'],'interpreter'
    , 'latex', 'FontSize', 16);
ylabel(['Y $\lbrack \mu m \rbrack $'],'interpreter'
    , 'latex', 'FontSize', 16);
zlabel(['Z $\lbrack nm \rbrack $'],'interpreter','
    latex', 'FontSize', 16);
title(['In vitro - choose cross section points'],'
    interpreter','latex', 'FontSize', 16);
[x_cs, y_cs] = getpts(gcf);
D = [x_cs'; y_cs'];
hold on
scatter(x_cs, y_cs, ...
    'MarkerFaceColor',[1 0 0], 'MarkerEdgeColor'
        , [0 0 0], 'LineWidth', 2)
filename = fullfile(pwd, run, strcat(folder, '
    _avg_cs_iv_marker.png'));
saveas(gcf, filename);
filenamefig = fullfile(pwd, run, strcat(folder, '
    _avg_cs_iv_marker.fig'));
saveas(gcf, filenamefig);

% define the boundary vectors

```

## 11 Protocols

```
delta_x = x_cs(2) - x_cs(1);
delta_y = y_cs(2) - y_cs(1);
n_st = 100;
stepwidth_x = delta_x/ n_st;
stepwidth_y = delta_y/ n_st;

start_x = [n_st;1];
for m = 1 : n_st
    start_x(m) = x_cs(1);
end

stepping_x = [n_st; 1];
stepping_x(1)= 0;
for o = 2 : n_st
    stepping_x(o)= stepwidth_x;
end

x_displacement = cumsum(stepping_x);
x_cross_section = start_x + x_displacement;

delta_x = x_cs(2) - x_cs(1);
delta_y = y_cs(2) - y_cs(1);
n_st = 100;
stepwidth_x = delta_x/ n_st;
stepwidth_y = delta_y/ n_st;

start_y = [n_st;1];
for m = 1 : n_st
    start_y(m) = y_cs(1);
end
```

```

stepping_y = [n_st; 1];
stepping_y(1)= 0;
for o = 2 : n_st
    stepping_y(o)= stepwidth_y;
end

y_displacement = cumsum(stepping_y);
y_cross_section = start_y + y_displacement;
xy_cs = [x_cross_section, y_cross_section];

Z_cs= interp2(x_grid_com,y_grid_com,z_poly_com,
    x_cross_section, y_cross_section);
Z_cs_fix= interp2(x_grid_com,y_grid_com,
    zprofile_fix_trans_com ,x_cross_section,
    y_cross_section);
dist_cs = linspace(0, sqrt(delta_y^2 + delta_x^2),
    100);
figure
plot(dist_cs(:), Z_cs,'r','LineWidth',2)
hold on;
plot(dist_cs(:), Z_cs_fix,'b','LineWidth',2);
xlabel(['Cross section along the cut $\lbrack \mu m$
    $\rbrack $'],'interpreter','latex', 'FontSize',
    16);
ylabel(['Z-Profiles $\lbrack nm \rbrack $'],'
    interpreter','latex', 'FontSize', 16);
title(['Cross section through the Z-profiles'],'
    interpreter','latex', 'FontSize', 16);
legend('in vitro','fixated');
hold off;

```

## 11 Protocols

```
filename = fullfile(pwd, run, strcat(folder, '
    Z_at_cross_section.png'));
saveas(gcf, filename);
filenamefig = fullfile(pwd, run, strcat(folder, '
    Z_at_cross_section.fig'));
saveas(gcf, filenamefig);

%%%%%%%%%%%%%%%%%%%%%%%%%%%%%%%%%%%%%%%%%%%%%%%%%%%%%%%%%%%%%%%%%%%%%%%%delta Z
%%%%%%%%%%%%%%%%%%%%%%%%%%%%%%%%%%%%%%%%%%%%%%%%%%%%%%%%%%%%%%%%%%%%%%%%
delta = z_poly_com - zprofile_fix_trans_com;
figure
surf(x_grid_com,y_grid_com, delta , 'LineStyle', '
    none');
colormap(parula);
caxis([0 80]);
set(gca, 'Xdir', 'reverse')
az = 180 ;
el = 90;
view(az, el);
filename = fullfile(pwd, run, strcat(folder, '
    _delta_z.png'));
saveas(gcf, filename);
filenamefig = fullfile(pwd, run, strcat(folder, '
    _delta_z.fig'));
saveas(gcf, filenamefig);
datname = fullfile(pwd, run, strcat(folder, '_delta.
    dat'));
dlmwrite(datname, delta);

figure
histogram(delta);
```

```

filename = fullfile(pwd, run, strcat(folder, '
    _histogram.png'));
saveas(gcf, filename);
filenamefig = fullfile(pwd, run, strcat(folder, '
    _histogram.fig'));
saveas(gcf, filenamefig);

actual_delta = - z_poly_com +
    zprofile_fix_trans_com;
figure
surf(x_grid_com,y_grid_com, actual_delta , '
    LineStyle', 'none');
colormap(parula);
caxis([0 80]);
set(gca, 'Xdir', 'reverse')
az = 180 ;
el = 90;
view(az, el);
filename = fullfile(pwd, run,  strcat(folder, '
    actual_delta_z.png'));
saveas(gcf, filename);
filenamefig = fullfile(pwd, run,  strcat(folder, '
    actual_delta_z.fig'));
saveas(gcf, filenamefig);
datname = fullfile(pwd, run, strcat(folder, '
    actual_delta.dat'));
dlmwrite(datname, actual_delta);

%%%%%%%%%%%%%% determine mean, std, max and min
%%%%%%%%%%%%%%

```

## 11 Protocols

```
delta_mean = mean(delta(:), 'omitnan');
delta_std = std(delta(:), 'omitnan');
delta_min = min(delta(:));
delta_max = max(delta(:));
delta_stats = [delta_mean, delta_std, delta_min,
              delta_max];

delta_all = [delta_all; delta_stats];
end
datname = fullfile(top_level_folder, strcat(run, '
        _delta_stats.dat'));
dlmwrite(datname, delta_all);

%%%%%%%%%%%%%%%%%%%%%%%%%%%%%%%%%%%%%%%%%%%%%%%%%%%%%%%%%%%%%%%%%%%%%%%% functions
%%%%%%%%%%%%%%%%%%%%%%%%%%%%%%%%%%%%%%%%%%%%%%%%%%%%%%%%%%%%%%%%%%%%%%%%
function [x_grid, y_grid, zprofile, x2, y2, z] =
    load_zprofile(rifile, zfile, gridresolution)
% the variables in the [] are returned
% read z-profile file and extract grid and z values
    at grid points
% x_grid, y_grid and zprofile are the output of
    load_zprofile function
% the function takes filename and a gridresolution
    as variables
% first read data from the scanning results
ridata = importdata(rifile);
x = ridata(:,1);
y = ridata(:,2);
ri = ridata(:,3);
%generate a grid in x-y plane
```

```

[x_grid , y_grid] = meshgrid(min(x):gridresolution:
    max(x) , min(y):gridresolution:max(y));
%ri_grid = griddata(x, y, ri , x_grid , y_grid , '
    natural');
%Read the dat file containing x-y-and zs (zmin,
    zaverage - std, zaverage, zaverage+std, zmax)
    information and read each of the
%colomns seperately
threeDdata = importdata(zfile);
x2 = threeDdata(:,1);
y2 = threeDdata(:,2);
z = threeDdata(:,3);
zprofile = griddata(x , y , z , x_grid , y_grid , '
    natural');
end

```

```

function [x_grid, y_grid] =
    create_meshgrid_from_matrix(data_matrix,
    gridresolution)
% data matrix contains the coordinates of x, y
    which should be
% plotted z is generated by the function '
    load_zprofile' <- did not work
[x_grid , y_grid] = meshgrid(min(data_matrix(1,:)):
    gridresolution:max(data_matrix(1,:)) , ...
                                min(data_matrix(2,:)
                                ):gridresolution:
                                max(data_matrix
                                (2,:)));
%z_profile_2 = griddata(data_matrix(1,:) ,
    data_matrix(2,:) , z , x_grid , y_grid , 'natural

```

## 11 Protocols

```
    ');  
end  
  
function [x_grid, y_grid] = create_common_meshgrid(  
    xlims, ylims, gridresolution)  
[x_grid , y_grid] = meshgrid(min(xlims):  
    gridresolution:max(xlims) , ...  
                               min(ylims):  
                               gridresolution:  
                               max(ylims));  
end  
  
function [zprofile] = create_zprofile(x, y, z,  
    x_grid, y_grid)  
zprofile = griddata(x , y , z , x_grid , y_grid , '  
    natural');  
end
```

# Appendix

## 12.1 Angle validation

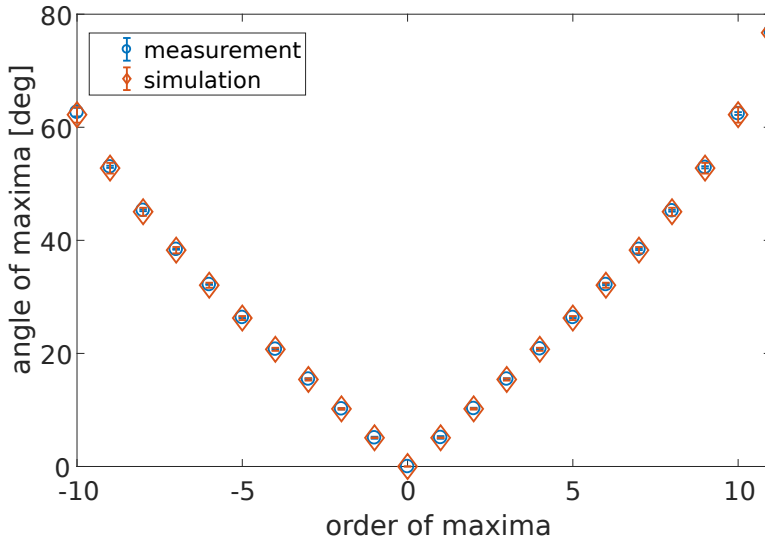


**Figure 12.1:** An interference pattern was created on the BFP during illumination of a chromium grid. The position of the maxima has been evaluated and compared to the theoretically expected values.

## 12.2 Additional measurements and specifications

### 12.2.1 Scanning parameters

Area scan 1 has a ROI of  $29 \times 30 \mu\text{m}^2$ , a lateral resolution of  $1 \mu\text{m}$  (distance of scanning points). 50 images were recorded at each scanning point with a temporal resolution of 100 ms. This results in a measurement time of 73 minutes and 340 GB data volume. Parameters chosen for analysis:  $3.5 \text{ nm Cr}$ ,  $37 \text{ nm Au}$ , least squares method,  $T = 5$ .

Area scan 2 has a ROI of  $29 \times 19 \mu\text{m}^2$ , a lateral resolution of  $1.5 \mu\text{m}$ . 30 images were recorded at each scanning point with a temporal resolution of 200 ms. The temporal resolution was chosen lower than before because the cell was beating with a frequency of  $\sim 0.3 \text{ Hz}$ . This results in a measurement time of 25 minutes and 58 GB data volume. Parameters chosen for analysis:  $2.8 \text{ nm Cr}$ ,  $37 \text{ nm Au}$ , least squares method,  $T = 10$ .

### 12.2.2 Detached lamella

### 12.2.3 Surface defects

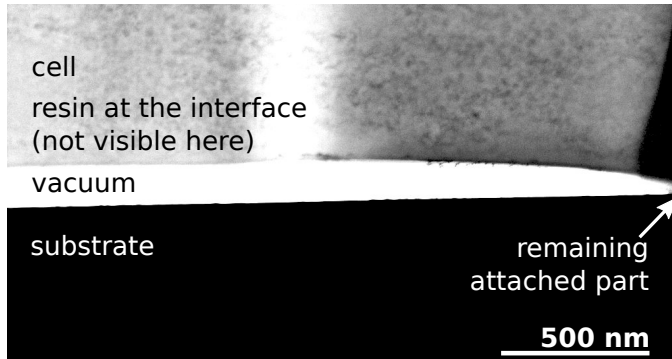


**Figure 12.2:** The lamella was damaged during the sample mounting at the TEM. The cell detached from the substrate and the contact only remained at the edges of the lamella.

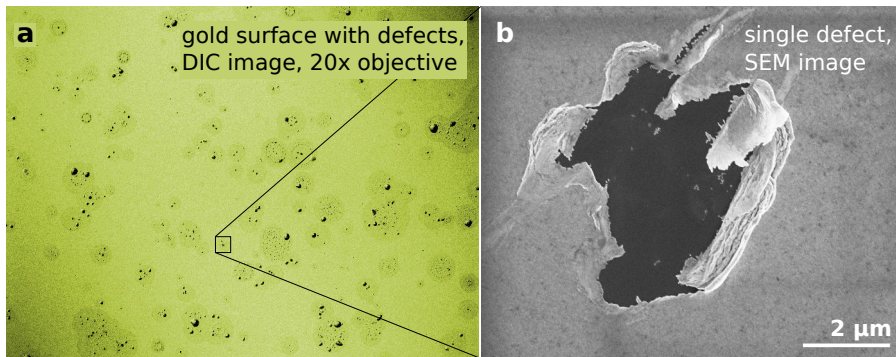


**Figure 12.3:** Investigation of defects in the gold surface after cell culture. a) The DIC image reveals the coffee-ring-like assembly of the defects. b) The SEM image shows that the small dots seen in the DIC images are indeed holes in the gold surface.

## 12.3 Analysis software optimization

The development of the analysis software *SPRing* was realized by Hossein Hassani as a part of his master's thesis [58] and constantly optimized in collaboration ever since.

Trying to track the critical angle in order to evaluate the changes of the intracellular refractive index during action potentials, least squares optimization of the entire reflectance curve did not give sufficient accuracy. This failure was caused by noise of the reflectance curves determined from individual BFP images.

The analysis process was split into two separate steps and it was tried to fit these parts of the curve separately. Therefore, several approaches were tested. The fitting of the critical angle was limited to the angle spectrum corresponding to a narrow region ( $\pm 2^\circ$ ) around typical values found for the critical angle. These typical values of the critical angle correspond to cytosolic RI values which can be reached under physiological conditions ( $RI = 1.34 - 1.4$ ) [63].

In order to limit the considered area to such a small region, I designed a specific weighing function  $F$  based on the Fermi-Dirac distribution  $n = \frac{1}{1 + e^{(E-\mu)/(kT)}}$ .  $n$  is 1 for small values of  $E$  and 0 for high values while the slope of the function depends on the temperature  $T$ . Multiplying a function  $n$  of this shape with its inverted function  $1 - n$ , allows us to design a pulse function  $F$  with adjustable slope:

$$F = \frac{1}{1 + e^{(RI - RI_{max})/T}} \cdot \left( 1 - \frac{1}{1 + e^{(RI - RI_{min})/T}} \right) \quad (12.1)$$

Here, I replaced the energies  $E$  and  $\mu$  by the variable refractive index  $RI$  and  $RI_{min/max}$ , respectively and dropped the Boltzmann constant  $k$ .

Additionally, a Gaussian function was considered as an alternative to the weighing function F.

For the analysis of the distance, several different approaches were implemented. It was tried to track the position of the resonance angle by finding the minimal value in the curve and afterwards using a look-up-table to assign a cell-substrate distance. The second approach was based on the detection of the *free fall angle* which is the angle at which the detected intensity is half of the sum of the maximum and the minimum of the curve. Again, a specifically designed look-up table was used to assign a distance.

The third approach was to divide the curve into two sections and detect the *center of mass* of the curve. Two look-up tables were determined to assign values for the refractive index and the distance.

In order to evaluate, which approach leads to the best results, I generated a test data set (see Figure 5.15). This data set is part of a time-dependent single spot measurement of a beating cardiomyocyte. I extracted the reflectance profiles of 65 individual BFP images and analyzed each profile manually. This test data set was then used as a model.

Hossein Hassani implemented a set of analysis techniques that he applied to the data set and compared the results to the manual analysis. In Figure 12.4 - Figure 12.9, the deviations between the automatically and the manually analyzed data are shown for many different combinations of analysis approaches. The mean difference between the manual and automatic approach as well as the standard deviation were evaluated. Additionally, the morphology of the signals was compared using the following expressions (derived by Hossein Hassani):

$$\Delta_{morph_{RI}} = \sum \left| \frac{RI_a - \overline{RI}_a}{std_{RI_a}} - \frac{RI_a - \overline{RI}_m}{std_{RI_m}} \right| \quad (12.2)$$

$$\Delta_{morph_d} = \sum \left| \frac{d_a - \bar{d}_a}{std_{d_a}} - \frac{d_a - \bar{d}_m}{std_{d_m}} \right| \quad (12.3)$$

$a, m$  indicate the automatically and the manually analyzed values, respectively.  $\bar{RI}, \bar{d}$  refer to the mean values while  $std_{RI,d}$  refers to the standard deviation of the respective variable.

As one can see in Figure 12.4 - Figure 12.9, there is a large deviation between the different analysis approaches. The results that were generated using the Fermi-dirac-pulse with  $T = 10$  in combination with the resonance angle-detection and a least-squares optimization, are always among the best for this test-data set. Therefore, these analysis parameters were used for the data analysis if not stated otherwise.

The accuracy and precision of this automated analysis in comparison to a manual fitting procedure were evaluated in section 5.4.3.

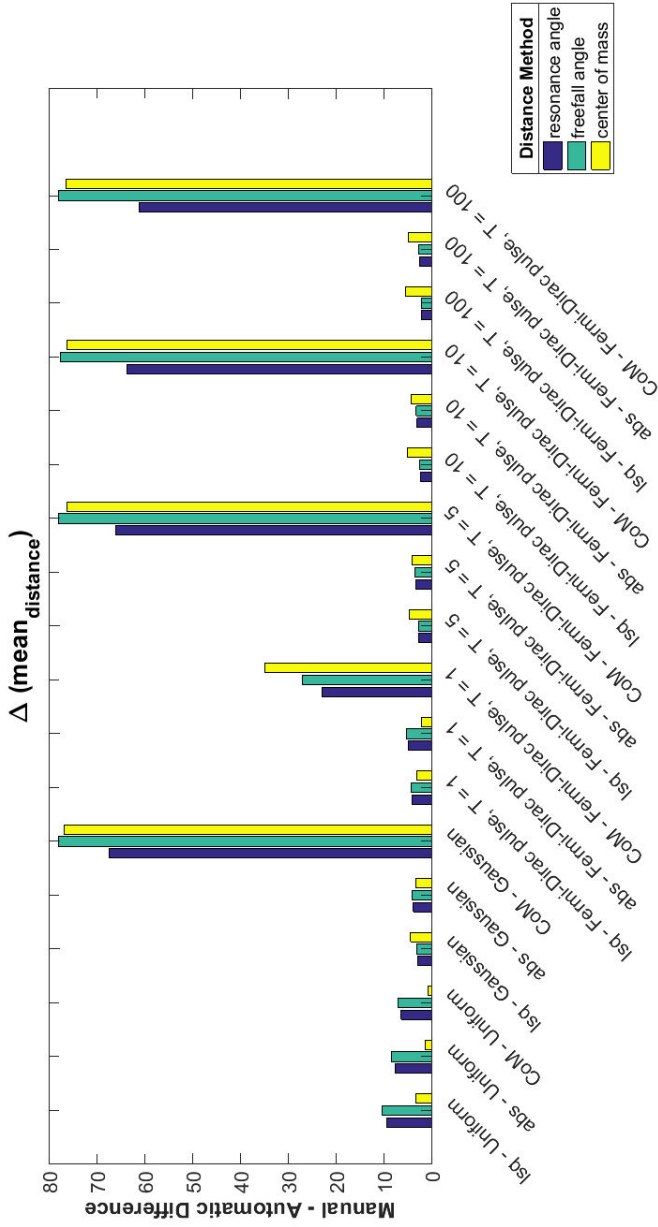
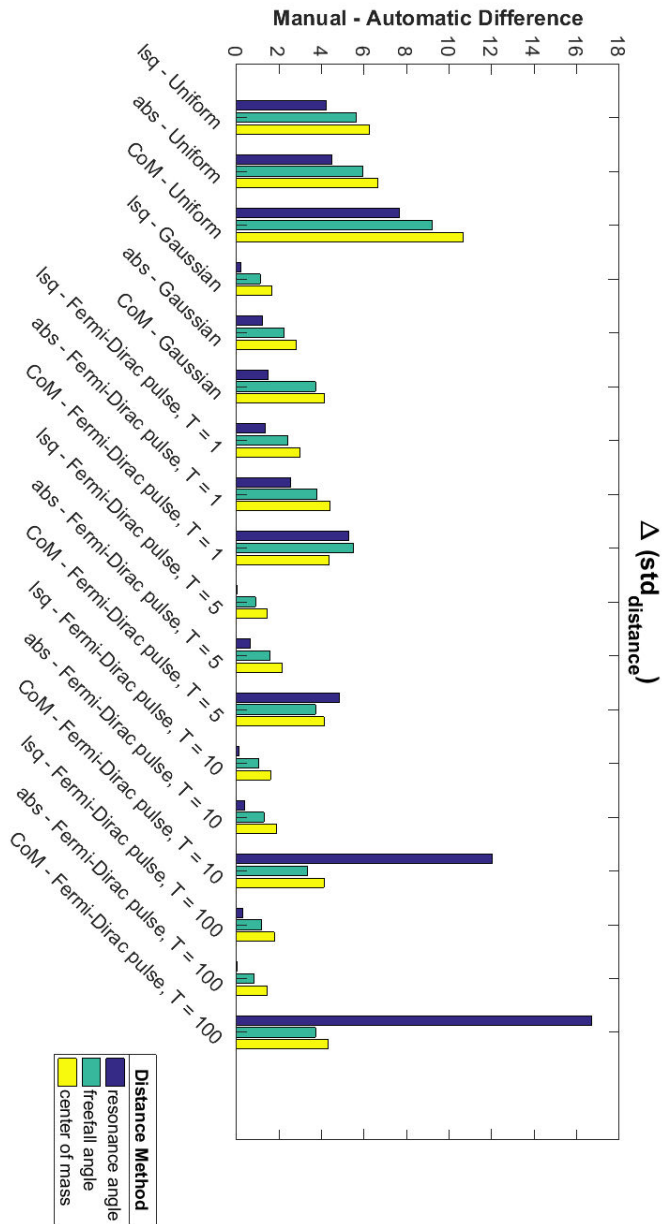


Figure 12.4: Mean difference between the automatically and manually analyzed cell-substrate distance. Image courtesy of Hossein Hassani.

**Figure 12.5:** Standard deviation of the difference between the automatically and manually analyzed cell-substrate distance. Image courtesy of Hossein Hassani.



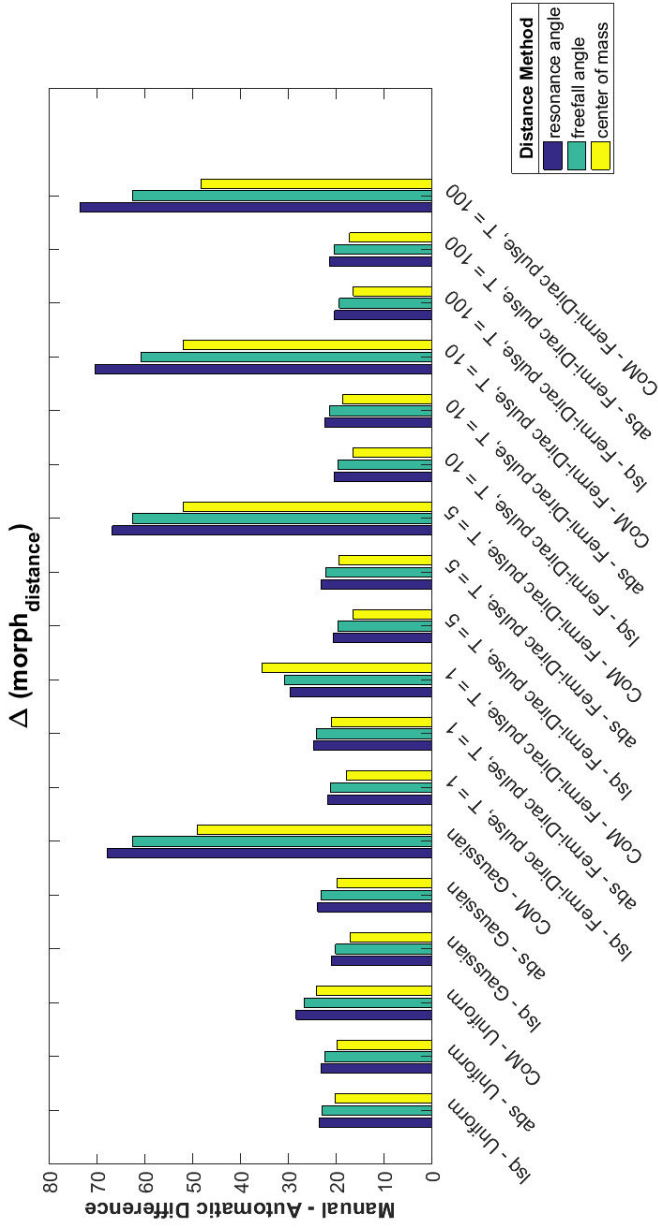
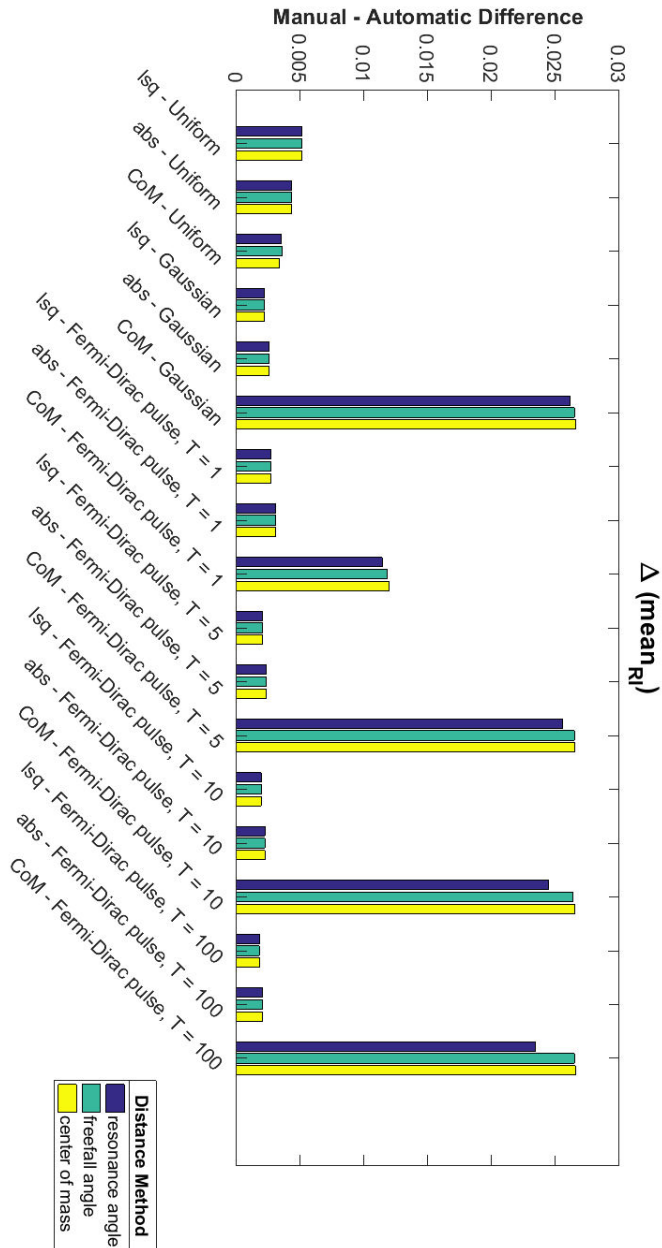


Figure 12.6: Deviation of the shape of the between the automatically and manually analyzed cell-substrate distance curve. Image courtesy of Hossein Hassani.

**Figure 12.7:** Mean difference between the automatically and manually analyzed cytosolic refractive index. Image courtesy of Hosein Hassani.



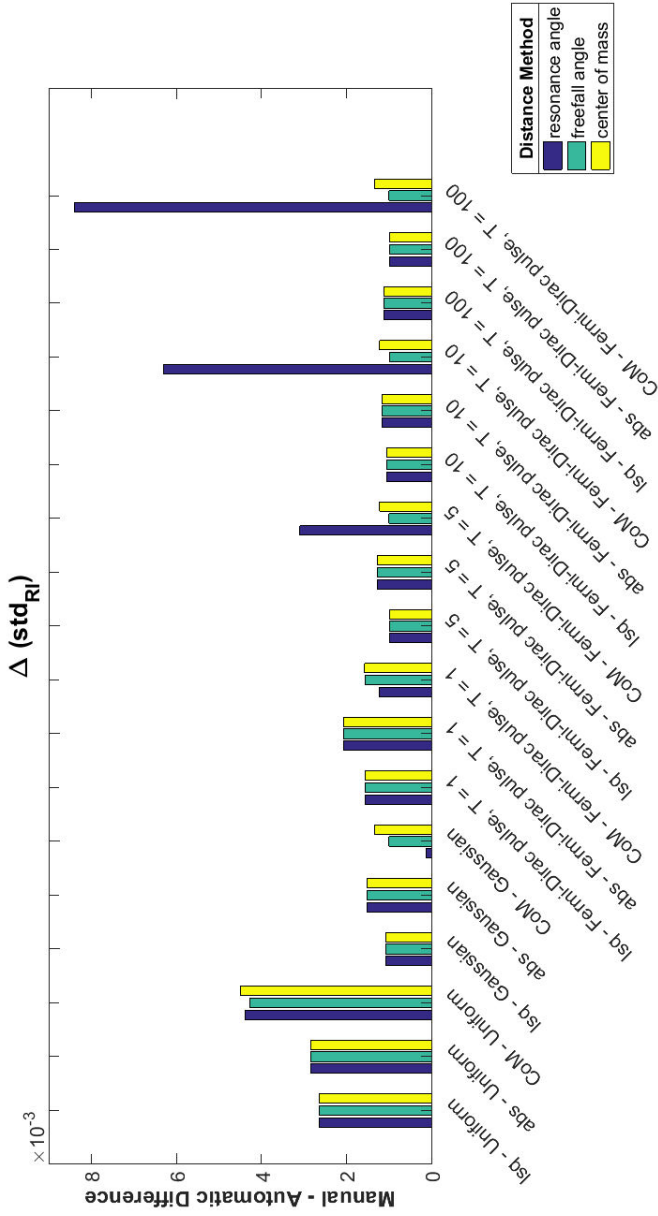
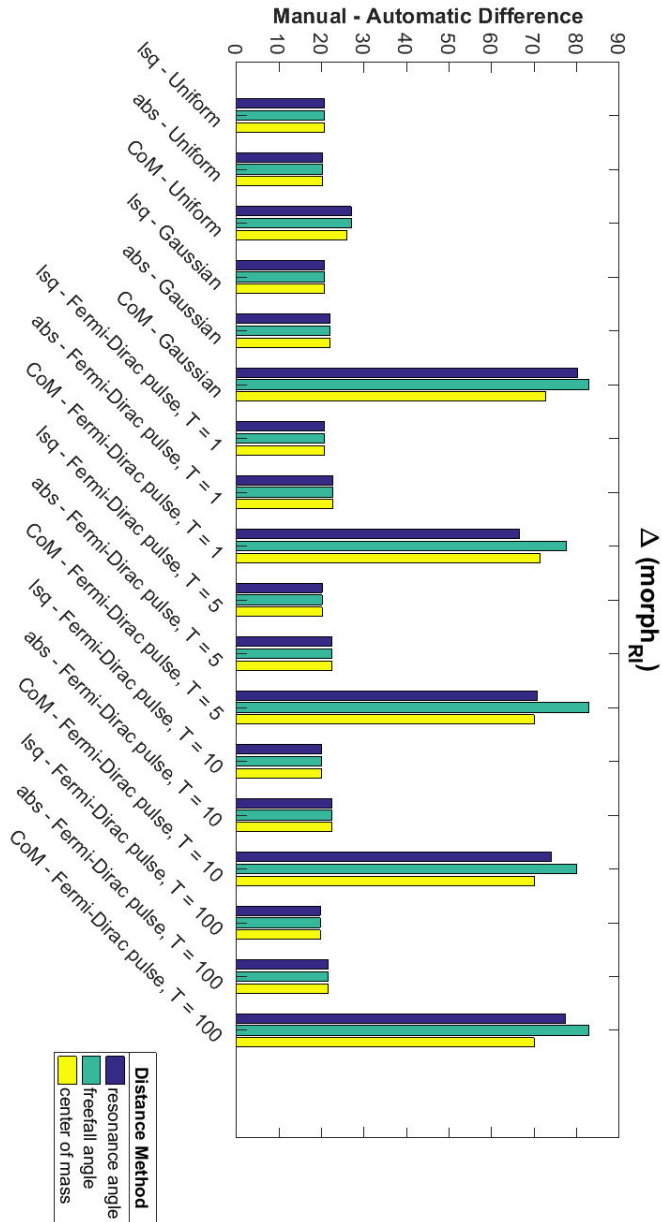


Figure 12.8: Standard deviation of the difference between the automatically and manually analyzed cytosolic refractive index. Image courtesy of Hossein Hassani.

**Figure 12.9:** Deviation of the shape of the between the automatically and manually analyzed cytosolic refractive index. Image courtesy of Hossein Hassani.



# Bibliography

- [1] Günter Wrobel et al. "Influence of the First Amplifier Stage in MEA Systems on Extracellular Signal Shapes". en. In: *Biosensors and Bioelectronics* 22.6 (Jan. 2007), pp. 1092–1096. ISSN: 0956-5663. DOI: 10.1016/j.bios.2006.03.023.
- [2] Aviad Hai et al. "Spine-Shaped Gold Protrusions Improve the Adherence and Electrical Coupling of Neurons with the Surface of Micro-Electronic Devices". eng. In: *Journal of the Royal Society, Interface* 6.41 (Dec. 2009), pp. 1153–1165. ISSN: 1742-5662. DOI: 10.1098/rsif.2009.0087.
- [3] Dorothea Brüggemann et al. "Nanostructured Gold Microelectrodes for Extracellular Recording from Electrogenic Cells". In: *Nanotechnology* 22.26 (2011), p. 265104.
- [4] Manuel Wesche et al. "A Nanoporous Alumina Microelectrode Array for Functional Cell–Chip Coupling". en. In: *Nanotechnology* 23.49 (2012), p. 495303. ISSN: 0957-4484. DOI: 10.1088/0957-4484/23/49/495303.
- [5] Andreas Offenhausser et al. "Field-Effect Transistor Array for Monitoring Electrical Activity from Mammalian Neurons in Culture". en. In: 12 (1997), p. 8.
- [6] Christoph Sprössler et al. "Electrical Recordings from Rat Cardiac Muscle Cells Using Field-Effect Transistors". In: *Physical Review E* 60.2 (Aug. 1999), pp. 2171–2176. DOI: 10.1103/PhysRevE.60.2171.
- [7] Georg Steinhoff et al. "Recording of Cell Action Potentials with AlGa<sub>N</sub>/Ga<sub>N</sub> Field-Effect Transistors". In: *Applied Physics Letters* 86.3 (Jan. 2005), p. 033901. ISSN: 0003-6951. DOI: 10.1063/1.1853531.

- [8] Micha E. Spira and Aviad Hai. "Multi-Electrode Array Technologies for Neuroscience and Cardiology". en. In: *Nature Nanotechnology* 8.2 (Feb. 2013), pp. 83–94. ISSN: 1748-3387, 1748-3395. DOI: 10.1038/nnano.2012.265.
- [9] Sabrina Weidlich. "Nanoscale 3D Structures towards Improved Cell-Chip Coupling on Microelectrode Arrays". PhD thesis. RWTH Aachen, 2017.
- [10] Daniel Axelrod. "Cell-Substrate Contacts Illuminated by Total Internal Reflection Fluorescence". en. In: *The Journal of Cell Biology* 89.1 (Apr. 1981), pp. 141–145. ISSN: 0021-9525, 1540-8140. DOI: 10.1083/jcb.89.1.141.
- [11] Dieter Braun and Peter Fromherz. "Fluorescence Interferometry of Neuronal Cell Adhesion on Microstructured Silicon". en. In: *Physical Review Letters* 81.23 (Dec. 1998), pp. 5241–5244. ISSN: 0031-9007, 1079-7114. DOI: 10.1103/PhysRevLett.81.5241.
- [12] Günter Wrobel et al. "Transmission Electron Microscopy Study of the Cell-Sensor Interface". en. In: *Journal of The Royal Society Interface* 5.19 (Feb. 2008), pp. 213–222. ISSN: 1742-5689, 1742-5662. DOI: 10.1098/rsif.2007.1094.
- [13] Francesca Santoro et al. "Interfacing Electrogenic Cells with 3D Nanoelectrodes: Position, Shape, and Size Matter". en. In: *ACS Nano* 8.7 (July 2014), pp. 6713–6723. ISSN: 1936-0851, 1936-086X. DOI: 10.1021/nn500393p.
- [14] Karl-Friedrich Giebel et al. "Imaging of Cell/Substrate Contacts of Living Cells with Surface Plasmon Resonance Microscopy". en. In: *Biophysical Journal* 76.1 (Jan. 1999), pp. 509–516. ISSN: 00063495. DOI: 10.1016/S0006-3495(99)77219-X.
- [15] Koji Toma, Hiroshi Kano, and Andreas Offenhäusser. "Label-Free Measurement of Cell–Electrode Cleft Gap Distance with High Spatial Resolution Surface Plasmon Microscopy". en. In: *ACS*

- Nano* 8.12 (Dec. 2014), pp. 12612–12619. ISSN: 1936-0851, 1936-086X. DOI: 10.1021/nn505521e.
- [16] Eva Kreysing et al. “Nanometer-Resolved Mapping of Cell-Substrate Distances of Contracting Cardiomyocytes Using Surface Plasmon Resonance Microscopy”. In: *ACS Nano* (Sept. 2018). ISSN: 1936-0851. DOI: 10.1021/acsnano.8b01396.
- [17] Richard Klabunde. *Cardiovascular Physiology Concepts*. Philadelphia, PA: Lippincott Williams & Wilkins/Wolters Kluwer, 2012. ISBN: 1-4511-1384-6.
- [18] Bruce Alberts et al. *Molecular Biology of the Cell*. New York, NY: Garland Science, Taylor and Francis Group, 2015. ISBN: 978-0-8153-4464-3.
- [19] Iain D. Campbell and Martin J. Humphries. “Integrin Structure, Activation, and Interactions”. In: *Cold Spring Harbor Perspectives in Biology* 3.3 (Mar. 2011). ISSN: 1943-0264. DOI: 10.1101/cshperspect.a004994.
- [20] Mark Bear, Barry Connors, and Michael A. Paradiso. *Neurowissenschaften*. Heidelberg: Spektrum, 2009. ISBN: 978-3-8274-2075-6.
- [21] Allen M. Samarel. “Costameres, Focal Adhesions, and Cardiomyocyte Mechanotransduction”. eng. In: *American Journal of Physiology. Heart and Circulatory Physiology* 289.6 (Dec. 2005), H2291–2301. ISSN: 0363-6135. DOI: 10.1152/ajpheart.00749.2005.
- [22] Martin Flück et al. “Fibre-Type Specific Concentration of Focal Adhesion Kinase at the Sarcolemma: Influence of Fibre Innervation and Regeneration”. en. In: *Journal of Experimental Biology* 205.16 (Aug. 2002), pp. 2337–2348. ISSN: 0022-0949, 1477-9145.
- [23] Thomas Pollard and William C. Earnshaw. *Cell Biology*. Heidelberg: Spektrum, Akad. Verl, 2007. ISBN: 3-8274-1861-5.

## Bibliography

- [24] Timo Betz et al. "Growth Cones as Soft and Weak Force Generators". en. In: *Proceedings of the National Academy of Sciences* 108.33 (Aug. 2011), pp. 13420–13425. ISSN: 0027-8424, 1091-6490. DOI: 10.1073/pnas.1106145108.
- [25] Nils Hersch et al. "The Constant Beat: Cardiomyocytes Adapt Their Forces by Equal Contraction upon Environmental Stiffening". eng. In: *Biology Open* 2.3 (Mar. 2013), pp. 351–361. ISSN: 2046-6390. DOI: 10.1242/bio.20133830.
- [26] Thermo Fisher Scientific. *Fluo-4, AM, Cell Permeant, Product: F14201*. <https://www.thermofisher.com/order/catalog/product/F14201>. (accessed 2018-05-15T17:27:53Z).
- [27] Gleb Shtengel et al. "Interferometric Fluorescent Super-Resolution Microscopy Resolves 3D Cellular Ultrastructure". en. In: *Proceedings of the National Academy of Sciences* 106.9 (Mar. 2009), pp. 3125–3130. ISSN: 0027-8424, 1091-6490. DOI: 10.1073/pnas.0813131106.
- [28] Eric Betzig. *3/9/15 at UC Berkeley*. UC Berkeley, TED talk, Mar. 15.
- [29] A. S. G. Curtis. "The Mechanism of Adhesion of Cells to Glass: A Study by Interference Reflection Microscopy". en. In: *The Journal of Cell Biology* 20.2 (Feb. 1964), pp. 199–215. ISSN: 0021-9525, 1540-8140. DOI: 10.1083/jcb.20.2.199.
- [30] F.S. Sjöstrand and V. Hanzon. "Membrane Structures of Cytoplasm and Mitochondria in Exocrine Cells of Mouse Pancreas as Revealed by High Resolution Electron Microscopy". In: 7 (Apr. 1954).
- [31] Cornelia Monzel et al. "Probing Biomembrane Dynamics by Dual-Wavelength Reflection Interference Contrast Microscopy". en. In: *ChemPhysChem* 10.16 (Nov. 2009), pp. 2828–2838. ISSN: 14394235, 14397641. DOI: 10.1002/cphc.200900645.

- [32] Armin Lambacher and Peter Fromherz. "Fluorescence Interference-Contrast Microscopy on Oxidized Silicon Using a Monomolecular Dye Layer". en. In: *Applied Physics A: Materials Science & Processing* 63.3 (Aug. 1996), pp. 207–216. ISSN: 0947-8396, 1432-0630. DOI: 10.1007/s003390050374.
- [33] Helga Sorribas et al. "Adhesion Proteins for a Tight Neuron–Electrode Contact". en. In: *Journal of Neuroscience Methods* 104.2 (Jan. 2001), pp. 133–141. ISSN: 01650270. DOI: 10.1016/S0165-0270(00)00333-2.
- [34] Aftin M. Ross et al. "Physical Aspects of Cell Culture Substrates: Topography, Roughness, and Elasticity". en. In: *Small* 8.3 (Feb. 2012), pp. 336–355. ISSN: 16136810. DOI: 10.1002/smll.201100934.
- [35] Andreea Belu et al. "Ultra-Thin Resin Embedding Method for Scanning Electron Microscopy of Individual Cells on High and Low Aspect Ratio 3D Nanostructures: ULTRA-THIN RESIN EMBEDDING METHOD". en. In: *Journal of Microscopy* 263.1 (July 2016), pp. 78–86. ISSN: 00222720. DOI: 10.1111/jmi.12378.
- [36] Francesca Santoro et al. "Revealing the Cell–Material Interface with Nanometer Resolution by Focused Ion Beam/Scanning Electron Microscopy". en. In: *ACS Nano* 11.8 (Aug. 2017), pp. 8320–8328. ISSN: 1936-0851, 1936-086X. DOI: 10.1021/acsnano.7b03494.
- [37] Alexey I. Chizhik et al. "Metal-Induced Energy Transfer for Live Cell Nanoscopy". en. In: *Nature Photonics* 8.2 (Feb. 2014), pp. 124–127. ISSN: 1749-4885, 1749-4893. DOI: 10.1038/nphoton.2013.345.
- [38] Theodor Förster. "Zwischenmolekulare Energiewanderung und Fluoreszenz". de. In: *Annalen der Physik* 437.1-2 (1948), pp. 55–75. ISSN: 00033804, 15213889. DOI: 10.1002/andp.19484370105.

## Bibliography

- [39] James Pawley. *Handbook of Biological Confocal Microscopy*. New York, NY: Springer, 2006. ISBN: 978-0-387-45524-2.
- [40] Jörg Enderlein. "Single-Molecule Fluorescence near a Metal Layer". en. In: *Chemical Physics* 247.1 (Aug. 1999), pp. 1–9. ISSN: 03010104. DOI: 10.1016/S0301-0104(99)00097-X.
- [41] Silke Seyock et al. "Interfacing Neurons on Carbon Nanotubes Covered with Diamond". en. In: *RSC Advances* 7.1 (2017), pp. 153–160. ISSN: 2046-2069. DOI: 10.1039/C6RA20207A.
- [42] John Bozzola. *Electron Microscopy : Principles and Techniques for Biologists*. Sudbury, Mass: Jones and Bartlett, 1999. ISBN: 978-0-7637-0192-5.
- [43] Lukas Novotny. *Principles of Nano-Optics*. Cambridge: Cambridge University Press, 2006. ISBN: 978-0-521-83224-3.
- [44] Koyo Watanabe et al. "Scanning and Non-Scanning Surface Plasmon Microscopy to Observe Cell Adhesion Sites". en. In: *Biomedical Optics Express* 3.2 (Feb. 2012), p. 354. ISSN: 2156-7085, 2156-7085. DOI: 10.1364/BOE.3.000354.
- [45] Alexander W Peterson et al. "High Resolution Surface Plasmon Resonance Imaging for Single Cells". en. In: *BMC Cell Biology* 15.1 (2014), p. 35. ISSN: 1471-2121. DOI: 10.1186/1471-2121-15-35.
- [46] Xian-Wei Liu et al. "Plasmonic-Based Electrochemical Impedance Imaging of Electrical Activities in Single Cells". In: *Angewandte Chemie International Edition* 56.30 (), pp. 8855–8859. DOI: 10.1002/anie.201703033.
- [47] Lotfi Berguiga et al. "Time-Lapse Scanning Surface Plasmon Microscopy of Living Adherent Cells with a Radially Polarized Beam". en. In: *Applied Optics* 55.6 (Feb. 2016), p. 1216. ISSN: 0003-6935, 1539-4522. DOI: 10.1364/AO.55.001216.

- [48] Sabine Szunerits and Rabah Boukherroub. *Introduction to Plasmonics : Advances and Applications*. Singapore: Pan Stanford Publishing, 2015. ISBN: 978-981-4613-13-2.
- [49] Max Born and Emil Wolf. *Principles of Optics : Electromagnetic Theory of Propagation, Interference and Diffraction of Light*. Cambridge New York: Cambridge University Press, 1999. ISBN: 0-521-64222-1.
- [50] Erwin Kretschmann. "Die Bestimmung optischer Konstanten von Metallen durch Anregung von Oberflächenplasmaschwingungen". de. In: *Zeitschrift für Physik A Hadrons and nuclei* 241.4 (Aug. 1971), pp. 313–324. ISSN: 0939-7922. DOI: 10.1007/BF01395428.
- [51] Andreas Otto. "Excitation of Nonradiative Surface Plasma Waves in Silver by the Method of Frustrated Total Reflection". en. In: *Zeitschrift für Physik A Hadrons and nuclei* 216.4 (Aug. 1968), pp. 398–410. ISSN: 0939-7922. DOI: 10.1007/BF01391532.
- [52] Bo Huang, Fang Yu, and Richard N. Zare. "Surface Plasmon Resonance Imaging Using a High Numerical Aperture Microscope Objective". In: *Analytical Chemistry* 79.7 (2007), pp. 2979–2983. DOI: 10.1021/ac062284x.
- [53] Alexander W. Peterson et al. "Surface Plasmon Resonance Microscopy: Achieving a Quantitative Optical Response". In: *The Review of scientific instruments* 87.9 (Sept. 2016), p. 093703. ISSN: 0034-6748. DOI: 10.1063/1.4962034.
- [54] Han-Min Tan et al. "High Resolution Quantitative Angle-Scanning Widefield Surface Plasmon Microscopy". In: *Scientific Reports* 6 (Feb. 2016), p. 20195.
- [55] Kouyou Watanabe, Nobuhiro Horiguchi, and Hiroshi Kano. "Optimized Measurement Probe of the Localized Surface Plasmon Microscope by Using Radially Polarized Illumination". en. In: *Ap-*

## Bibliography

- plied Optics* 46.22 (Aug. 2007), p. 4985. ISSN: 0003-6935, 1539-4522. DOI: 10.1364/AO.46.004985.
- [56] Lotfi Berguiga et al. "Amplitude and Phase Images of Cellular Structures with a Scanning Surface Plasmon Microscope". en. In: *Optics Express* 19.7 (Mar. 2011), p. 6571. ISSN: 1094-4087. DOI: 10.1364/OE.19.006571.
- [57] Koyo Watanabe et al. "High Resolution Imaging of Patterned Model Biological Membranes by Localized Surface Plasmon Microscopy". en. In: *Applied Optics* 49.5 (Feb. 2010), p. 887. ISSN: 0003-6935, 1539-4522. DOI: 10.1364/AO.49.000887.
- [58] Hossein Hassani, Roger Wördenweber, and Andreas Offenhäusser. "Simulation and Analysis of Cell-Substrate Interface in Surface Plasmon Resonance Microscopy". Monography. ICS-8, Forschungszentrum Jülich: Universität Köln, Apr. 2017.
- [59] Michael Bass et al. *Handbook of Optics*. New York: McGraw-Hill, 2010. ISBN: 978-0-07-149889-0.
- [60] Aleksandar D. Rakić et al. "Optical Properties of Metallic Films for Vertical-Cavity Optoelectronic Devices". In: *Appl. Opt.* 37.22 (Aug. 1998), pp. 5271–5283. DOI: 10.1364/AO.37.005271.
- [61] Dmitry I. Yakubovsky et al. "Optical Constants and Structural Properties of Thin Gold Films". In: *Opt. Express* 25.21 (Oct. 2017), pp. 25574–25587. DOI: 10.1364/OE.25.025574.
- [62] Richard A. Meyer. "Light Scattering from Biological Cells: Dependence of Backscatter Radiation on Membrane Thickness and Refractive Index". en. In: *Applied Optics* 18.5 (Mar. 1979), p. 585. ISSN: 0003-6935, 1539-4522. DOI: 10.1364/AO.18.000585.
- [63] Mirjam Schürmann et al. "Cell Nuclei Have Lower Refractive Index and Mass Density than Cytoplasm". en. In: *Journal of Biophotonics* 9.10 (Oct. 2016), pp. 1068–1076. ISSN: 1864063X. DOI: 10.1002/jbio.201500273.

- [64] Eugene Hecht. *Optik*. München: De Gruyter, 2014. ISBN: 978-3-11-034796-8.
- [65] Ifan Hughes and Thomas Hase. *Measurements and Their Uncertainties : A Practical Guide to Modern Error Analysis*. Oxford New York: Oxford University Press, 2010. ISBN: 978-0-19-956633-4.
- [66] Ida Z. Kozma, Patrizia Krok, and Eberhard Riedle. "Direct Measurement of the Group-Velocity Mismatch and Derivation of the Refractive-Index Dispersion for a Variety of Solvents in the Ultra-violet". In: *J. Opt. Soc. Am. B* 22.7 (July 2005), pp. 1479–1485. DOI: 10.1364/JOSAB.22.001479.
- [67] John E. Saunders et al. "Refractive Indices of Common Solvents and Solutions at 1550nm". EN. In: *Applied Optics* 55.4 (Feb. 2016), pp. 947–953. ISSN: 2155-3165. DOI: 10.1364/AO.55.000947.
- [68] Petr Pacak. "Polarizability and Molecular Radius of Dimethyl-Sulfoxide and Dimethylformamide from Refractive Index Data". en. In: *Journal of Solution Chemistry* 16.1 (Jan. 1987), pp. 71–77. ISSN: 0095-9782, 1572-8927. DOI: 10.1007/BF00647016.
- [69] I. H. Malitson. "Interspecimen Comparison of the Refractive Index of Fused Silica,†". In: *J. Opt. Soc. Am.* 55.10 (Oct. 1965), pp. 1205–1209. DOI: 10.1364/JOSA.55.001205.
- [70] J. Rheims, J. Köser, and T. Wriedt. "Refractive-Index Measurements in the near-IR Using an Abbe Refractometer". en. In: *Measurement Science and Technology* 8.6 (1997), p. 601. ISSN: 0957-0233. DOI: 10.1088/0957-0233/8/6/003.
- [71] *Olympus Microscopy Resource Center — Evanescent Field Penetration Depth - Java Tutorial*. <http://olympus.magnet.fsu.edu/primer/java/tirf/penetration/index.html>. (accessed 2018-06-01T10:32:18Z).

## Bibliography

- [72] Carl Zeiss Microscopy, LLC, United States > Fluorescence Dye and Filter Database > Overview Filter Sets > Filter Set. <https://www.micro-shop.zeiss.com/?s=7332906525ee43&l=en&p=us&f=f&a=v&b=f&id=488015-0000-000&o=>. (accessed 2018-05-15T18:01:34Z).
- [73] Benjamin Wolters. "Zell-Biomechanische Untersuchungen von Modellen Des Herzmuskelgewebes". In: *Dissertation, Rheinische Friedrich-Wilhelms-Universität Bonn* (2015), p. 185.
- [74] Jin Lu and Jinghong Li. "Label-Free Imaging of Dynamic and Transient Calcium Signaling in Single Cells". en. In: *Angewandte Chemie International Edition* 54.46 (Nov. 2015), pp. 13576–13580. ISSN: 14337851. DOI: 10.1002/anie.201505991.
- [75] Xian-Wei Liu et al. "Plasmonic-Based Electrochemical Impedance Imaging of Electrical Activities in Single Cells". eng. In: *Angewandte Chemie (International Ed. in English)* 56.30 (July 2017), pp. 8855–8859. ISSN: 1521-3773. DOI: 10.1002/anie.201703033.
- [76] Ivan Valent et al. "Spatial and Temporal Ca<sup>2+</sup>, Mg<sup>2+</sup>, and ATP<sup>2-</sup> Dynamics in Cardiac Dyads during Calcium Release". en. In: *Biochimica et Biophysica Acta (BBA) - Biomembranes* 1768.1 (Jan. 2007), pp. 155–166. ISSN: 00052736. DOI: 10.1016/j.bbamem.2006.08.020.
- [77] John J. Molina et al. "Ions in Solutions: Determining Their Polarizabilities from First-Principles". en. In: *The Journal of Chemical Physics* 134.1 (Jan. 2011), p. 014511. ISSN: 0021-9606, 1089-7690. DOI: 10.1063/1.3518101.
- [78] Martyn P. Mahaut-Smith et al. "Properties of the Demarcation Membrane System in Living Rat Megakaryocytes". In: *Biophysical Journal* 84.4 (Apr. 2003), pp. 2646–2654. ISSN: 0006-3495. DOI: 10.1016/S0006-3495(03)75070-X.

- [79] Hongyuan Jiang and Sean X. Sun. "Cellular Pressure and Volume Regulation and Implications for Cell Mechanics". en. In: *Biophysical Journal* 105.3 (Aug. 2013). JiangCellularPressureandVolumeRegulation2013, pp. 609–619. ISSN: 00063495. DOI: 10.1016/j.bpj.2013.06.021.
- [80] B. Ian Hutchins and Susan Wray. "Capture of Microtubule Plus-Ends at the Actin Cortex Promotes Axophilic Neuronal Migration by Enhancing Microtubule Tension in the Leading Process". English. In: *Frontiers in Cellular Neuroscience* 8 (2014). ISSN: 1662-5102. DOI: 10.3389/fncel.2014.00400.
- [81] Andrew G. Clark, Kai Dierkes, and Ewa K. Paluch. "Monitoring Actin Cortex Thickness in Live Cells". en. In: *Biophysical Journal* 105.3 (Aug. 2013), pp. 570–580. ISSN: 00063495. DOI: 10.1016/j.bpj.2013.05.057.
- [82] Mathias P. Clausen et al. "Dissecting the Actin Cortex Density and Membrane-Cortex Distance in Living Cells by Super-Resolution Microscopy". In: *Journal of Physics D* 50.6 (Feb. 2017). ISSN: 0022-3727. DOI: 10.1088/1361-6463/aa52a1.
- [83] Emilie L. Grzywa et al. "High-Resolution Analysis of Neuronal Growth Cone Morphology by Comparative Atomic Force and Optical Microscopy". en. In: *Journal of Neurobiology* 66.14 (Dec. 2006), pp. 1529–1543. ISSN: 00223034, 10974695. DOI: 10.1002/neu.20318.
- [84] Junichi Nakai, Masamichi Ohkura, and Keiji Imoto. "A High Signal-to-Noise  $\text{Ca}^{2+}$  Probe Composed of a Single Green Fluorescent Protein". en. In: *Nature Biotechnology* 19.2 (Feb. 2001), pp. 137–141. ISSN: 1546-1696. DOI: 10.1038/84397.
- [85] Berthold K. P. Horn. "Closed-Form Solution of Absolute Orientation Using Unit Quaternions". en. In: *Journal of the Optical Society*

## *Bibliography*

*of America A 4.4* (Apr. 1987), p. 629. ISSN: 1084-7529, 1520-8532.

DOI: 10.1364/JOSAA.4.000629.

Band / Volume 175

**Operando Chemistry and Electronic Structure of Electrode / Ferroelectric Interfaces**

S. Gonzalez (2018), 172 pp  
ISBN: 978-3-95806-341-9

Band / Volume 176

**Magnetic Properties of Self-assembled Manganese Oxide and Iron Oxide Nanoparticles**

Spin Structure and Composition  
X. Sun (2018), ii, 178 pp  
ISBN: 978-3-95806-345-7

Band / Volume 177

**Model-based reconstruction of magnetisation distributions in nanostructures from electron optical phase images**

J. Caron (2018), XXI, 183 pp  
ISBN: 978-3-95806-346-4

Band / Volume 178

**Simultaneous dual-color imaging on single-molecule level on a Widefield microscope and applications**

R. Ledesch (2018), ix, 119 pp  
ISBN: 978-3-95806-348-8

Band / Volume 179

**Methoden der Leitfähigkeitsuntersuchung mittels Rasterkraftmikroskop und deren Anwendung auf Barium Titanat Systeme**

B. Reichenberg (2018), x, 144 pp  
ISBN: 978-3-95806-350-1

Band / Volume 180

**Manipulation of magnetism in iron oxide nanoparticle / BaTiO<sub>3</sub> composites and low-dimensional iron oxide nanoparticle arrays**

L. Wang (2018), VI, 151 pp  
ISBN: 978-3-95806-351-8

Band / Volume 181

**Creating and characterizing a single molecule device for quantitative surface science**

M. Green (2018), viii, 142 pp (untersch. Pag.)  
ISBN: 978-3-95806-352-5

Band / Volume 182

**8<sup>th</sup> Georgian-German School and Workshop in Basic Science**

A. Kacharava (Ed.) erscheint nur als CD (2018)  
ISBN: 978-3-95806-353-2

Band / Volume 183

**Topological properties of complex magnets from an advanced *ab-initio* Wannier description**

J.-P. Hanke (2018), xi, 173 pp

ISBN: 978-3-95806-357-0

Band / Volume 184

**Translation Initiation with 70S Ribosomes: A Single Molecule Study**

C. Remes (2018), iv, 113 pp

ISBN: 978-3-95806-358-7

Band / Volume 185

**Scanning tunneling potentiometry at nanoscale defects in thin films**

F. Lüpke (2018), iv, 144 pp (untersch. Pag.)

ISBN: 978-3-95806-361-7

Band / Volume 186

**Inelastic neutron scattering on magnetocaloric compounds**

N. Biniskos (2018), iii, 92 pp

ISBN: 978-3-95806-362-4

Band / Volume 187

**Magnetic Order and Excitation in Frustrated Pyrochlore 5d - Transition Metal Oxides**

E. Feng (2018), iv, 182 pp

ISBN: 978-3-95806-365-5

Band / Volume 188

**Finite-Difference Time-Domain Simulations Assisting to Reconstruct the Brain's Nerve Fiber Architecture by 3D Polarized Light Imaging**

M. Menzel (2018), ix, 296 pp

ISBN: 978-3-95806-368-6

Band / Volume 189

**Characterization of the cell-substrate interface using surface plasmon resonance microscopy**

E. M. Kreysing (2018), xiii, 260 pp

ISBN: 978-3-95806-369-3



Schlüsseltechnologien / Key Technologies  
Band / Volume 189  
ISBN 978-3-95806-369-3